12-2017

Exploration of Equal Tune Transverse Coupling in the Spallation Neutron Source Accumulator Ring

Robert Edward Potts III
University of Tennessee, Knoxville, rpotts1@vols.utk.edu

To the Graduate Council:

I am submitting herewith a dissertation written by Robert Edward Potts III entitled "Exploration of Equal Tune Transverse Coupling in the Spallation Neutron Source Accumulator Ring." I have examined the final electronic copy of this dissertation for form and content and recommend that it be accepted in partial fulfillment of the requirements for the degree of Doctor of Philosophy, with a major in Physics.

Geoffrey L. Greene, Major Professor

We have read this dissertation and recommend its acceptance:

Sarah M. Cousineau, Jeffrey A. Holmes, Soren P. Sorensen, Charles S. Feigerle

Accepted for the Council:

Dixie L. Thompson

Vice Provost and Dean of the Graduate School

(Original signatures are on file with official student records.)

Exploration of Equal Tune Transverse Coupling in the Spallation Neutron Source Accumulator Ring

A Dissertation Presented for the

Doctor of Philosophy

Degree

The University of Tennessee, Knoxville

Robert Edward Potts III

December 2017

For all my mentors, thank you for challenging me to go further.

Acknowledgements

As I reach the conclusion of my doctorate, I am very thankful to look back on a time well spent. I know that at every level this work could not have been possible without the constant support and encouragement of my family, friends, and mentors. I am, in some part, the person I am today because of the support of each of these people. I am grateful for the opportunity to thank some of them here.

First, I would like to thank my parents and family for supporting me and prioritizing my education throughout my entire life. They have been there for me in an inestimable number of ways, from practicing multiplication tables to teaching me programming to paying for school. They have sacrificed both time and money for my education, and I am eternally grateful.

I would like to thank my wonderful advisor, Dr. Sarah Cousineau. Sarah is an amazing accelerator physicist and group leader. I have always been impressed by her ability to continually deliver top-quality research, papers, and talks. She truly sets the standard of excellence. She has gone out of her way to support me, both while I conducted my research and while I have been writing. I know that there are many students, including myself, who have benefited significantly from her mentorship. Thank you for always supporting students, especially this one.

I have honestly benefited from having two advisors in accelerator physics. When I started, I was twice advised to make sure that I had a friendly face on my committee. I would like to thank Dr. Jeffrey Holmes for always being that friendly face. No matter how confusing a question might be, Jeff has always been willing to guide me

towards the right answer. And, whenever I have hit problems with my simulations, Jeff has been there with a little keyboard onomatopoeia to help me.

I have had the fortunate struggle of working for a very distinguished committee. My heartfelt thanks go to Drs. Geoffrey Greene, Sarah Cousineau, Charles Feigerle, Jeffrey Holmes, and Soren Sorensen. Each has taken time out of his or her busy schedule to support, instruct, and mentor me during this difficult journey. I thank them for always expecting my best. My first quantum mechanics course at the University of Tennessee was with Geoff. He quickly learned of my desire to research accelerator physics at the SNS. I will never forget how he has gone out of his way to support me ever since. I was advised to reach out to Dr. Feigerle because he helped design the SNS stripper foil. I have always appreciated his immediate willingness to support me and provide an outside perspective on my research. Finally, I am thankful to Dr. Sorensen for his magnificent and spontaneous questions. He has a profound knack for testing both a student's general knowledge and comprehension of how their research connects with the general field of physics. This has led to some truly interesting dialogue, including one case that ended with Dr. Sorensen stating that if the student knew the answer to his question then they could go together to claim the next Nobel Prize.

The work presented in this study would not have been possible without years of dedication from Dr. Willem Blokland. He has been responsible for developing the initial Electron Scanner diagnostic device into a fully-functioning prototype, ready for regular use. He has always been willing to go on shift to help configure the device for use. He has also been willing to extensively review the hardware and software with me to make sure that I fully understand how the device works. He has been responsible for developing and maintaining countless diagnostic at the SNS, all of which now produce outstanding research. And, again, the principal work in this study would have been dramatically different without his years of dedication.

It is difficult to properly acknowledge the important role that a group of people can play. That having been said, I am very appreciative of the years of support and

mentoring from the SNS Beam Science and Technology (BeST) Group, especially that of Drs. Sarah Cousineau, Jeffrey Holmes, Willem Blokland, Michael Plum, Andrei Shishlo, Nicholas Evans, Christopher Allen, Alexander Aleksandrov, Timofey Gorlov, Thomas Pelaia, and the late Viatcheslav Danilov. Years ago, the APBIIS Group welcomed me to their regular accelerator physics team meetings. Being a part of the group and sharing coffee has meant a great deal to me over the years.

I would like to thank Drs. John Galambos, Kevin Jones, and George Dodson for their general leadership and mentorship. While they have not been directly involved with my research, they have always been willing to talk to me about the bigger picture in accelerator physics research and their personal research experiences.

I have benefited tremendously from the continual support of Angela Woody, Lisa Eady, Gerald Smith, and Jayme Green. They have held and continue to hold the scientific staff together by making sure that everything runs seamlessly.

Of course, the SNS would not be possible without an all-around world-class staff and the endless hours of dedication required of them to maintain and operate the most intense pulsed spallation neutron source in the world. I have particularly enjoyed my time on shift with all of the operators. I would like to thank them for making sure that I didn't break a multi-billion dollar machine. I thought I came close once or twice, but they have always watched my back. I would like to thank Julius Fazekas for providing me with any survey information that I need and explaining it to me. I would also like to thank Joey Weaver for configuring hardware for several of my studies and making sure that everything went well.

I would like to thank the faculty and staff of the United States Particle Accelerator School for their continued support. In particular, Drs. William Barletta and S.Y. Lee for their dedication to accelerator physics education. It is not possible to mention the accelerator school without thanking Susan Winchester and Irina Novitski for their continual support of the program and personal encouragement over many years.

I would like to thank the many educators and administrative staff who have had a profound impact on my life. You often hear pessimists share the false maxim

"Those Who Can't Do, Teach". However, especially at times like this, I fondly remember the poem *The Bridge Builder*. I am very grateful to all those bridge builders who have dedicated their lives to supporting, educating, and mentoring others. I would especially like to thank the following. Dean Linda Snodgrass, Mr. David Mouron and the late Mr. Bill Walton for encouraging me to pursue math and science throughout my time at McCallie High School. Drs. Thomas Gally and Darrel Smith for their awesome mentorship, which started during my first year at Embry-Riddle Aeronautical University and has continued to this day. Dr. Marianne Breinig for helping me become a better instructor and being the qualifying exam drill sergeant that all graduate physics students need. And, Chrisanne Romeo, Maria Fawver, Brad Gardner, and Julie Harden for always taking care of me at the University of Tennessee.

One of the highlights of my time in Knoxville has been joining the Masonic fraternity. This organization has become an extension of my family and has allowed me to connect with the world at large. Through this organization, I have met many people across the world, most of whom would have otherwise remained at a perpetual distance.

I would like to thank my excellent team of reviewers: Gilbert and Marjorie Grimsley, Claire A. Ellis, Ph.D., and Noah Birge. They have gone way above and beyond in providing immediate and helpful feedback. I would also like to thank Noah Birge, Chase Sliger, and Paul Thompson for listening to me practice my defense and providing constructive feedback.

Finally, I would like to thank my friends, whose tireless encouragement has made the difference over the years.

To everyone, thank you for your continued support.

Vouchesafe thine aid,

Almighty Father of the Universe,

to this our present convention...

OPENING TO A TRADITIONAL MASONIC PRAYER

Abstract

The development of hadron machines is one of the main areas of focus in accelerator technology and is specifically called out as a priority in the high energy physics 10-year plan[70]. The trend for future accelerators is to move towards very high-intensity high-power accelerators to be used as proton drivers for secondary particles, target stations, and high-energy accelerators. These accelerators require lower beam losses and more stringent beam controls to maintain typical loss levels and meet specific final beam distributions.

This study focuses on the recently documented coupling resonance in the Spallation Neutron Source (SNS) accumulator ring. It was previously demonstrated that certain beam configurations resulted in a loss of independent control of the on-target transverse beam profiles[12]. This is an issue for SNS production operations. Yet there has not been a robust experimental exploration of the coupling resonance aimed at understanding the effect on the evolution of the beam distribution. The SNS is an ideal facility for this exploration.

We studied the coupling experimentally using traditional wire scanners and a novel Electron Scanner. We demonstrated coupling in both the RMS size and beam profile that was correlated with the tune split. The coupling started at low intensity and had an inverse relationship with intensity; indicating that it is not a Montague resonance. We modeled one experiment using a realistic self-consistent particle-in-cell simulation in PyORBIT. We demonstrated strong coupling that was very sensitivity to the tune split. By comparing fringe field models, we demonstrated that fringe fields

are the source of the resonance. Our final experiment focused on mitigating the effects during operations. We used the Electron Scanner to demonstrate that the most recent production settings produced no coupling. Further mitigation of the resonance should not be necessary, provided that the tunes remain split. Additionally, we calibrated the newly installed Electron Scanner by measuring the undeflected electron beam, the Twiss parameters, and establishing a benchmark with the wire scanner emittance station. In conclusion, this dissertation constitutes a significant advancement to the overall knowledge of equal tune resonances in circular particle accelerators, especially the effect on the beam profiles.

Table of Contents

List of Tables

List of Figures

Chapter 1

Introduction

Particle accelerators were developed to investigate the fundamental properties of matter. Since their origins, the development of accelerators has been driven by their application to other areas of research. More powerful accelerators have facilitated an increased understanding of the world. However, as the technology has developed and become more recognized, accelerators have also been applied to various other fields, including medical physics and food sanitation. Modern accelerators have reached a level of development where they are starting to be used as proton drivers for secondary particles, target stations, and other applications. These applications are collectively referred to as accelerator driven systems (ADSs). Accelerators used in ADSs push the frontiers of accelerator physics. The trend for future accelerators is to continue increasing beam intensity, beam power, and machine reliability. With these increases, tighter control restraints are required in order to maintain acceptable safety levels and achieve more advanced technical objectives. Specifically, these new applications require lower beam losses and more stringent beam controls to maintain typical loss levels and meet specific final beam distributions. Therefore, the development of hadron machines for use in ADSs is one of the main areas of focus in accelerator technology and is specifically called out as a priority in the high energy physics 10-year plan[70].

The Spallation Neutron Source (SNS) is the most powerful pulsed spallation neutron source in the world. One of the accelerator requirements is to maintain a specific uniform beam distribution on the final target. This uniform distribution reduces peak particle densities, which are associated with increasing target lifetimes. For this specific reason, the SNS was designed to allow independent control of the transverse beam distributions. However, a resonance in the accumulator ring has been associated with a reduction of control in certain beam configurations. The goals of the proposed thesis are to characterize the fourth-order coupling resonance in the SNS ring, and to design and test mitigation methods.

This chapter is devoted to creating a general framework for this study, including reviewing the history of the field and establishing the objectives of this study. In Section 1.1 we introduce the key concepts in accelerator beam dynamics associated with this work. In Section 1.2 we review existing research into resonances. In Section 1.3 we introduce the SNS and discuss how this work benefits the SNS operations. In Section 1.4, we introduce the three goals of this study. Finally, in Section 1.5, we discuss the organization of this study.

1.1 Understanding Beam Dynamics

When designing an experiment using only a few low-energy particles traveling short distances in a low quality vacuum, the ability to control the path of the particles is not an issue. As various technologies developed, higher beam energies and greater number densities brought into question the internal dynamics and collective motion of the beam.

1.1.1 Space Charge Forces

Traditionally, the effects of Coulomb repulsion, or space charge, have been negligible compared with those of the external focusing fields due to the low number density

of particles being accelerated. With the accelerator advancements of the 1950's, including strong focusing[9] and the parameterization of the transverse equations of motion[10], it became possible to design and build facilities that had greater particle densities and higher beam energies. It was not until this time that it became necessary for accelerator physicists to incorporate intra-beam dynamics into their machine designs.

Until recently, space charge effects were considered a problem mainly for linear accelerators, where particle densities are higher and particle velocities are lower. With the latest generation of modern accelerators, whose construction began around the end of the century, it was recognized that space charge effects could be significant in synchrotrons as well, due to both the high beam intensities and the periodic nature of the system. Though the beam particle densities are lower in synchrotrons than in linacs, longer storage times and tighter beam loss constraints result in more stringent requirements on beam control. It is now widely accepted that controlling the beam loss in high intensity hadron machines requires a firm understanding of the space charge effects.

One particular space charge effect that is problematic for the most recent generation of high intensity machines is space-charge-induced coupling in the transverse planes, which compromises the independent control of the transverse beam distributions. It is desirable in any modern synchrotron to have independent control of the transverse planes. The reasons are two-fold: 1) A lack of precise beam control in each plane can lead to undesirable beam loss and radiation; and, 2) Beam targets and interaction point regions often have separate tightly constrained specifications for the beam configuration, such as size or peak density, in each plane.

1.1.2 Resonances

Forces external to the designed accelerator lattice can cause resonances within the beam when they occur at regular intervals in the beam motion. When resonances are

not properly anticipated or mitigated, they can result in a loss of control of the beam dynamics, including a complete loss of the beam. The most common and dangerous source of resonances are the physical imperfections of the lattice. While physical imperfections cannot be avoided, the beam parameters can be selected to reduce the effects of these errors. A more detailed presentation of resonances will be presented in Chapter 3.

1.2 History of Resonances

Prior to modern accelerators, resonances were studied extensively in the context of classical mechanics. Resonances were later applied to accelerators as beam dynamics became an important topic for accelerator design and development. The first applications were solely focused on resonances induced by alignment errors and non-linearities in design lattice elements. As accelerator beam intensities increased, the focus shifted away from more common and well-documented lower order lattice resonances towards higher order lattice resonances and space charge induced resonances.

1.2.1 Lattice Resonances

In 1958, Courant and Snyder officially published their seminal paper parameterizing betatron oscillations and applying the theory of resonances to circular accelerators[10]. Primarily focused on lattice errors and unstable beam configurations, Courant and Snyder derived integer and half-integer resonances, as well as second-order coupling resonances. They generally expanded these resonances to higher orders and discussed cases of instability arising from sum resonances.

In the period surrounding this research, other scientists around the world both expanded on present theories and devised various other methods for analytically deriving resonances. Moser used the method of isoenergetic reduction, which allowed

him to address rational tune values[67]. Schoch reproduced the work of Moser using periodic kicks in 1955 and later applied the method of "slowly varying amplitude and phase" to derive resonances and concluded with remarks regarding the construction of the CERN Proton Synchrotron (PS)[83]. Hagedorn extended Moser's work to two-dimensional systems[28] and then applied that work to betatron oscillations with the help of Schoch [29].

In 1976, Guignard would publish an essential guide to all coupled resonances, in which he would analytically derive the coupling coefficient, bandwidth and growth rates of resonances[27]. Two years later Guignard applied this research by examining the effects of various sources of perturbations, using the CERN Intersecting Storage Rings as an example[26].

In addition to analytical theories, lattice resonances have a long history of experimental studies. Of particular interest to our research are studies focusing on higher order resonances. In 1971, Morton and Spencer needed to optimize the luminosity of the Stanford Linear Accelerator Complex storage ring, SPEAR[66]. This was achieved through the use of several skew quadrupoles placed in the lattice to minimize the quadrupolar coupling, created from rotational alignment errors present in the lattice quadrupoles. Several decades later Safranek discussed using this same methodology to minimize coupling when he presented a new design and measurement of a low emittance lattice for the SPEAR storage ring[79].

In his text *Accelerator Physics*, Lee presented experimental results collected from the Indiana University Cyclotron Facility Cooler Ring as an example of linear coupling resonances[55]. In the IUCF, the primary source of the resonance was a solenoid used for cooling, however quadrupole tilt and orbit deviations in sextupoles were not ruled out. Independent control of the beam tunes were obtained by using skew quadrupoles.

Lee continued to explain that while sextupoles are traditionally associated with third order resonances, all higher order multipoles are capable of nonlinearities that, while usually negligible, can produce other higher order resonances under the right circumstances. In 1973, Ohnuma published results stating that sextupoles in the

Main Ring at the National Accelerator Laboratory were inducing a fourth order resonance[68]. The tune of the beam was selected to avoid the traditional third order resonances associated with sextupoles. However, they had not expected that second order effects of the strong sextupoles would produce intense fourth order resonances. This was discovered by noting the strength of the resonance and the dependence on the sextupole settings. Ohnuma cites private correspondence with Ruggiero as stating similar effects were being studied at SLAC's Positron-Electron Project and the ongoing development of Brookhaven National Laboratory's ISABELLE. All three accelerators would rely on strong sextupoles for long term beam storage during normal operations.

1.2.2 General Developments in Space Charge Resonances

In 1968, Montague published on the fourth-order non-linear coupling resonances which now bear his name[65]. Montague's work focused on the effects of tune-dependent coupling between the transverse planes of motion due to space charge. While others published on space charge effects, this work described the first resonances induced by space charge forces.

Sacherer was another early researcher in this area and was known for his 1968 dissertation describing the effects of space charge forces on the beam envelope equations for circular accelerators and outlining key modes of oscillation[78]. The works of Montague and Sacherer contributed significantly to the understanding of space charge related beam dynamics problems in high intensity accelerators.

Other early works in this area were two papers by Lee and Riabko, the first of which developed a Hamiltonian formulation for a charged-particle beam[57] and the second of which used this Hamiltonian to further investigate the critical envelope mismatch needed for halo formation in space-charge dominated beams[76]. Later, Lee and Okamoto expanded on their previous works by deriving equations of motion for space-charge dominated beams in synchrotrons[56]. Fedotov and Gluckstern

also published papers on halo formation from the alternative perspective of an analytical derivation of the effect from beam mismatch[17] and from an analysis of numerical simulations of stationary beam distributions using non-ideal smooth focusing lattices[24].

In 2001, Galambos, Danilov and Holmes demonstrated that simulations could reproduce experimental results when space-charge effects were taken into account[23, 47]. These publications provided a necessary link between experiment and theory. Cousineau, Holmes, and Lee later investigated the effects of lattice structure and finite momentum spread on the resonance behavior through simulations[13]. In her thesis, Cousineau related these simulations to experimental results and investigated the collective motion of the beam[11].

1.2.3 Hoffman at GSI

Among the first synchrotron facilities to present research on space charge coupling was the GSI Helmholtz Center for Heavy Ion Research (GSI) in Germany. The SIS18 booster was added to the GSI facility in 1990. Unlike the SNS, the SIS18 is a rapid-cycling synchrotron, whereby the particle energy is increased while increasing the magnetic fields to maintain a fixed particle orbit. Hofmann, Franchetti, and others have extensively studied the presence of coupling in the SIS18 booster through analytic calculations and simulations. Hofmann's analytical work is typically based on static Kapchinskij-Vladimirskij (KV) beams[53] which linearize the equations of motion and allow analytic solutions to be determined[33]. These solutions often rely heavily on RMS values to describe the beam and are unable to take into account more realistic beam distributions. Of particular interest to our research, Hofmann and Franchetti presented theory and simulations on the coherent resonance coupling due to space charge in synchrotrons with tunes allowing for Montague resonance[39]. Fedotov, Holmes and Gluckstern presented the results of simulation studies looking

at higher order beam modes driven by space charge coupling resonance, including Montague resonances, in the early SNS lattice design[18].

1.2.4 Sakai at KEK and Hotchi at J-PARC

Montague resonances are particularly relevant in high intensity small tune split facilities like the SIS18 and the SNS. Another facility of this type is the rapid cycling synchrotron at Japan's High Energy Accelerator Research Organization (KEK). In 2000, Sakai reported a similar coupling effect in the KEK booster and stated that the problem limited their ability to achieve higher intensities[80]. In 2001, Sakai confirmed that the intensity limiting effect was due to space charge[81].

In the years that followed KEK was combined with other facilities and recommissioned in 2007 as the Japan Proton Accelerator Research Complex (J-PARC). The facility commissioning publication included single particle tracking simulations of the beam storage mode[49]. It found multiple sources for third and fourth order resonances, including an octupole field component in the main magnets and the same second-order effect of the sextupoles as noted by Ohnuma[68]. In 2015, Hotchi indicated that they had moved the operational tune parameters onto the second order difference resonance to avoid more serious multipole resonances[48].

1.2.5 Métral at CERN

In 2005, Métral published on a series of space charge studies conducted at the CERN PS[64]. One study conducted between 2002 and 2004 focused on intensity-dependent emittance transfer between the two transverse planes due to a Montague resonance. This study compared experimentally measured emittances during resonance crossing to those of simulations of the same. While the study had great success, they only addressed the beam in terms of emittance and failed to describe the change in profile due to the resonance. This same topic has been brought up in discussions of the *Working Group A: Beam Dynamics in High-Intensity Circular Machines* at

the International Committee for Future Accelerators' (ICFA) Workshop on High Intensity and High Brightness Hadron Beams (HB). In 2012, this working group noted that experiments and simulations regarding the Montague resonance were still being conducted at the CERN PS[20]. In 2014, the same working group discussed moving the CERN PS Booster (PSB) tune onto the Montague Resonance[51]. After over a decade of experiments and simulations, the Montague resonance is still a topic for discussion regarding both the CERN PS and PSB.

1.3 The Spallation Neutron Source

Located at Oak Ridge National Laboratory, the SNS is the world's most intense pulsed neutron spallation source. The SNS accelerator is a 1.4+ MW proton driver that produces 700 ns pulses of approximately 10^{14} protons at energies around 1 GeV. To accomplish this, the SNS linac accelerates minipulses of $10^{11} H^-$ to 1 GeV and accumulates them in the 248 m circumference SNS ring. The accumulated beam is transported through a final beam line to a liquid mercury target for neutron spallation. In order to prevent excessive damage to the stainless steel target shell during beam operations, the on-target beam requirements, such as the beam size and peak density, are very tightly controlled. Deviation from these parameters can lead to a shortened lifetime of the target.

In addition to the very high beam intensities, the SNS has flexibility in generating beam configurations, and it boasts an extensive suite of beam diagnostics. Moreover, the space charge coupling phenomenon is routinely observed at the SNS[12] at the design lattice settings, and presents a challenge for satisfying the on-target beam parameter requirements during operations while also minimizing beam losses. Specifically, when space charge coupling becomes a significant effect, it impairs the ability to control the beam size and configuration independently in each plane, resulting in unpredictable final beam distributions. As new applications require the development of very high intensity hadron accelerators to be used as proton

drivers for secondary particles, target stations, and high-energy accelerators, the beam requirements of these facilities become even more stringent.

As shown, the problem of space-charge-induced coupling in synchrotrons has been approached mainly through theoretical or semi-analytic works that assume idealized conditions for the lattice and utilize primarily RMS beam parameters. The results of these studies, while insightful, are not directly applicable to machine scenarios where the lattices are complex and the parameters of interest are not well described by RMS quantities. Some experimental studies have been conducted at CERN and J-PARC, however there has yet to be a robust experimental exploration of the space charge coupling phenomenon aimed at understanding the effect of space-charge-induced coupling on the evolution of the full beam distribution. This topic is the target of the proposed thesis.

1.4 Objectives

This dissertation will focus on advancing our knowledge of this resonance beyond RMS parameterization and will answer the more complex question of how the beam distributions are effected. These results will be of particular interest to any future high intensity hadron machines that seek control over specific beam distributions. The specific goals of this dissertation are as follows.

1.4.1 Goal No. 1

Due to the strict beam loss requirements, high-intensity hadron accelerators frequently have specific beam requirements that go beyond RMS parameters. The second goal of this dissertation is to expand the understanding of this resonance beyond the RMS-based parameterizations currently used for coupling resonances. This will be accomplished by experimentally measuring the effects of the resonance on the beam distribution using the electron scanner. The electron scanner is located

in the accumulator ring and is a device capable of providing profiles in the horizontal and vertical planes during the accumulation and storage of the beam. The electron scanner is unique to the SNS and it will allow us to provide an unprecedented view of the effects of the resonance.

1.4.2 Goal No. 2

As the history of resonances has shown, determining the sources of beam dynamics are not always as straightforward as they appear. Coupling resonances have been known to be caused by rotated quadrupoles, first and second order effects of sextupoles, octupole field components and even space charge. The first goal of this dissertation is to establish the source of the resonance in the SNS.

1.4.3 Goal No. 3

The original objective for this research has always been to mitigate the coupling effect for regular facility operations. The third and final goal of this dissertation is to investigate mitigation of the coupling effect. Due to the inherent flexibility of the SNS lattice, we have a range of tunes accessible to accomplish this goal, specifically $Q_x = [6-7]$ and $Q_y = [4-7]$. The current production tune was chosen largely because it avoids resonances that would induce large beam losses. At the time that this tune point was selected, the effects of this coupling were unknown. It was suggested that future studies should be conducted to determine the full effect of the coupling[16], but this work was not carried out prior to this study.

This final goal will require development of a lattice to split the SNS tune beyond the measured stop band for the coupling. Constraints determining a feasible lattice configuration include, but are not limited to, staying within the prescribed magnet field ranges, maintaining reasonably small beta functions to avoid increased beam loss, meeting the design requirements of the dispersion free bending achromats, and

avoiding other known resonances. The new tune point will need to be experimentally tested in the accelerator for the production beam configuration to check for coupling.

1.5 Organization

Chapter 1 provides historical background, highlights publications of interest, and explains the relevance and objectives of this research. Chapter 2 introduces the accelerator physics concepts necessary to understand the work presented. Chapter 3 provides an overview of the essential theory of resonances, focusing on coupling resonances and how they apply to the SNS. Chapter 4 describes recent developments of the electron scanner, specifically application development, measurement of local lattice parameters, and profile benchmark. Chapter 5 presents a study of stored beams using both wire scanners and the electron scanner. Chapter 6 presents a study of SNS production-style beams using primarily the electron scanner. Chapter 7 presents a study using modern accelerator software to simulate the study of stored beams presented in Chapter 5. Chapter 8 summarizes the results of this research and presents any final thoughts.

Chapter 2

Theory of Beam Dynamics

In Chapter 2, we will review basic particle accelerator physics. The objective of this Chapter is to provide background knowledge to those that might not be readily familiar with the principle theories required to understand the work presented in this dissertation.

Initially, we will describe single particle motion in accelerators. Specifically, in Section 2.1, we will discuss the passage of particles through a series of magnets and drift sections, collectively referred to as elements, via transportation matrices. The simplest representation of an accelerator is a series of elements, which is referred to as a lattice. In Section 2.2, we will discuss the motion of the particles around the ideal or reference orbit via Hill's Equation. From the solution to Hill's equation, we are able to derive the motion of the particles in phase space. This leads to the definition of emittance, tune and the Twiss parameters.

Building on single particle dynamics, we describe the collective motion of the beam in real space and phase space. In Section 2.3, we introduce the concept of the beam envelope as it describes the collective motion of the particles and allows us to describe the overall size of the beam. In Section 2.4, we define the emittance in terms of the beam distribution. In Section 2.5, we discuss how the Twiss parameters can

be transported through the accelerator lattice. Finally, in Section 2.6, we introduce space charge, or the effects of Coulomb repulsion.

2.1 Matrix Formulation for Lattice Elements

The transportation of a particle beam through an accelerator is, in many regards, analogous to the transportation of light through a series of optics. Each element within the accelerator lattice uses magnetic fields to bend the path of each particle in the beam. We describe the current state of each particle with the horizontal and vertical betatron phase space coordinates or betatron state vectors. These are generically written as (x, x'), where x represents the position of the particle in either of the transverse directions, and x' represents the derivative of the position with respect to the position in the lattice, s. These betatron state vectors allow us to write the particle's future state as the matrix multiplication of the effect of the lattice element and the current state:

$$\begin{pmatrix} x_1 \\ x_1' \end{pmatrix} = m \cdot \begin{pmatrix} x_0 \\ x_0' \end{pmatrix} \tag{2.1}$$

where m is the transportation matrix for a given lattice element. The transportation matrix describes how the lattice element effects the path of the particle. The transportation matrix for a drift element is equal to

$$m_{\text{Drift}} = \begin{pmatrix} 1 & l \\ 0 & 1 \end{pmatrix} \tag{2.2}$$

where l is the length of the drift space. Unlike traditional optics, most accelerator elements do not have the same effect in both transverse directions. Due to the geometry of the magnetic field, a quadrupole focuses in one direction and defocuses

in the opposite direction. The transportation matrices for a quadrupole magnet are

$$m_{\text{Focusing Quadrupole}} = \begin{pmatrix} \cos\left(\sqrt{K}l\right) & \frac{1}{\sqrt{K}}\sin\left(\sqrt{K}l\right) \\ -\sqrt{K}\sin\left(\sqrt{K}l\right) & \cos\left(\sqrt{K}l\right) \end{pmatrix} \tag{2.3}$$

and

$$m_{\text{Defocusing Quadrupole}} = \begin{pmatrix} \cosh\left(l\sqrt{|K|}\right) & \frac{1}{\sqrt{|K|}}\sinh\left(l\sqrt{|K|}\right) \\ \sqrt{|K|}\sinh\left(l\sqrt{|K|}\right) & \cosh\left(l\sqrt{|K|}\right) \end{pmatrix} \tag{2.4}$$

where K is the focusing function and l is the length of the element. In the thin lens approximation, as $l \to 0$, we find that the transportation matrix for both elements can be written as

$$m_{\text{Quadrupole}} = \begin{pmatrix} 1 & 0 \\ -1/f & 1 \end{pmatrix} \tag{2.5}$$

where f is the focal length of the quadrupole. The focal length is defined as $f = \lim_{l\to 0} \frac{1}{|K|l}$, where f < 0 is a focusing quadrupole and f > 0 is a defocusing quadrupole.

The simplest example of a focusing lattice is the FODO lattice, which consists of alternating pairs of focusing and defocusing quadrupoles separated by drift spaces. If the drift lengths are properly selected, then the overall effect of the alternating quadrupoles will focus the beam in both transverse directions. Figure 2.1 shows an example of a simple FODO lattice. The top portion of the graphic shows the FODO lattice as a ray diagram from a traditional optics lattice. The middle portion of the graphic shows the focusing function along the length of the FODO lattice. The focusing and defocusing quadrupoles are represented by blocks of equal height and width but opposite sign. The bottom portion of the graphic shows the evolution of the transverse phase space as the beam advances through the FODO lattice. The beam is shown to be initially diverging, focused by the first quadrupole, converging until the second quadrupole, reaching a beam waist at the second quadrupole, and

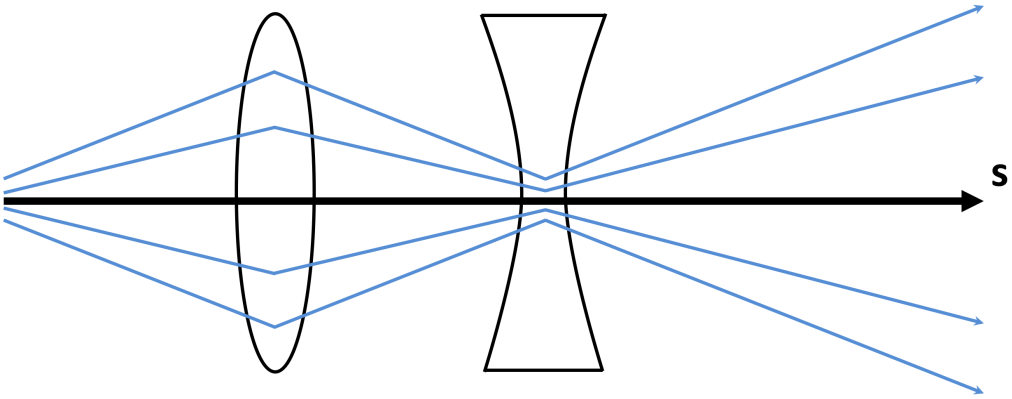

Traditional Optics Schematic

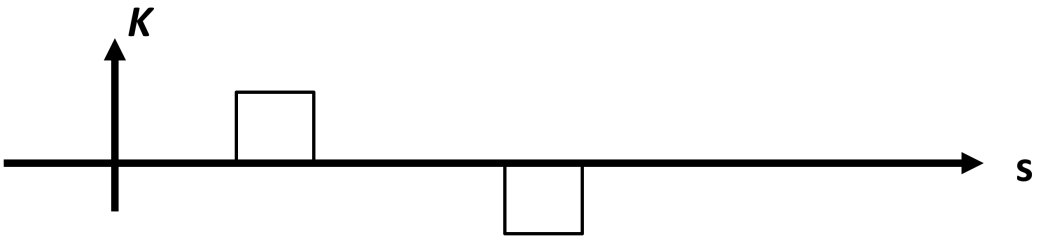

Accelerator Optics Schematic

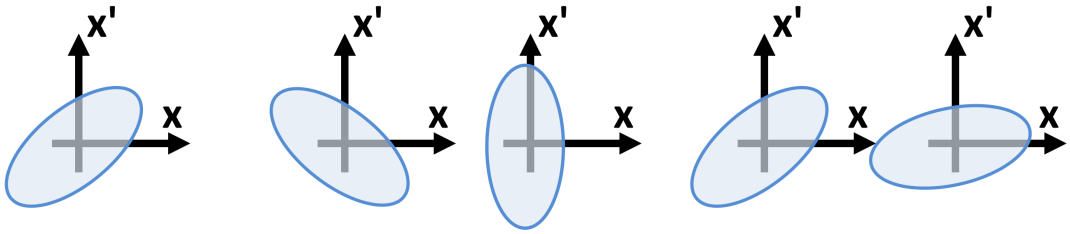

Phase Space Diagrams

Figure 2.1: Example of a FODO Lattice in traditional and accelerator optics schematics with the relative phase space diagrams.

diverging afterwards. It is possible to expand the transportation matrices to handle both transverse dimensions at the same time in a 4-dimensional matrix. This also allows for the inclusion of coupling effects. The transportation matrices of complex lattices are all typically handled within accelerator simulation software, along with realistic beam dynamics.

2.2 Hill's Equation

Accelerator lattices are designed so that a particle with the design energy and coordinates passes directly through the center of all lattice elements. This path is called the reference orbit. In a real accelerator, there is no ideal particle following the reference orbit. Each particle in the distribution oscillates about the reference orbit. In circular accelerators the reference orbit must be closed. Figure 2.2 shows how the curvilinear coordinates follow the reference orbit. For small oscillations about the reference orbit, it is possible to use well-established formulas for periodic motion, such as Hill's Equation, adapted for accelerators. In the absence of space charge forces, Hill's Equation for transverse particle motion in an accelerator lattice is written as

$$x''(s) + K_x(s)\ x(s) = 0 \tag{2.6}$$

where x is the amplitude of the oscillation from the reference orbit along either of the transverse axes (horizontal or vertical), s is the distance along the reference orbit, the primes denote derivatives with respect to s, and $K_x(s)$ is the focusing function of the accelerator lattice. The focusing function is periodic in s for periodic lattices, such as circular accelerators[55, 88]. Hill's Equation defines the betatron oscillations of particles around the reference orbit. As discussed in the previous section, we can determine the motion of individual particles through any portion of beamline by multiplying the individual transfer matrices, $K_x(s)$, of each lattice element. For

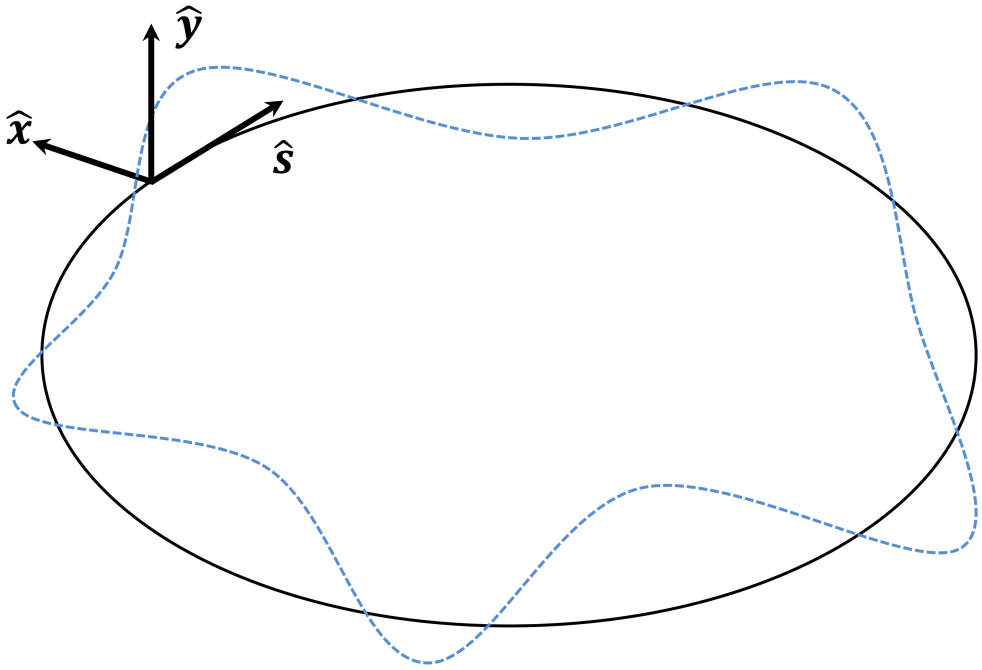

Figure 2.2: Curvilinear coordinate system $(\hat{x}, \hat{y}, \hat{s})$ for the equations of motion in circular particle accelerators. The reference orbit is shown in black and the particle's orbit is shown in blue.

stable motion in circular accelerators, we seek solutions of the form

$$x(s) = A\, w(s)\, \cos\big(\psi(s) + \delta\big) \tag{2.7}$$

where A and δ are the constants of integration determined by the initial conditions, $w(s)$ is an amplitude function required to have the same period as the lattice, and $\psi(s)$ is the phase advance function equivalent to $\sqrt{K_x(s)}\, s$. By inserting this general solution into Hill's Equation, we find

$$\begin{aligned}\big[A\ K_x(s)\ w(s) + A\ w''(s) - A\ w(s)\ \psi'^2(s)\big]\cos\big(\psi(s)+\delta\big) \\ - \big[A\ w(s)\ \psi''(s) - 2A\ w'(s)\ \psi'(s)\big]\sin\big(\psi(s)+\delta\big) = 0.\end{aligned} \tag{2.8}$$

We can now solve the sine and cosine terms independently. The sine term yields the phase advance equation,

$$\psi'(s) = \frac{c}{w^2(s)} \tag{2.9}$$

where c is a constant of integration. After substituting our new formula for $\psi'(s)$, the cosine term yields the betatron envelope equation,

$$w^3(s)\Big[w''(s) + c\ w(s)\Big] = c^2. \tag{2.10}$$

We will revisit the betatron envelope equation in Section 2.3.

Upon reexamining the general solution in Equation 2.7, we find that it can also be rewrite as

$$x(s) = w(s)\Big[A_1\ \cos\psi(s) + A_2\ \sin\psi(s)\Big] \tag{2.11}$$

where we have chosen to expand the cosine, and replace both of the constants of integration, A and δ, with A_1 and A_2. The derivative of the new general form is

$$\begin{aligned} x'(s) = &\Big[A_1\ w'(s)\ + A_2\ \psi'(s)\ w(s)\Big]\ \cos\psi(s) \\ &+\Big[A_2\ w'(s) - A_1\ \psi'(s)\ w(s)\Big]\ \sin\psi(s). \end{aligned} \tag{2.12}$$

We can apply initial conditions to determine the constants of integration. We state that $x(s = s_0) = x_0$ and $x'(s = s_0) = x'_0$. Additionally, the phase advance, $\psi(s)$, is measured with respect to some initial location and we are free to assume that $\psi(s = s_0) = 0$. Therefore, $\cos\psi(s_0) = 1$ and $\sin\psi(s_0) = 0$. Applying these initial conditions, we find that

$$A_1 = \frac{x_0}{w(s)} \tag{2.13}$$

from Equation 2.11, and

$$A_2 = \frac{x'_0\ w(s) - x_0\ w'(s)}{c} \tag{2.14}$$

from Equation 2.12. We can reinsert these definitions into the general solution and its derivative, Equations 2.11 and 2.12. This can be written as the following matrix equation

$$\begin{pmatrix} x(s) \\ x'(s) \end{pmatrix} = \begin{pmatrix} \cos\psi(s) - \frac{w(s)w'(s)}{c}\sin\psi(s) & \frac{w^2(s)}{c}\sin\psi(s) \\ -\frac{1+\left[\frac{w(s)w'(s)}{c}\right]^2}{\frac{w^2(s)}{c}}\sin\psi(s) & \cos\psi(s) + \frac{w(s)w'(s)}{c}\sin\psi(s) \end{pmatrix} \cdot \begin{pmatrix} x_0 \\ x'_0 \end{pmatrix} \tag{2.15}$$

where the phase advance from s_0 to s is determined by $\psi(s) = \int_{s_0}^{s} c\,ds\,/\,w^2(s)$. In Equation 2.15, we find that $w^2(s)$ is always scaled by the constant of integration c. Therefore, it is customary in accelerator physics to define more fundamental variables and rewrite the equation. The new variables are

$$\beta(s) \equiv \frac{w^2(s)}{c} \tag{2.16}$$

and

$$\alpha(s) \equiv -\frac{1}{2}\frac{d\beta(s)}{ds} \tag{2.17}$$

where $\alpha(s)$ can be simplified to $-\big[w(s)\,w'(s)\big]/c$ by inserting the definition of $\beta(s)$. By rewriting Equation 2.15 in terms of these new variables, we find that

$$\begin{pmatrix} x(s) \\ x'(s) \end{pmatrix} = \begin{pmatrix} \cos\psi(s) + \alpha(s)\,\sin\psi(s) & \beta(s)\,\sin\psi(s) \\ -\frac{1+\alpha^2(s)}{\beta(s)}\,\sin\psi(s) & \cos\psi(s) - \alpha(s)\,\sin\psi(s) \end{pmatrix} \cdot \begin{pmatrix} x_0 \\ x'_0 \end{pmatrix}. \tag{2.18}$$

We can see that it also makes sense to define $\gamma = \big(1+\alpha^2\big)/\beta$. We refer to α, β, and γ collectively as the Twiss or Courant-Snyder Parameters. These are <u>not</u> related to the Lorentz factor, γ, or relativistic speed, β. The updated general solution in Equation 2.7 becomes

$$x(s) = A'\sqrt{\beta(s)}\cos\Big(\psi(s) + \delta\Big) \tag{2.19}$$

where A' is the updated constant of integration that incorporates c, $\beta(s)$ is the betatron function of the lattice, $\psi(s)$ is the phase advance of the particle, and δ is the constant of integration for the particle's phase. We would now like to determine the constant of integration, A', in terms of the Twiss parameters. We find that the derivative of the updated general solution in Equation 2.19 is

$$x'(s) = A'\frac{1}{\sqrt{\beta(s)}}\frac{\beta'(s)}{2}\cos\Big(\psi(s)+\delta\Big) - A'\sqrt{\beta(s)}\sin\Big(\psi(s)+\delta\Big)\psi'(s). \tag{2.20}$$

Using $\alpha(s) \equiv -\beta'(s)/2$ and $\psi'(s) = 1/\beta(s)$, this simplifies to become

$$\alpha(s)\,x(s) + \beta(s)\,x'(s) = -A'\sqrt{\beta(s)}\sin\Big(\psi(s)+\delta\Big)\;\psi'(s). \tag{2.21}$$

We can then square Equations 2.19 and 2.21 and add them. This produces the following formula for the constant of integration

$$\varepsilon = \gamma\,x^2 + 2\,\alpha\,x\,x' + \beta\,x'^2 \tag{2.22}$$

where we define $\varepsilon = A'^2$. This is referred to as the Courant-Snyder invariant, but is most commonly known as the emittance. The phase space area enclosed within the Courant-Snyder invariant is equal to $\pi\varepsilon$, where the π is frequently included in the units as [πmm-mrad]. Figure 2.3 shows the phase space ellipse for the particle. The final general solution to Hill's equation is

$$x(s) = \sqrt{\varepsilon_x \, \beta_x(s)} \cos\Big(\psi_x(s) + \delta\Big) \tag{2.23}$$

where ε_x and δ are constants of integration, $\psi_x(s)$ is the betatron phase, and $\beta_x(s)$ is the betatron amplitude function[92]. The quantity ε_x represents the total phase space area intercepted by the particle, and is conserved in the absence of nonlinearities in the lattice[15]. The betatron amplitude function describes the effect of the various focusing magnets on the path of the particle, and is sensitive to the strength and arrangement of magnets in the lattice. As the particles proceed from element to element, they undergo a phase advance, $\Delta\psi_x$, along their phase space trajectory. Figure 2.4 shows an example of the phase advance of the individual particle and the rotation of the beam in phase space as the beam is transported through the lattice. The total phase advance of a particle per lattice period is called the tune. For circular accelerators, the tune is defined as the total phase space advance per complete revolution around the circumference of the accelerator and is defined as

$$\nu_x \text{ or } Q_x = \frac{\Delta\psi_x(s_0 \to s_0)}{2\pi} \equiv \frac{1}{2\pi} \oint \frac{ds}{\beta_x(s)}. \tag{2.24}$$

As we will discuss throughout this study, the transverse tunes play a critical role in accelerator beam dynamics.

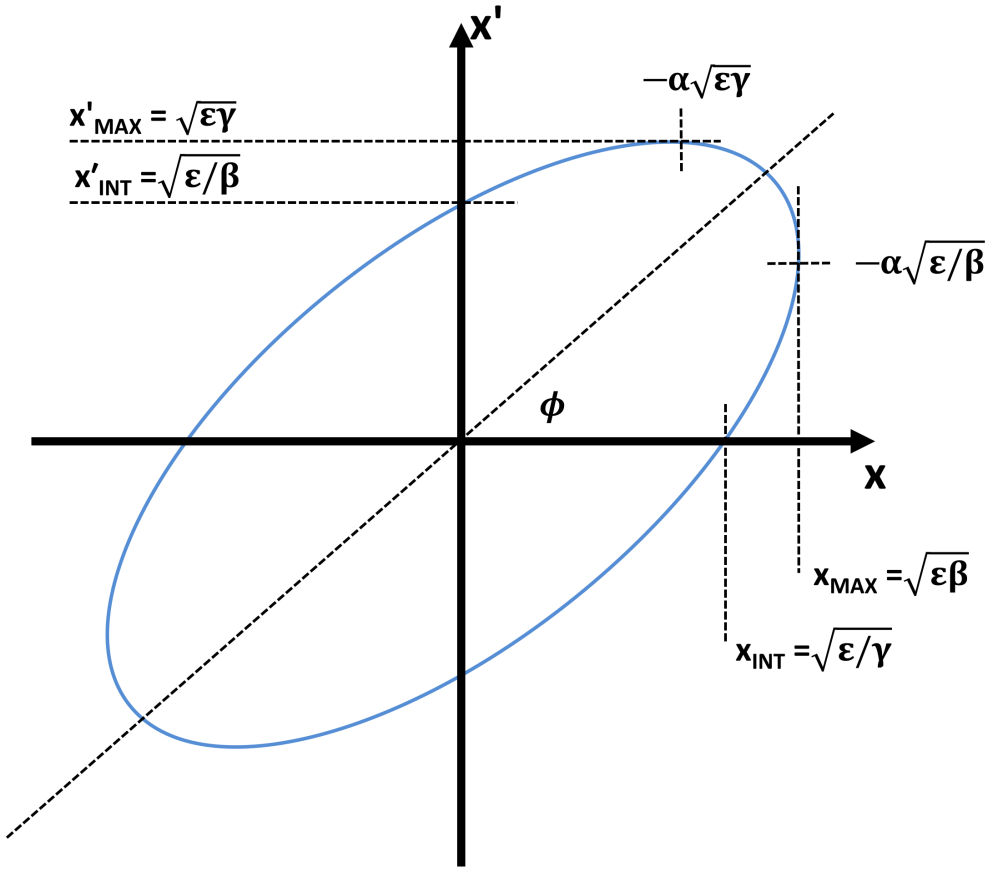

Figure 2.3: Phase space ellipse

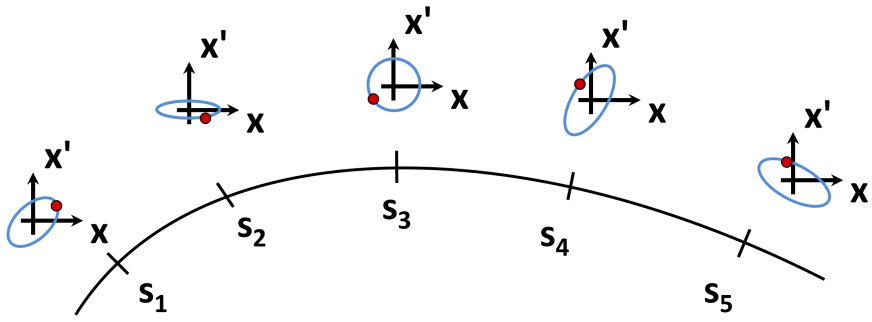

Figure 2.4: The transverse phase space of the beam as it advances through the lattice from s_1 to s_5. The rotation of the phase space ellipse is shown in blue and the particle's location is shown in red.

2.3 Envelope Equations

The discussion has so far been limited to single particle dynamics. However, we need to understand the beam as an ensemble. By considering the path of the particles that lie along the furthest edges of the beam at each location, we can write a similar system of equations that describe the entire beam ensemble. Figure 2.5 shows the beam envelope relative to the path of individual particles within the beam. To find the extremum of the stable closed orbit motion defined by Equation 2.23, we can set $\cos\big(\psi_x(s) + \delta\big) = \pm 1$. Thus, we find that the envelope of an ensemble of particles is defined by

$$R_x(s) = \pm\sqrt{\varepsilon_x}\sqrt{\beta_x\,(s)} \tag{2.25}$$

where $R_x(s)$ is the envelope radius of the beam. We can quickly see that the overall size of the beam depends only on the emittance, or phase space area, and the betatron function at any particular location[55, 93]. If we interpret the beam envelope, $R_x(s)$, as being represented by the RMS of the beam, then we find that

$$\varepsilon_{\,\mathrm{RMS}} = \frac{x_{\,\mathrm{RMS}}(s)^2}{\beta(s)}. \tag{2.26}$$

If we insert the envelope radius given in Equation 2.25 into the betatron envelope equation given in Equation 2.10, we find

$$R_x''(s) + K_x(s)\,R_x(s) - \frac{\varepsilon_x^2}{R_x^3} = 0 \tag{2.27}$$

where K_x is the focusing function, R_x is the envelope radius, and ε_x is the emittance. It can be shown that the beam envelope oscillates at roughly twice the particle tune[8].

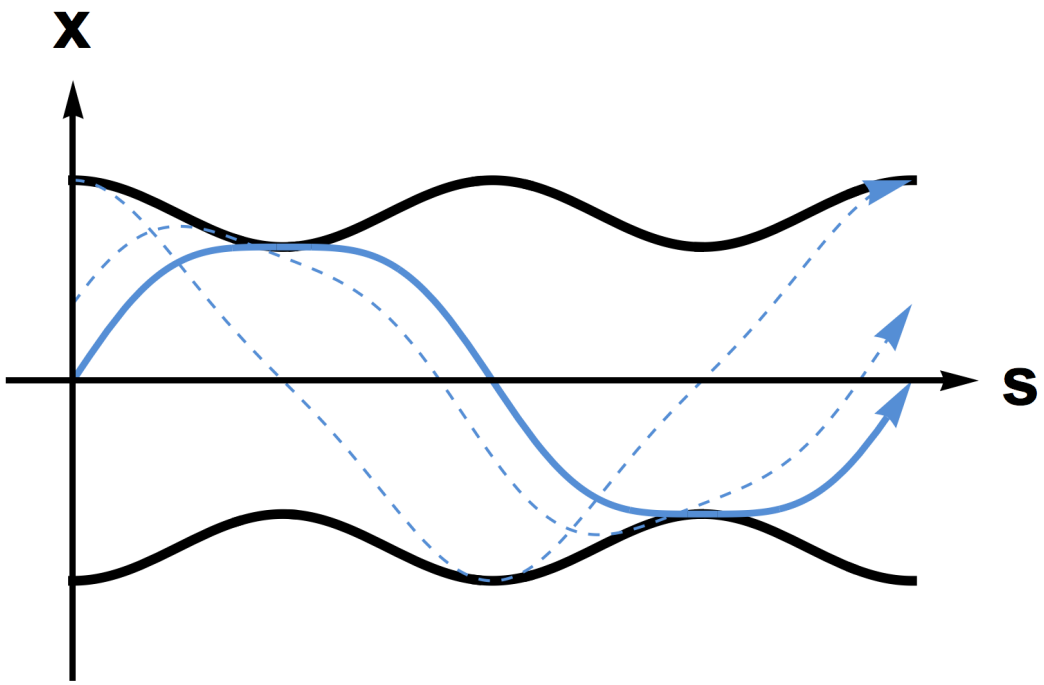

Figure 2.5: Example of a beam envelope in a periodic lattice. The beam envelope is represented by the two solid black lines at the extremes of the orbit, and the three blue inner lines demonstrate the variation in the orbit for different values of δ.

2.4 RMS Emittance

Additionally, when we need to discuss the beam as an ensemble of particles, we can define the emittance in terms of the beam distribution. We can write the average position and velocity of the beam distribution as

$$\langle x \rangle = \int x \, \rho(x, x') \, dx \, dx' \tag{2.28}$$

and

$$\langle x' \rangle = \int x' \, \rho(x, x') \, dx \, dx' \tag{2.29}$$

where $\rho(x, x')$ is the normalized distribution function. The RMS widths of the beam distribution can then be written as

$$\sigma_x^2 = \int (x - \langle x \rangle)^2 \, \rho(x, x') \, dx \, dx' \tag{2.30}$$

and

$$\sigma_{x'}^2 = \int (x' - \langle x' \rangle)^2 \, \rho(x, x') \, dx \, dx'. \tag{2.31}$$

Additionally, the correlation between the position and velocity is

$$\sigma_{xx'}^2 = \int (x - \langle x \rangle) \, (x' - \langle x' \rangle) \, \rho(x, x') \, dx \, dx'. \tag{2.32}$$

Using these definitions of the beam distribution, we can write the RMS emittance as

$$\varepsilon_{\,\mathrm{RMS}} \equiv \sqrt{\sigma_x^2 \, \sigma_{x'}^2 - \sigma_{xx'}^2}. \tag{2.33}$$

This section is used for a practical application later in this study. RMS beam measurements are used to calculate the wire scanner emittance measurements and errors by using the Least Squared Model (LSM). The results are presented in Section 4.4. In Sections A.3 and A.4, we review the mathematics behind determining the errors of the initial beam distribution and the Twiss parameters, respectively.

2.5 Twiss Transport

Liouville's Theorem states that the phase space area of the beam is constant provided that the lattice elements are linear transformations[55, 93]. Therefore the emittance of the beam is conserved in a linear lattice. We can describe the phase space of the beam at any point along the accelerator lattice using the Twiss parameters. It now becomes important to know how to transport the Twiss parameters, and therefore the phase space ellipse, through the accelerator lattice. We can use a general solution of Hill's Equation and the constant emittance to determine transportation matrices that will advance the Twiss parameters from one location in the lattice to the next.

In this section, it is essential to remember that the Twiss parameters, focusing function, and matrix transportation elements are all functions of the lattice position. In order to simplify the notation, we will use the notation $\beta(s_0) = \beta_0$ and $K(s) = K$. If we assume the initial conditions of $x(s = 0) = x_0$ and $x'(s = 0) = x'_0$, then we can rewrite the general matrix transportation as

$$x(s) = C(s)\, x_0 + S(s)\, x'_0 \tag{2.34}$$

where $C(s)$ and $S(s)$ are functions of the position along the reference orbit, s. We can use the derivative of the solution to create the following matrix equation

$$\begin{pmatrix} x \\ x' \end{pmatrix} = \begin{pmatrix} C(s) & S(s) \\ C'(s) & S'(s) \end{pmatrix} \cdot \begin{pmatrix} x_0 \\ x'_0 \end{pmatrix} \tag{2.35}$$

where $C'(s)$ and $S'(s)$ are the derivatives of the functions $C(s)$ and $S(s)$ with respect to s, respectively. This equation allows us to advance the betatron state vector from position s_0 to s. As an example, Equations 2.3 and 2.4 show the transportation matrices for a focusing and defocusing quadrupole, respectively. We also know that the transportation matrix is invertible. This means that we can use matrix algebra

to find the following equation for $x_0(x, x')$ and $x_0'(x, x')$

$$\begin{pmatrix} x_0 \\ x_0' \end{pmatrix} = \frac{1}{|C(s)\,S'(s) - C'(s)\,S(s)|} \begin{pmatrix} S'(s) & -S(s) \\ -C'(s) & C(s) \end{pmatrix} \cdot \begin{pmatrix} x \\ x' \end{pmatrix}. \tag{2.36}$$

Additionally, we know that the phase space area of the beam must remain constant. Therefore, the determinant of the transformation matrix must equal one for any single element or series of elements. The emittance at the initial position, s_0, is

$$\varepsilon = \gamma_0\, x_0^2 + 2\,\alpha_0\, x_0\, x_0' + \beta_0\, x_0'^2. \tag{2.37}$$

If we substitute the simplified form of Equation 2.36 into Equation 2.37, then we find

$$\begin{aligned} \varepsilon =& \gamma_0 \left[S'(s)^2\, x^2 - 2S'(s)\, S(s)\, x\, x' + S(s)^2\, x'^2\right] \\ &+2\,\alpha_0 \left[-S'(s)\, C'(s)\, x^2 + \Big(S'(s)\, C(s) + S(s)\, C'(s)\Big)\, x\, x' - S(s)\, C(s)\, x'^2\right] \\ &+\beta_0 \left[C'(s)^2\, x^2 - 2\, C'(s)\, C(s)\, x\, x' + C(s)^2\, x'^2\right]. \end{aligned} \tag{2.38}$$

We can rearrange this equation so that it looks like the formula for the emittance at the final position, s.

$$\begin{aligned} \varepsilon =& \Big[\gamma_0\, S'(s)^2 - 2\,\alpha_0\, S'(s)\, C'(s) + \beta_0\, C'(s)^2\Big]\, x^2 \\ &+\Big[-2\,\gamma_0\, S'(s)\, S(s) + 2\,\alpha_0 \Big(S'(s)\, C(s) + S(s)\, C'(s)\Big) - 2\,\beta_0\, C'(s)\, C(s)\Big]\; x\, x' \\ &+\Big[\gamma_0\, S(s)^2 \; - 2\,\alpha_0\, S(s)\, C(s) + \beta_0\, C(s)^2\Big]\, x'^2 \end{aligned} \tag{2.39}$$

Recalling that the emittance is a constant, we can compare the emittance formula at the final position, Equation 2.39, with the emittance formula for the initial position, Equation 2.37. After examining the coefficients of the beam distribution terms, we can see that the Twiss parameters at the initial position can be transported to the

final position using

$$\begin{pmatrix} \beta(s) \\ \alpha(s) \\ \gamma(s) \end{pmatrix} = M \cdot \begin{pmatrix} \beta_0 \\ \alpha_0 \\ \gamma_0 \end{pmatrix} \tag{2.40}$$

where the Twiss transportation matrix is defined as

$$M = \begin{pmatrix} C(s)^2 & -2\,C(s)\,S(s) & S(s)^2 \\ -C(s)\,C'(s) & C'(s)\,S(s) + C(s)\,S'(s) & -S(s)\,S'(s) \\ C'(s)^2 & -2\,C'(s)\,S'(s) & S'(s)^2 \end{pmatrix}. \tag{2.41}$$

This Twiss transportation equation is used in Section 4.3.2 to determine the Twiss parameters at the locations of the Electron Scanner. The value of β is known at the two nearest quadrupoles, located at s_0 and s_1. The top row of the Twiss transportation equation can be written out as

$$\beta_1 = C(s)^2\,\beta_0 - 2\;C(s)\,S(s)\,\alpha_0 + S(s)^2\,\gamma_0. \tag{2.42}$$

Substituting the definition of γ, we find the following equation for α_0

$$\alpha_0 = \frac{\beta_0\,C(s)\,S(s) \pm \sqrt{\beta_1\,\beta_0\,S(s)^2 - S(s)^4}}{S(s)^2}. \tag{2.43}$$

This allows us to use the knowledge of β at the initial and final location and the transportation matrix between the locations to determine the value of α_0.

The general error function is:

$$\Delta f\,(x_1, x_2, ..., x_i)^2 = \sum_{i=1}^{p} (\frac{\partial f}{\partial x_i})^2 \Delta x_i^2. \tag{2.44}$$

Therefore, the error for our calculated α_0 parameter is

$$\Delta\alpha_0 = \sqrt{\left(\frac{\partial\alpha_0}{\partial\beta_0}\right)^2 \Delta\beta_0^2 + \left(\frac{\partial\alpha_0}{\partial\beta_1}\right)^2 \Delta\beta_1^2} \tag{2.45}$$

where we are only focusing on the error contributions from the measured β values. As discussed in Section 4.3, we rely on an established accelerator simulation application to calculate the transportation matrix. We are making the assumption that the major error contributions will come from the newly measured β values. This is a reasonable assumption as this application has been used in numerous other studies to successfully compare simulated results to experimental results.

2.6 Effects of Space Charge

At higher intensities, internal forces, specifically Coulomb repulsion, become non-negligible compared to external fields and can no longer be neglected. Here the beam dynamics become significantly more complicated than the single particle dynamics previously discussed. Fortunately, the original Hill's Equation presented in Equation 2.6 can be modified to include space charge, resulting in

$$x''(s) + K_x(s)\ x(s) = F_{\text{Space Charge}} \tag{2.46}$$

where $F_{\text{Space Charge}} \propto$ Beam Intensity$/\gamma^3\beta^2$. The space charge term is also dependent on the particle's location within the beam distribution[15]. The specific form of Hill's Equation is now dependent on the beam distribution and can be challenging to solve analytically even for simple cases. Examining the general form of the equation, we can see that the space charge term provides a net defocusing effect that is present throughout the transportation process[55]. This defocusing effect produces a downward shift in the transverse tunes of each particle. This is known as the space charge tune shift and is defined as

$$\Delta\nu_x = \frac{1}{4\pi}\oint \beta_x(s)\ \Delta K_{\text{Space Charge}}\ ds \tag{2.47}$$

where $\Delta K_{\text{Space Charge}}$ is the defocusing effect of the space charge forces. In certain idealized beam distributions, the space charge term is independent of the particle location and, therefore, all of the particles experience the same defocusing effect. However, in realistic beams, all particles experience defocusing effects of varying strengths depending on the beam distribution and the particle's location. Typically, the particles near the center of the beam experience larger tune shifts than the particles on the edges of the beam. The result is a spread in the distribution of single particle tunes. This effect is called the Laslett or incoherent space charge tune shift. Figure 2.6 shows an example of the typical space charge tune shift seen at the SNS. The space charge tune shift provides us with a figure of merit for understanding the relative strength of space charge in accelerators. Intense beams can suffer from large space charge tune shifts that can shift the beam into a resonance region. The sources and effects of resonances will be the focus of Chapter 3. [15, 54, 55, 89]

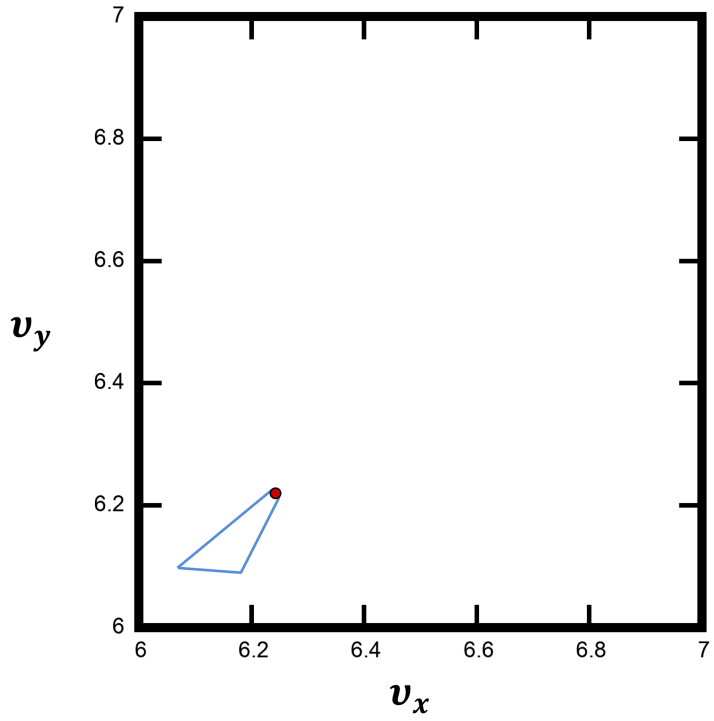

Figure 2.6: Tune space diagram demonstrating the effect of space charge on the SNS beam distribution. The nominal SNS tune point is shown as a red point and the typical SNS space charge tune spread is shown as a blue triangle.

Chapter 3

Theory of Resonances

In order to put this study into context within an accelerator, it becomes necessary to describe the fundamental theory of resonances. This chapter will be devoted to this task and is structured as follows. In Section 3.1 we review the general theory of resonances. In Section 3.2 we discuss lattice resonances, including effects from fringe fields, and how they apply to the SNS. In Section 3.3 we discuss the Montague resonance, or the space charge resonance, and how it might apply to the SNS. Finally, in Section 3.4, we describe the resonances in the tune space around the nominal SNS tune point.

3.1 Overview

Our discussion in Chapter 2 focused on ideal lattices and the theory of transporting charged particle beams. The assumption was made that each element in the lattice was manufactured and installed to exact design specifications. The linear terms in the external forces were designed into the accelerator through lattice elements, such as the focusing quadrupoles, and were accounted for in the focusing function, $K(s)$. In the presence of additional forces not included in the designed lattice, the quasi-harmonic motion of the beam becomes a driven harmonic system with one or more resonant frequencies. The driving force of this system can be the result of any number

of sources, e.g. lattice imperfections, space charge forces, etc. For instance, in the case of a dipole magnet error, a small kick is imparted on the beam once per turn. Therefore, the particles experience the same momentum kick on every turn if the tune of the beam is an integer. The result is called an integer tune resonance and will cause large beam losses within a few revolutions. It has been well established that integer and half integer tunes should be avoided in lattice designs due to the universal prevalence of the driving sources and the dangerous nature of these resonances. We will discuss both dipole and quadrupole field errors in Section 3.2. [15, 55, 78, 88, 92]

A resonance occurs when the frequency of the external force approaches the natural frequency of the system. When these frequencies are equal, particles can become trapped in resonant islands or forced outside of the dynamic aperture and lost. Therefore, resonances are associated with a loss of control over the beam dynamics. Before discussing specific sources and resulting resonances, we begin with a general derivation of resonances for nth-order multipole perturbations.

In the context of ring dynamics, it is convenient to use Floquet's coordinates to help simplify the examination of transverse resonances. Floquet's coordinates normalize the transverse oscillations and allow us to think of the independent coordinate in the ring as cyclical. We transform from our standard coordinate system (u, s) to Floquet's coordinates (w, φ) by using

$$w(\varphi) = \frac{u(s)}{\sqrt{\beta(s)}} \qquad \varphi = \int_0^s \frac{d\bar{s}}{\beta(\bar{s})}. \tag{3.1}$$

The ideal transverse motion of particles is described by Hill's equation in Equation 2.6. Resonances occur from perturbations to Hill's equation. We can think of these perturbations in the ring as adding a driving term to Hill's equation. The source of the driving term determines the dependence, if any, on the position of the particle. These perturbations can be summed, and the revised Hill's equation becomes

$$w'' + \nu_{w,0}^2 \, w = \sum_{n,r} P_{n\,r}(\varphi)\, w^{n-1}\, v^{r-1} \tag{3.2}$$

where $w(\varphi)$ and $v(\varphi)$ each describe either of the transverse coordinates, $\nu_{w,0}$ is the unperturbed tune for the w direction, n and r are integers indicating the order of the perturbing force in each of the transverse coordinates, and $P_{n\,r}(\varphi)$ is the strength of the coupling term. When $r = 1$, the perturbation does not couple the motion. This equation can also be written for the v direction.

Here we look to simplify and rewrite Hill's equation to find specific conditions that produce resonances. Examining the perturbations, we find that the strength of the perturbation is cyclical and can be written as a Fourier series,

$$P_{n\,r}(\varphi) = \sum_{m} P_{n\,r\,m} e^{i\,m\,\varphi}. \tag{3.3}$$

Additionally, for Hill's equation to remain valid, we expect the perturbations to be small. Therefore, a valid first-order approximation would be to assume that the transverse coordinates in the perturbing terms are equal to the unperturbed coordinates. In Equation 2.23, we showed that the solution to Hill's equation is sinusoidal. This can be rewritten as the sum of exponential terms with arbitrary constants. Therefore, we find that

$$w^{n-1} \approx w_0^{n-1} = \sum_{|l| \leq n-1} W_l e^{i\,l\,\nu_{w,0}\,\varphi} \tag{3.4}$$

$$v^{r-1} \approx v_0^{r-1} = \sum_{|q| \leq r-1} V_q e^{i\,q\,\nu_{v,0}\,\varphi}. \tag{3.5}$$

Finally, we substitute Equations 3.3, 3.4, and 3.5 into Equation 3.2 to find

$$w'' + \nu_{w,0}^2\, w = \sum P_{nrm}\, W_l\, V_q\, e^{i\,\varphi(m + l\,\nu_{w,0} + q\,\nu_{v,0})}. \tag{3.6}$$

Therefore, the perturbation will resonate with the motion of the beam if $(m + l\,\nu_{w,0} + q\,\nu_{v,0}) = \nu_{w,0}$. This can be simplified as $(l-1)\,\nu_{w,0} + q\,\nu_{v,0} = -m$. Likewise, the motion in the v direction resonates if $(m + l\,\nu_{w,0} + q\,\nu_{v,0}) = \nu_{v,0}$. This can be simplified as

$l\,\nu_{w,0} + (q-1)\,\nu_{v,0} = -m$. Therefore, the condition governing the occurrence of resonances can be generalized as

$$n_x\,\nu_x + n_y\,\nu_y = p \tag{3.7}$$

where n_x, n_y, and p are integers. Resonances are referred to by their order, which is defined as $|n_x| + |n_y|$. The order of the resonance indicates the multipole term that causes the resonance. The strength of the resonance decreases rapidly with increasing order, and so, except in long term storage rings, we are typically only concerned with resonances up to the 5th order. Ultimately, it is impossible to completely avoid resonances. Accelerator physicists focus first on the lower order resonances during design and development. These have the largest impact on the beam dynamics and need to be accounted for first. The effects of higher order resonances are often the source of beam studies, such as this one, after the machine is commissioned. Figure 3.1 shows resonance diagrams. The second resonance diagram emphasizes the impossibility of avoiding all higher order resonances.[26, 55, 65, 83, 92]

Resonances can affect the transverse planes independently or they can couple the betatron oscillations between the transverse planes. This coupling is especially evident for field errors of higher order multipoles, where the field strength in one plane may depend on the beam position in the alternate plane[93]. Depending on the relative signs of n_x and n_y, these resonances are either called sum (same sign) or difference (opposite sign) resonances. Sum resonances can result in large beam loss and are specifically avoided in lattice designs. Difference resonances typically do not result in a direct beam loss but rather couple the transverse planes in an exchange of energy, where the sum of the total energy remains constant[15, 92]. Difference resonances are often present and can impact the beam evolution.

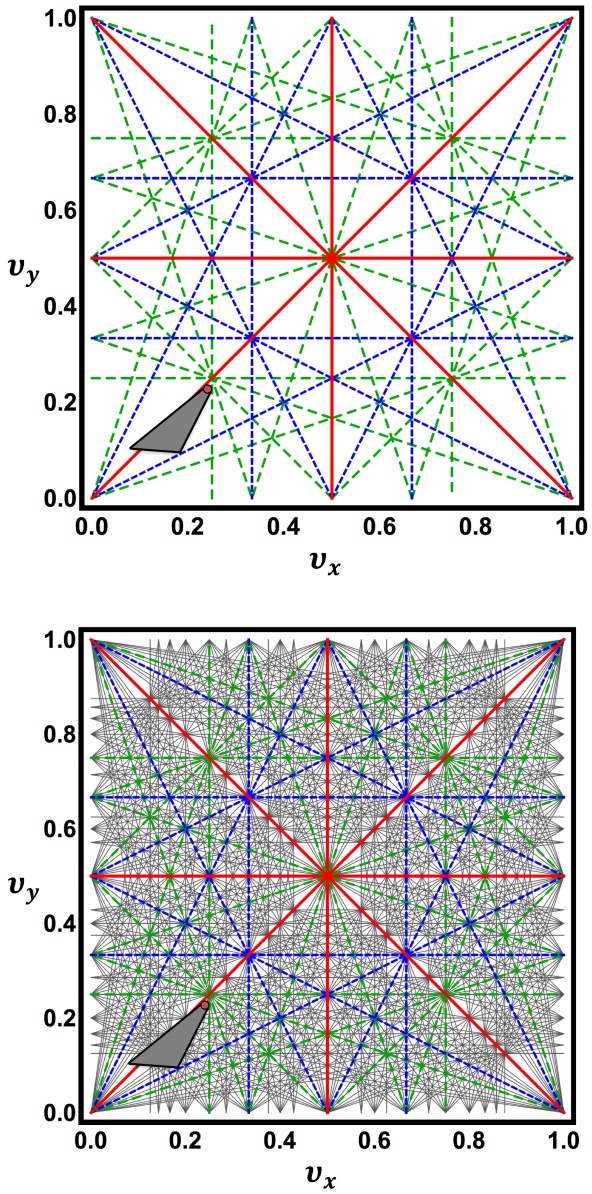

Figure 3.1: Resonance diagrams with low order resonances, first through fourth order, on the top and high order resonances, first through eight order, on the bottom. First order resonances are shown as the black framed box, second order resonances are shown with solid red lines, third order resonances are shown with small-dashed blue lines, and fourth order resonances are shown with long-dashed green lines. All higher order resonances are shown with thin black lines. The nominal SNS tune point is shown as a red point and the typical SNS space charge tune spread is shown as a black triangle.

3.2 Lattice Resonances

In this section, we will discuss the most common driving terms present in all accelerators. Specifically, we will discuss dipole errors in Section 3.2.1, quadrupole errors in Section 3.2.2, and fringe fields in Section 3.2.3.

3.2.1 Dipole Errors

Dipole magnets are used in accelerators to curve the path of the beam. An error in the integrated strength of a dipole creates in an extra kick in the orbit of the beam. The result of this kick is that the beam is bumped into a different orbit, which may or may not be closed. We can represent the erroneous kick with the addition of a delta function to closed orbit Hill's equation, Equation 2.6. This produces

$$y'' + K(s)\, y(s) = \delta(s - s_0)\, \theta \tag{3.8}$$

where θ is the strength of the dipole error at s_0. This shift in the orbit can also be shown through the betatron state vector before and after the kick.

$$y_{\,\text{Before}} = \begin{pmatrix} y_0 \\ y_0' - \theta \end{pmatrix} \qquad y_{\,\text{After}} = \begin{pmatrix} y_0 \\ y_0' \end{pmatrix}. \tag{3.9}$$

If the orbit of the particle is to remain closed, then this relationship must be true after each consecutive revolution. The added shift would otherwise result in lost particles. Therefore,

$$M \begin{pmatrix} y_0 \\ y_0' \end{pmatrix} = \begin{pmatrix} y_0 \\ y_0' - \theta \end{pmatrix} \tag{3.10}$$

where the matrix M is the transportation matrix for one turn. The transportation matrix for $s_0 \to s$ was previously defined in Equation 2.18. The transportation matrix

for one turn is defined as

$$M = \begin{pmatrix} \cos 2\pi\nu + \alpha_0 \sin 2\pi\nu & \beta_0 \sin 2\pi\nu \\ -\frac{1+\alpha_0^2}{\beta_0} \sin 2\pi\nu & \cos 2\pi\nu - \alpha_0 \sin 2\pi\nu \end{pmatrix} \tag{3.11}$$

where $\varphi \to 2\pi\nu$, and α_0 and β_0 are the Twiss parameters at s_0. Using double angle trigonometry identities and basic algebra, we are able to show that the solution to Equation 3.10 is

$$\begin{pmatrix} y_0 \\ y_0' \end{pmatrix} = \begin{pmatrix} \frac{\beta_0\,\theta}{2\sin\pi\nu} \cos\pi\nu \\ \frac{\theta}{2\sin\pi\nu} (\sin\pi\nu - \alpha_0 \cos\pi\nu) \end{pmatrix}. \tag{3.12}$$

In the denominator of the position and the momentum, we have $\sin\pi\nu$. Therefore, the betatron state vector will become infinite for any tune that is an integer. Figure 3.2 examines the phase space diagrams for two cases where the particle sees a dipole error. The first case assumes that the tune is an integer and we can see that the effects of the kick add each turn. This illustrates how a dipole error results in a dangerous resonance for beam with an integer tune. The second case assumes that the tune is a half integer and we can see that the effect of the dipole error is mitigated. We will see in the next section why half integer tunes are also avoided.

3.2.2 Quadrupole Errors

Quadrupoles are the most common magnets in every accelerator. They are used to focus the beam as it is transported along the beamline. An error in the integrated strength of a quadrupole results in a focusing error, shifting the betatron function from the design or ideal. This error is equivalent to inserting an extra quadrupole into the lattice. The transportation matrix for this new quadrupole is

$$m_{\text{Error}} = \begin{pmatrix} 1 & 0 \\ -k(s_1)\,ds_1 & 1 \end{pmatrix} \tag{3.13}$$

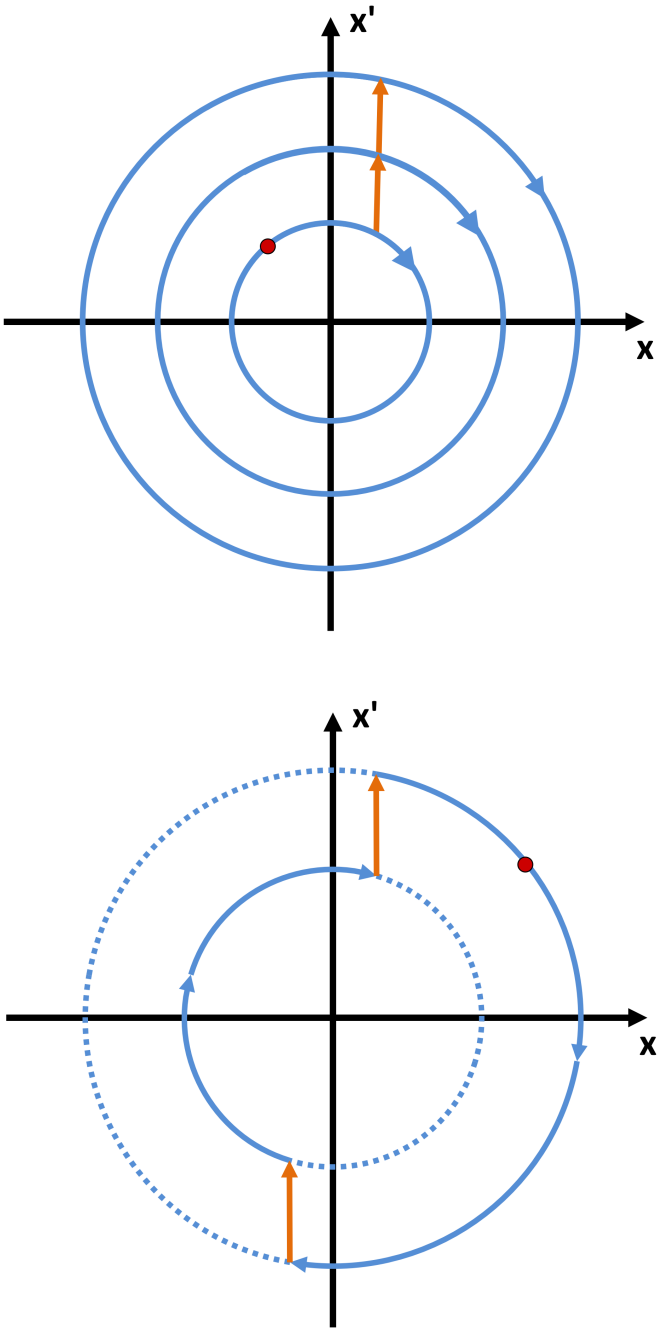

Figure 3.2: Effect of a dipole error on a beam with an integer tune (top) and a half integer tune (bottom). A reference particle is shown as a red circle traveling along an orbit in phase space indicated with blue arrows, with the effects of the dipole errors shown as orange arrows.

where k represents the quadrupole error in an element of length ds_1 located at s_1. Therefore the new single turn transportation matrix becomes the ideal transportation matrix times the transportation matrix for the quadrupole error. Hill's Equation can be rewritten to include the extra focusing term as

$$u'' + [K_0(s) + k(s)]\ u(s) = 0 \tag{3.14}$$

where K_0 represents the focusing function from the ideal lattice. [55]

By examining the transportation matrix, we can see that the quadrupole error exerts an added momentum kick on each particle during each pass through the lattice at s_1. This kick is equal to $\Delta y' = -k(s_1)\, y\, ds_1$. Therefore, each particle experiences a kick proportional to its distance from the y-axis. Particles above and below the y-axis experience kicks in opposite directions. This effect can be seen in Figure 3.3. Beams with a tune that is a multiple of the half integer will experience momentum kicks that add each turn and produce large beam loss. This explains why accelerators are also designed to avoid the half integer resonance.

The addition of the error element produces a shift in the tune. We can determine the tune shift from quadrupole errors by calculating the difference between the tune of the ideal lattice and the tune of the new lattice. The tune shift is

$$\Delta\nu = \frac{1}{4\pi}\,\beta(s_1)\,k(s_1)\,ds_1 \tag{3.15}$$

where β is the betatron function at the location of the quadrupole error. The fact that a shift in the quadrupole strength results in a shift in the tunes has a practical application that will be utilized in Section 4.3.1. We will incrementally change the current of specific quadrupoles and measure the tune shift. This will allow us to calculate the value of the betatron function at the location of the changing quadrupole.

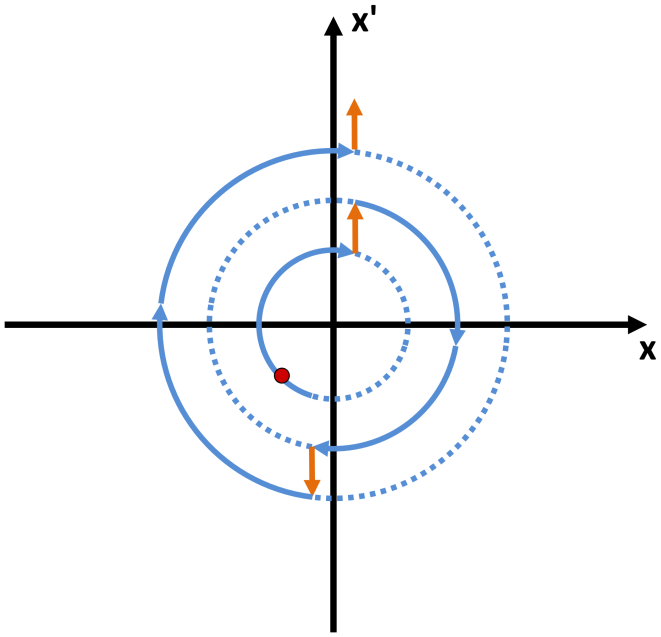

Figure 3.3: Effect of a quadrupole error on a beam with a half integer tune. A reference particle is shown as a red circle traveling along an orbit in phase space indicated with blue arrows, with the effects of the quadrupole errors shown as orange arrows.

3.2.3 Fringe Fields

When introducing accelerator theory, it is customary to assume that the fields of all quadrupoles drop to zero immediately outside of the magnet and that the field within is at a constant strength. This is known as a hard edge field distribution. The effective length is defined as

$$l_{\text{Effective}} = \frac{\int g(s)ds}{g_0} \tag{3.16}$$

where g is the gradient of the quadrupole field, and g_0 is the field gradient in the middle of the quadrupole. This effective length is larger than the quadrupole core length. The intention is that the integrated strength of the quadrupole is the same. The real field extends past the core and gradually falls to zero. A more accurate model of fringe fields is the trapezoidal field approximation. Figure 3.4 illustrates different fringe field models compared to a realistic field. A hard edge model is generally used during lattice design because it quickly applies the correct integrated strength. After the general design is determined, more realistic fringe fields are used to refine the designed lattice. Finally, once the quadrupoles are manufactured, these fields are measured for comparison with the design model and for use in realistic computer simulations.[92]

The fringe field of a quadrupole has been shown to produce octupole-like momentum kicks[58, 61]. Fringe fields are considered an important contributor to SNS beam dynamics because the quadrupole magnet aperture is comparable to the quadrupole magnet length[71]. Additionally, the leading-order of the relative momentum deflection scales with the emittance and inversely with the effective magnet length[91]. The SNS beam size is large and the magnets are relatively short. Therefore, the octupole kick experienced by the beam due to the quadrupole fringe field is large compared to other facilities. The fact that quadrupole fringe fields produce a fourth order multipole perturbation could be a potential source of the equal tune coupling resonance in the SNS accumulator ring.

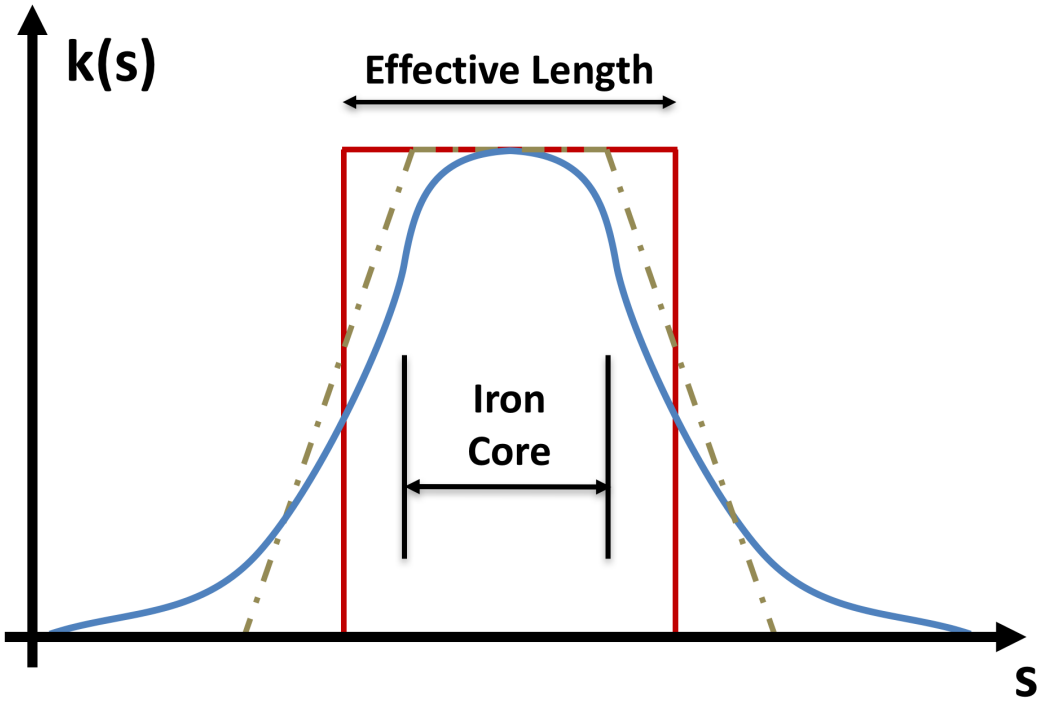

Figure 3.4: The most common quadrupole fringe field models compared to the measured field. The hard edge model is shown in red, the trapezoidal model is shown in gold, and the measured field is shown in blue.

3.3 Montague Resonances

As we illustrated in Section 3.1, the perturbations to Hill's equation are driven by $e^{ip\varphi}$. Due to the nature of this resonance driving force, the dominant condition for difference resonances will always arise for $p = 0$. Therefore, the resonance condition of greatest importance becomes $n_x\,\nu_x + n_y\,\nu_y = 0$. For beams with small tune separation, n_x must equal $-n_y$. The case of $n_x = 1$ and $n_y = -1$ leads to a linear resonance. We excluded this by the design of the accelerator and the selection of coordinate axes to eliminate xy cross terms. Effectively, we assume that the coordinate axes of the beam distribution are oriented such that they are in alignment with the coordinate axes of the accelerator lattice. The next resonance, $n_x = 2$ and $n_y = -2$, is historically referred to as the Montague resonance[65]. The Montague resonance is a fourth order difference resonance that is typically driven by space charge, and the resonance condition is written as

$$2\,\nu_x - 2\,\nu_y = 0. \tag{3.17}$$

We discussed previously that the strongest driving terms for resonances of order N are terms of the Nth multipole. Therefore, a fourth order multipoles will provide the strongest driving term for a fourth order resonance. We can generalize the transverse beam distribution as a two-dimensional Gaussian. The space-charge of this distribution produces the necessary multipole terms to drive the resonance.[65] The beam is particularly sensitive to the Montague resonance because the frequency of the beam envelope is roughly twice the particle tune[8]. The original work by Montague was based on single particle models with static beam distributions. It has been shown in recent works that a more comprehensive self-consistent model is required to account for the strong collective effects that are present[36, 42, 62].

The system of focus for this study is the equal tune coupling resonance. One possible source is the Montague resonance, which can be described as the coupling of two independent oscillators through space charge forces. As previously stated, this is a particular fourth order difference resonance driven by space charge and is represented

by $2\,\nu_x - 2\,\nu_y = 0$. It was initially investigated by Montague[65] and Sacherer[78]. Later, it was analytically expanded by Hofmann[33–37, 40–42] and others[62, 63, 77]. It has been the focus of several simulation studies primarily by Hofmann[34, 35, 38] and it has been briefly studied experimentally by Sakai[80, 81] and Metral[62, 63].

The primary mathematical framework used to describe space-charge-dependent transverse coupling in a collection of particles is the Vlasov Equation. The Vlasov Equation is a partial differential equation derived by applying Liouvilles theorem to the continuity equation. Liouvilles theorem states that the volume of a phase space element does not change in Hamiltonian motion. The Vlasov Equation is

$$-\frac{\partial f}{\partial t} + \frac{\partial H}{\partial q_i}\frac{\partial f}{\partial p_i} - \frac{\partial H}{\partial p_i}\frac{\partial f}{\partial q_i} = 0 \tag{3.18}$$

where f is the number of particles in the phase space volume, H is the Hamiltonian, and q_i and p_i are the phase space coordinates of both transverse planes[88]. Due to the complex nature of the Vlasov Equation, analytic solutions often use highly simplified static beam distributions and require idealized lattice configurations to have easily interpretable results[33]. Therefore, it is common to rely on simulations to solve the Vlasov Equation for realistic beam distributions and lattices.

Montague's original research was based on a single particle approach using a static Gaussian distribution to define the space charge potential. This approach neglects the effects of the time-varying collective space charge forces. Hofmann replaced the single particle approach of Montague by a self-consistent KV beam distribution and used the Vlasov Equation to describe the beam dynamics[37]. The transverse KV beam distribution is composed of particles on the shell of a 4-dimensional ellipsoid. Due to the geometry of the distribution, all of the particles feel an identical space charge focusing. Therefore, all of the particles have the same space charge tune shift and external forces will not deform the distribution. This simplified self-consistent beam distribution allows collective beam effects to be studied. Hofmann studied the coherent frequencies and stability properties of KV beams under Montague resonance

with different focusing constants. He showed that space-charge-dominated beams are able to develop coupling between the transverse planes without the presence of lattice errors to drive the coupling[33]. While this work is a useful analytic approach that provides a basic understanding of the beam dynamics, it is difficult to generalize to more realistic beam distributions.

Later, Hofmann utilized simulations of waterbag distribution beams in realistic lattices to investigate the effects of the Montague resonance in more realistic situations. The waterbag distribution is a uniform distribution of particles in both transverse phase spaces. Unlike the KV distribution, the waterbag distribution can be deformed by external forces and displays a tune spread due to the varying effects of space charge forces. Through simulations, Hofmann found that a static waterbag model predicted only half the maximum emittance exchange of the self-consistent waterbag model. This was due to the absence of a coherent response. Among other results, Hofmann showed that the maximum growth rates of the resonance are roughly proportional to the space charge tune shift[34].

Hofmann posed the question of whether the effects of Montague resonances would be important in the evolution of the SNS beam. Additionally, he called for further more systematic studies of the Montague resonance[34]. Based on recent experimental observations[12], one possible explanation is that the effects of the Montague resonance influence the evolution of the SNS beam for certain beam configurations.

3.4 SNS

Both of the transverse tunes in SNS are approximately 6.2 and have been indicated on the resonance diagrams in Figure 3.1 along with the approximate space charge tune shift. The first concern in designing the lattice is that the beam does not cross the nearest integer resonance. The space charge tune shift is approximately $\sim$0.15 . Therefore, the horizontal and vertical tunes should not be set below $\sim$6.15 without

careful study. This sets the lower bounds of the working space. The working space is sufficiently far away from the half integer to avoid concerns of any second order resonances. However, the quarter integer resonances bound the tune on the upper edges at 6.25. Additionally, the selected tune point is only $\Delta\nu \approx 0.03$ away from the equal tune resonance, which bounds the tune on the left. At the time the working point was selected, it was believed that this would not be a problem.[30, 31] The focus of the proposed thesis is to investigate the effects of the coupling resonance on the SNS beam through experiments and realistic simulations, and determine whether the source is due to fringe field effects or a Montague resonance.

Chapter 4

Electron Scanner

The Electron Scanner is a novel diagnostic device in the final stages of development at the SNS. Several other facilities have proposed similar devices. However, electron beam profile monitors are uncommon even in experimental beam facilities and our device is unique for a major production accelerator. Our Electron Scanner has only been used for preliminary studies for device development. Therefore, it was necessary to calibrate the experimental results prior to use in a dedicated beam physics study. This chapter will be devoted to the task of calibration and is structured as follows. In Section 4.1, we introduce background information regarding the Electron Scanner, including the history, theory, and present limitations. In Section 4.2, we discuss the analysis package. This includes providing an overview of the analysis methodology and results in Section 4.2.1, detailing the efforts to calibrate the RMS size by measuring the scale and rotation of the electron beam in Section 4.2.2, and performing consistency checks on the data in Section 4.2.3. In Section 4.3, we determine the lattice parameters at the location of the Electron Scanner. This includes measuring the betatron functions at nearby quadrupoles in Section 4.3.1, and propagating the Twiss parameters to the Electron Scanner in Section 4.3.2. The results from Sections 4.2 and 4.3 are used in Section 4.4 to establish an emittance

benchmark using the wire scanners. Finally, in Section 4.5, we summarize the status of the Electron Scanner and the contributions made to its development.

4.1 Introduction

The Electron Scanner is a non-destructive beam profile monitor located in the Accumulator Ring. Figure 4.1 shows the locations of the Electron Scanner and Ring-to-Target Beam Transport (RTBT) Wire Scanners. The Electron Scanner is composed of two identical devices within a meter of each other, one to measure each of the transverse profiles (horizontal and vertical). Figure 4.2 shows the Electron Scanner as it is installed in the SNS Accumulator Ring. The Electron Scanner uses a time-homogeneous low-energy electron beam to scan the transverse planes of the proton beam. As we will discuss later in this section, it has several unique and valuable characteristics in comparison to traditional diagnostic devices.

There are two primary concepts for using the deflection of a low-energy electron beam to measure the profiles of high intensity beams. The earliest involved using the deflection of a fixed electron beam[72]. In this method, the electron beam projects a loop onto a screen. The size and rate of change of the loop allow you to measure the charge distribution of the high intensity beam. In 1993, Tsyganov advanced the design by sweeping an electron beam across the path of the circulating proton beam[90]. This likewise deflects the electron beam and the derivative of the projected curve with respect to the undeflected curve allows you to determine the beam profile. However, Tsyganov's electron beam swept through the beam at an angle of 90 degrees and, therefore, the exact beam profile could not be uniquely determined. The original design was intended for the Superconducting Super Collider, which was never built. This design later became the basis of the SNS design.

In 2005, the SNS Beam Instrumentation and Accelerator Physics groups conducted a feasibility study with researchers from Budker Institute of Nuclear Physics in Novosibirsk, Russia[1]. The study investigated the possibility of using a low-energy

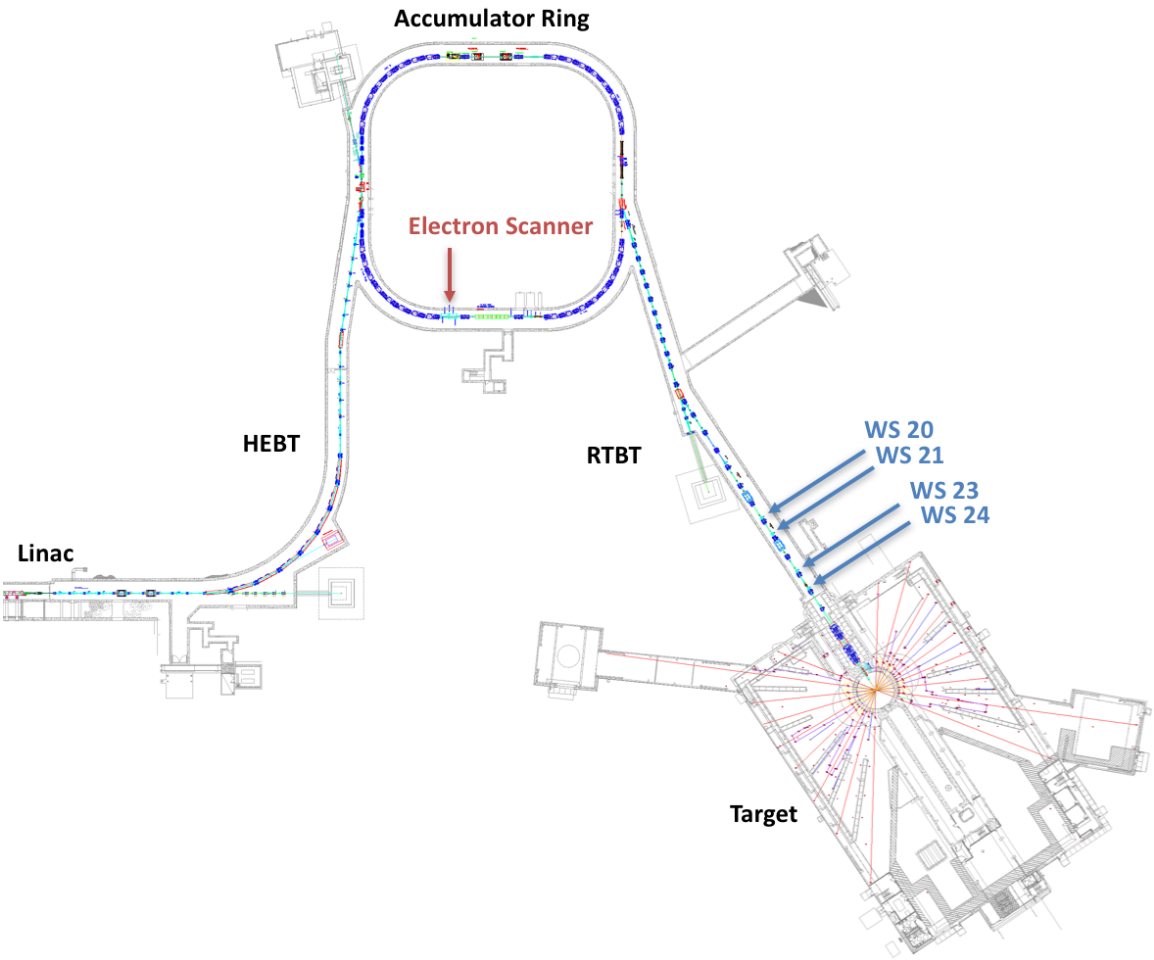

Figure 4.1: Schematic layout of the SNS High-Energy Beam Transport (HEBT), Accumulator Ring, and Ring-to-Target Beam Transport (RTBT) with key diagnostic devices indicated. The Electron Scanner, indicated in red, is located in the Accumulator Ring. The four wire scanners used in these studies, indicated in blue, are located in the RTBT.

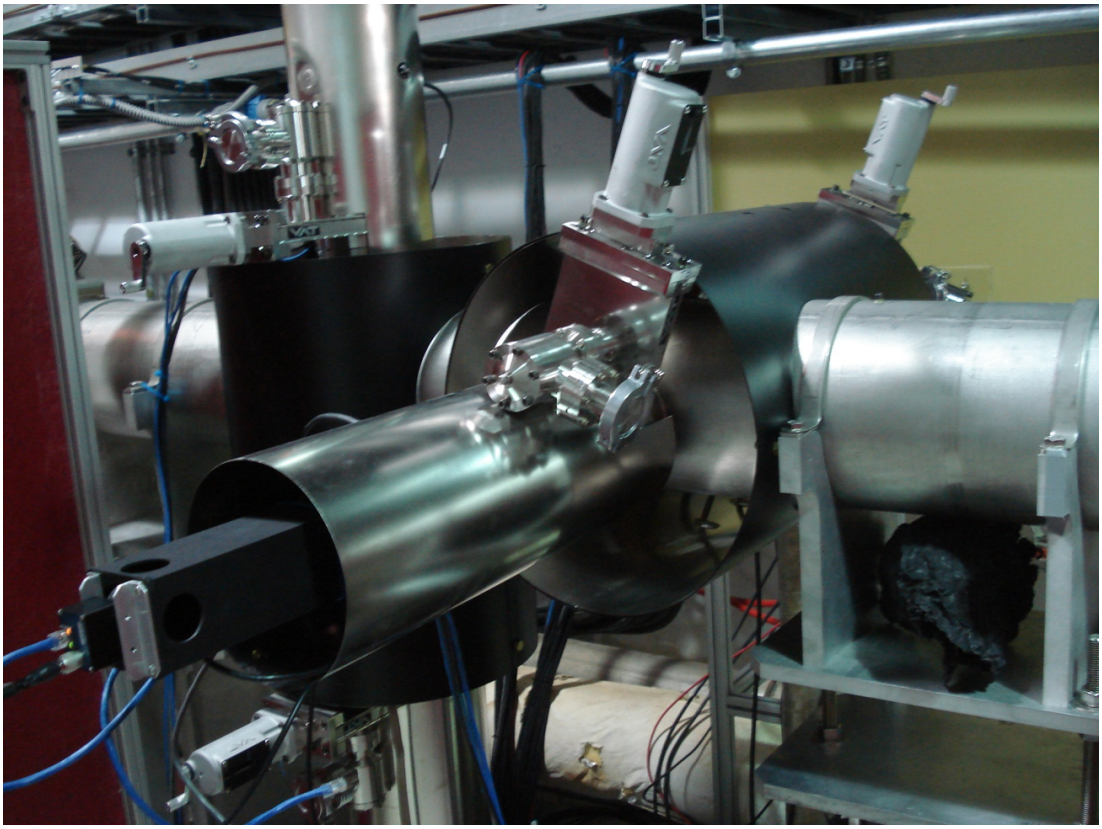

Figure 4.2: Image of the Electron Scanners located in the Accumulator Ring. The Electron Scanner in the foreground (horizontal pipe) collects the vertical profiles and the Electron Scanner in the background (vertical pipe) collects the horizontal profiles. The proton beam circulates in the Accumulator Ring from the right side of the image to the left. Image courtesy of J. Fazekas.

electron beam probe to measure profiles of the high-intensity SNS proton beam. The study used computer simulations of the diagnostic setup to determine whether accurate profiles of the realistic proton beam distribution could be measured with an electron beam profile monitor. The paper examined two methods of measuring beam profiles: tomography for 2D reconstruction and 1D profile reconstruction. The study concluded that it was feasible to use an electron scanner for profile measurements in the SNS Accumulator Ring. The final device uses the more direct 1D profile reconstruction discussed later in this section.

The feasibility study was extended in 2007 by Logachev who expanded the theory, ran numerical simulations, and began development of an instrument for use in the SNS[60]. In 2008, Logachev calculated the necessary lattice elements for an SNS Electron Scanner and demonstrated experimental results in the SNS Accumulator Ring[59]. Blokland was responsible for rotating the SNS electron beam, which allowed the profiles to be calculated from the derivative of the beam curve[4]. This was one of the main advancements to the SNS design over previous designs.

The SNS Beam Instrumentation team became the primary owner after the installation of the Electron Scanner. Over the next few years, improvements were made to the Electron Scanner hardware, data collection, analysis package, and results[2, 4, 5].

The Electron Scanner obtains profiles by passing an electron beam diagonally across the SNS Accumulator Ring beam pipe. In the absence of the proton beam, the electron beam projects a slanted line on the projection screen. As the circulating proton beam passes the diagnostic device, the electron beam is deflected in the presence of the electromagnetic field of the proton beam. The path, whether deflected or undeflected, is then projected across a pair of wires that serve as beam markers. These markers create gaps in the electron beam, providing a scale for the size of the beam. The beam is finally projected onto a fluorescent screen and an image of the projection is captured. This process is shown in Figures 4.3. Figure 4.4 demonstrates the deflection of the electron beam due to proton beams of various intensities.

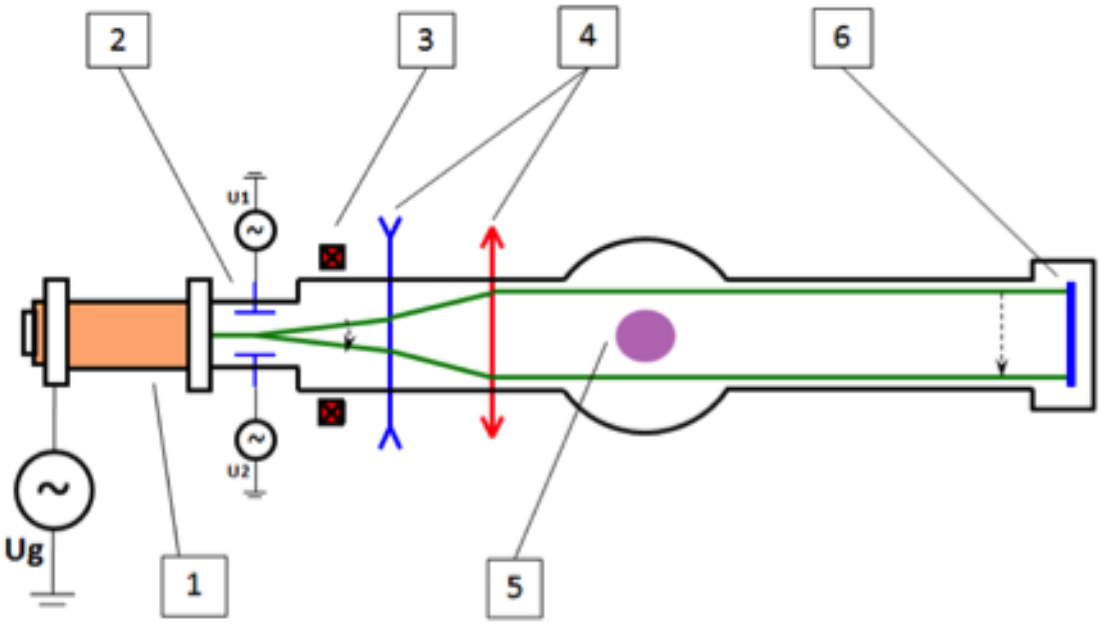

Figure 4.3: A schematic diagram of the Electron Scanner at the SNS[4]. The electron beam, shown as green lines, is emitted from the electron gun (1) and is deflected across the beam pipe by the deflection scan system (2). The dipole correctors (3) and quadrupole magnets (4) serve to properly focus the beam across the path of the proton beam (5). The deflected electron beam then forms an image on the projection screen (6), which is captured as the measurement for analysis.

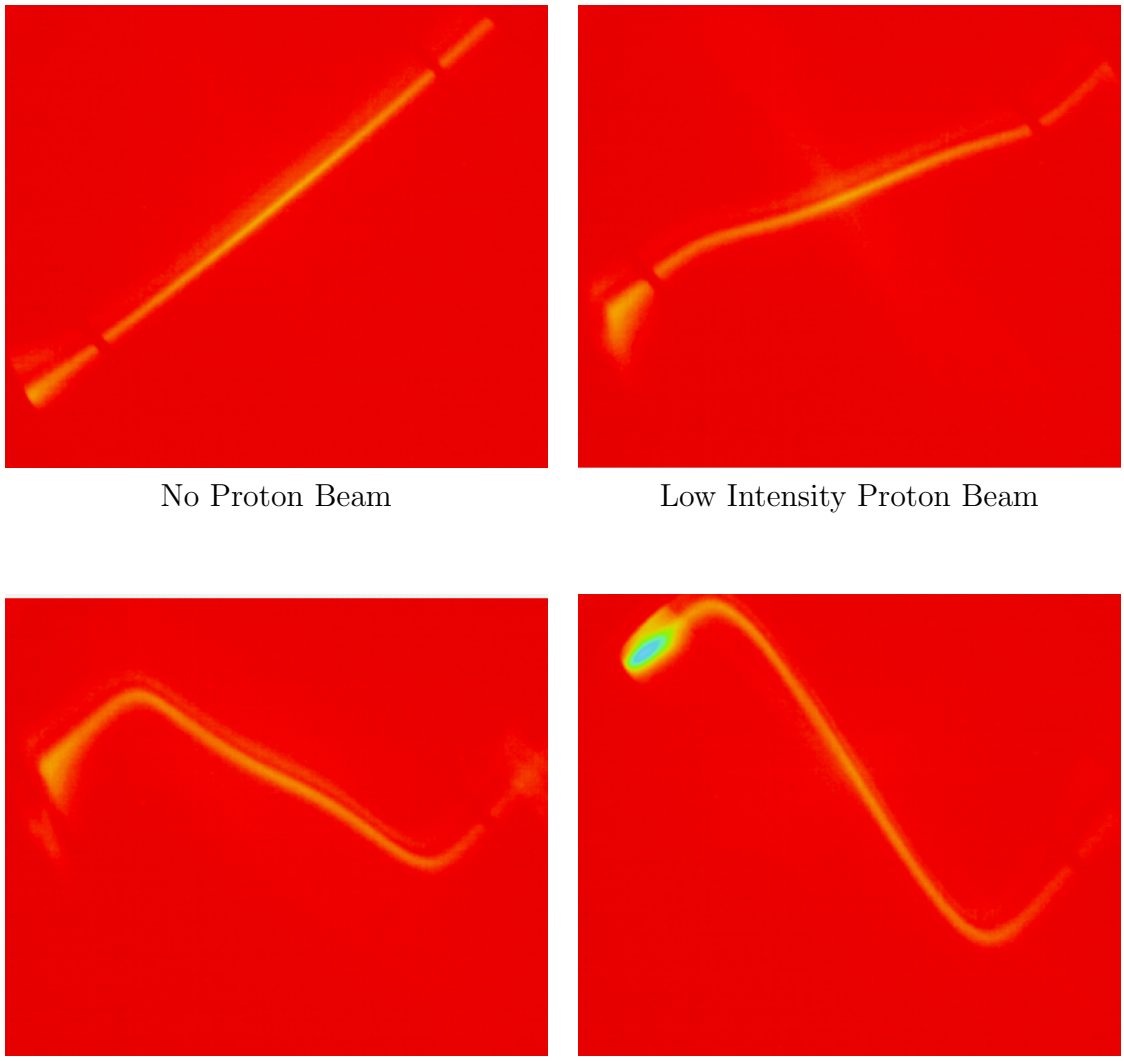

Figure 4.4: Unprocessed Electron Scanner images demonstrating the deflection of the electron beam, shown in yellow, for different proton beam intensities. The marker cutouts can be clearly seen in the first image. These examples are taken from image slices 5, 11, 14, and 19 of turn 840 in the production tune case with skew quadrupoles discussed in Chapter 6, respectively. See Section 4.2.1 for details about the images and analysis methodology.

By tilting the electron beam, we add a z-component to the path of the beam which allows the 1D profile reconstruction. Specifically, the transverse profile is derived from the size of the deflection along the projection with respect to the undeflected beam[1]. A summary of this process is shown in Figure 4.5. The distribution of the proton beam is related to the deflection of the electron beam by

$$\frac{\mathrm{d}\theta}{\mathrm{d}x} = \int_L \frac{e}{mv^2} \cdot \frac{\delta(x,y)}{\varepsilon_0} dy \tag{4.1}$$

where e, m, and v are the electron charge, mass and velocity, respectively, $\delta(x,y)$ is the proton beam density distribution, and θ is the deflection of the electron beam with respect to the undeflected electron beam. The proton beam density is related to the electric field of the beam by Maxwell's Equation:

$$\delta(x,y) = \epsilon_o(\frac{\partial \mathrm{E}_x}{\partial x} + \frac{\partial \mathrm{E}_y}{\partial y}) \tag{4.2}$$

where $\vec{E}$ is the electric field of the proton beam.

The Electron Scanner has several advantages over traditional wire scanners. The first advantage is the non-destructive nature of the Electron Scanner. This allows us to collect data parasitically to regular production operations. This means that the Electron Scanner could become a helpful diagnostic tool for regular use during operations in the future. Second, the Electron Scanner has the ability to capture 20 ns slices of the accumulating 700 ns proton beam. Due to this time resolution, we are capable of capturing profiles of the beam at different longitudinal positions. This is especially useful because the SNS beam is not always uniformly distributed along the longitudinal axis. Examining many profiles together can provide a more detailed understanding of the longitudinal profile and how it evolves. This differs from the SNS wire scanners which sum along the longitudinal length of the beam by measuring the integrated charge induced by the full length of the beam pulse. Additionally, the short scan time means that any variation in transverse profiles can be studied across the

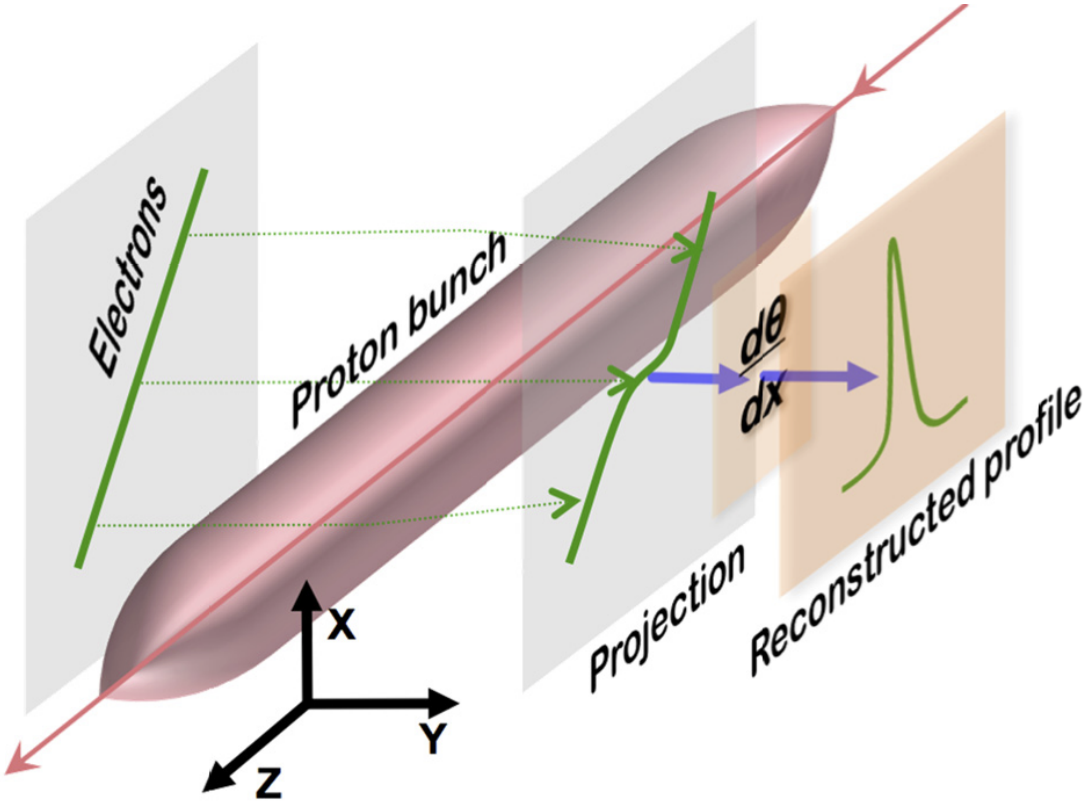

Figure 4.5: (Left) The electron beam is deflected diagonally across the path of the circulating proton beam. (Center) The fields of the passing proton beam deflect the electron beam, which is then projected onto the phosphorous screen. (Right) The derivative of this projection provides the reconstructed transverse beam profile.[2]

longitudinal length of the beam. Third, each Electron Scanner profile represents the profile from within a single proton beam pulse. A wire scanner profile is composed of numerous data points that are each from separate proton beam pulses. Therefore the Electron Scanner is capable of detecting pulse-to-pulse variations that a wire scanner cannot. It is important to remember that each Electron Scanner slice is captured from a separate accumulating beam. These three advantages over traditional wire scanners make the Electron Scanner a unique and powerful diagnostic tool.

The main limiting factors of the SNS Electron Scanner are the high voltage transformer and the beam pipe aperture sizes. The amount of voltage used effects the size of the deflection of the electron beam for a given proton beam intensity. The high voltage transformer arcs around 60 kV. This limits the peak proton beam intensity that can be scanned before the deflection of the electron beam goes off the screen. The apertures determine what view the Electron Scanner has into the SNS beam pipe. Therefore, the apertures limit the maximum size of the proton beam that can be scanned[5]. The Electron Scanner beam pipes were rotated from the ideal angle in order to maximize the size of the aperture. The vertical aperture has a tighter restriction on the beam size than the horizontal. This limitation caused problems for our vertical measurements in Chapter 6. Additionally, given these limitations and the prototype nature of the hardware, the device expert was needed to optimally configure the device before each experimental shift.

4.2 Analysis Package

The analysis package is built in LabVIEW and allows users to rapidly process raw images and produce finished root mean square (RMS) sizes and beam profiles. This is especially important due to the size of the datasets frequently produced by the Electron Scanner. These frequently contain 300 to 800 raw images per experimental configuration. The study presented in this study is the first use of the device and software for any non-development purpose. Therefore it is important to present an

example of each major step of the analysis package and some of the main image artifacts that were documented during this research.

4.2.1 Methodology

The methodology of the analysis package follows the same procedure outlined as the theory discussed in Section 4.1. The general procedure is to determine the path of the beam from the raw images, calculate a spline curve from this data, calculate the derivative of the spline curve and fit a second spline curve along the derivative. The second spline curve is the beam profile. The following screenshots illustrate the specific steps taken to produce final data.

Figure 4.6 shows an unprocessed image from the Electron Scanner imported into LabVIEW. The electron beam, shown in yellow, is overlaid with a user-defined starting line, shown in green. This starting line is used to quickly locate an initial location within the beam to start the analysis. The two voids near either end of the projection are the beam marker locations. The beam markers are 60 mm apart. We will use the projected spacing to indicate whether the undeflected electron beam was parallel as it passed through the circulating proton beam. The edges of the beam are created by the edge of the projection screen, which is 85 mm in diameter. In Section 4.2.2, we will discuss these beam markers and edges as references for the scale of the beam size.

Figure 4.7 shows how the analysis package uses the initial starting line to locate the path of the electron beam and creates initial slices, shown in blue. These initial slices are used to determine the direction of the beam.

Figure 4.8 shows how the analysis package follows the entire path of the electron beam and slices it across the width of the beam. The intensity of the image along each slice is fit to a Gaussian curve. The peak of each Gaussian curve, shown in black, is used to define the center of the electron beam along the path.

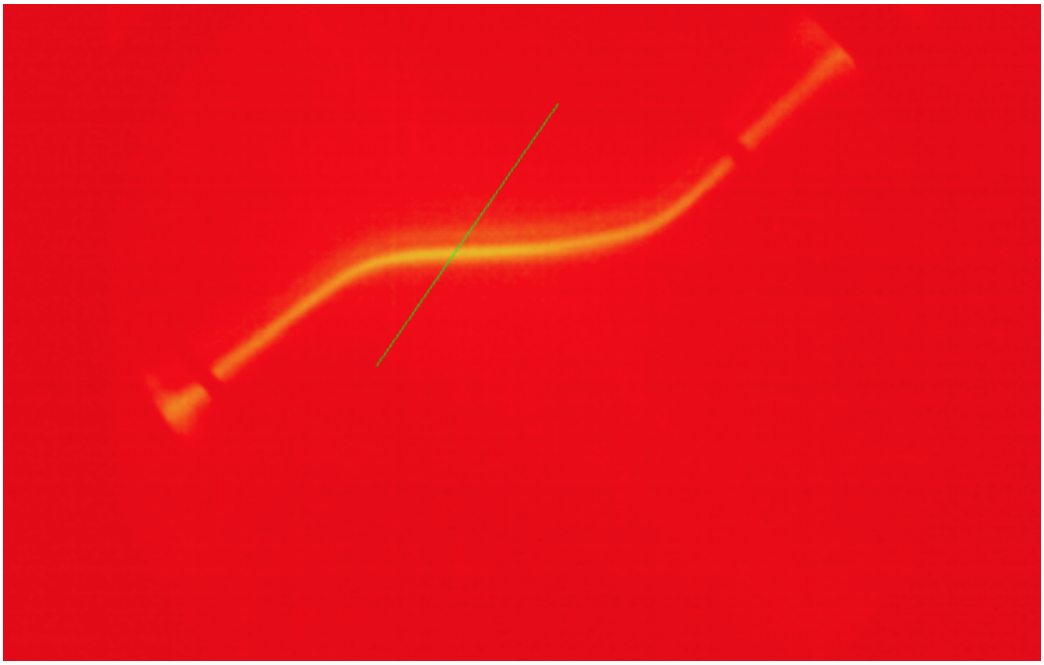

Figure 4.6: Unprocessed Electron Scanner image with the electron beam, shown in yellow, and the user-defined overlay line, shown in green, to indicate the starting area.

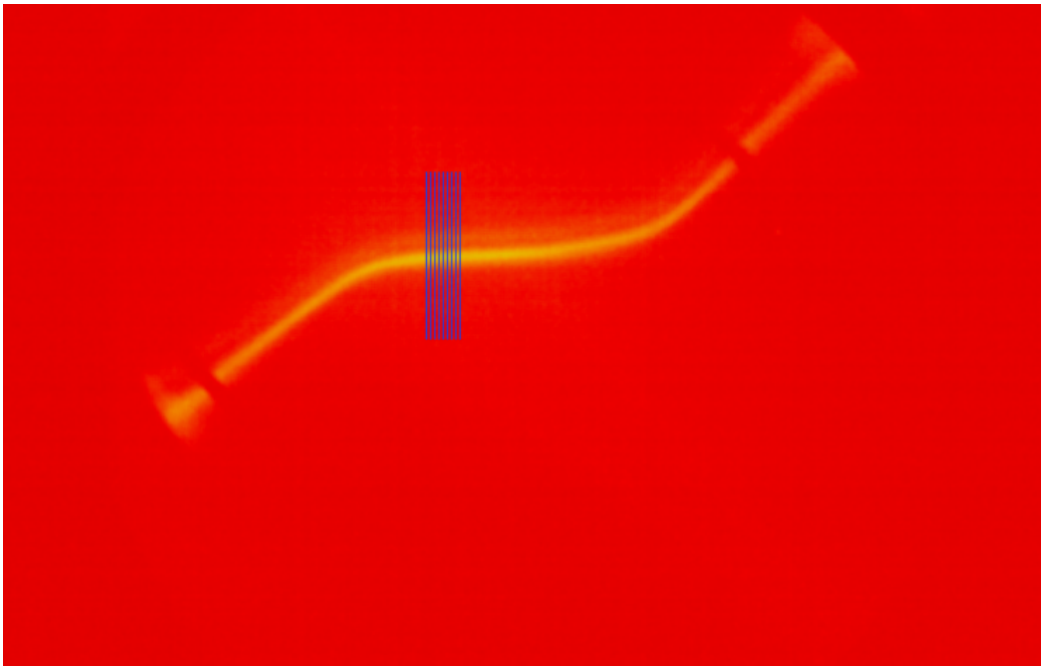

Figure 4.7: Electron Scanner image where the initial analysis slices, shown in blue, define the algorithm's starting area.

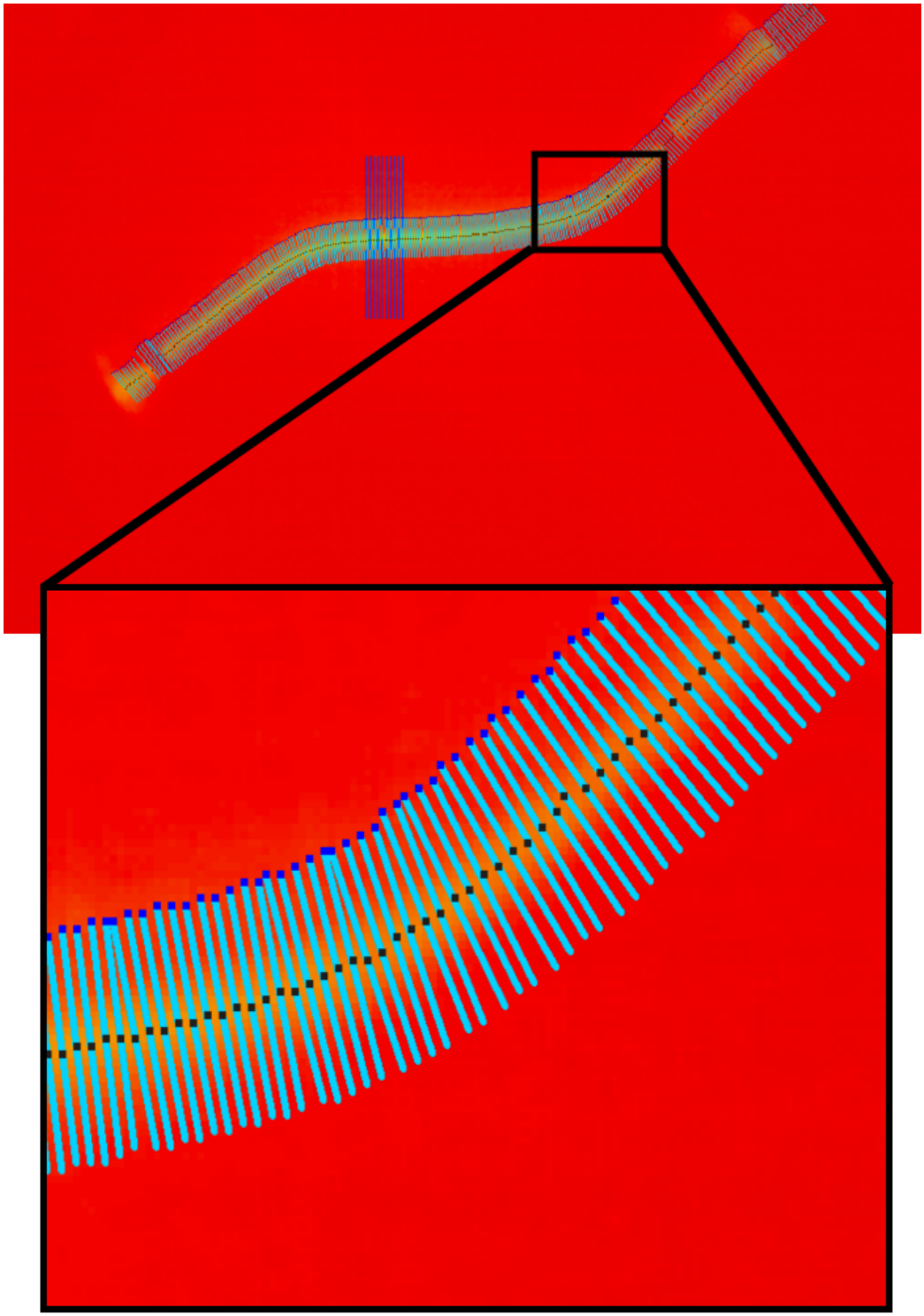

Figure 4.8: Processed Electron Scanner image with analysis slices, shown in blue. Gaussian peaks, shown in black, are used to represent the center of the electron beam. The inset shows how the analysis follows the path through the right-hand bend.

Figure 4.9 shows how the analysis package fits a spline curve, shown in red, through the set of Gaussian peaks, shown in green. This spline curve is used to calculate a smoother set of points representing the path of the projected beam. This results in a reduction of noise in the final profile after the derivative of the path is taken. The spline fit technique also allows the projection of the beam to be traced through the cutouts made by the electron scanner beam markers.

Figure 4.10 shows the final profiles produced by the analysis package. The derivative of the spline curve with respect to the undeflected beam is shown in blue. The final beam profile, shown in green, is produced by fitting a spline curve to this derivative. The derivative of the raw Gaussian peaks is shown in red. The noise reduction benefits of utilizing a spline fit to represent the data prior to taking the derivative are obvious by comparing the final profiles.

Figure 4.11 demonstrates four types of artifacts occasionally seen during data collection. The top left image contains a large bright spot at the right edge of the beam path. This is likely an artifact of the electron gun producing off energy or "free" electrons that are not properly accelerated. These free electrons do not follow the design path through the proton beam and can create bright spots on the phosphor screen. The analysis package can compensate for some bright spots, depending on the size and location. This only presents a problem if the deflection of the beam spreads into the bright spots. Otherwise the bright spots occur in the beam floor and can be ignored. The top right image contains an off-screen beam path. This happens when the proton beam intensity increases enough to create a large deflection in the electron beam. The analysis package compensates by directly connecting the two path segments along the edge of the image. If the off-screen path length is small, then this will have a minimal effect on the profile. However, this generally becomes a reoccurring and increasing problem for accumulating beams. The bottom left image contains a ghost beam path. It is unclear what causes this problem. One possibility is a ripple in the high voltage power supply. In general, the ghost path is fainter than the correct path and the analysis package has no problem analyzing the image. The

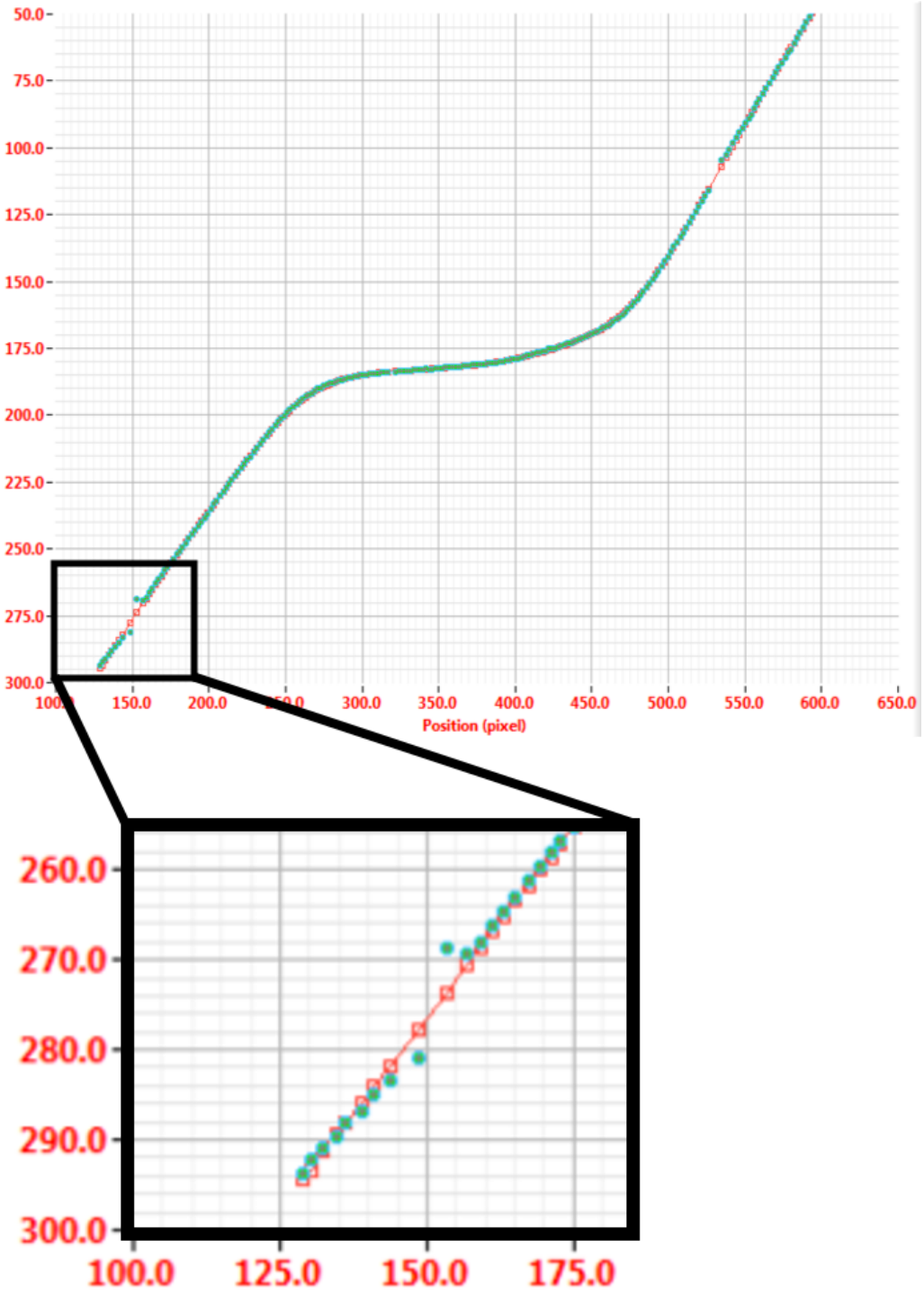

Figure 4.9: Processed Gaussian peaks, shown in green, are used to find a spline curve, shown in red. The inset shows a close up of the image focusing on the left-hand beam marker gap.

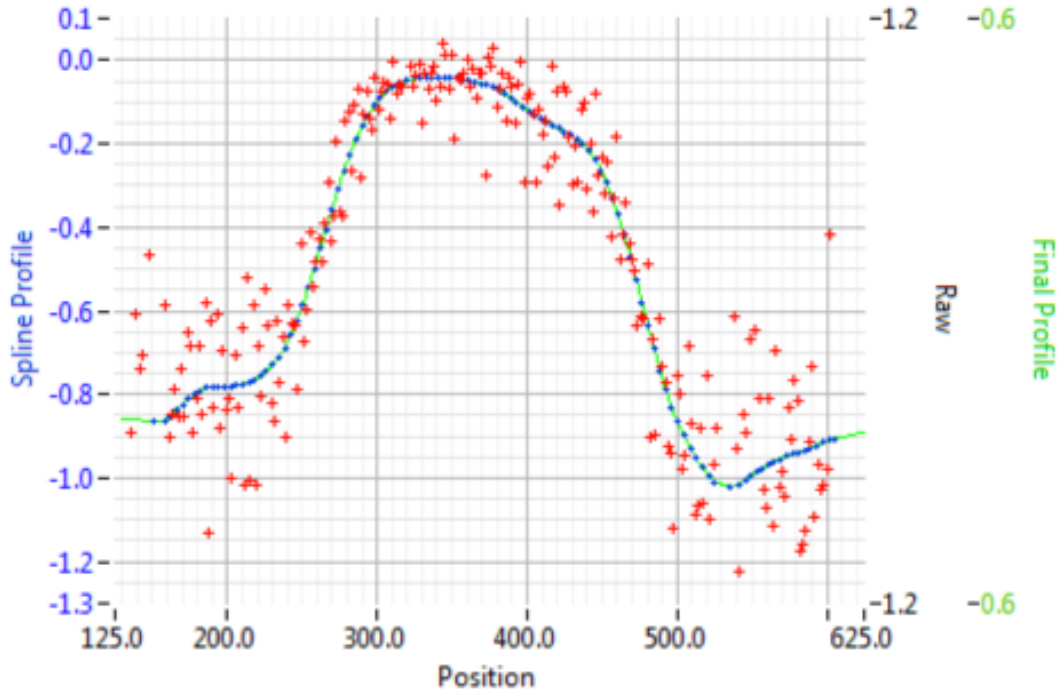

Figure 4.10: Final beam profile from the Electron Scanner, shown in green, is the spline fit of the derivative of the processed spline curve, shown in blue. The derivative of the Gaussian peaks without the benefits of the noise reducing spline fit is shown in red for comparison.

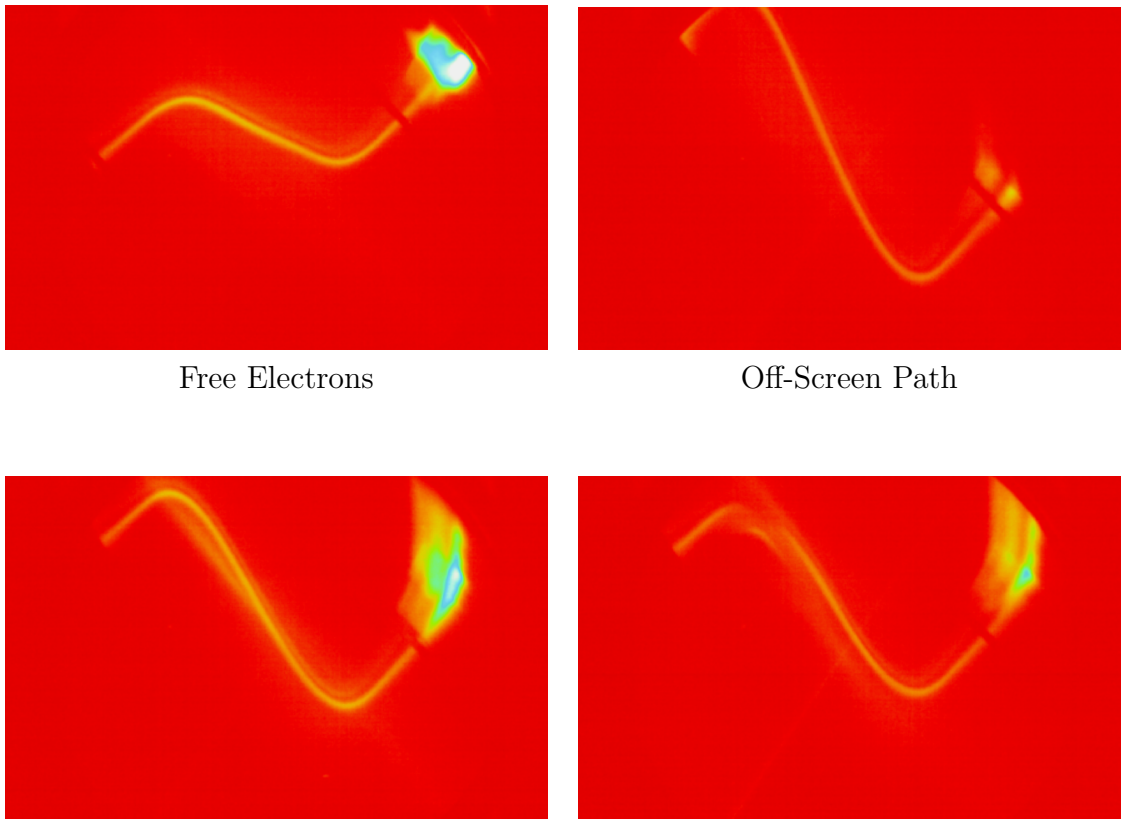

Figure 4.11: Several unprocessed Electron Scanner images demonstrating various types of documented artifacts. These examples are taken from turn 495 slice 14, turn 885 slice 16, and turn 720 slices 18 and 19 in the equal tune case without skew quadrupoles discussed in Chapter 6, respectively.

bottom right image contains a broken beam path. It is also unclear what causes these discontinuities. One possibility is an arc that rapidly drops the high voltage, creating a different level of deflection and a break in the path. If the break in the path is small, then the analysis package usually resolves the path reasonably well, although small discontinuities are inevitable. In this specific example, the bottom images occurred in series. Whether they are actually related is unclear from the data on hand. Both the ghost beam path and broken beam path artifacts have been seen independent of each other. The analysis package is capable of tracing the beam path through some of these artifacts due to the robustness of the methodology and algorithm. However, in over 70% of cases, beam slices with artifacts are discarded and the adjacent slices are averaged to approximate the lost profile. This substitution generally works, but it is not capable of resolving repeating issues, such as large beam deflection off screen due to high intensity beams.

The Electron Scanner is capable of collecting 40 profiles within the longitudinal period of the Accumulator Ring. Figure 4.12 shows an example of how these can be combined to create a 3D rendering of the 1D profiles of the beam. This 3D rendering allows us to quickly see the variation in transverse profiles across the whole bunch length. Additionally, by comparing multiple 3D renderings, we are able to quickly determine whether the beam is changing longitudinally. Figure 4.13 is a composite of multiple Electron Scanner 3D renderings showing the proton beam at various points during accumulation[3]. This can quickly present the full evolution of the proton beam. This is especially useful for demonstrating multi-turn effects, such as coupling or RF bunching.

In addition to creating 3D renderings of profiles, we have the ability to sum the profiles longitudinally within a single bunch. This produces a single-turn sum profile similar to profiles produced by the wire scanners. We will use these Electron Scanner sum profiles for two additional purposes. First, we will use this sum profile to calculate the RMS size. Second, we will assemble an evolution of the transverse beam profile over the duration of the experiment using the sum profiles. Thus, each

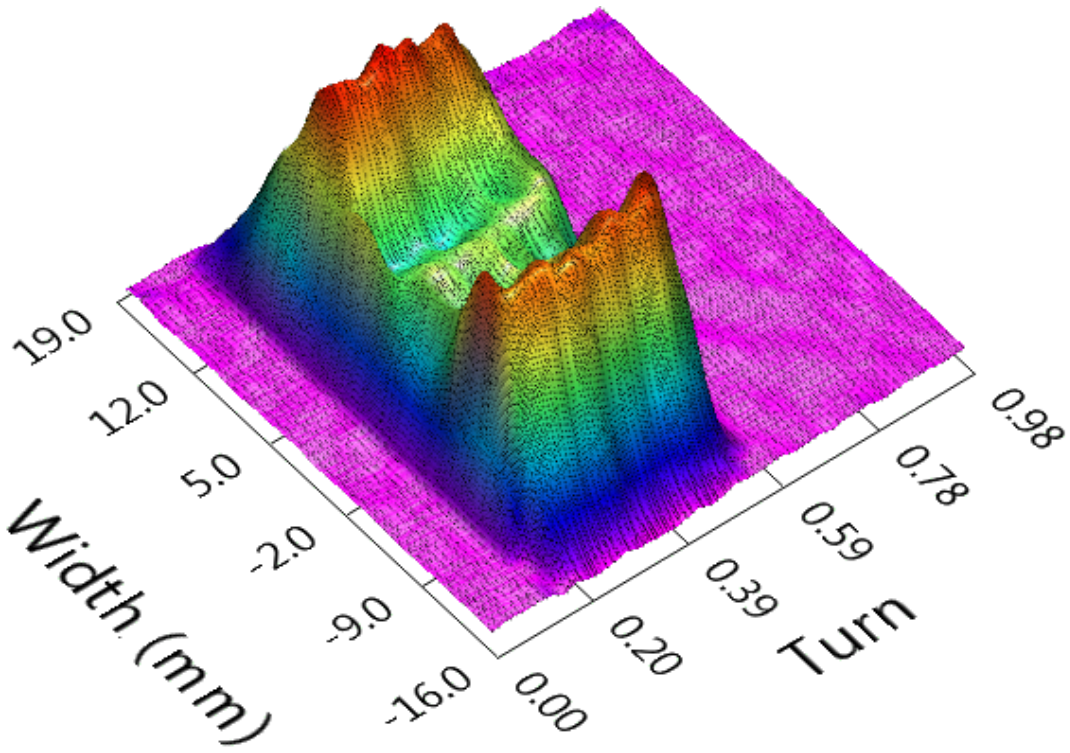

Figure 4.12: A 3D Electron Scanner rendering of a single turn of low intensity proton beam.

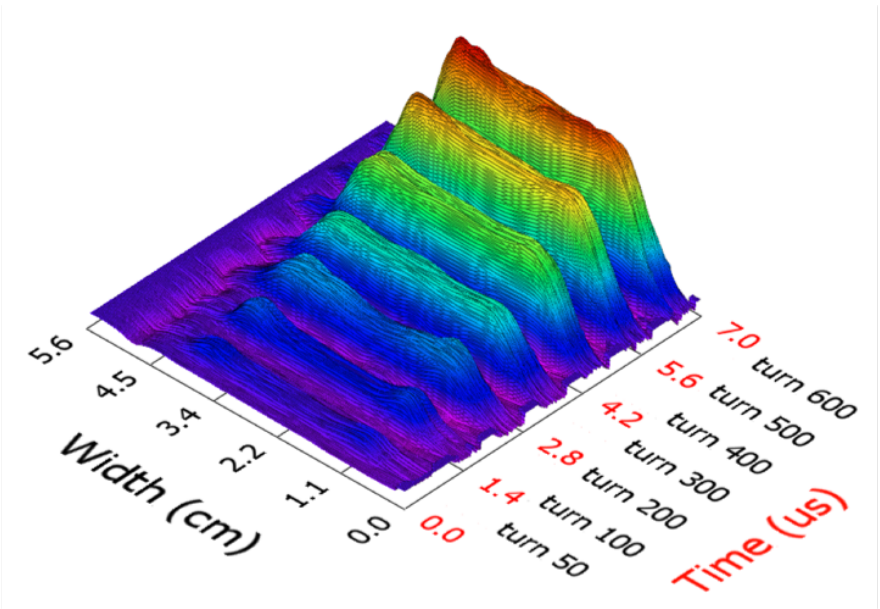

Figure 4.13: A set of 3D Electron Scanner renderings of a high-intensity proton beam during accumulation at turns 50, 100, 200, 300, 400, 500 and 600[3].

profile evolution will display the change in profile during both the accumulation and storage of the beam. However, the profile evolution will only present the sum of the bunch and will not show any longitudinal dynamics. Both the RMS size and profile evolutions are used throughout Section 5.4 and Chapter 6.

4.2.2 Calibration

In this section, we discuss calibration of the electron beam scale in the Electron Scanner analysis package. Without references for the scale, the Electron Scanner images would have no ability to describe the absolute size of the beam. This would limit the device to providing only general profile shapes or qualitative data. There are two parts to properly scaling the Electron Scanner data.

The first part is determining the exact rotation of the undeflected beam. While the angle of the rotation is expected to be 45°, the rotation of the horizontal and vertical devices needed to be measured. This value is necessary for properly determining the derivative of the deflected beam with respect to the undeflected beam. The derivative is deformed without an accurate understanding of the path of the undeflected beam.

The second part is determining the scale of the image, or the equivalent physical size of each pixel in the device images. As we mentioned before, the Electron Scanner was designed with two references, the beam markers and edges. The electron beam edges provide the definitive reference as to the size of the screen and, therefore, the size of the projected electron beam. The beam markers provide a reference for the alignment of the electron beam across the path of the circulating proton beam. The Electron Scanner quadrupoles are responsible for properly focusing the beam across the pipe. If the path of the electron beam is not parallel across the pipe, then the projected image will be scaled from the actual size. If the electron beam is diverging, then the projected image will provide a profile wider than at the point of the deflection. If the electron beam is converging, then the projected image will provide a profile narrower than at the point of deflection. Therefore, the relative

scaling for the beam is important to the overall calibration. Figure 4.14 illustrates the effects of diverging and converging electron beams.

Figure 4.15 shows the user interface developed for simultaneously measuring both the rotation and scale of the undeflected beam. The software has been integrated into the analysis package. When an Electron Scanner image is loaded, this screen allows future users to check the beam calibration. The user can use the beam marker indicators, shown in yellow, and the beam edge indicators, shown in blue, to quickly indicate the correct locations on the image. The distances and angles are measured and the results returned on the right hand side.

In order to confirm that the values were not changing during the experiments, multiple measurements needed to be made. Measurements were made prior to and following data collection for each of the five Electron Scanner configurations studied in Section 5.4. Specifically, we used the first image captured, image 0 of turn 5, and the last image captured, image 39 of turn 395. The experiment calibration always involves tuning a temporal offset to place the initial bunch in the center of the scan period. This is to ensure that the proton beam is not accidentally split between two Electron Scanner data sets. It also guarantees that there should never be any proton beam present during these images. The results of the measurements are shown in Table 4.1.

In each measurement, the scale of the image is calculated by using the known distance between the edges of the beam divided by the measured distance using the calibration screen. As previously stated, the phosphorous screen forms the edge of the beam and is known to be 85 mm in diameter. The scale factor has the units of mm per pixel. The angle of the rotation of the beam is determined by the angle of the beam markers with respect to the horizontal axis of the image. The angle is calculated by the placement of the markers in the calibration screen and has the units of radians. The statistical error of each measurement was calculated using the

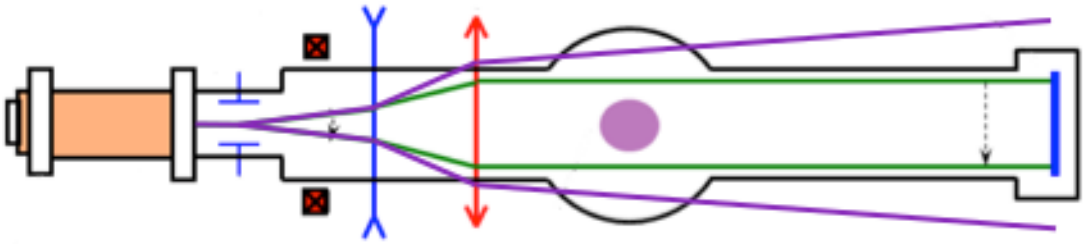

Diverging Electron Beam

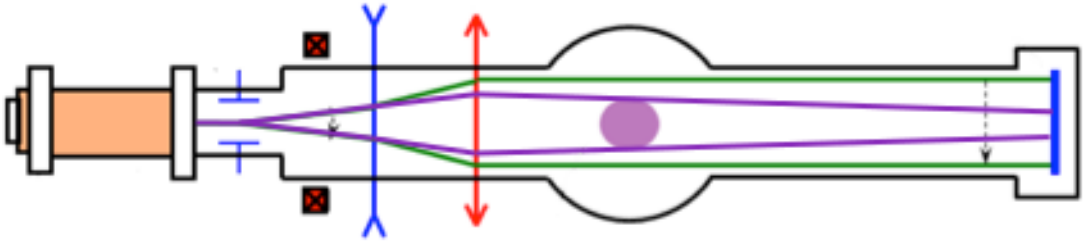

Converging Electron Beam

Figure 4.14: Schematic diagrams of the Electron Scanner showing the effect of focusing errors. The properly focused electron beam is shown as green lines. The diverging and converging electron beams are shown as purple lines.

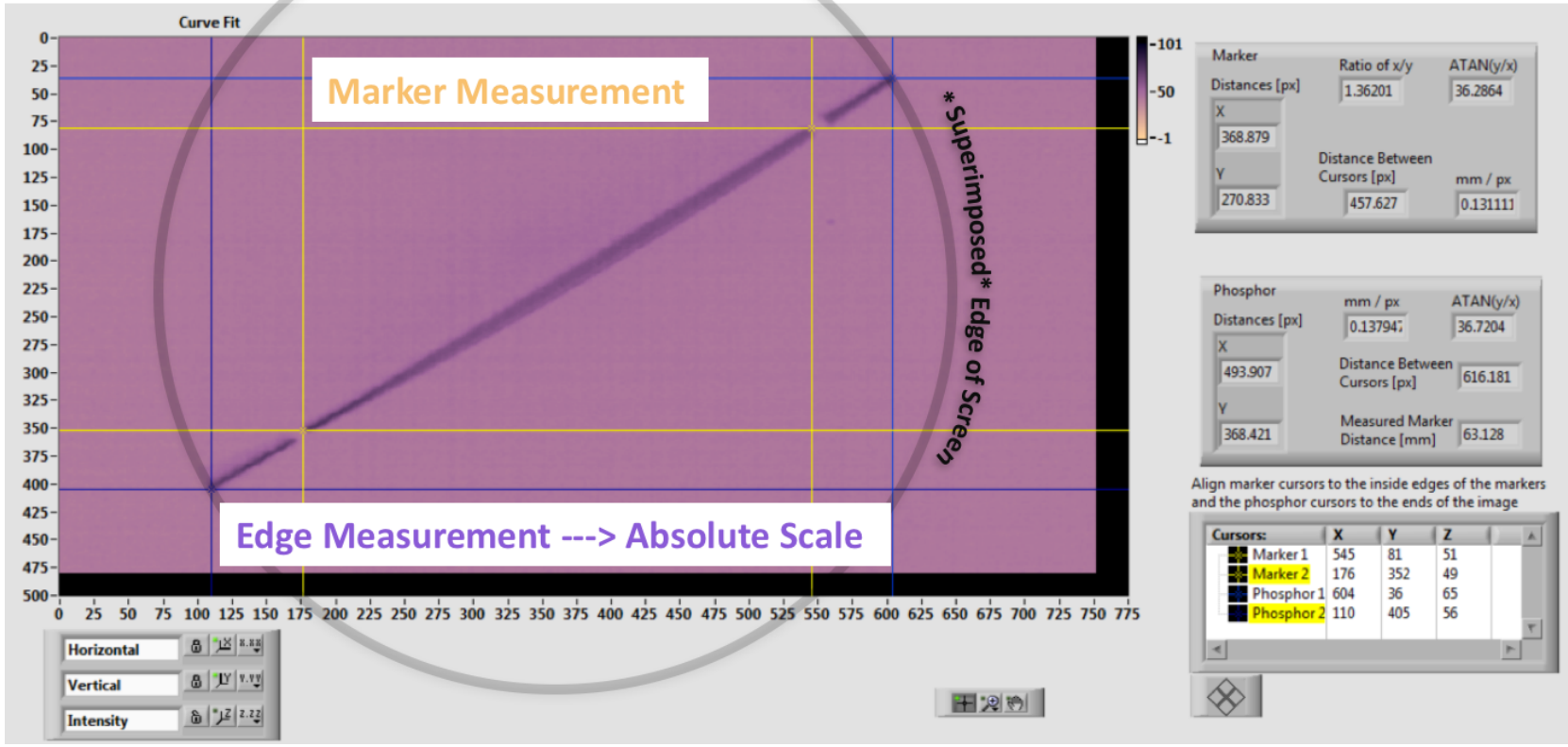

Figure 4.15: Electron Scanner beam calibration screen. The undeflected electron beam is shown in dark purple and the user placed indicators are shown in blue and yellow. The circle was added to the screenshot to show the relative position of the edge of the phosphorous screen.

Table 4.1: Measurements of the rotation and scale of the undeflected Electron Scanner beams

Experimental Case		Horizontal		Vertical	
Tune	Intensity	Scale [mm/px]	Angle [°]	Scale [mm/px]	Angle [°]
		Turn 5 - Slice 0			
Equal	Low	0.1381	36.64	0.1384	71.54
Equal	Mid	0.1378	36.86	0.1385	71.36
Equal	Normal	0.1374	36.81	0.1384	71.52
Mid	Normal	0.1373	36.88	0.1386	71.63
Split	Normal	0.1373	36.70	0.1393	71.20
Average		0.1376	36.78	0.1386	71.45
Standard Deviation		3.19E-04	0.0930	3.38E-04	0.1523
		Turn 395 - Slice 39			
Equal	Low	0.1379	36.59	0.1385	71.36
Equal	Mid	0.1371	36.92	0.1387	71.60
Equal	Normal	0.1372	36.63	0.1383	71.47
Mid	Normal	0.1371	36.79	0.1395	71.47
Split	Normal	0.1374	36.89	0.1395	71.51
Average		0.1373	36.76	0.1389	71.48
Standard Deviation		3.01E-04	0.1335	5.06E-04	0.0773
		Combined Data			
Average		0.1375	36.77	0.1388	71.47
Standard Deviation		3.32E-04	0.12	4.50E-04	0.12

standard deviation:

$$\sigma_x = \sqrt{\frac{\sum_{i}^{N}(x_i - \bar{x})^2}{N}} \tag{4.3}$$

where x_i is the data point, $\bar{x}$ is the average, and N is the number of data points.

The final scale factor used by the LabVIEW Electron Scanner analysis package is determined by:

$$a_{\text{LabVIEW}} = a_{\text{Scale}} \times \tan\left(\theta_{\text{Rotation}}\right) \tag{4.4}$$

where a_{Scale} is the scale factor measured from the beam edge, θ_{Rotation} is the rotation of the beam measured from the beam markers, and a_{LabVIEW} is the final scale factor used in LabVIEW. The error for the final scale factor is:

$$\Delta a_{\text{LabVIEW}} = \Bigg[\left(\Delta a_{\text{Scale}} \times \tan\left(\theta_{\text{Rotation}}\right)\right)^2 + \left(a_{\text{Scale}} \times \sec^2\left(\theta_{\text{Rotation}}\right) \times \Delta\theta_{\text{Rotation}}\right)^2\Bigg]^{1/2} \tag{4.5}$$

where $\Delta\theta_{\text{Rotation}}$ and Δa_{Scale} are the errors previously determine from the standard deviation of the beam marker and edge data points, respectively, and $\Delta a_{\text{LabVIEW}}$ is the error of the final scale factors used by LabVIEW. The final LabVIEW scale factors were found to be 0.103 ± 5.1E-4 mm/px for the horizontal Electron Scanner and 0.414 ± 3.2E-3 mm/px for the vertical Electron Scanner. Using these results, the horizontal and vertical projected marker spaces were measured as 63.1 mm and 62.8 mm, respectively. The actual beam marker spacing on both the horizontal and vertical devices is 60 mm. This is equivalent to a $\sim 5\%$ correction in the width of the beam profile.

4.2.3 Confirming Data

We needed to confirm that the Electron Scanner produced viable data for our experiments prior to examining our main results. We used the integrated charge and centroid position measurements from the Electron Scanner data to check the overall consistency and reliability of the measurements. These figures serve as a sanity check for the Electron Scanner data. The integrated charge curve shows the calculated area under the profile at each turn in the evolution. The centroid position curve shows the calculated center of the profile for each turn in the evolution relative to the centroid marker. The centroid marker position can be changed but remains fixed for each individual dataset.

Figures 4.16 and 4.17 show the integrated charge and centroid position for the three nominal intensity beam configurations in Section 5.4. Figures 4.18 and 4.19 show the integrated charge and centroid position for the three equal-tune beam configurations in Section 5.4. For this experiment, we expect the charge to increase until turn 100 when accumulation stops and remain almost constant during storage. This confirms that the Electron Scanner captured the entire beam in each profile slice. If the integrated charge had had a consistent decrease over the storage period, that would have signaled that either the beam had large losses or that the beam had moved or spread outside of the Electron Scanner apertures. In this experiment, we expect the centroid to remain approximately stationary and not to exhibit any sudden changes. After the accumulation period, the centroid positions remain stationary. These figures indicate that the data captured and processed by the Electron Scanner is consistent with our expectations for nominal beam evolution.

Figures 4.20 and 4.21 show the integrated charge and centroid position for all of the production-style configurations from Chapter 6. The integrated charge measurements are almost identical for the four cases until the higher beam intensities. Additionally, the four cases show minimal centroid jitter with a small consistent shift of a few millimeters in the centroid position during the entire accumulation. This is a

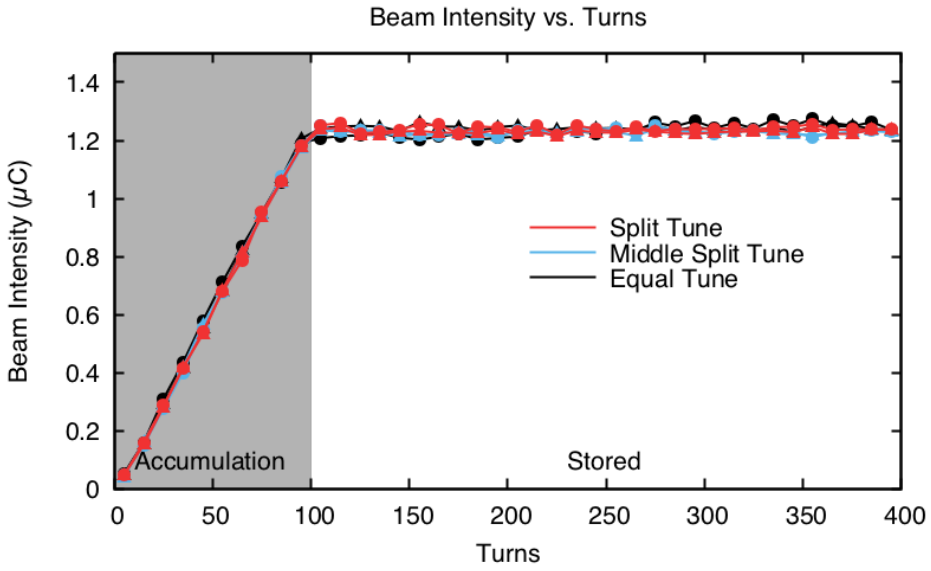

Figure 4.16: Comparison of the integrated charge curves for the split tune (red), middle split tune (blue), and equal tune (black) configurations for experiment three in the Simple Accumulation Experiments. The horizontal and vertical data are shown with '▲' and '●' points, respectively.

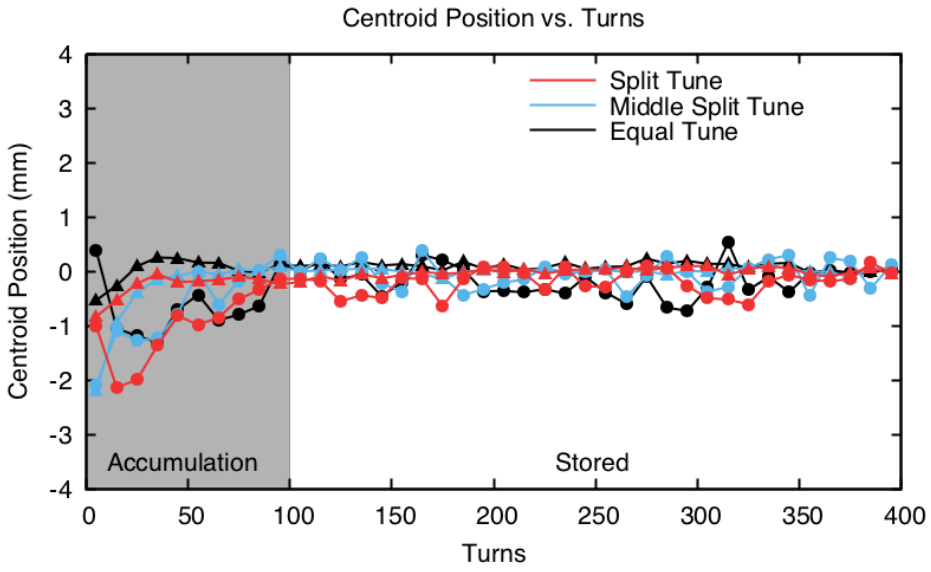

Figure 4.17: Comparison of the centroid position curves for the split tune (red), middle split tune (blue), and equal tune (black) configurations for experiment three in the Simple Accumulation Experiments. The horizontal and vertical data are shown with '▲' and '●' points, respectively.

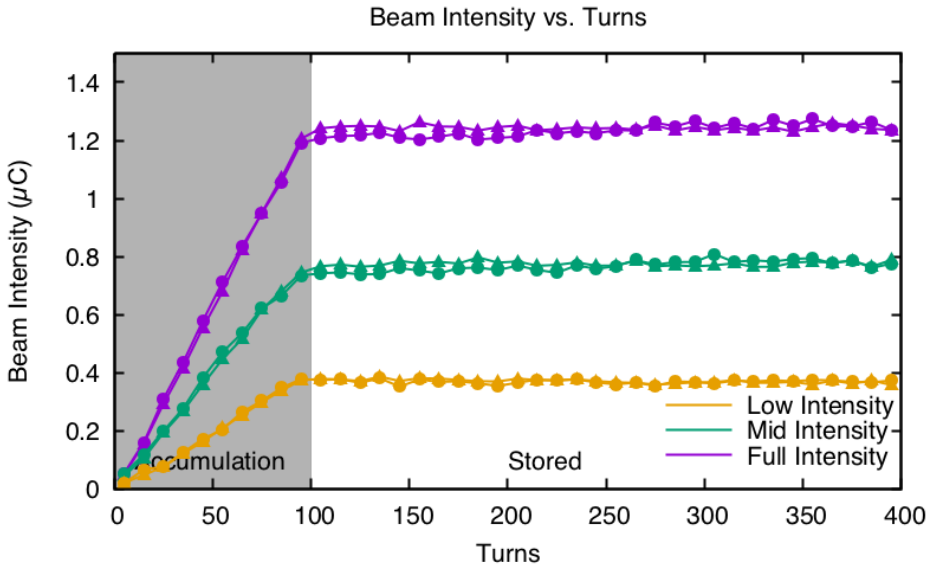

Figure 4.18: Comparison of the integrated charge curves for the equal-tune low intensity (gold), mid intensity (green), and full intensity (purple) configurations for experiment three. The horizontal and vertical data are shown with '▲' and '●' points, respectively.

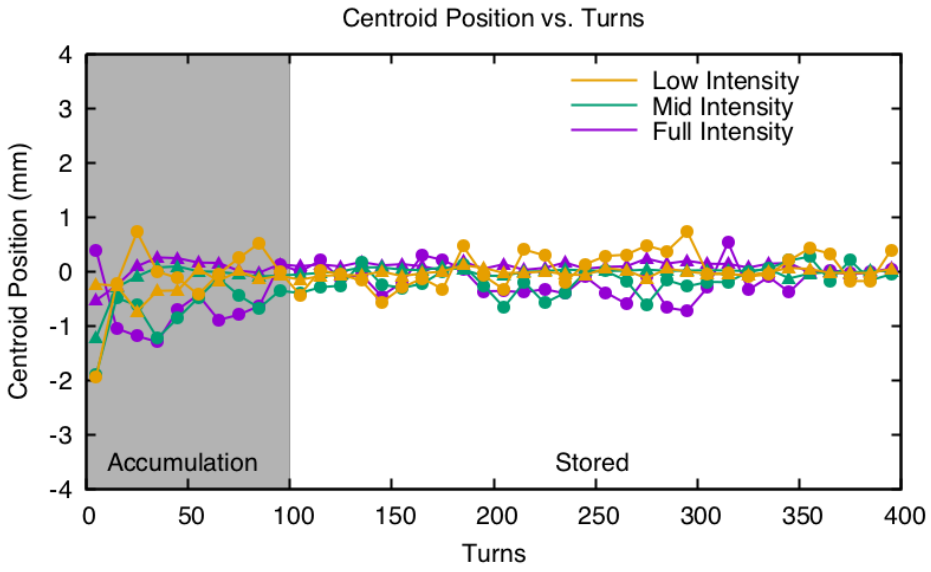

Figure 4.19: Comparison of the centroid position curves for the equal-tune low intensity (gold), mid intensity (green), and full intensity (purple) configurations for experiment three. The horizontal and vertical data are shown with '▲' and '●' points, respectively.

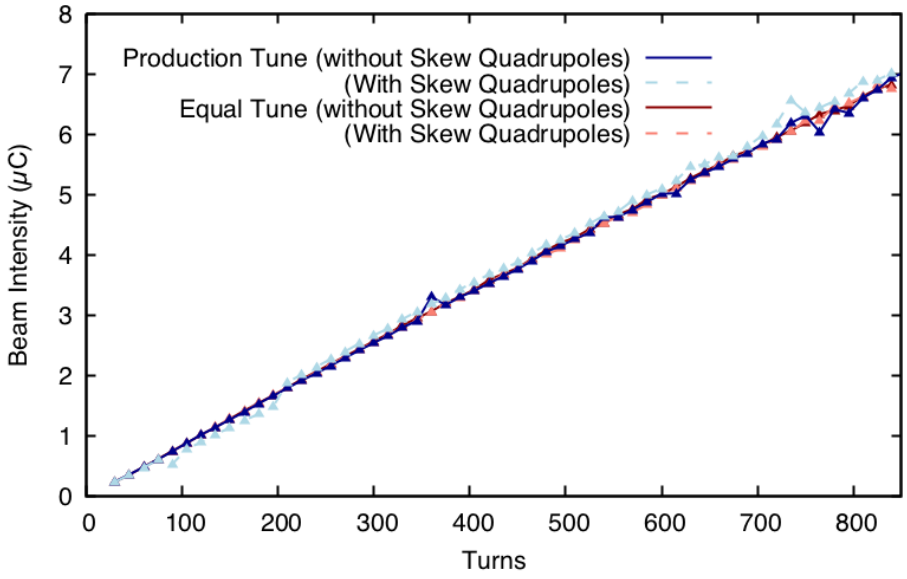

Figure 4.20: Comparison of the integrated charge for all configurations of the production-style experiment. The configurations without skew quadrupoles are shown with solid dark colored lines and the configurations with skew quadrupoles are shown with dashed light colored lines. The equal-tune configurations are shown in red and the production-tune configurations are shown in blue.

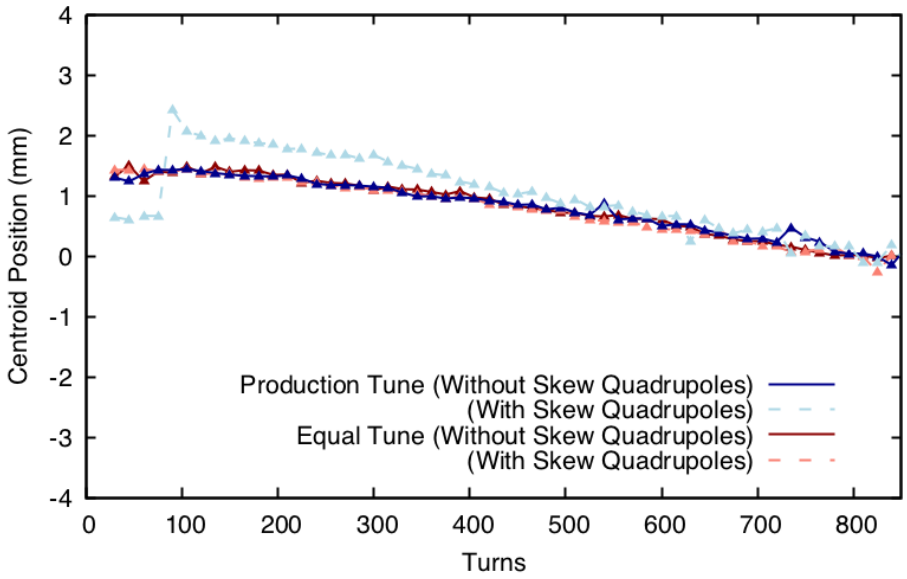

Figure 4.21: Comparison of the centroid position for all configurations of the production-style experiment. The configurations without skew quadrupoles are shown with solid dark colored lines and the configurations with skew quadrupoles are shown with dashed light colored lines. The equal-tune configurations are shown in red and the production-tune configurations are shown in blue.

nominal shift due to the injection kicker waveform and increasing beam intensity. The discontinuities present in the production tune case with skew quadrupoles are due to changes in the Electron Scanner device settings during the experiment. We originally believed that it would be necessary to collect data at multiple device settings. On-shift analysis of the data demonstrated that this was not necessary. Therefore, it was not repeated and the other three cases were collected with a single device setting.

Overall, the integrated charge and centroid position measurements confirm that the beam parameters evolved as we expected for each experiment. This allows us to separate any physical effects demonstrated in later chapters from the possibility of diagnostic device related issues.

4.3 Lattice Parameters

In Section 4.2, we determined scaling factors for the Electron Scanner measurement of the RMS beam sizes. These scaling factors help adjust the measured beam profile and account for effects of the Electron Scanner. However, a single measurement of the RMS beam size only provides a limited understanding of the beam. It is a measurement of the physical width of the beam at a single location and does not allow us to understand how the beam will transport. As discussed in Section 2.2, the emittance is a more accurate description of the beam as it represents the full phase space area of the beam. Measurement of the emittance requires a series of carefully spaced diagnostic devices to measure the RMS sizes at multiple locations. These devices act as an emittance measurement station by observing the rotation of the beam in phase space, as described in Section A.2. The Electron Scanner has only one location to measure the RMS size of each of the transverse planes. Therefore, the Electron Scanner is not capable of independently measuring the transverse emittances of the beam. However, we can simultaneously make measurements with the Electron Scanner and other diagnostic devices to appropriately gauge the emittances of the beam and establish a benchmark. This benchmark will allow us to translate the

Electron Scanner's measured RMS beam sizes to emittances, under the assumption that the Twiss parameters remain relatively constant with respect to the benchmark.

In order to establish an emittance to benchmark, we can calculate the emittance based on the maximum size of the beam envelope:

$$\varepsilon = \frac{x_{rms}^2}{\beta} \tag{4.6}$$

where x_{rms} is the RMS beam size and β is the betatron function. This relationship was introduced in Section 2.4. It allows the beam emittance, or total phase space area, to be calculated from the maximum physical size of the beam envelope and local betatron function. In order to use this relationship, we must first know the lattice parameters at the locations of the Electron Scanner.

We know that the tune of the beam is determined by the specific magnet settings of the entire lattice. As discussed in Section 3.2.2, the change in tune, or tune shift, for a distributed magnetic focusing gradient error can be calculated by:

$$\Delta\nu = \frac{1}{4\pi} \oint \beta(s_1)\ k(s_1)\ \mathrm{d}s_1 \tag{4.7}$$

where $\beta(s_1)$ and $k(s_1)$ are the beta function and small perturbation to the focusing function at the location s_1, respectively. For the instance where we are intentionally varying a single quadrupole, we can reduce this equation to:

$$\Delta\nu = \frac{1}{4\pi} \left\langle \beta(s_1) \right\rangle \Delta\,\mathrm{K\,l} \tag{4.8}$$

where $\left\langle \beta(s_1) \right\rangle$ is the beta function at the location of the quadrupole and $\Delta\,\mathrm{K\,l}$ is the change in the integrated quadrupole strength. Solving for $\left\langle \beta(s_1) \right\rangle$, we arrive at:

$$\left\langle \beta \right\rangle = 4\pi \frac{\Delta\nu}{\Delta\,\mathrm{K\,l}}. \tag{4.9}$$

This equation tells us that we can measure the horizontal and vertical beta functions at a specific location by varying the strength of the magnetic field. The change in magnetic fields will result in a small shift in the tune of the beam. The slope of the data, or the change in tunes over the change in integrated magnet strength, will allow us to calculate the betatron value. However, this technique only allows measurement of the betatron values in the presence of an independently controllable magnet.

The Electron Scanner is located in a drift between two quadrupoles, QH_D13 and QV_A01. This is shown in Figure 4.22. Each major quadrupole in the ring has an accompanying trim quadrupole capable of providing minor adjustments to the magnetic fields. These trim quads are often used for small changes to the tune of the beam. We will measure the betatron function at the location of the two trim quadrupoles by varying the trim quadrupole magnet settings and recording the horizontal and vertical tunes.

Then we will be able to propagate the Twiss parameters to the location of the Electron Scanner using matrix transformations. These Twiss parameters will allow us to estimate the emittance of the beam from measurements of the RMS size. With estimates of the emittances at the Electron Scanner, we can benchmark these measurements with the more veteran diagnostic devices, the RTBT wire scanners.

In Section 4.3.1, we measure the beta functions at QH_D13 and QV_A01 using the trim quadrupoles. Then, in Section 4.3.2, we calculate the alpha parameter at QH_D13 and propagate the Twiss parameters from QH_D13 downstream to the Electron Scanner.

4.3.1 Beta Measurement

In this section we discuss the data collection, and analysis for measuring the betatron function at QH_D13 and QV_A01. Key parameters for these quadrupoles are located in Table 4.2[31]. Quadrupole QH_D13 is upstream of the Electron Scanner. It is a standard 30Q58 SNS design quadrupole. This nomenclature refers to the magnet

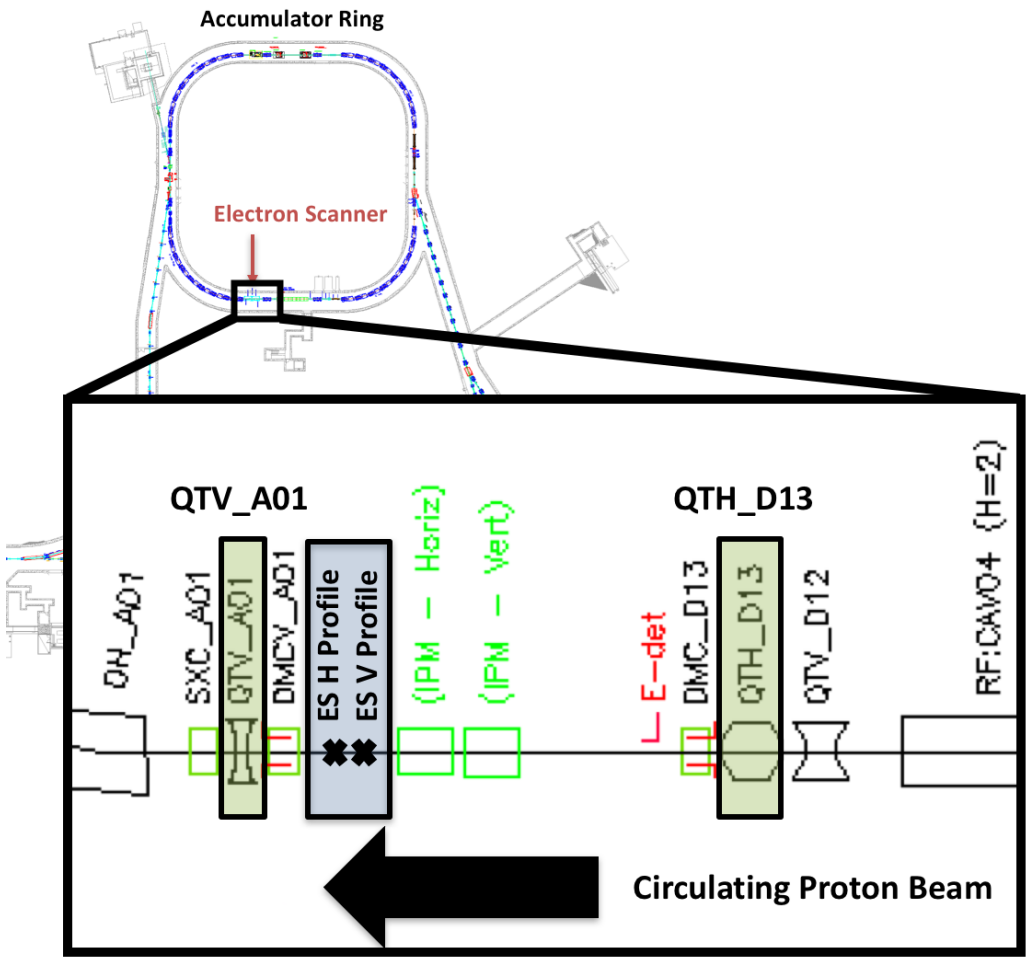

Figure 4.22: Schematic layout of the SNS with an inset showing the lattice optics around the Electron Scanner. The locations of the two Electron Scanner devices are shown in a blue box. The locations of the closest quadrupoles, QH_D13 and QV_A01, are shown in green boxes.

Table 4.2: Definition of Quadrupoles

		QH_D13	QV_A01
Length	[m]	0.673	0.500
Strength	[1/m^2]	0.662489425185	0.531517639759
Field Factor	[T/A]	0.001554	0.003123

having an aperture of 30 cm, a core length of 58 cm, and producing a quadrupole field. The trim quadrupole windings are rated for a maximum current of 40 A. Quadrupole QV_A01 is downstream of the Electron Scanner. It is a standard 21Q40 SNS design quadrupole with an aperture of 21 cm and a core length of 40 cm. The trim quadrupole windings are rated for a maximum current of 19 A. Each trim quadrupole is capable of both positive and negative current, allowing for a small correction to the magnetic field strength of the parent quadrupole. We are capable of calculating the magnetic field produced by a specific current using known field conversion factors for each of the quadrupoles.

The experimental procedure for measuring the lattice parameters was as follows. This experiment had a single trim quadrupole power supply connected to QTV_A01 and another trim quadrupole power supply connected to QTH_D13. We started with both trim quadrupoles set to zero. Then we injected a clean single mini-pulse and extended the ring storage time to 150 turns. We used the injection kickers to create a large offset for clearer BPM measurements. BPM turn-by-turn data was collected for 11 settings for QTV_A01 and 15 settings for QTH_D13 over the full range of the trim quadrupole windings. The tune was measured for each setting.

The measurements of the β functions at D13 and A01 are shown in Figures 4.23 and 4.24. The fits are calculated using a linear fit with Python's SciPy Library. SciPy's Orthogonal Distance Regression Package (ODR) [52] allows direct fitting of real data with errors. To determine the statistical error for the tune measurements, we collected a sample of eleven tune measurements for the same beam configuration. We then calculated the standard deviation of the horizontal and vertical tunes. The statistical errors for the tunes are $\Delta\nu = (0.000121, 0.000089)$. To determine the error for the magnetic field strength, we needed to convert the current to the strength of the magnetic field using

$$\Delta \mathrm{B} = \mathrm{a}\ \Delta \mathrm{I} \tag{4.10}$$

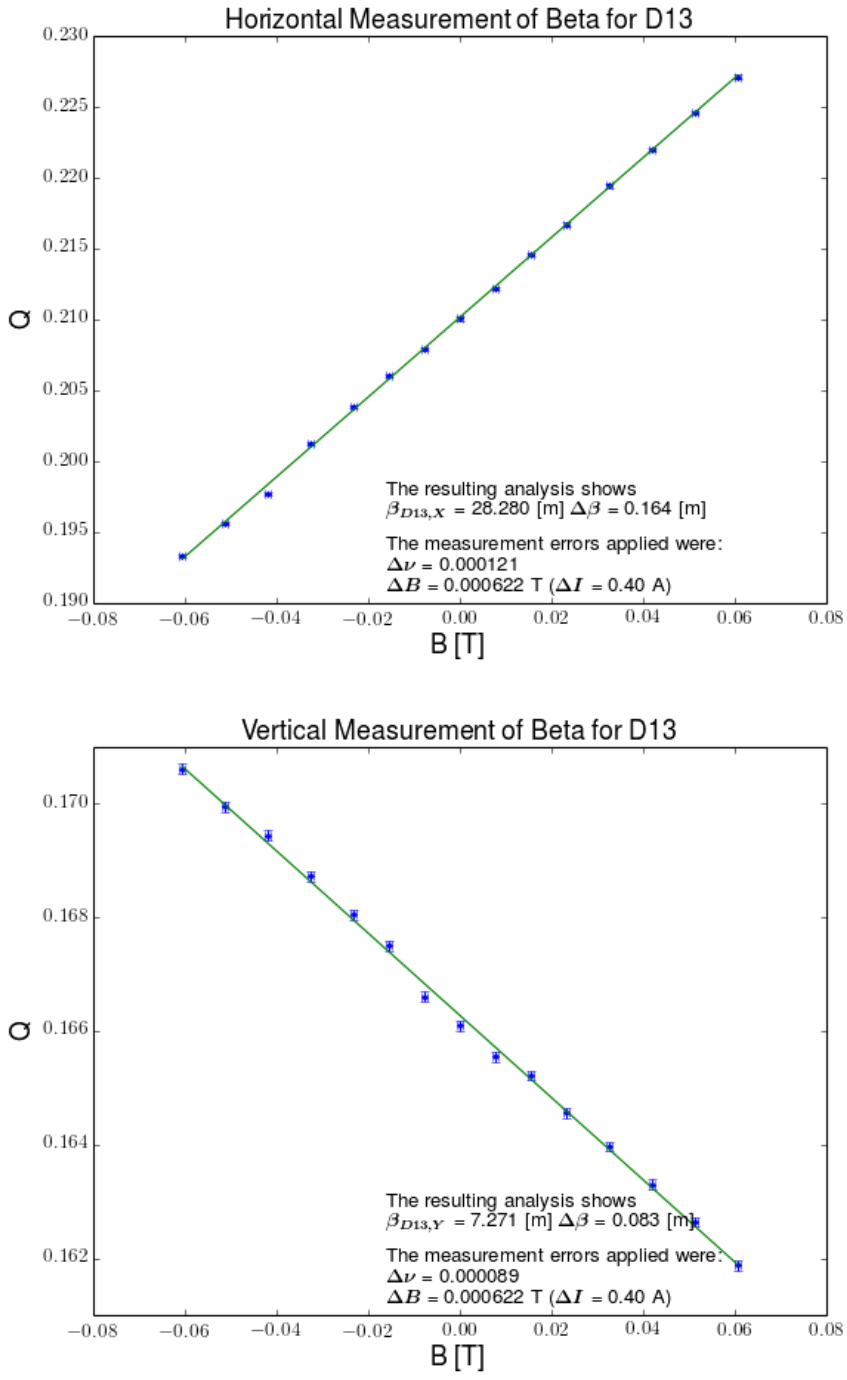

Figure 4.23: Measurement of the horizontal and vertical beta values for QH_D13, respectively.

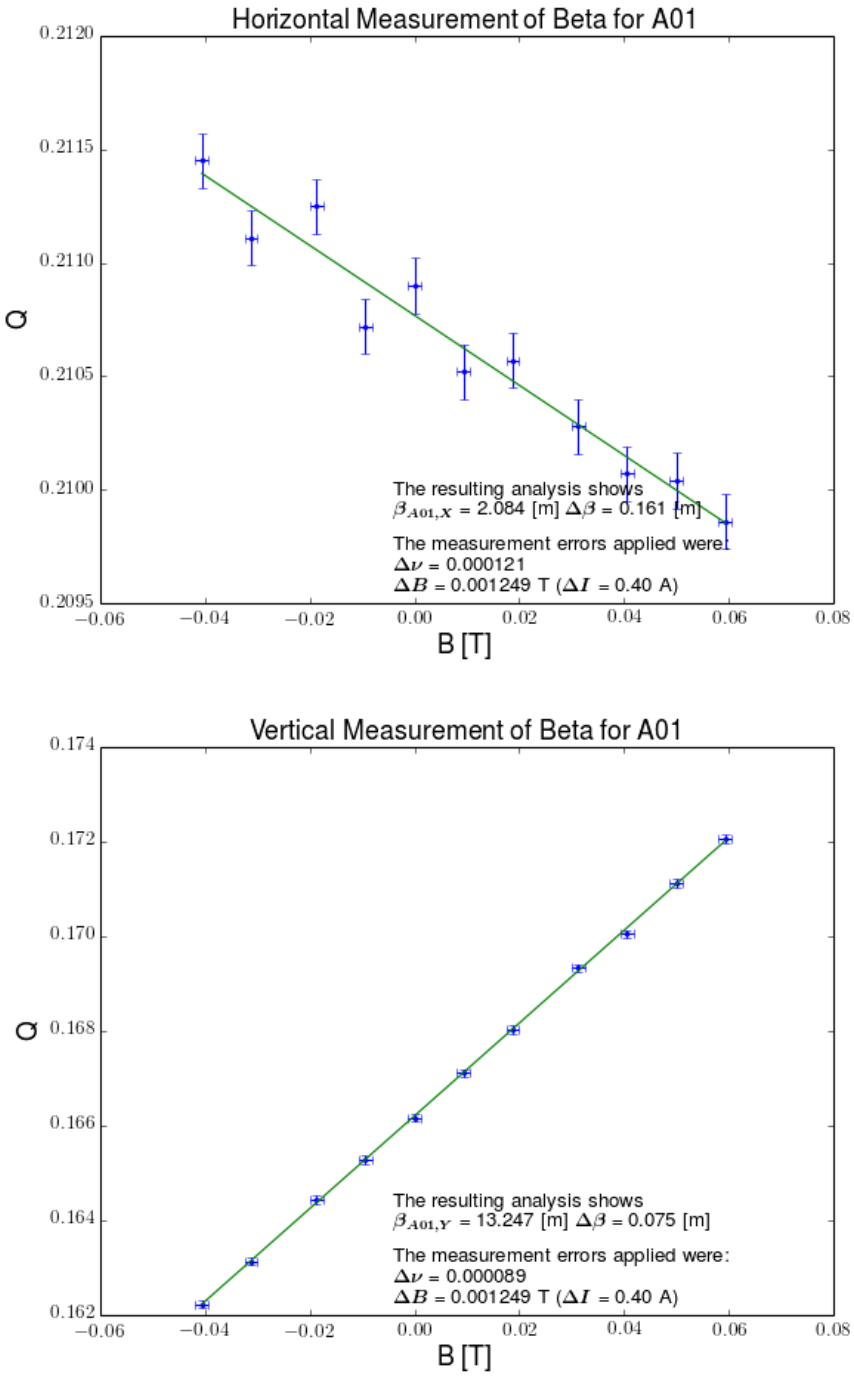

Figure 4.24: Measurement of the horizontal and vertical beta values for QV_A01, respectively.

where a is the known field factor. Both trim quadrupoles are operated by 40 A power supplies. The error on the output current is 0.1% of the full range of the power supply. Using ΔI = 0.4 Amps and the field conversion factors in Table 4.2, we found ΔB = 0.000622 T for QH_D13 and 0.000121 T for QV_A01.

The final measured horizontal and vertical beta values for QH_D13 were β_x = 28.280 m $\pm$ 0.164 m and β_y = 7.271 m $\pm$ 0.083 m, respectively. The final measured horizontal and vertical beta values for QV_A01 were β_x = 2.084 m $\pm$ 0.161 m and β_y = 13.247 m $\pm$ 0.075 m, respectively.

4.3.2 Propagating Lattice Parameters

In the previous section, we measured the β values at the center of the quadrupoles. In this section, we use those values to calculate the remaining Twiss parameters and propagate them from the quadrupoles to the Electron Scanner. We will rely on the theory of accelerator optics previously explained in Section 2.2. The first step of the process is to determine the positions of the important lattice elements. The second step will be to determine the α value at the center of the QH_D13 quadrupole. Finally, we will be able to quickly propagate those Twiss parameters to the locations of the Electron Scanner.

There is an accurate model of the SNS lattice design developed using a common accelerator application known as the Methodical Accelerator Design (MAD) program[50]. The known information about each lattice element is entered into the MAD lattice file. This information includes, but is not limited to, the type, position, strength, and name of each element. We are able to produce a complete model of the Accumulator Ring lattice using MAD. This model is necessary for executing many common particle simulation programs. Additionally, MAD produces tables and figures with the positions and predicted lattice parameters for each element. The horizontal and vertical MAD model and measured lattice parameters for each lattice element in the region of the Electron Scanner can be found in Tables 4.3

and 4.4, respectively. Figures 4.25 and 4.26 show the beta and alpha MAD model and measured values for each lattice element in the region of the Electron Scanner, respectively.

Another important addition to Tables 4.3 and 4.4 is the inclusion of the center of the quadrupoles, shown in green. MAD lists the location of each element as the end of the element. Hence, both MAD trim quadrupole elements appear after the position for the center of the quadrupoles. This is an important point as the β values were measured at the center of the two quadrupoles, D13 and A01. Assuming that the values were for the end of the quadrupoles would result in vastly different and incorrect results.

Our next step is to use the measured beta functions at the two quadrupoles to calculate the complete Twiss parameters (β, α, γ) at the location of the upstream quadrupole, QH_D13. All of these calculations were performed using Mathematica and the final results are shown in Tables 4.3 and 4.4. The lattice elements between the two quadrupoles are the drift space between the quadrupoles and half of each quadrupole. This process was repeated for both the horizontal and vertical dimensions. The only change necessary was to swap the quadrupole matrix used (i.e. quadrupoles which focus in one dimension, defocus in the other). As previously shown, drift spaces are a function of only the length of space. The drift length can be calculated by taking the distance between the centers of the quadrupoles and subtracting half of the quadrupole lengths. This distance is equal to 6.8635 m. Quadrupoles are a function of their length and field strength, which are both known and found in Table 4.2. Using this information, we can establish the transportation matrices,

$$m_{\text{Transfer}} = m_{\text{Half of QV\_A01}} \cdot m_{\text{Drift}} \cdot m_{\text{Half of QH\_D13}} \tag{4.11}$$

where m represents the transport matrix of each element. Using Equations 2.40 and 2.41, we can use the transportation matrix to calculate the Twiss transportation matrix. This will allow us to relate the Twiss parameters at QH_D13 to those at

Table 4.3: Horizontal Lattice Parameters Around The Electron Scanner

No.	Element Name	Position [m]	MAD Parameters		Experimental Parameters	
			β_x [m]	α_x [1]	β_x [m]	α_x [1]
525	QTV_D12	193.276	17.937	-7.114		
526	VV	193.698	24.454	-8.329		
	–Center of D13–	194.035	28.312	-2.848	28.280 ± 0.164	-2.701 ± 0.133
527	QTH_D13	194.371	28.099	3.467		
...	...	...	...	...		
539	IPM1	197.009	13.031	2.244		
	–Vertical Electron Scanner–	199.155	5.531	1.250	4.970 ± 0.495	1.214 ± 0.037
540	Q13D_K	199.313	5.148	1.177		
541	IPM2	199.313	5.148	1.177		
	–Horizontal Electron Scanner–	199.691	4.325	1.002	3.814 ± 0.448	0.947 ± 0.053
542	Q13D_L	199.692	4.324	1.002		
...	...	...	...	...		
554	Q1U	201.234	2.336	0.287		
	–Center of A01–	201.484	2.297	-0.129	2.084 ± 0.161	-0.218 ± 0.089
555	QTV_A01	201.734	2.469	-0.563		

Table 4.4: Vertical Lattice Parameters Around The Electron Scanner

No.	Element Name	Position [m]	MAD Parameters β_y [m]	MAD Parameters α_y [1]	Experimental Parameters β_y [m]	Experimental Parameters α_y [1]
525	QTV_D12	193.276	12.647	4.573		
526	VV	193.698	9.096	3.842		
	–Center of D13–	194.035	7.280	1.690	7.271 ± 0.083	1.671 ± 0.018
527	QTH_D13	194.371	6.706	0.057		
...	...	...	...	...		
539	IPM1	197.009	7.445	-0.338		
–Vertical Electron Scanner–		199.155	9.585	-0.659	9.742 ± 0.071	-0.674 ± 0.009
540	Q13D_K	199.313	9.795	-0.682		
541	IPM2	199.313	9.795	-0.682		
–Horizontal Electron Scanner–		199.691	10.333	-0.739	10.506 ± 0.070	-0.754 ± 0.010
542	Q13D_L	199.692	10.333	-0.739		
...	...	...	...	...		
554	Q1U	201.234	12.968	-0.970		
	–Center of A01–	201.484	13.026	0.742	13.247 ± 0.075	0.758 ± 0.013
555	QTV_A01	201.734	12.242	2.358		

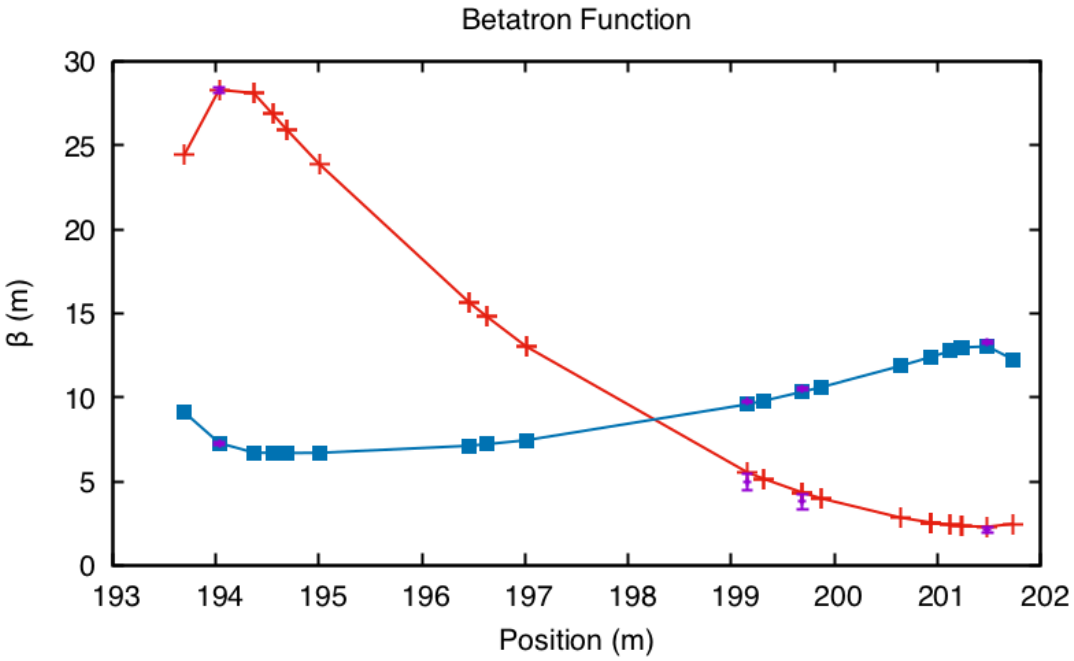

Figure 4.25: Horizontal (red) and vertical (blue) betatron functions for the lattice elements around the Electron Scanner. Measurements and errors are shown in purple.

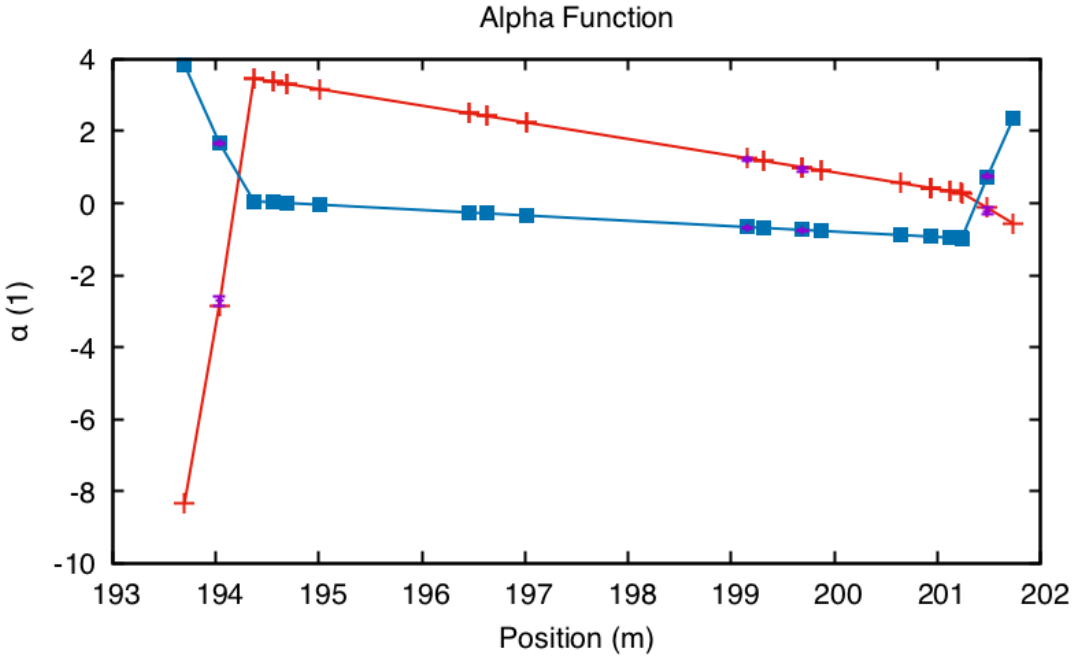

Figure 4.26: Horizontal (red) and vertical (blue) alpha functions for the lattice elements around the Electron Scanner. Measurements and errors are shown in purple.

QV_A01 using

$$T_{\text{QV\_A01}} = M_{\text{Twiss Transfer}} \cdot T_{\text{QH\_D13}} \tag{4.12}$$

where T is the array of Twiss parameters (β, α, γ) and M is the Twiss transportation matrix generated using $m_{\text{Transfer Matrix from QH\_D13 to QV\_A01}}$. As is discussed in Section 2.2, this matrix equation can be reduced by substituting the definition of γ. Using our knowledge of $\beta_{\text{QH\_D13}}$ and $\beta_{\text{QV\_A01}}$, we can solve the first row as a quadratic equation of $\alpha_{\text{QH\_D13}}$. We can check the two results for α by calculating both values of γ and comparing them to the value predicted by our MAD model. We now know β, α, γ at QH_D13 and are prepared to calculate the lattice parameters at the Electron Scanner positions.

The Twiss parameters at the Electron Scanner positions can be calculated using

$$\begin{pmatrix} \beta \\ \alpha \\ \gamma \end{pmatrix}_{\text{Electron Scanner}} = M_{\text{Drift}} \cdot M_{\text{Half of D13}} \cdot \begin{pmatrix} \beta \\ \alpha \\ \gamma \end{pmatrix}_{\text{Center of D13}} \tag{4.13}$$

where M is the Twiss transportation matrix. The horizontal and vertical Twiss parameters at the Electron Scanner positions are presented in blue in Tables 4.3 and 4.4, respectively. We confirm that the calculated value for $\beta_{\text{QV\_A01}}$ matches the measured value to show that our math is correct.

As discussed in Section 2.5, the errors for these Twiss parameters can be easily calculated with Equation 2.45:

$$\Delta \text{f} = \sqrt{\left(\frac{\partial \text{f}}{\partial \beta_{\text{QH\_D13}}}\right)^2 \Delta\beta^2_{\text{QH\_D13}} + \left(\frac{\partial \text{f}}{\partial \beta_{\text{QV\_A01}}}\right)^2 \Delta\beta^2_{\text{QV\_A01}}} \tag{4.14}$$

where f is the equation to find any given Twiss parameter, $\beta_{\text{QH\_D13}}$ and $\beta_{\text{QV\_A01}}$ are the measured betatron functions, and $\Delta\beta_{\text{QH\_D13}}$ and $\Delta\beta_{\text{QV\_A01}}$ are the calculated errors for the betatron measurements. The errors for the horizontal and vertical Twiss parameters at QH_D13, the Electron Scanner positions, and QV_A01 are located in

Table 4.5: Twiss Parameters

	β [m]	α [1]	γ [1/m]	ϕ [°]
		Horizontal		
WS20	6.572	0.827	0.256	-7.34
WS21	13.476	-1.477	0.236	6.29
WS23	16.834	-1.813	0.255	6.17
WS24	7.374	0.891	0.243	-7.02
HARP30	61.595	0.132	0.017	-0.12
ES	4.325	1.002	0.463	-13.71
		Vertical		
WS20	15.751	-1.648	0.236	6.00
WS21	7.488	0.88	0.237	-6.82
WS23	7.036	0.825	0.239	-6.82
WS24	15.806	-1.647	0.235	5.97
HARP30	21.923	1.544	0.154	-4.04
ES	9.585	-0.659	0.150	3.98

Tables 4.3 and 4.4, respectively. Table 4.5 shows a comparison of the Electron Scanner Twiss parameters with the harp and wire scanner Twiss parameters from MAD.

4.4 Wire Scanner Benchmark

In this section we will perform the final step of our calibration of the Electron Scanner. Once complete, this will allow the Electron Scanner to be used regularly in physics studies. The last step of our process is to use wire scanner emittance measurements that are taken in parallel to our Electron Scanner measurement to establish an emittance benchmark. As we did for the general profile calibration in Section 4.2.2, we will be using the five configuration cases presented in Section 5.4 for the emittance benchmark. This will allow us to establish our benchmark across multiple tunes,

beam intensities and at different points during the beam accumulation and storage. In this Section, we will not discuss the specific experimental configurations or the physics behind any of the data presented. We will only use the data as a tool for developing the benchmark. We will find a common multiplicative factor to scale the initial horizontal and vertical Electron Scanner emittances to the trusted wire scanner emittances.

The wire scanners are common diagnostics in accelerators around the world. At the SNS, we have various applications developed to assist in calculating emittances from wire scanner profiles. For this work, emittance calculations were performed using both the standard application and the Least Square Method (LSM). The LSM was important as it easily extends to allow a calculation of the emittance errors. The LSM process is discussed in Section A.3 and the Twiss errors are calculated in Section A.4.

Now that we have determined the Twiss parameters at the Electron Scanner, we can easily use this information and the RMS beam size measurements to calculate the emittances, as explained in Section 4.3. For each benchmark case, we collected Electron Scanner data from turn 5 to turn 395 in intervals of 10 turns. For the same cases, we collected wire scanner data at turns 100 and 400. In order to compare the data from the Electron Scanner with the wire scanner data, we interpolated and extrapolated the values at the relevant turns. For turn 100, we averaged the RMS beam sizes at turns 95 and 105. For turn 400, we used a straight line extrapolation of the RMS beam sizes from turns 385 and 395. Based on the analysis of the beam dynamics presented later in Section 5.4, these are reasonable approximations for both cases. The horizontal and vertical Electron Scanner RMS beam sizes and both the Electron Scanner and wire scanner emittances are presented in Tables 4.6 and 4.7, respectively. Figure 4.27 shows how the initial Electron Scanner emittances compare to the wire scanner emittances.

We seek an emittance scale factor, c, that when the initial Electron Scanner emittances are multiplied by c should produce the values measured by the wire

Table 4.6: Horizontal Benchmark Emittances

Case #	Electron Scanner RMS Size [mm]			Scanner Emittance	Wire Scanner Emittance	Emittance Scale Factor
	Turn 95/385	Turn 105/395	Turn 100/400	[π mm mrad]	[π mm mrad]	[-]
			Turn 100			
1	8.094	8.128	8.111	15.211	15.069	0.99
2	8.123	8.310	8.217	15.609	15.115	0.97
3	6.439	6.644	6.542	9.894	10.051	1.02
4	6.858	6.517	6.688	10.340	9.242	0.89
5	8.003	7.660	7.832	14.181	12.996	0.92
			Turn 400			
1	8.125	8.075	8.050	14.983	15.084	1.01
2	8.182	8.175	8.172	15.439	15.306	0.99
3	6.549	6.564	6.572	9.985	9.897	0.99
4	7.181	6.974	6.871	10.914	11.682	1.07
5	7.320	7.314	7.311	12.359	10.583	0.86

Table 4.7: Vertical Benchmark Emittances

Case #	Electron Scanner RMS Size [mm]			Scanner Emittance	Wire Scanner Emittance	Emittance Scale Factor
	Turn 95/385	Turn 105/395	Turn 100/400	[π mm mrad]	[π mm mrad]	[-]
				Turn 100		
1	8.041	8.115	8.078	6.808	3.011	0.44
2	8.453	8.591	8.522	7.577	3.079	0.41
3	11.644	10.985	11.315	13.356	9.836	0.74
4	11.256	11.361	11.309	13.342	10.123	0.76
5	9.014	10.169	9.592	9.598	6.195	0.65
				Turn 400		
1	7.712	7.704	7.700	6.186	3.079	0.50
2	8.404	8.386	8.377	7.321	3.961	0.54
3	11.775	11.549	11.436	13.644	10.081	0.74
4	10.177	10.784	11.088	12.826	8.023	0.63
5	10.447	10.986	11.256	13.217	8.959	0.68

scanners:

$$\varepsilon_{\text{ Wire Scanner}} = c\, \varepsilon_{\text{ Electron Scanner}}. \tag{4.15}$$

Therefore, the emittance scale factor can be defined by:

$$c = \frac{\varepsilon_{\text{ Wire Scanner}}}{\varepsilon_{\text{ Electron Scanner}}} = \frac{\beta_{\text{ Electron Scanner}}}{x^2_{\text{RMS, Electron Scanner}}}\, \varepsilon_{\text{ Wire Scanner}}. \tag{4.16}$$

These emittance scale factors are shown as the final columns in Tables 4.6 and 4.7. The emittance scale factor for each of the cases and the final average emittance scale factors are presented in Table 4.8. The final Electron scanner emittance scale factors are $c_{\text{ Horizontal}} = 0.97 \pm 0.043$ and $c_{\text{ Vertical}} = 0.61 \pm 0.11$. The scale factor allows us to determine the measured systematic error in the emittance measurement and the error of the scale factor is the statistical error about the systematic error. In other words, the horizontal and vertical Electron Scanner emittance measurements had a 3% and 39% systematic error, and 4.3% and 11% statistical error, respectively. As was previously mentioned, the vertical diagnostic device has a larger aperture restriction that resulted in a larger angle of rotation. Hence, we would expect that the vertical measurements would have larger errors than the horizontal measurements. However, the unpublished physics model previously predicted the systematic error in the vertical direction to be less than 20%. This could indicate a problem with the vertical measurements possibly related to the very small vertical emittance combined with the small local vertical betatron function.

Figure 4.28 shows the benchmarked Electron Scanner emittances in comparison to the wire scanner emittances. These emittance scale factors will allow future users of the Electron Scanner to quickly equate their RMS beam size measurements to emittances. The emittance of the beam is a more effective descriptor of the beam size and allows for further insight into how the beam will transport through the entire accelerator. Therefore, this is a useful tool for future physics studies at the SNS.

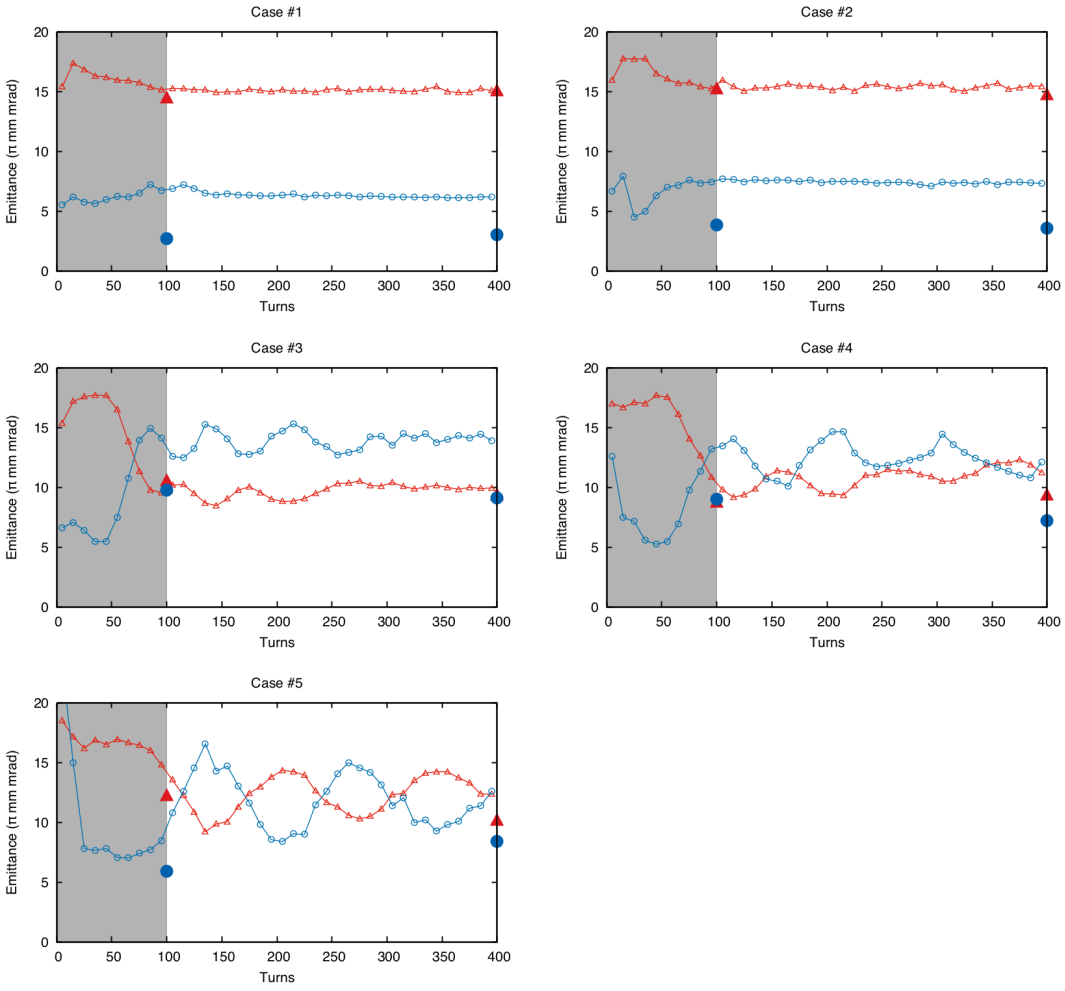

Figure 4.27: Initial Electron Scanner emittances compared to wire scanner emittances for all cases prior to benchmarking. The Electron Scanner emittances are calculated using the measured the Twiss parameters and Electron Scanner RMS values. The Electron Scanner data is shown with connecting lines and hollow data points. The wire scanner data is shown as solid data points. The horizontal data is shown with red triangles and the vertical data is shown with blue circles.

4.5 Summary

The purpose of this Chapter was to introduce and calibrate the Electron Scanner prior to use in a major physics study. In Section 4.1, we explained the basic theory of the Electron Scanner and discussed its history and current limitations. In Section 4.2, we discussed the analysis package. Specifically, we outlined the methodology used, made measurements to calibrate the data, and confirmed the integrity of our experimental data using the integrated charge and centroid position measurements. In Section 4.3, we measured the betatron function at the adjacent quadrupoles, QH_D13 and QV_A01. Then, using these measurements, we calculated the Twiss parameters and errors at the quadrupoles and the Electron Scanner positions. These Twiss parameters were essential to relating measurements of the beam with the Electron Scanner to those made with other diagnostic devices. Finally, in Section 4.4, we benchmarked the Electron Scanner emittance measurements to parallel measurements made using the Wire Scanner emittance measurement station. The final Electron Scanner emittance scale factors are $c_{\text{Horizontal}} = 0.97 \pm 0.043$ and $c_{\text{Vertical}} = 0.61 \pm 0.11$. This is equivalent to stating that the systematic errors in the horizontal and vertical Electron Scanner emittance measurements were 3% and 39%, and that the statistical errors were 4.3% and 11%, respectively. These values will allow future users of the Electron Scanner to quickly translate their RMS beam size measurements into emittances.

Table 4.8: Electron Scanner Emittance Scale Factors

Case #	Horizontal	Vertical
1	1.00	0.47
2	0.98	0.47
3	1.00	0.74
4	0.98	0.69
5	0.89	0.66
Final Emittance Scale Factors	0.97	0.61
Standard Deviation	0.043	0.113

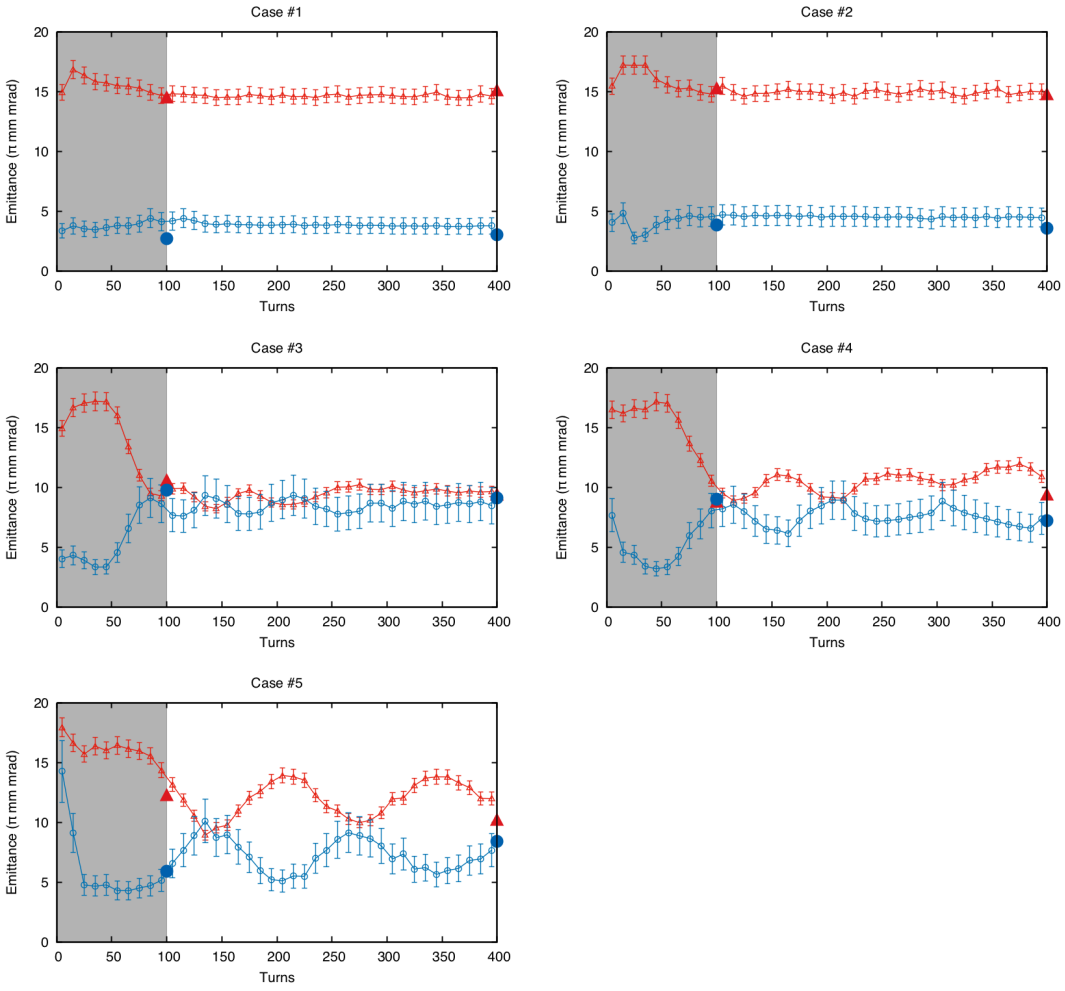

Figure 4.28: Benchmarked Electron Scanner emittances compared to wire scanner emittances for all cases. The Electron Scanner emittances are calculated using the measured the Twiss parameters and Electron Scanner RMS values, and are scaled by the final emittance scale factors. The Electron Scanner data is shown with connecting lines and hollow data points. The wire scanner data is shown as solid data points. The horizontal data is shown with red triangles and the vertical data is shown with blue circles.

Chapter 5

Simple Accumulation Experiments

In the process of investigating a documented physical effect with unknown origins, it is best to reduce the complexity of the problem to isolate the key parameters. Our initial motivation was to create an experiment with a simplified accumulation and beam dynamics that would allow us to explore the effects of tune and intensity on coupling. There have been three parts to the evolution of this experiment. In the first part, we use a simplified accumulation-only configuration to study the effect of the coupling on an accumulating beam using wire scanners. This dataset demonstrates that the onset of the coupling was actually at a much lower beam intensity than expected. In the second part, we continue to use wire scanners to observe the same simplified accumulation configuration for the first portion of the experiment and then stored the beam for the remainder of the turns. This dataset demonstrates a full exchange of the emittances for the coupled case. Unfortunately, our data collection was hampered by the large time consumption associated with running wire scanners. In the third and final part, we re-examine a similar beam configuration while taking advantage of the benefits of the Electron Scanner. This last dataset demonstrates a strong coupling in both the RMS size and profile of the beam. This dataset also demonstrated large amplitude oscillations for lower intensity beams.

This chapter will be devoted to describing experiments with a simple accumulation pattern and reviewing their results. The structure will be as follows. In Section 5.1, we review the general parameters of the experiments. In Section 5.2, we review the configuration and results of the accumulation-only experiment. In Sections 5.3 and 5.4, we review the configurations and results of the accumulation followed by storage experiments using the wire scanners and the Electron Scanner, respectively. Finally, in Section 5.5, we summarize the results of the three simplified accumulation experiments.

5.1 General Beam Configuration

In this section, we review the general beam configuration of the experiments. Each of the three experiments had similar accelerator configurations with the exception of minor differences as noted in each experiment's section. To simplify the beam dynamics, we made the following changes to the nominal SNS production configuration. First, we flat-topped the injection kickers to remove the effects of injection painting. Next, we manually shorted the ring RF or placed it in stand-by to remove any longitudinal effects. In order to make sure the beam remained clear of the extraction gap, the beam was injected to fill only 39% of the ring circumference. This is approximately half of the production injection fill length. Next, we used the ring sextupoles to minimize the chromatic tune shift and better isolate the effects of the space charge tune shift. Finally, we used the ring skew quadrupoles to eliminate any signs of transverse lattice coupling seen by monitoring the turn-by-turn centroid motion of a single bunch injected off the ideal path.

Tune The nominal betatron tunes of the SNS Accumulator Ring are $\nu_x = 6.23$ and $\nu_y = 6.20$.

Geometry During SNS production cycles, the size of the beam in the ring is optimized to reduce losses throughout the ring while matching the on-target beam requirements. The horizontal and vertical injection kickers are used to control the beam size. The measured parameter for characterizing beam size are the injection offsets. The nominal production values are approximately 30 mm and 30 mm[31]. The MAD beta values at the injection spot are ($\beta_x \sim 10.29, \beta_y \sim 11.06$). Therefore, the transverse emittances are approximately equal, $\epsilon \sim x^2/\beta$. We describe the physical profile of this beam as symmetric.

Energy and Intensity The nominal beam energy of the SNS ranges between 920 MeV and 980 MeV. The beam energy depends on the specific configuration of RF cavities in the linac. The nominal beam intensity of the SNS ranges from 8e13 ppp to 1.3e14 ppp, or from 12.8 μC to 20.7 μC. The beam intensity depends on the number of turns of accumulated beam and the specific chopping pattern, as well as other parameters such as beam losses and beam current from the ion source. Both the beam energy and the beam intensity typically remain constant during a production cycle.

5.2 Experiment One: Accumulation-Only

In experiment one, we studied a beam with a simplified accumulation-only configuration using wire scanners. This experiment was an initial exploration into the coupling effect versus the tune and injection offset parameters. The specific experimental configurations are presented in Section 5.2.1. The results of experiment one are presented in Section 5.2.2.

5.2.1 Configuration

An overview of the precise beam settings for experiment one are documented in Tables 5.1, 5.2 and 5.3. To allow a simple and direct means of comparison, each case in experiment one is assigned a case number in the configuration tables.

Tune We expected that the coupling effect would increase in strength as we approached an equal tune based on previous work[12]. Therefore, we collected data over a grid of tune points surrounding the ($\nu_x = 6.20, \nu_y = 6.20$) and ($\nu_x = 6.17, \nu_y = 6.17$) equal-tune points.

Geometry For coupled beams, a change in one transverse plane will affect the opposite plane. The transverse planes of beams with low or no coupling remain independent and unaltered by a change in the opposite plane. The primary sizes investigated were approximately 25 mm by 25 mm, or "symmetric" beams, and 25 mm by 17 mm, or "asymmetric" beams.

Energy and Intensity The nominal beam energy during our experiment was 938.0 MeV for the two shifts where split tune datasets were collected and 932.9 MeV for the shift where the equal tune datasets were collected. Our full accumulation beam intensities varied between 3.02e13 ppp and 3.20e13 ppp, or 4.93 μC and 5.13 μC respectively. The ion source current was higher on the third shift. Our priority was to match the beam intensities between data points across shifts. Therefore, all of the equal tune cases have less turns of accumulation than the split tune cases. As indicated in Tables 5.1, 5.2 and 5.3, the difference in accumulated turns ranges from zero turns at low intensity to 50 turns at maximum beam intensity. Figure 5.1 depicts the evolution of the beam intensity for the cases in experiment one.

During the final shift of experiment one, time allowed for data collection of one extra beam configuration. From an on-shift analysis of the previous data collected, we decided that studying the effects of storage on a highly coupled configuration would

Table 5.1: Beam Configurations for Shift One of the Split Tune Cases for Experiment One

Primary Diagnostic Device	Wire Scanners (WS20, WS21, WS23, WS24 located in the RTBT)		
Shift Date	April 1st, 2013		
Accumulation & Storage	Accumulation Only		
Turns of Accumulation	50, 100, 150, 200, 250, 300, 350, 500		
Turns of Storage	None		
Case Number	1	2	3
Maximum Beam Intensity	3.08e13 ppp 4.93 μC	3.05e13 ppp 4.89 μC	3.08e13 ppp 4.93 μC
Q_x	6.23563	6.23389	6.17943
Q_y	6.17249	6.17273	6.23898
ΔQ	0.06314	0.06116	-0.05955
Beam Tune	Split Tune		
Injection Kickers	Flat-topped Waveform		
X Injection Size	23.7 mm	24.6 mm	25.5 mm
Y Injection Size	23.6 mm	16.8 mm	25.8 mm
Beam Geometry	Symmetric	Asymmetric	Symmetric
Beam Energy	938.0 MeV		
Ring RF	Stand-by		
Ring Pattern Width	39%		
Ring Chromaticity	Zeroed		
Linear Coupling	Checked and, if necessary, removed with skew quadrupoles		

Table 5.2: Beam Configurations for Shift Two of the Split Tune Cases for Experiment One

Primary Diagnostic Device	Wire Scanners (WS20, WS21, WS23, WS24 located in the RTBT)			
Shift Date	April 29th, 2013			
Accumulation & Storage	Accumulation Only			
Turns of Accumulation	50, 100, 150, 200, 250, 300, 350, 500			
Turns of Storage	None			
Case Number	4	5	6	7
Maximum Beam Intensity	3.07e13 ppp 4.92 μC	3.03e13 ppp 4.85 μC	3.06e13 ppp 4.90 μC	3.05e13 ppp 4.89 μC
Q_x	6.17081	6.17095	6.20086	6.20250
Q_y	6.19893	6.19822	6.16888	6.16807
ΔQ	-0.02812	-0.02727	0.03198	0.03443
Beam Tune	Split Tune			
Injection Kickers	Flat-topped Waveform			
X Injection Size	25.7 mm	25.7 mm	25.7 mm	25.5 mm
Y Injection Size	24.2 mm	17.1 mm	17.2 mm	25.8 mm
Beam Geometry	Symmetric	Asymmetric	Asymmetric	Symmetric
Beam Energy	938.0 MeV			
Ring RF	Stand-by			
Ring Pattern Width	39%			
Ring Chromaticity	Zeroed			
Linear Coupling	Checked and, if necessary, removed with skew quadrupoles			

Table 5.3: Beam Configurations for the Equal Tune Cases for Experiment One

Primary Diagnostic Device	Wire Scanners (WS20, WS21, WS23, WS24 located in the RTBT)				
Shift Date	September 8th, 2013				
Accumulation & Storage	Accumulation Only				
Turns of Accumulation	50, 100, 140, 180, 230, 270, 320, 450				
Turns of Storage	None				Extended by 100 turns of storage for each data point
Case Number	8	9	10	11	12
Maximum Beam Intensity	3.20e13 ppp 5.13 μC	3.15e13 ppp 5.05 μC	3.15e13 ppp 5.05 μC	3.19e13 ppp 5.11 μC	3.17e13 ppp 5.08 μC
Q_x	6.19946		6.16842	6.17012	6.16980
Q_y	6.19857		6.16991	6.17097	6.17081
ΔQ	0.00089		-0.00149	-0.00085	-0.00101
Beam Tune	Equal Tune				
Injection Kickers	Flat-topped Waveform				
X Injection Size	23.1 mm	23.6 mm	23.7 mm	22.9 mm	22.7 mm
Y Injection Size	16.8 mm	23.0 mm	16.9 mm	23.0 mm	22.8 mm
Beam Geometry	Asymmetric	Symmetric	Asymmetric	Symmetric	Symmetric
Beam Energy	932.9 MeV				
Ring RF	Stand-by				
Ring Pattern Width	39%				
Ring Chromaticity	Zeroed				
Linear Coupling	Checked and, if necessary, removed with skew quadrupoles				

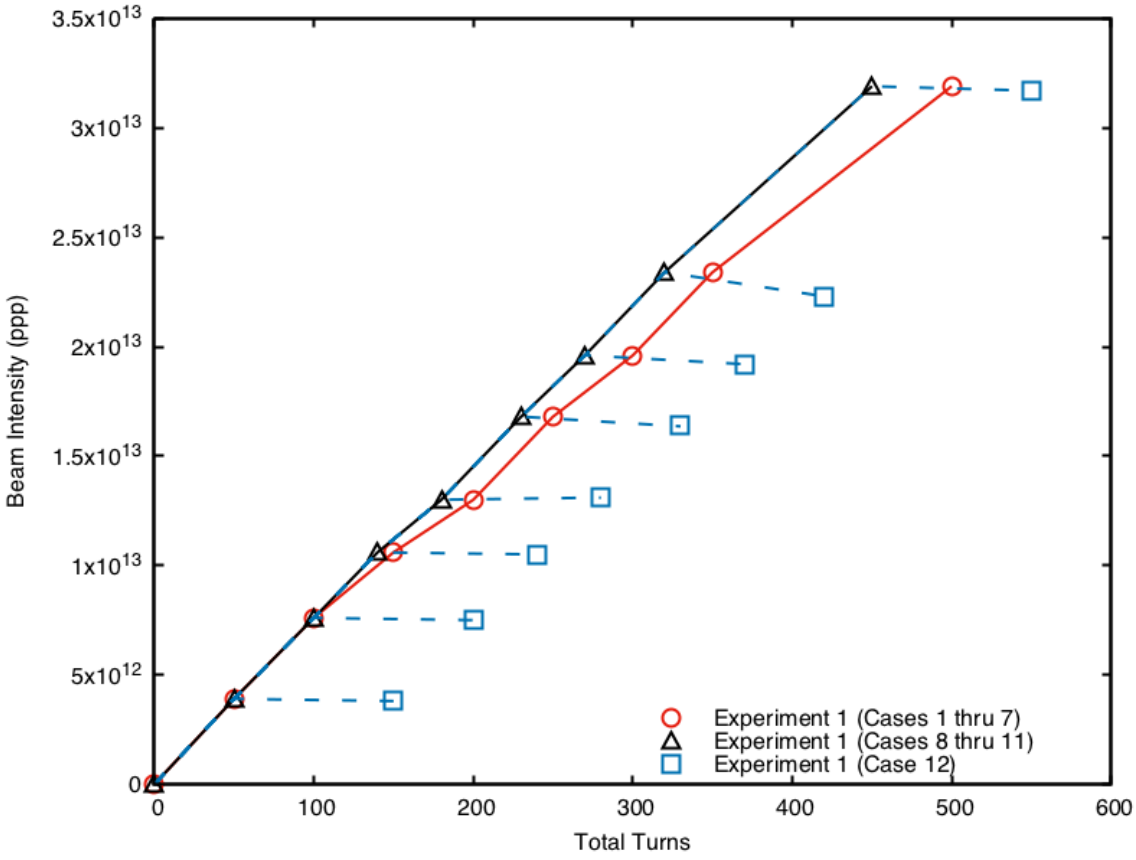

Figure 5.1: Comparison of configurations for experiment one. The beam intensity is shown on the vertical axis and the total number of turns are shown on the horizontal axis. The split-tune accumulation-only configuration for cases 1 through 7 are shown with a solid red line with '◯' points. The equal-tune accumulation-only configuration for cases 8 through 11 are shown with a solid black line with '△' points. The accumulation extended with storage configuration for case 12 is shown with dashed blue lines with '□' points. Lines indicate the evolutionary path followed for each data point, and markers indicate the relative location of data collection. Sloped lines indicate periods of accumulation and flat lines indicate periods of storage.

be the most informative use of the limited shift time. Therefore, case 12 uses the same configuration as case 11 with the addition that 100 turns of storage were added prior to each extraction to the wire scanners. For example, for the second data point in case 11, the beam was accumulated for 100 turns and extracted for measurement. For the same data point in case 12, the beam was accumulated for 100 turns, stored for 100 turns, and extracted for measurement. This is shown in Figure 5.1 by comparing the configuration for cases 8 through 11 with the configuration for case 12. Storing the beam in this manner allowed us to study the coupling effect with additional beam evolution time.

5.2.2 Results

In this section we review the results of experiment one, where wire scanners were used as the primary diagnostic device. Our main objective will be to examine the effects of tune and beam geometry. In our final results, we will take an initial look at the effects of storage using case 12.

The wire scanners and data processing are discussed in Appendix A. The wire scanners allow us to collect profiles along the horizontal, vertical and diagonal dimensions. The diagonal profile is generally used only for confirmation. With each scan, we collect data from wire scanners 20, 21, 23, and 24 along the final section of the RTBT, shown in Figure 4.1. Therefore, each scan provides us with two primary profiles from each of the four wire scanner devices, or eight profiles. Data collection for a typical beam configuration will require up to eight scans at various points during the beam evolution. This equates to a potential sixty-four profiles for each of the twelve cases. As discussed in Section A.2, we will use all of this data to determine the transverse emittances. For examining the evolution of the transverse profiles, we will only use the horizontal and vertical profiles from wire scanner 24.

A waterfall plot is a method of representing the evolution of the profile during the experiment. The baseline of each profile collected is vertically offset from the

horizontal axis in increments of 0.05. In this manner, the bottom profile represents the earliest measurement in the evolution of the beam and the top profile represents the last measurement in the evolution. Comparing horizontal and vertical waterfall plots can provide insight into the evolution of the overall shape of the beam. Additionally, waterfall plots from different beam configurations can be placed next to each other for simple comparison of the evolution of the beam along one dimension. A particularly useful tool is to lay the waterfall plots out in a grid based on the tunes of the various configurations. In this layout, the horizontal tune of the configurations increases from the left side of the page to right and the vertical tune increases from the bottom of the page to top. The images along the diagonal always have approximately equal tunes.

Accumulation-Only

Figures 5.2 and 5.3 show the horizontal and vertical waterfall plots for the symmetric beam cases in experiment one, respectively. Figures 5.4 and 5.5 show the horizontal and vertical waterfall plots for the asymmetric beam cases in experiment one, respectively. These four figures represent the primary data collected for experiment one as documented in Tables 5.1, 5.2, and 5.3. Each subfigure is appropriately marked with case numbers to indicate the specific beam configurations. The common legend indicates the number of turns accumulated for each profile. Legend entries with two turns listed indicate the number of turns for the unequal tune cases followed by the number of turns for the equal tune cases.

A cursory examination shows that the lower intensity profiles tend to have variations in the placement and number of peaks. This is due to the placement of individual bunches in phase space during accumulation, which is based on the specific tunes and injection kicker waveforms. This difference is not due to coupling and washes out due to the injection of additional bunches and the effect of strong space charge forces.

A careful inspection will yield four important results from these figures:

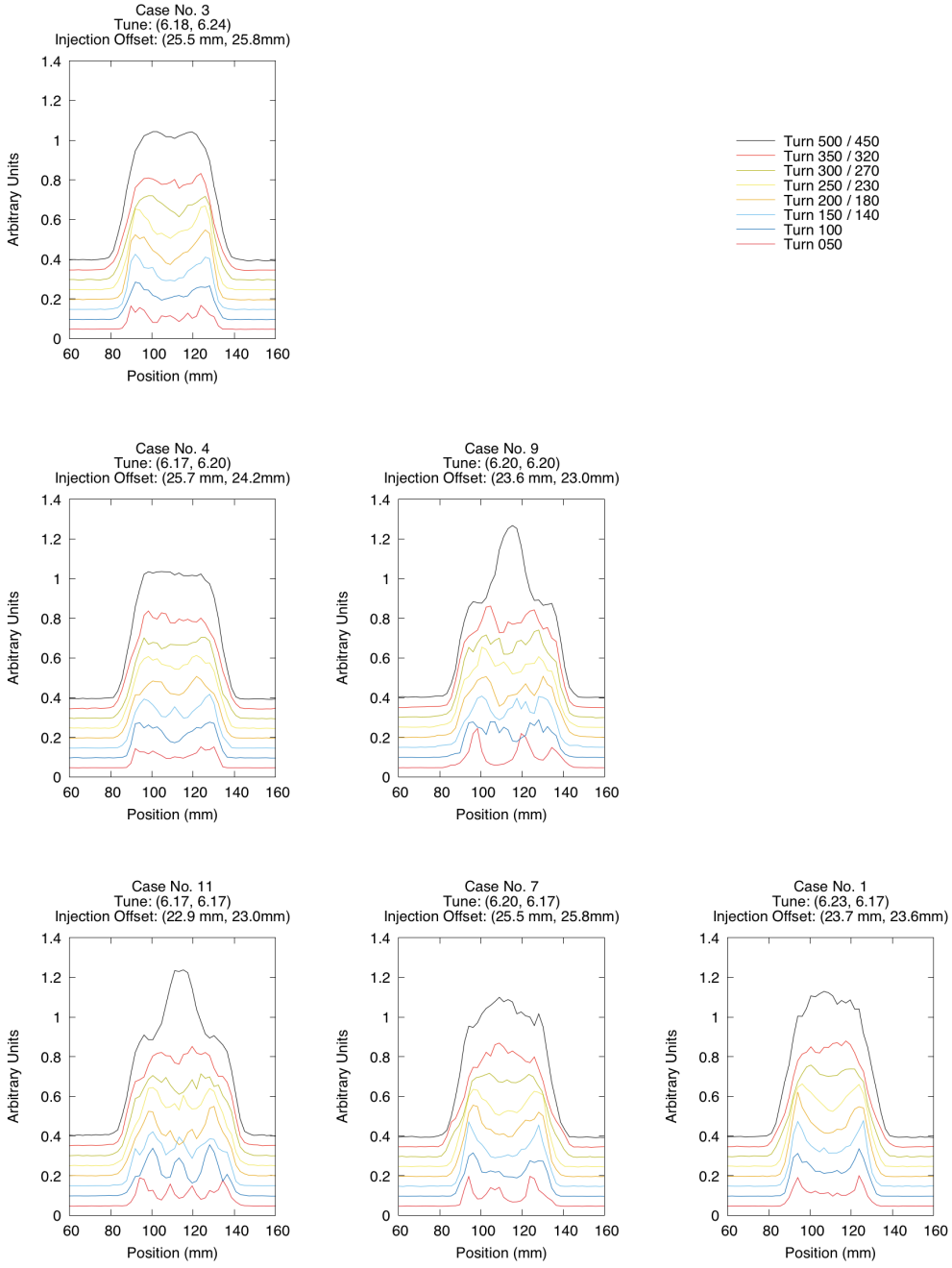

Figure 5.2: Horizontal wirescan waterfall plots for the symmetric beam cases in experiment one.

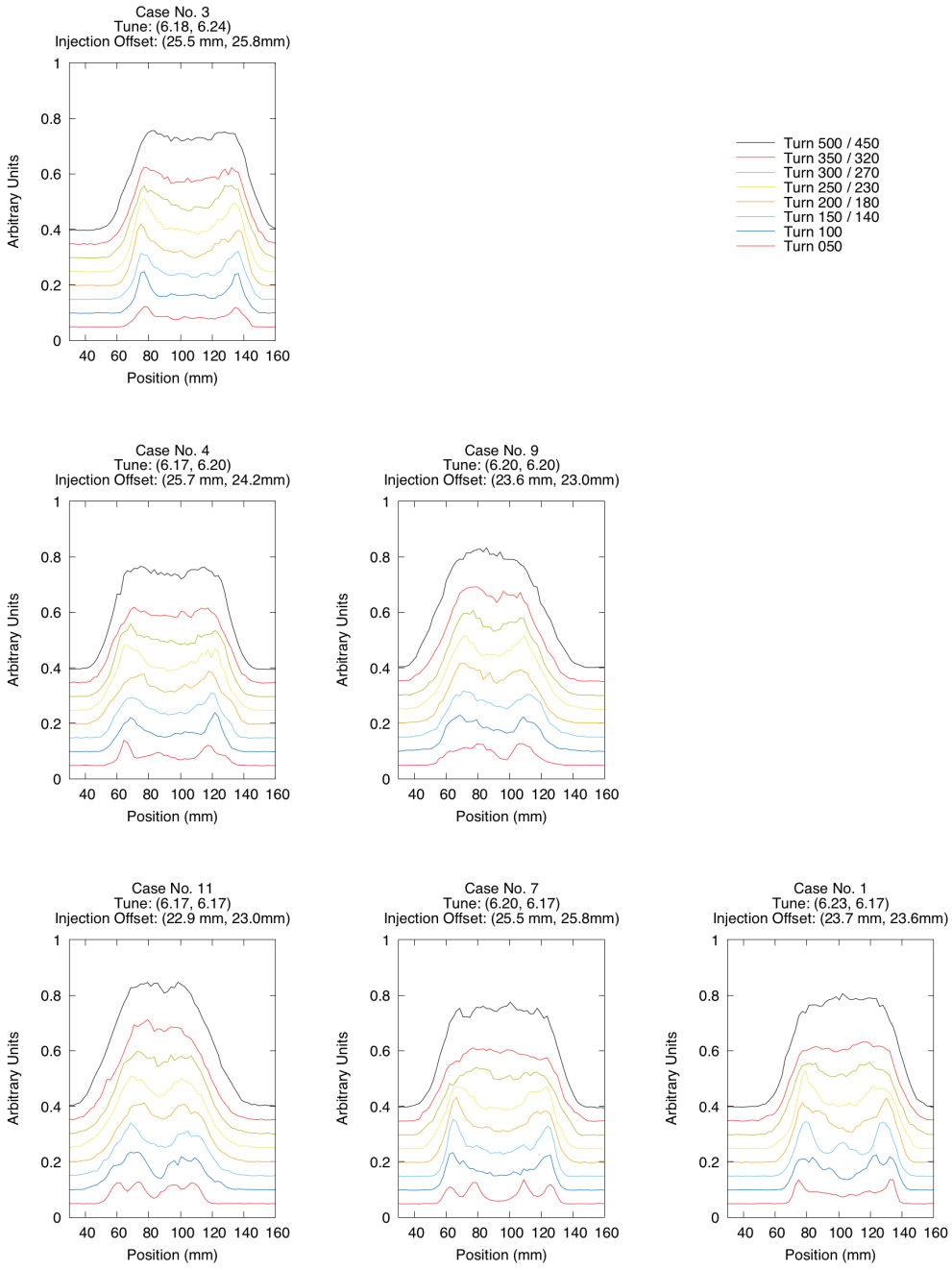

Figure 5.3: Vertical wirescan waterfall plots for the symmetric beam cases in experiment one.

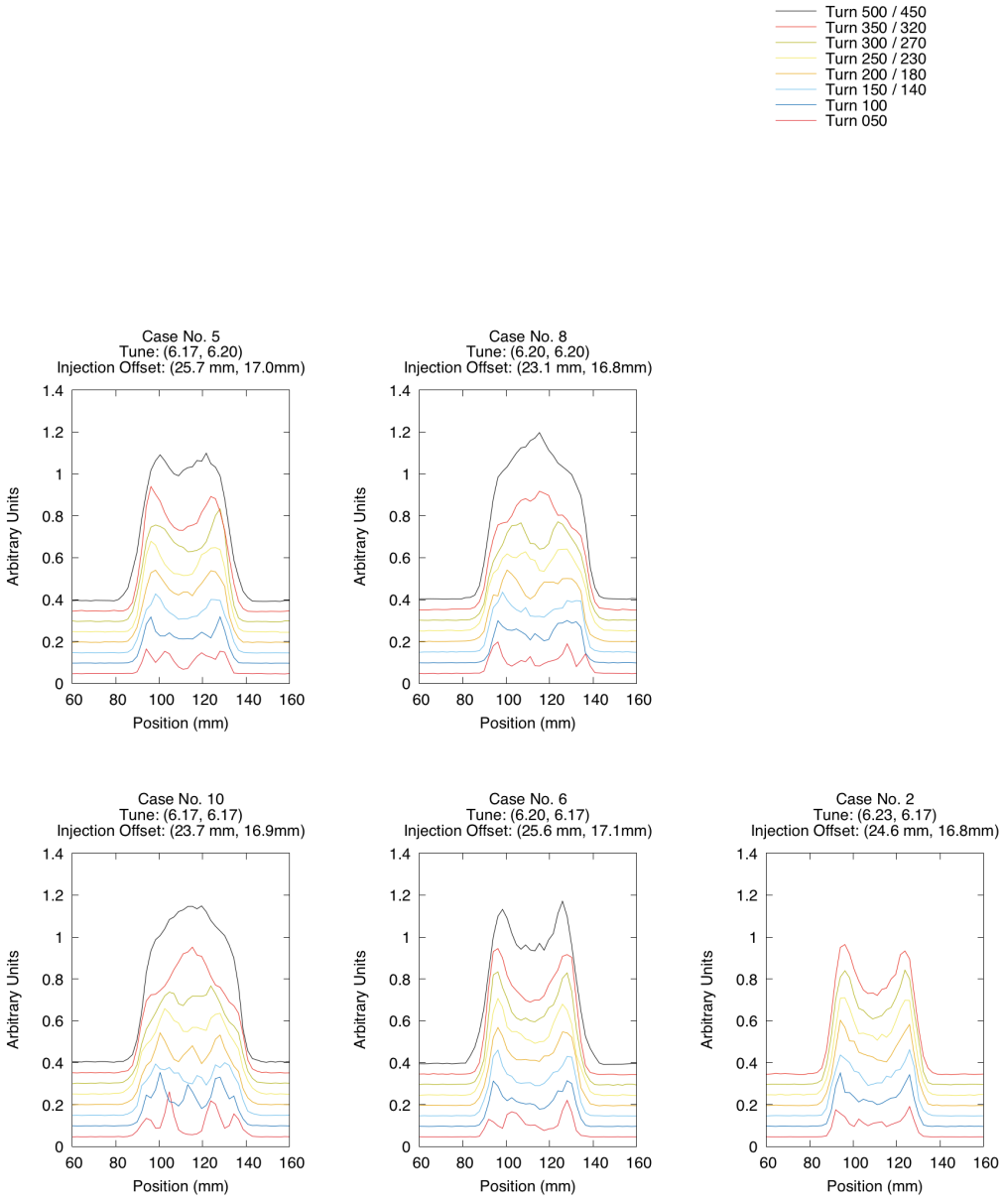

Figure 5.4: Horizontal wirescan waterfall plots for the asymmetric beam cases in experiment one.

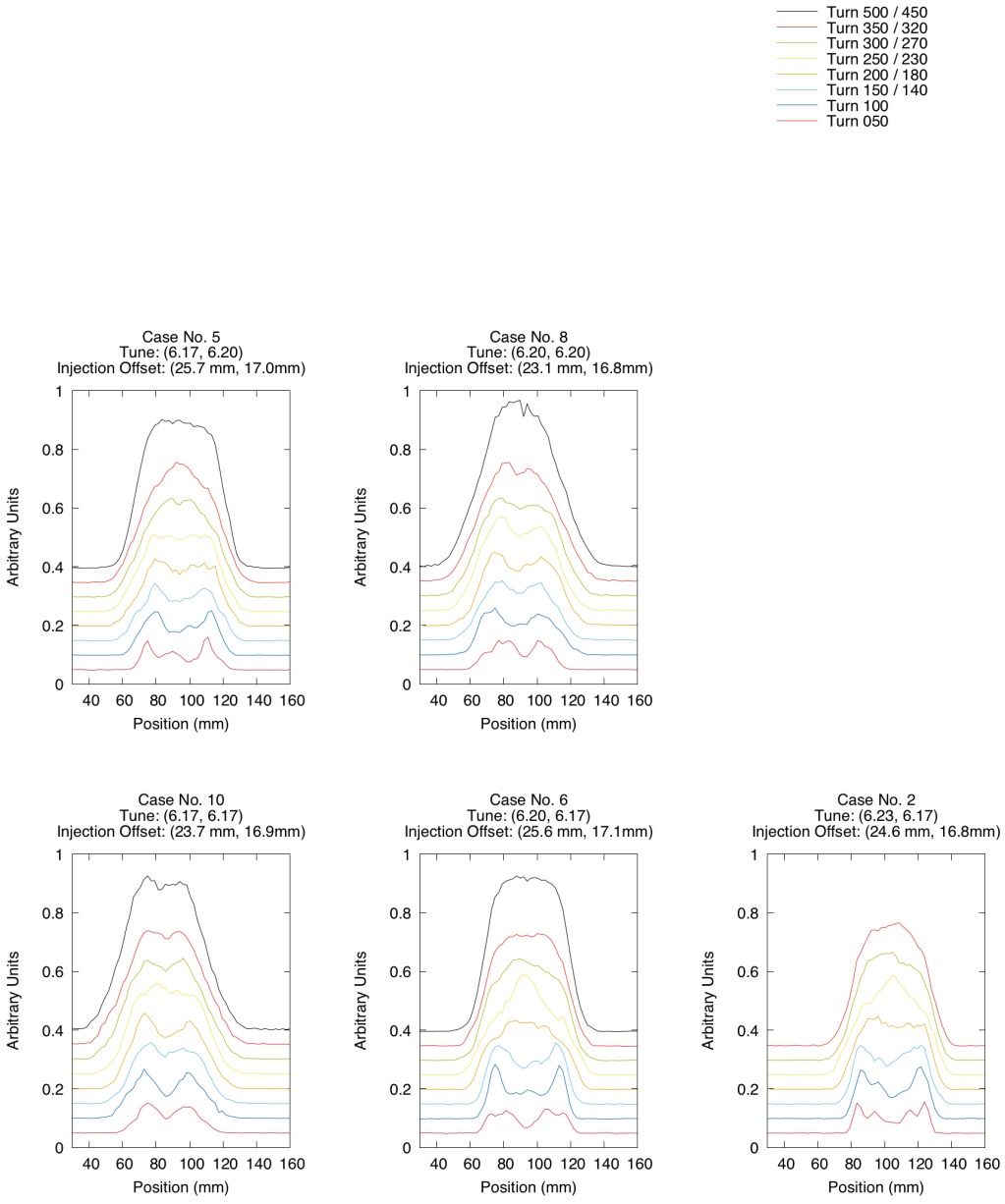

Figure 5.5: Vertical wirescan waterfall plots for the asymmetric beam cases in experiment one.

1. The evolution of beams with different tunes does not differ greatly for all cases with unequal tunes. An example of this is depicted in Figure 5.6, which compares case 1 (top) where Q = (6.24, 6.17) and case 7 (bottom) where Q = (6.20, 6.17). Both cases represent expected beam evolutions for the SNS, specifically a hollow beam is painted and filled by space charge during the accumulation. Both cases have a symmetric geometry and have final profiles that are flat-topped with similar widths and heights. The change in horizontal tune of ∼0.03 between the cases does not heavily impact the final beam distribution. These beams would both be described as having uncoupled transverse beam profiles because small changes to one transverse dimension, such as tune or injection offset, will not yield a significant change in the opposite transverse dimension.

2. The evolution of equal tune beams differs greatly from uncoupled beams. An example of this is depicted in Figure 5.7, which compares case 7 (top) where Q = (6.20, 6.17) and case 11 (bottom) where Q = (6.17, 6.17). In this example, both cases also start with the symmetric beam geometry. We used case 7 in our previous example and demonstrated how it appeared to be uncoupled. Cases 7 and 11 differ by the same amount of change in the horizontal tune, ∼0.03, as do cases 1 and 7, previously compared in Figure 5.6. While cases 1 and 7 share similar evolutions and final beam profiles, there is a large change in the evolution of the beam for case 11, which has equal tunes. There are two noteworthy differences in the evolution of the equal tune beam. First, the final horizontal profile is not flat-topped but rather peaked with tiered shoulders. Second, the final vertical profile has broad trailing edges, which creates a much larger beam footprint. Both of these differences represent problems for meeting the beam-on-target specifications for peak beam density and beam size, respectively.

3. The evolution of beams with different injection offsets does not differ greatly provided that neither case has equal tunes. An example of this is depicted

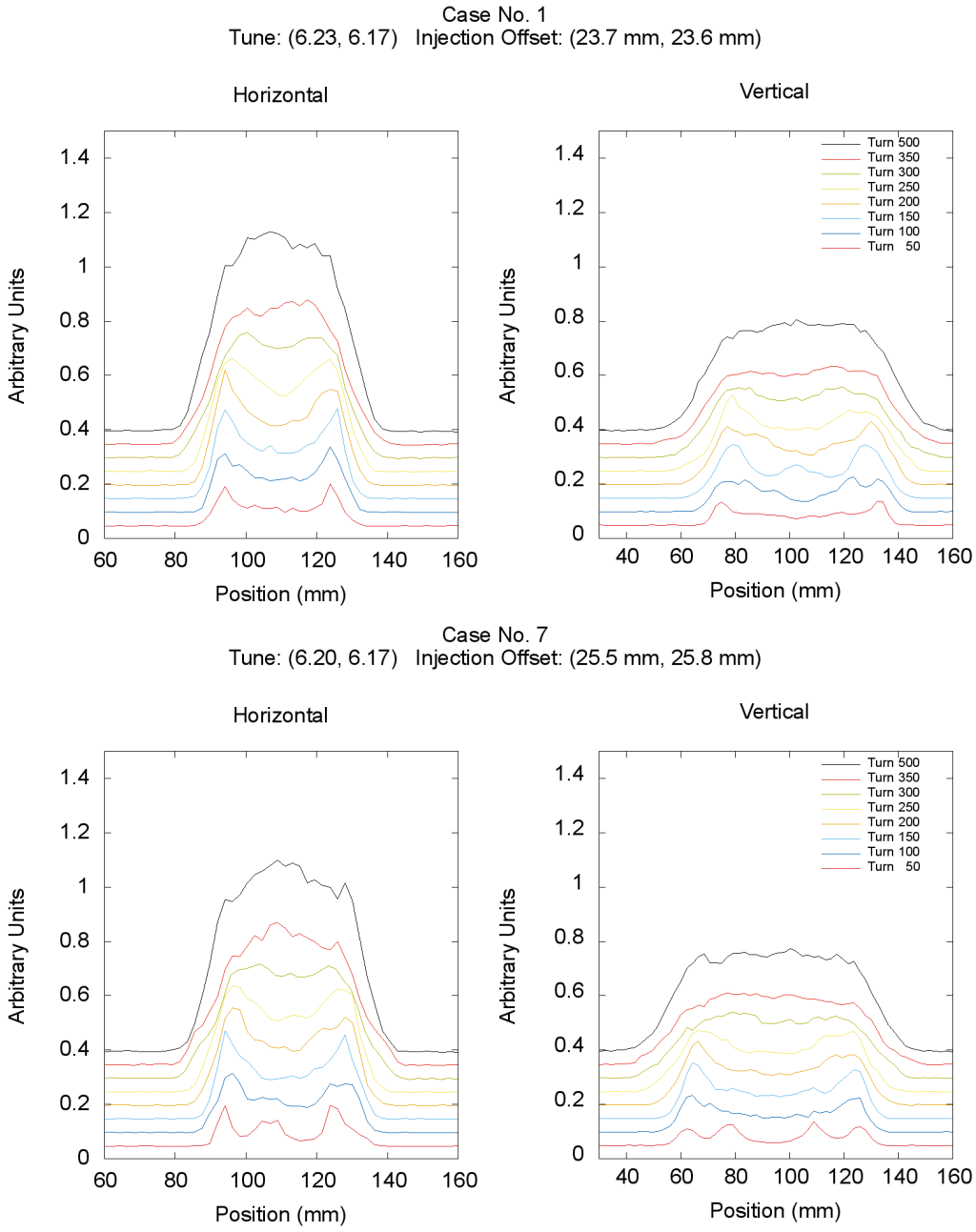

Figure 5.6: Comparison of wirescan waterfall plots for two cases both with unequal tunes.

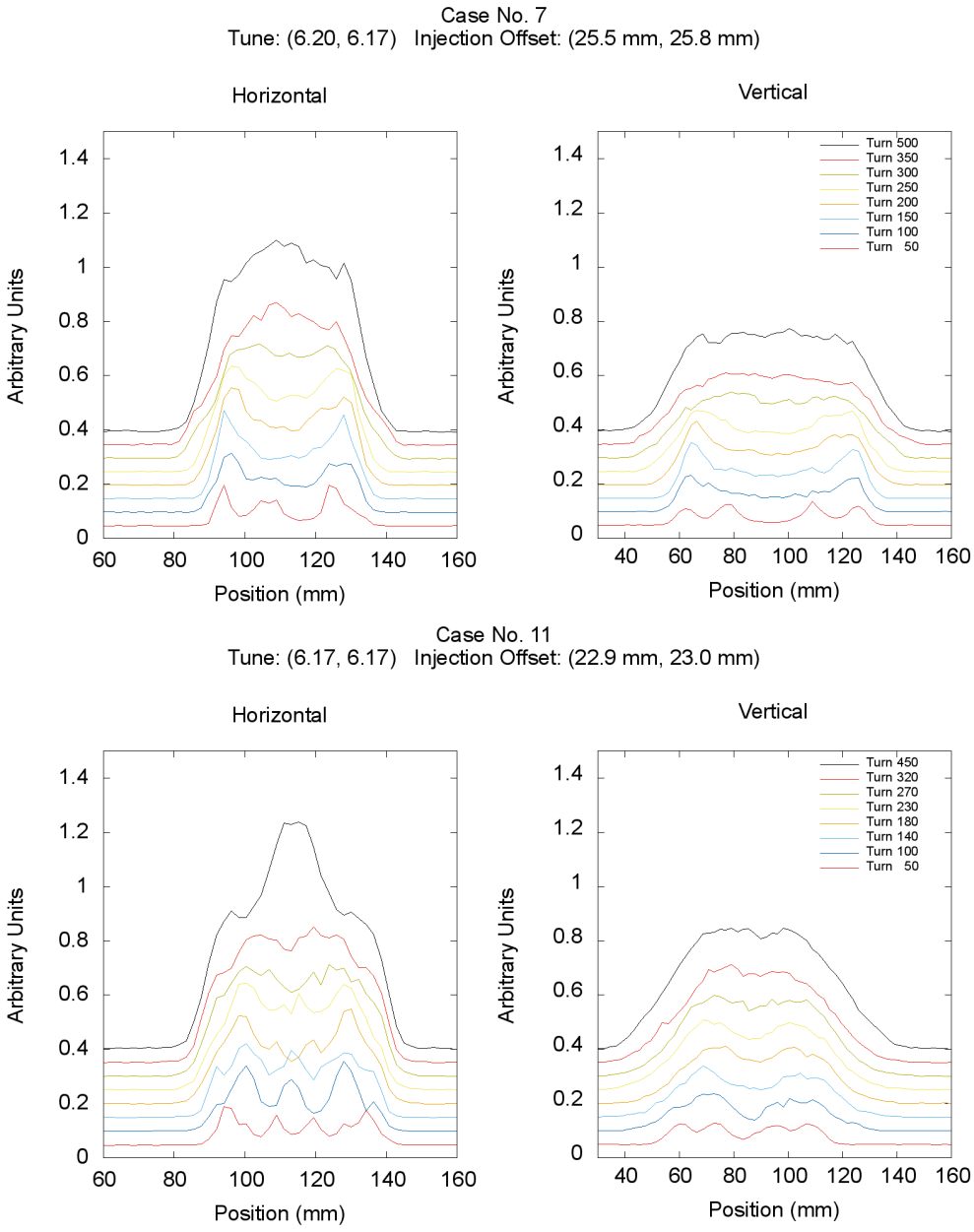

Figure 5.7: Comparison of wirescan waterfall plots for two cases where one has unequal tunes (top) and the second has equal tunes (bottom).

in Figure 5.8, which compares case 4 (top) with injection offsets of (25.7 mm, 24.2 mm) and case 5 (bottom) with injection offsets of (25.7 mm, 17.0 mm). Both cases have an unequal tune of (6.17, 6.20) and represent expected beam evolutions. Although the final profiles are slightly different, both are flat-topped and of similar horizontal widths. The vertical widths are different as expected due to the different vertical injection offsets. The difference in profiles is minimal and is likely due to the difference in beam densities and, therefore, space charge forces.

4. The evolution of equal tune beams are coupled. An example of this is depicted in Figure 5.9, which compares case 8 (top) with injection offsets of (23.1 mm, 16.8 mm) and case 9 (bottom) with injection offsets of (23.6 mm, 23.0 mm). Both cases have an equal tune of (6.20, 6.20). Therefore, our previous results with equal tune beams imply that we should expect strong coupling to be present in both cases. Note that the change in injection offsets between these cases is comparable to the change in the previous example. In the previous example, where the tunes were unequal, the change in final beam profile was minimal, excluding the expected change in the width of the vertical profile. In this example, where the tunes are equal, the vertical injection offset produces a significant change in both transverse profiles. A common technique to meet beam-on-target specifications is to alter the injection offsets in one or both planes during production runs. If changing one injection offset alters the beam in both planes, then the ability to meet beam-on-target specifications could become compromised for equal tune beams. Therefore, this coupled response presents a problem for regular operations where the injection offsets are altered to meet the beam-on-target specifications.

An important reason for having a series of wire scanners is to measure the Twiss parameters. A discussion of Twiss parameters can be found in Section 2.2. A complete description of how the wire scanner profiles are used to measure the Twiss parameters

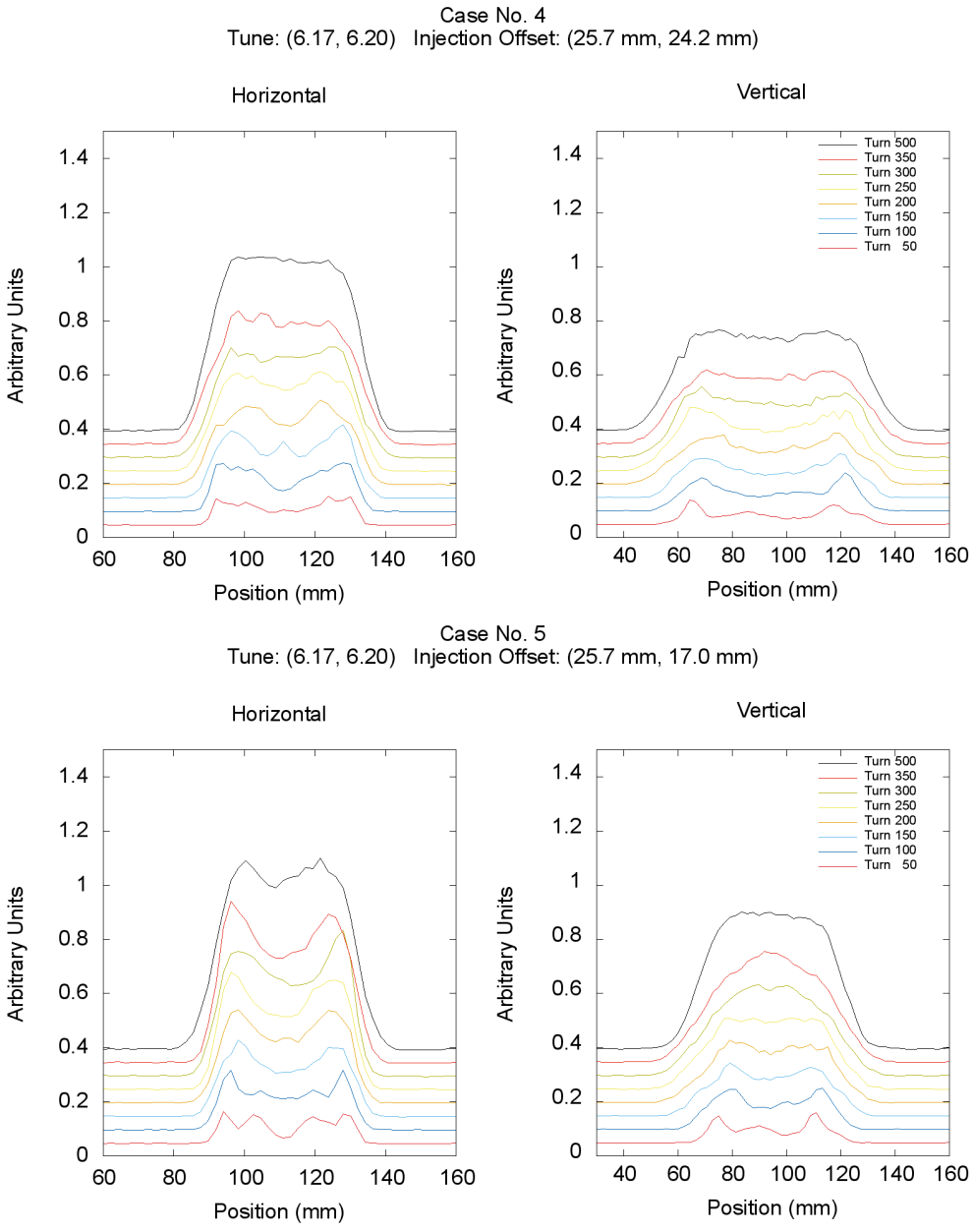

Figure 5.8: Comparison of wirescan waterfall plots for two cases with the same unequal tunes but different beam geometries. The top case has a symmetric beam geometry and the bottom case has an asymmetric beam geometry.

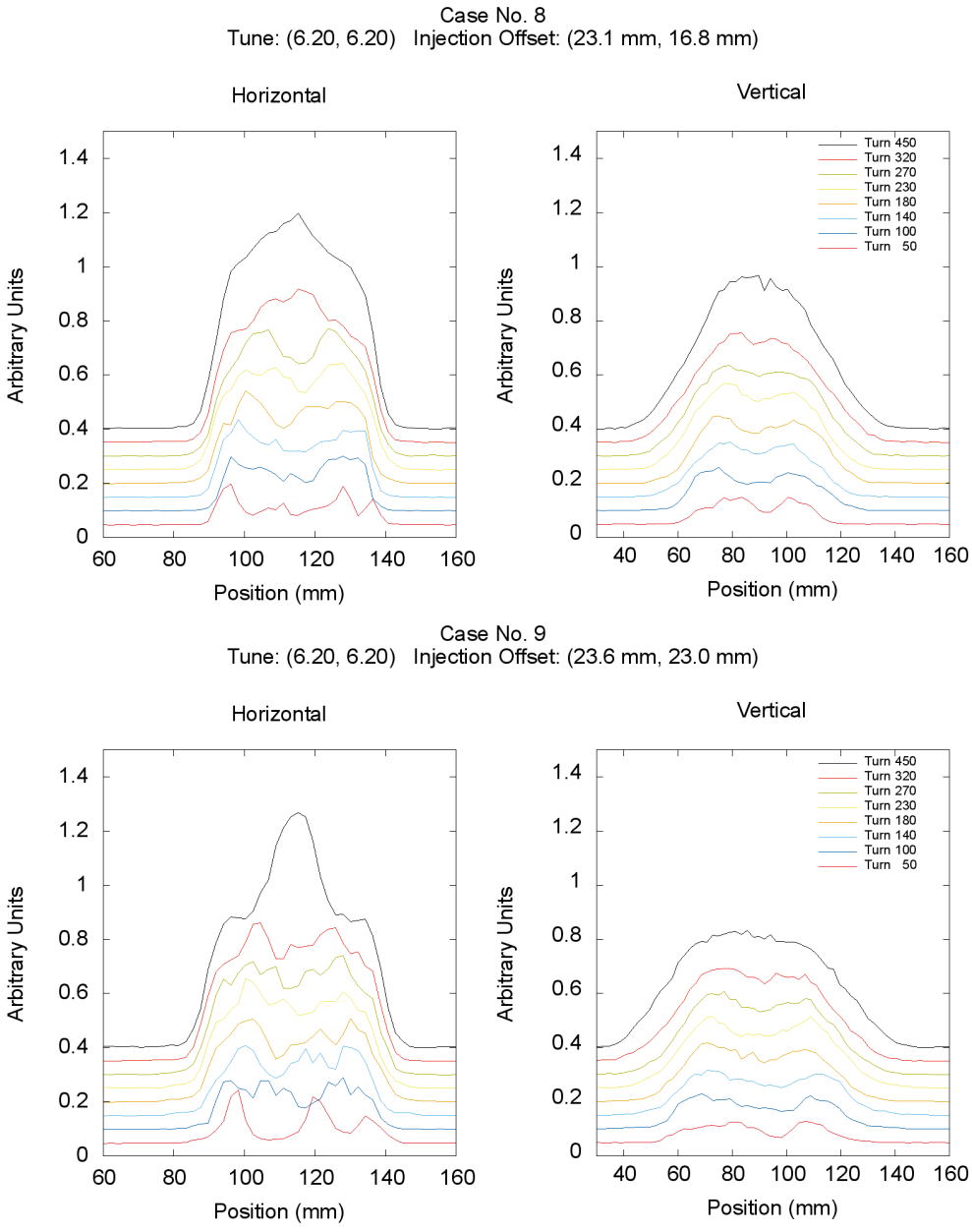

Figure 5.9: Comparison of wirescan waterfall plots for two cases with the same equal tunes but different beam geometries. The top case has an asymmetric beam geometry and the bottom case has a symmetric beam geometry.

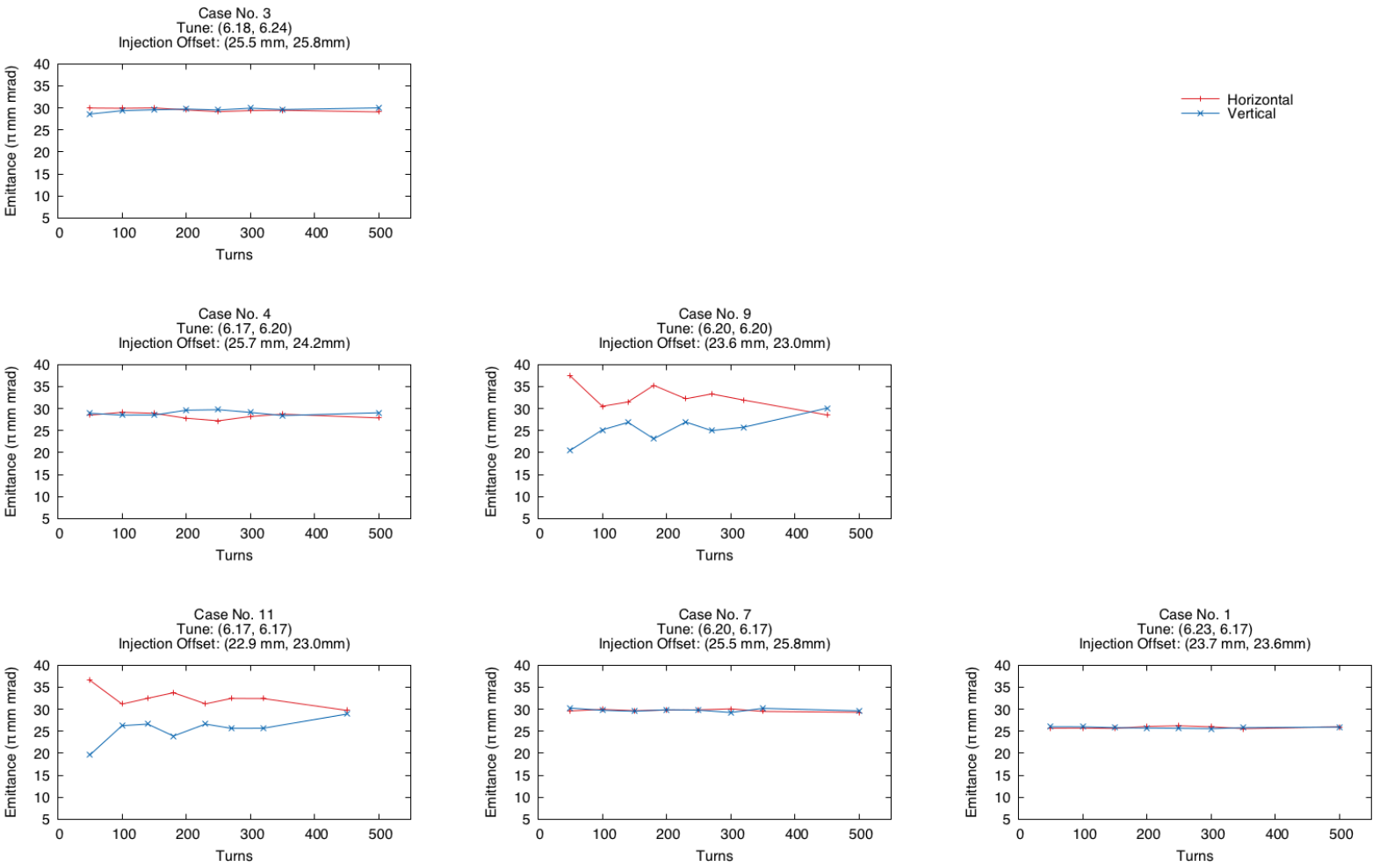

Figure 5.10: Emittance evolutions for symmetric beam cases.

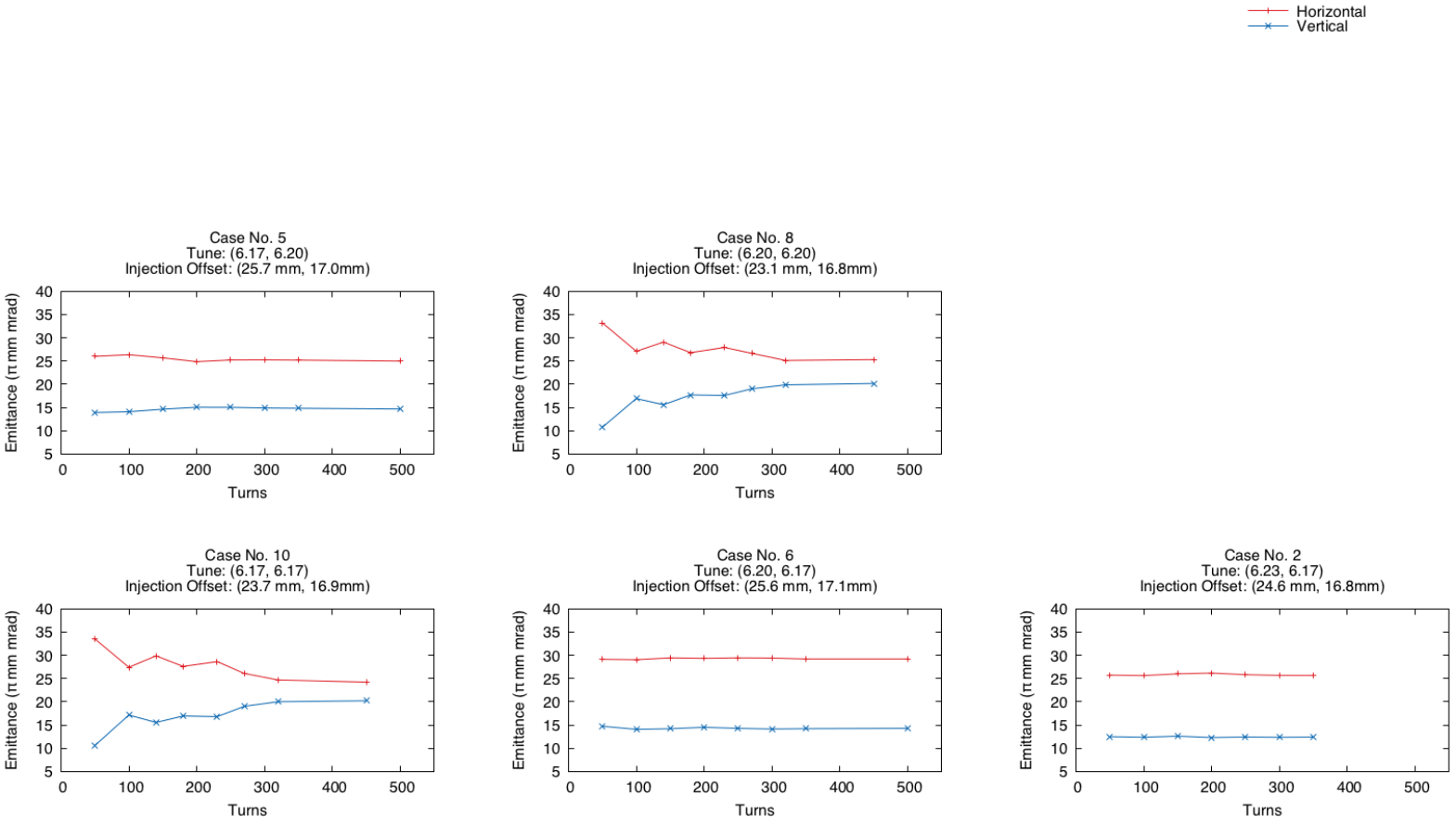

Figure 5.11: Emittance evolutions for asymmetric beam cases.

can be found in Section A.2. For our experiment, the primary Twiss parameter of concern are the transverse emittances, or the horizontal and vertical phase space areas occupied by the beam. Each wire scanner dataset yields a horizontal and vertical emittance. The change in these values during the experiment represents the evolution of the transverse phase space area. Emittances are a valuable metric for comparison because they provide more information than a simple one-dimensional projection, like an individual wire scanner profile. Figure 5.10 depicts the emittance evolution plots for the symmetric beam cases for experiment one. The profiles for these cases were depicted in Figures 5.2 and 5.3. Figure 5.11 depicts the emittance evolution plots for the asymmetric beam cases for experiment two. The profiles for these cases were depicted in Figures 5.4 and 5.5. Figures 5.10 and 5.11 are appropriately marked with the case numbers corresponding to the experimental configurations listed in Tables 5.1, 5.2, and 5.3.

The expected behavior of beams at the SNS is that they are injected into the ring to a specified size using the injection kickers and evolve with relatively constant emittances. We do not expect the beam emittance to oscillate during the nominal accumulation. There are three important results from these figures:

1. A cursory examination of both figures reveals that the cases with unequal tunes evolve with relatively constant emittances, regardless of the beam geometry. Additionally, the horizontal emittance is larger than the vertical emittance in all asymmetric cases because we intentionally used a larger horizontal injection offset to create a larger horizontal beam size. This implies that the cases with unequal tunes evolve as expected and are free from coupling.

2. The emittance evolution of equal tune beams differs greatly from uncoupled split-tune beams. An example of this is depicted in Figure 5.12, which compares case 5 (blue) with tunes of (6.17, 6.20) and case 8 (red) with tunes of (6.20, 6.20). There are a few noteworthy points to this result. The equal tune case shows coupled oscillations between the two transverse planes. These coupled

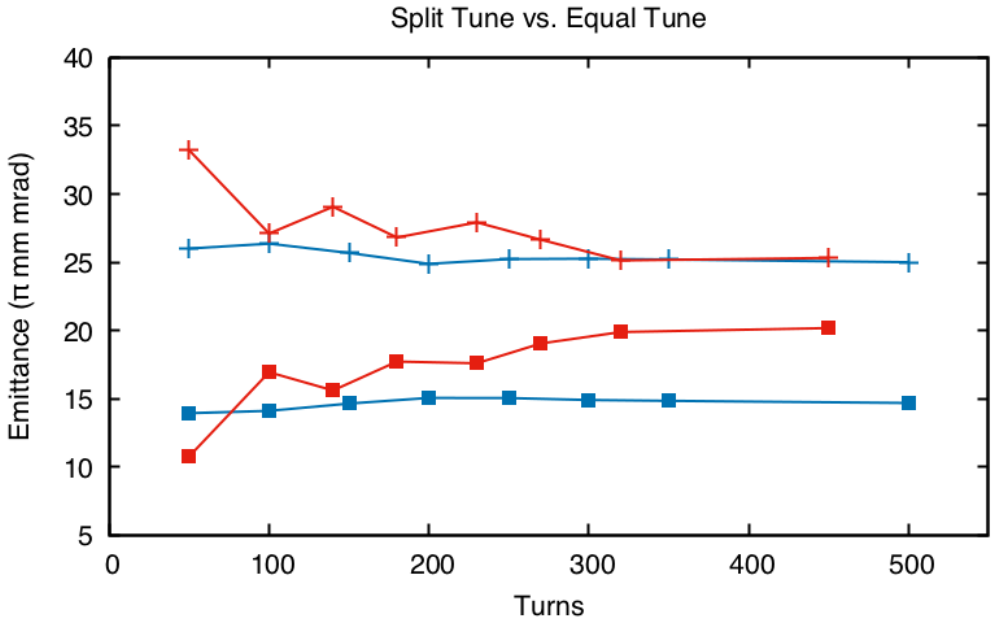

Figure 5.12: Comparison of the emittance evolutions for case 5 (blue) with tunes of (6.17, 6.20) and case 8 (red) with tunes of (6.20, 6.20). Both beams have asymmetric geometries. The horizontal emittances are indicated with '+' and the vertical emittances are indicated with '■'.

oscillations damp during the beam evolution and appear to have a conserved total emittance. While both cases start with an asymmetric beam geometry, the final equal-tune beam is almost symmetric with a larger vertical beam than was intended. This demonstrates the effect of emittance exchange when moving onto the equal tune resonance.

When this research was initially started, Montague resonances were thought to be the source of the coupling. As discussed in Section 3.3, Montague resonances are a coupling of equal tune beams due to space charge. This hypothesis implied that the coupling would either start at high beam intensities or amplify with increasing beam intensities, where space charge forces effects are stronger. However, the results of this experiment demonstrate coupling that starts at low intensity and dampens over time while the beam intensity is increasing. This indicates that a Montague resonance is not the most likely source of the coupling. This opened the question of what effect could create this coupling. These results strongly influenced the configurations chosen for experiments two and three.

3. The emittance evolution of equal tune beams are similar between different injection offsets. An example of this is depicted in Figure 5.13, which compares case 10 (red) with injection offsets of (23.7 mm, 16.9 mm) and case 11 (blue) with injection offsets of (22.9 mm, 23.0 mm). Both cases have an equal tune of (6.17, 6.17) and, regardless of beam geometry, show clear damped coupling between the transverse emittances. All of the unequal-tune symmetric cases shown in Figure 5.10 started with equal emittances. This is to be expected as the beams were designed to be symmetric using the injection offsets. However, the equal-tune symmetric cases do not start with the same equal emittances despite using the same injection offsets. Additionally, all of the equal tune cases display a strong coupling with symmetric damped oscillations around the conserved total emittance regardless of the beam symmetry. This result led

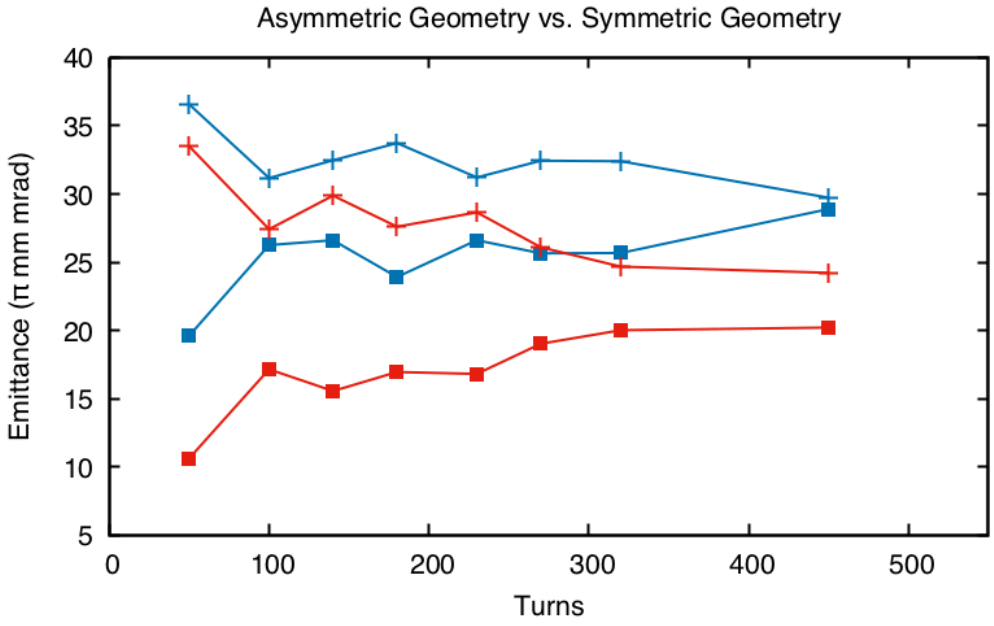

Figure 5.13: Comparison of the emittance evolutions for case 10 (red) with injection offsets of (23.7 mm, 16.9 mm) and case 11 (blue) with injection offsets of (22.9 mm, 23.0 mm). Both beams have the tunes (6.17, 6.17). The horizontal emittances are indicated with '+' and the vertical emittances are indicated with '■'.

us to the conclusion that the specific beam geometry does not play a strong role in the evolution of coupled beams. Therefore, future experiments used the asymmetric beam geometries to better facilitate Electron Scanner aperture restrictions, as noted in Chapter 4.

Accumulation Extended With Storage

As discussed in Section 5.2.1, storage configuration one was an extension of experiment one designed to make the best use of extra time on the third experiment shift. This configuration extended each data point following accumulation by 100 turns of storage and was only used for case 12. Figure 5.14 compares the horizontal and vertical profiles of case 11 (top), which had constant accumulation, and case 12 (bottom), which was extended with storage following accumulation. Cases 11 and 12 both have similar symmetric equal-tune configurations. While the profiles share a strong resemblance, the profiles typically display smoother or more dilute features after 100 turns of storage. The horizontal data has fewer and softer peaks, while the vertical data has a single central peak with smooth trailing edges. The comparison of these cases again demonstrates what we have already shown, that the coupling effect rounds out the profile data and creates trailing edges.

Figure 5.15 compares the emittance evolutions of case 11 (blue), which had constant accumulation, and case 12 (red), which was extended with storage following accumulation. At low beam intensities, the coupling has a larger impact on the stored beam and increased the split between transverse emittances. At high beam intensities, the emittances have almost returned to the same values as the case without storage. This implies that space charge forces dilute the coupling effect and are not the instigator of the coupling. These results, combined with the previous results from experiment one, led us to investigate low-intensity stored beams for experiment two.

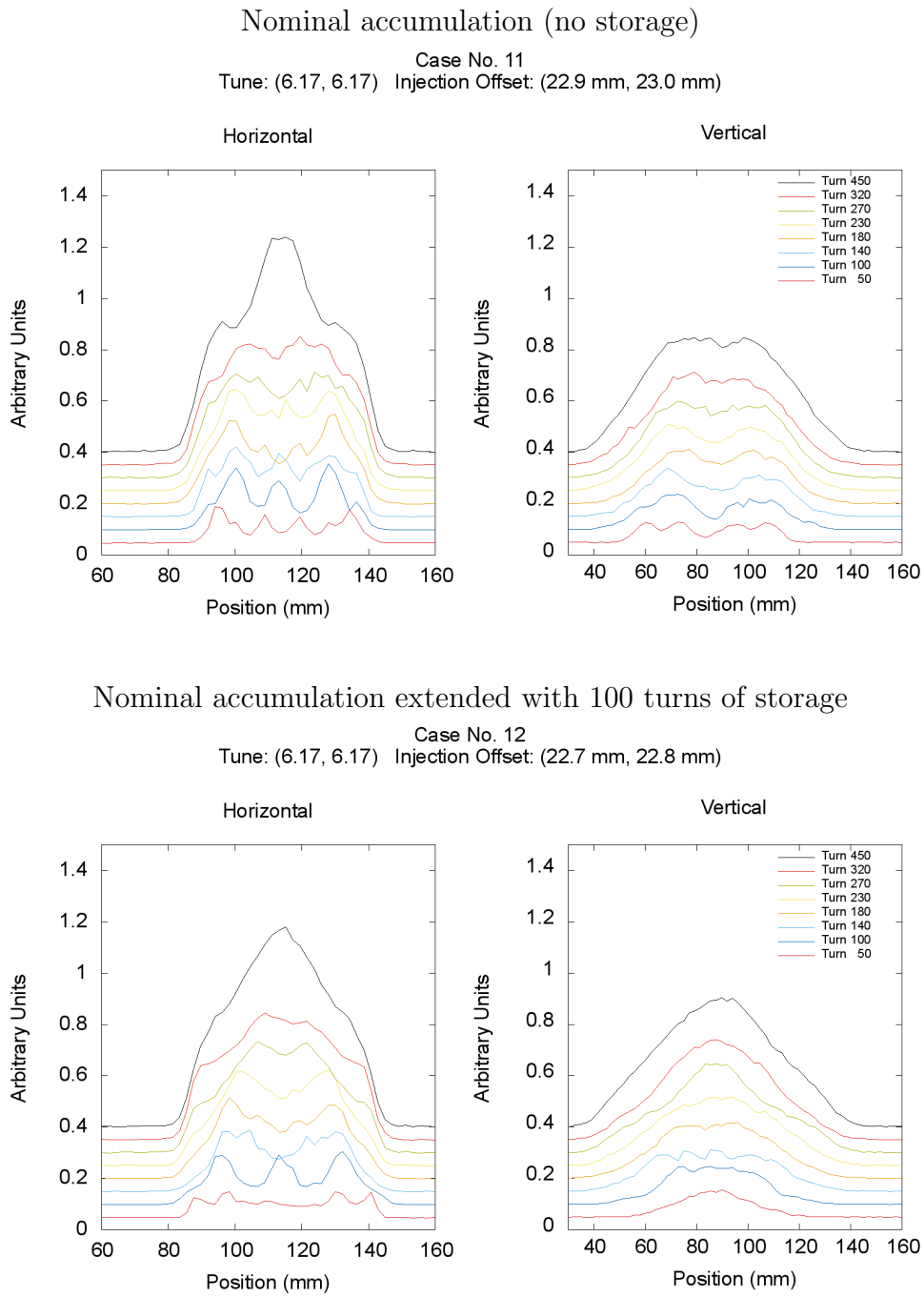

Figure 5.14: Comparison of the wirescan waterfall plots for the simplified accumulation with extended storage case (bottom) and the corresponding simplified accumulation-only case (top). The key for both figures indicates the number of turns accumulated. Profiles in the bottom figures were stored for 100 turns following accumulation.

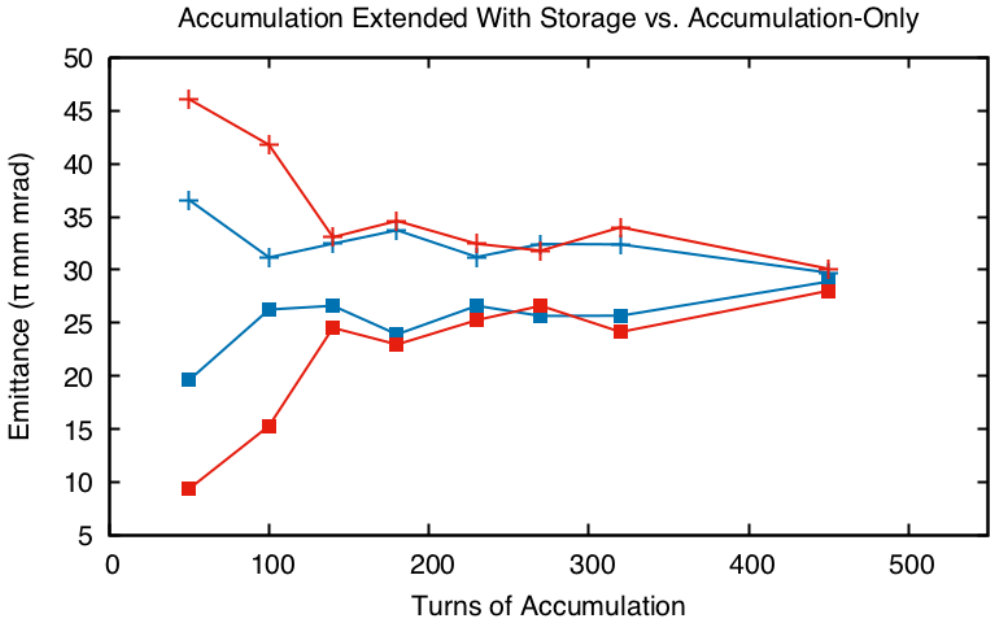

Figure 5.15: Comparison of the emittance evolution for the simplified accumulation with extended storage case (red) and the corresponding accumulation-only case (blue). The horizontal emittances are indicated with '+' and the vertical emittances are indicated with '■'.

5.3 Experiment Two: Accumulation Followed By Storage Using Wire Scanners

Experiment one had two important outcomes that impacted future experiments. The first result was that the coupling effect started at low beam intensities. The second result was that the effects of the coupling were damped with increasing beam intensities. Therefore, later experiments studied coupling by storing low intensity beams. These results provide an initial contradiction to the hypothesis that the coupling is caused by a Montague Resonance, which is driven by space charge. Experiment two used traditional wire scanners to collect data at numerous points along the evolution of two beam configurations. The specific experimental configurations are presented in Section 5.3.1. The results of experiment two are presented in Section 5.3.2.

5.3.1 Configuration

In the storage configuration used in experiment one, the first and second profiles are not direct continuations of the same beam. The second profile was accumulated for more turns prior to being stored for 100 turns. The evolutionary paths of the beams are different. Therefore, we were only able to compare each profile from the stored case (case 12) with the profile from the same configuration in the accumulation-only results (case 11), which shared the same number of turns of accumulation.

In experiment two, we used a second method of storing the beam. For the first 50 turns, we accumulated the beam using the same simplified configuration used in experiment one and then we stored the accumulated beam for up to 110 turns. However, we collected several measurements during both accumulation and storage of this beam.

In the new storage configuration, all of the profiles are connected along the same evolutionary path. Therefore, we were able to directly compare all of the profiles

Table 5.4: Beam Configurations for Experiment Two

Primary Diagnostic Device	Wire Scanners (WS20, WS21, WS23, WS24 located in the RTBT)	
Shift Date	February 23rd, 2015	
Accumulation & Storage	Accumulation Followed By Storage	
Turns of Accumulation	10, 25, 50	
Turns of Storage	10, 20, 30, 50	10, 20, 30, 40, 50, 80, 110
Maximum Beam Intensity	3.33e12 ppp 0.53 μC	3.12e12 ppp 0.50 μC
Q_x	6.16997	6.19986
Q_y	6.19872	6.19893
ΔQ	-0.02875	0.00093
Beam Tune	Split Tune	Equal Tune
Injection Kickers	Flat-topped Waveform	
X Injection Size	25.8 mm	23.2 mm
Y Injection Size	17.1 mm	17.1 mm
Beam Geometry	Asymmetric	
Beam Energy	939.5 MeV	
Ring RF	Shorted	
Ring Pattern Width	39%	
Ring Chromaticity	Zeroed	
Linear Coupling	Checked and, if necessary, removed with skew quadrupoles	

during both accumulation and storage. There were three consequences. First, we were able to more closely examine the strong coupling effects during the early evolution of the equal tune beam. Second, this provided us with the opportunity to characterize the evolution of the coupling without the complication of increasing beam intensity. Finally, comparing this new data with data from experiment one allowed us to examine the impact of storage versus continued accumulation. An overview of the beam configurations for experiment two are located in Table 5.4.

Additionally, starting with experiment two, we stopped placing the ring RF in stand-by and started shorting it. The change was intended to ensure that there were no effects present from the ring RF. The ring RF mostly impacts the beam by longitudinally bunching the particles. Therefore, this change should not have had a significant impact on the such a short time scale.

Tune The results of experiment one allowed us to reduce the number of tune points studied in experiment two to one equal-tune point and one split-tune point.

Geometry Additionally, we learned from experiment one that it is easier to distinguish the effects of coupling when comparing asymmetric emittances. With symmetric or equal emittances, the concern was that the effects of low levels of coupling might not be clearly distinguishable from the already equal emittances. Therefore, we limited experiment two to the asymmetric beam geometry from experiment one.

Energy and Intensity The nominal beam energy during experiment two was 939.5 MeV. This is 6.6 MeV higher than during experiment one. This is a nominal change in beam energies between SNS productions periods and should not impact any comparison between experiments. Our beam intensities were 3.33e12 ppp for the split tune case and 3.12e12 ppp for the equal tune case, or 0.53 μC and 0.50 μC respectively. It is important to note that these beam intensities are an order of magnitude less than

in experiment one due to the fact that we are only accumulating one tenth the amount of beam. Figure 5.16 compares the configurations for experiments one and two. The reproducibility of this low intensity beam is demonstrated using the wire scanners at turn 10 in Section A.1.

5.3.2 Results

Figure 5.17 shows the horizontal and vertical waterfall plots for the two beam cases in experiment two. This figure represents the data collected for experiment two as documented in Table 5.4. The split tune beam (top) follows the expected uncoupled profile evolution, as previously shown with similar data in Section 5.2.2. The beam maintains most of its hollowness during storage due to the low beam intensity and a limited period of storage. In comparison, the equal tune beam (bottom) displays strong coupling between the transverse profiles. This is most clearly seen in Figure 5.18, which directly compares the profiles at three points during storage. In order to make this direct comparison between the transverse profiles, we must adjust the profiles to account for the strengths of the magnetic fields by scaling the widths of the beams. We do this by multiplying the position values $1/\sqrt{\beta}$. At turn 80 (left), the horizontal profile has a larger width than the vertical profile. This was determined by the injection offsets. At turn 100 (middle), the profiles have almost equal widths. At turn 130 (right), the horizontal beam is at a waist. The profiles exchanged widths in approximately the period from turn 80 to turn 130.

Figure 5.19 shows the emittance evolution for the beam cases in experiment two. The split tune emittances (top) are approximately constant and remain at the intended sizes for the duration of the experiment. Using the emittances, we can see a clear exchange of the equal tune emittances (bottom). The oscillation has a sinusoidal nature, though it is difficult to determine the long term nature of the oscillations without more turns of storage. Additionally, we are able to loosely compare the equal-tune beam with a similar case from experiment one. Figure 5.20 shows the

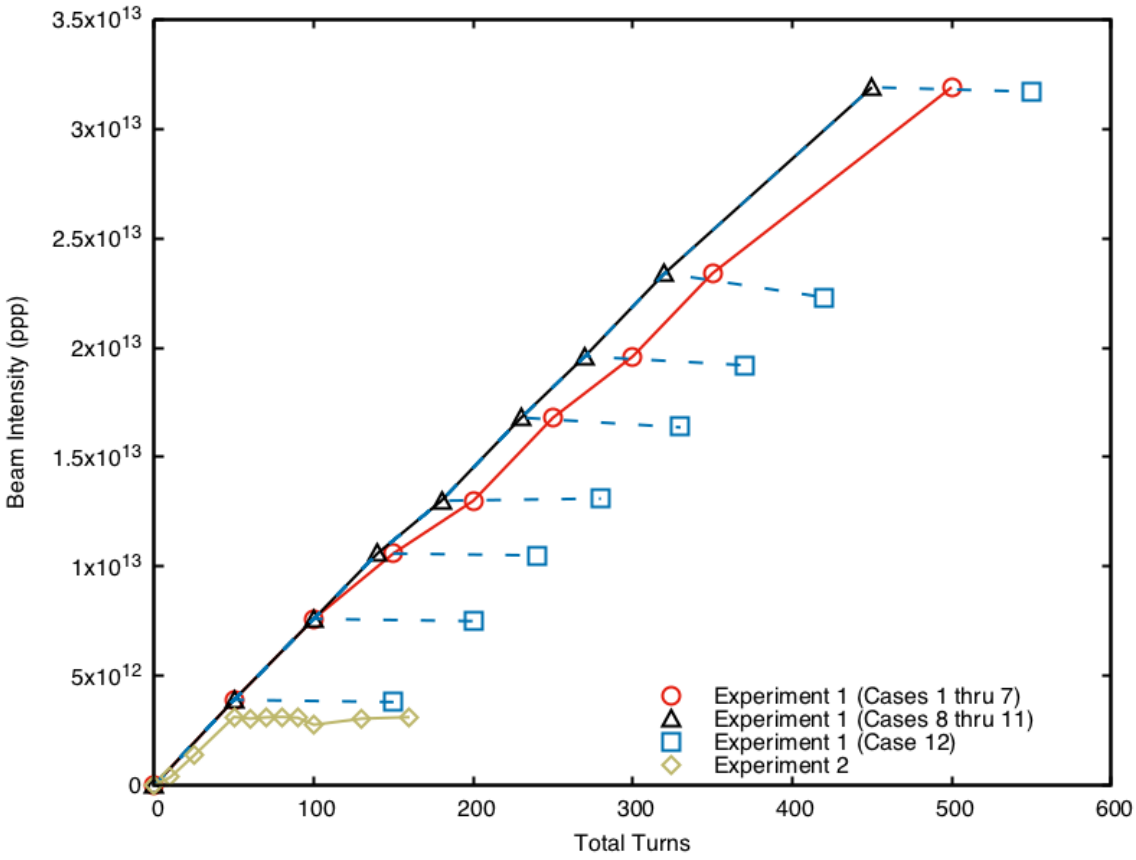

Figure 5.16: Comparison of configurations for experiments one and two. The beam intensity is shown on the vertical axis and the total number of turns are shown on the horizontal axis. The split-tune accumulation-only configuration for cases 1 through 7 of experiment one are shown with a solid red line with '◯' points. The equal-tune accumulation-only configuration for cases 8 through 11 of experiment one are shown with a solid black line with '△' points. The accumulation extended with storage configuration for case 12 of experiment one is shown with dashed blue lines with '□' points. The stored beam configuration of experiment two is shown with a brown line with '◇' points. Lines indicate the evolutionary path followed for each data point, and markers indicate the relative location of data collection. Sloped lines indicate periods of accumulation and flat lines indicate periods of storage.

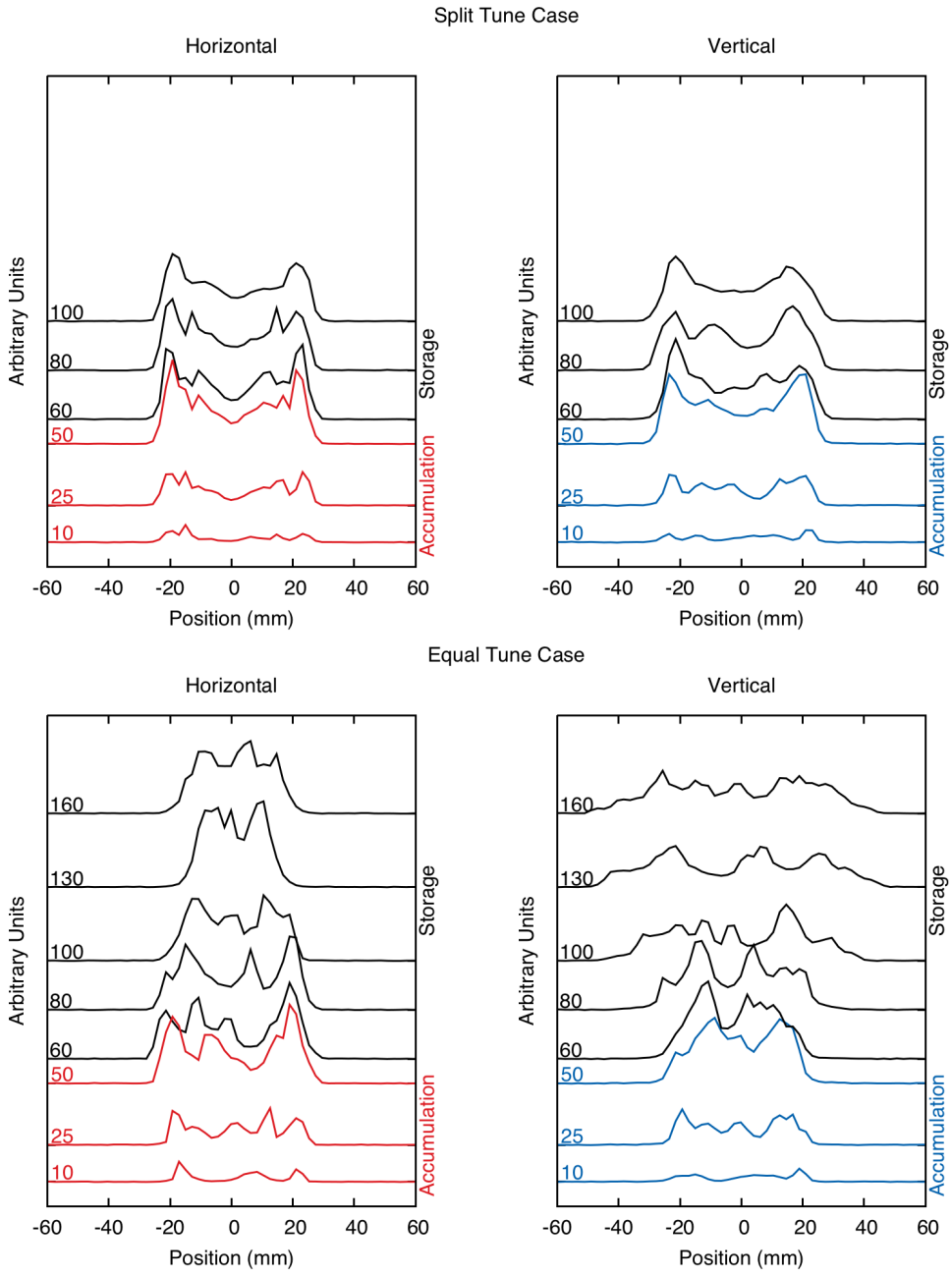

Figure 5.17: Comparison of the wirescan waterfall plots for experiment two. The split tune beam is shown on top, and the equal tune beam is shown on bottom. Each beam was accumulated for 50 turns, shown in color, and then stored, shown in black. The numbers on the vertical axis indicate the turn when each measurement was collected. To provide a relative scale for the evolution, each profile is vertically offset by 0.02 times the turn number.

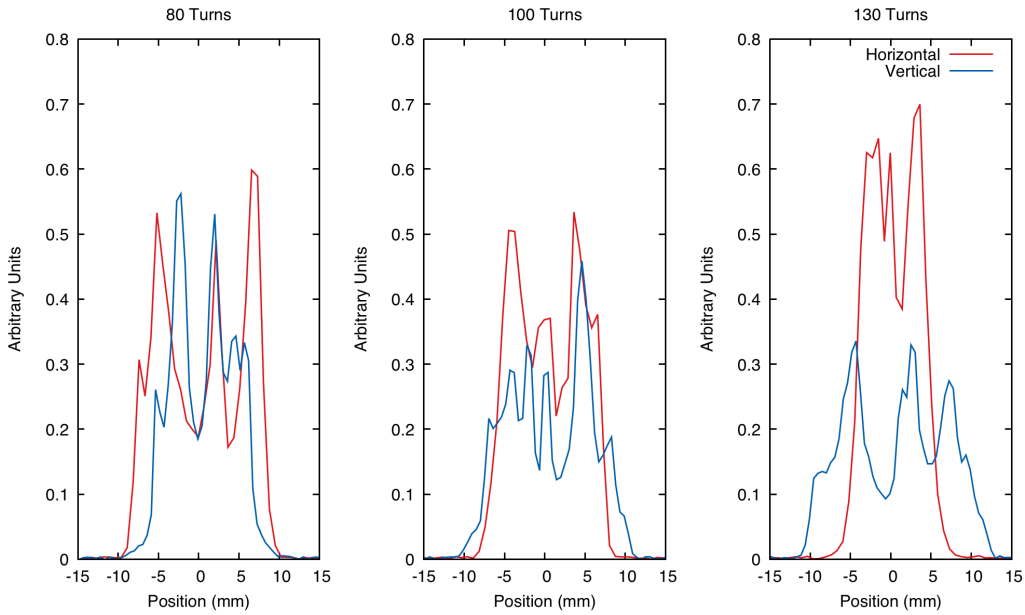

Figure 5.18: Comparison of the transverse beam profiles at three points during storage. Each beam was accumulated for 50 turns. The beams were stored for 30, 50, and 80 turns, respectively. These profiles have been scaled by the Twiss factor, $1/\sqrt{\beta}$, to account for the effects of the local magnetic fields and to allow for direct comparison of the physical sizes.

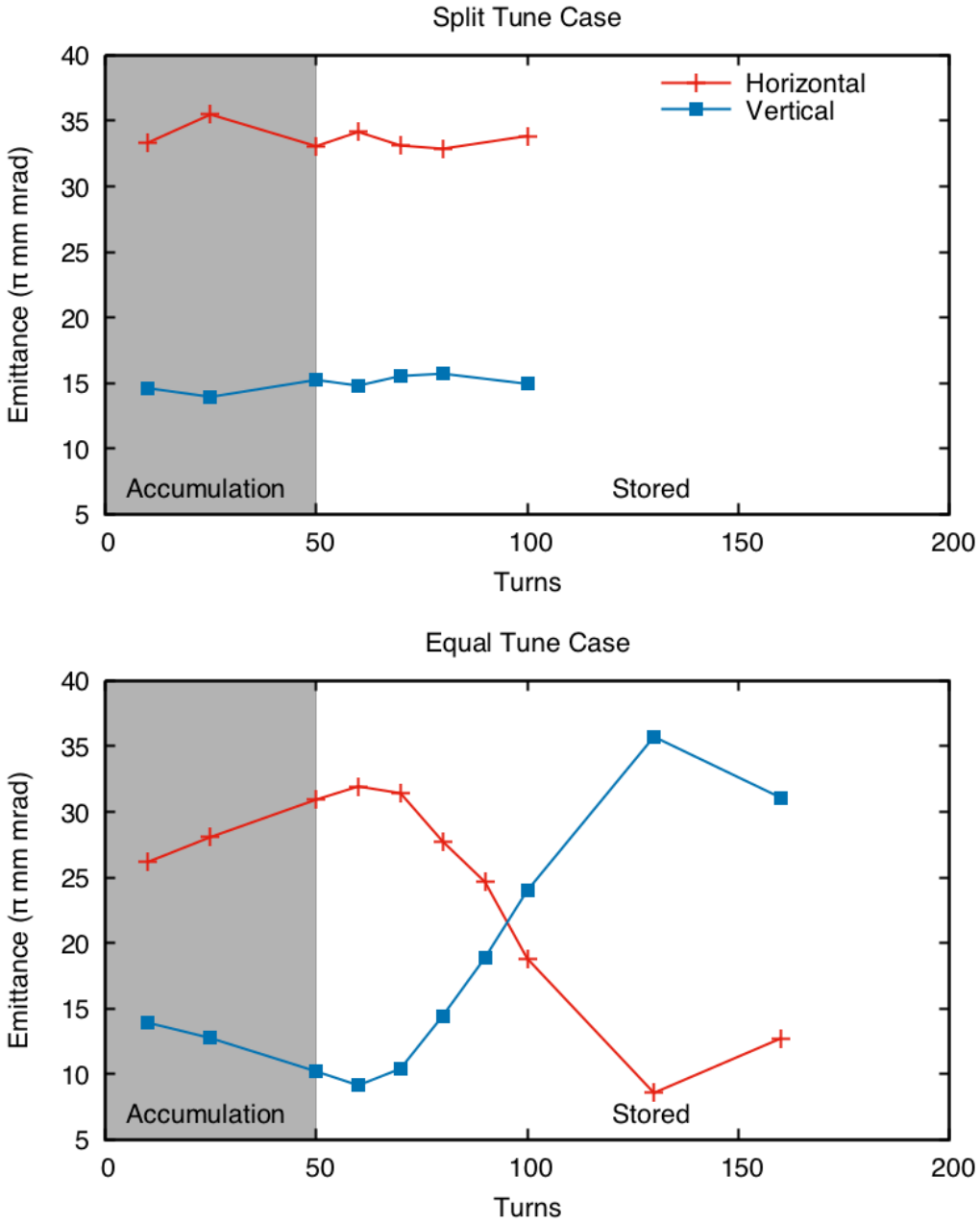

Figure 5.19: Comparison of the emittance evolutions for both simplified accumulation with storage cases. The horizontal emittances are indicated with '+' and the vertical emittances are indicated with '■'.

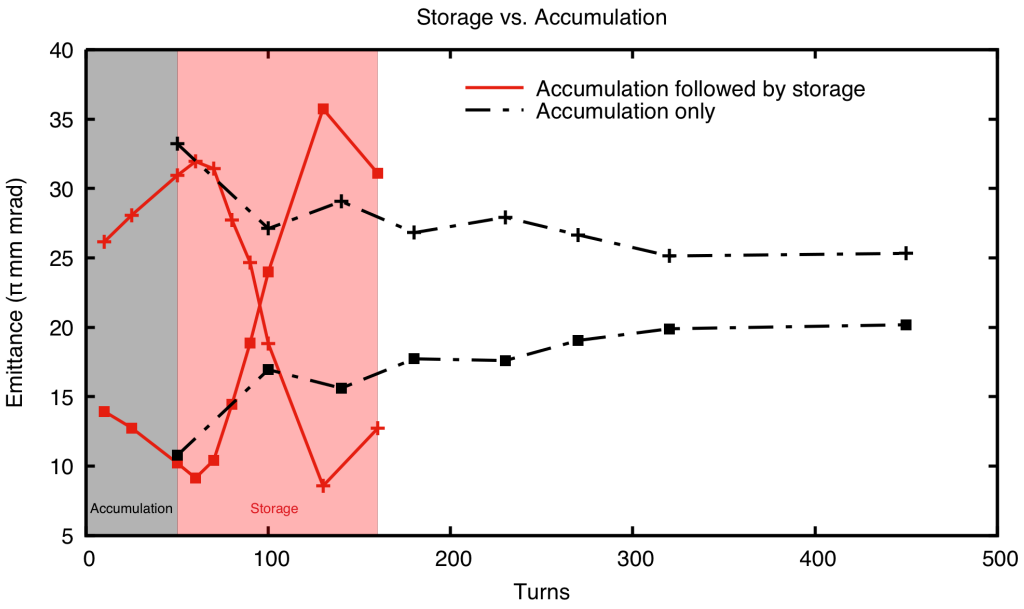

Figure 5.20: Comparison of the emittance evolution for the stored equal-tune case from experiment two (red) and the corresponding accumulation-only case, case 10, from experiment one (black, dashed). The horizontal emittances are indicated with '+' and the vertical emittances are indicated with '■'.

stored equal-tune emittance evolution from experiment two versus the accumulation-only equal-tune emittance evolution from case 8 in experiment one. Both cases have asymmetric geometries and the injection offsets of experiment two were chosen to be very similar to those in experiment one. At turn 50, we can see that the emittances for the two cases are almost equal. These similarities allow us to generally compare the evolution of the beam under constant accumulation versus the evolution of the beam under storage. We can see that the continued accumulation clearly dampens the amplitude of the oscillation. It also slightly decreases the frequency of the oscillation. Finally, the emittances of experiment two give us insight into what the low intensity emittances for experiment one might have been.

5.4 Experiment Three: Accumulation Followed By Storage Using The Electron Scanner

Experiment two confirmed that the coupling started at low beam intensities. It demonstrated that the coupling could create a complete exchange of transverse emittances. These results continue to support the theory that the coupling is not caused by a Montague resonance. The main limitation of experiment two was the large consumption of time required for data collection. Each wire scan took upwards of four minutes to collect and required brief operator interaction between data points to alter the number of turns of accumulation or storage. One of our main priorities became extending the storage period. Therefore it was necessary for us to increase the number of measurements, which required a more dynamic diagnostics device. In experiment three, we repeat experiment two using the Electron Scanner as the primary diagnostic.

As noted in Chapter 4, the Electron Scanner improves significantly on the time for data collection. A brief summary of the explanation of how this is accomplished is as follows. The Electron Scanner is located in the ring, allowing it to collect data during

the evolution of the beam without requiring extraction to the target for each scan. Therefore, we can set up the final beam configuration, including all accumulation and storage, and the Electron Scanner is able to sweep through the evolution in one fluid series of scans. This eliminates the need for any operator interaction during a full scan of one evolution, which increases the speed of the scan. Additionally, the Electron Scanner has a much faster rate of data collection. We take advantage of this by collecting full longitudinal sweeps of the beam at much smaller intervals than we were able to with the wire scanners. These two reasons increase the overall data collection speed. Another benefit is that the non-destructive nature of the Electron Scanner removes any concerns about creating large beam losses during scans. Together these improvements make the Electron Scanner a far more dynamic device and the superior choice for studies of the full evolution of the beam.

The most unique feature of the Electron Scanner is its ability to measure profiles from numerous bunches during the evolution of the beam. These profiles can then be combined to clearly show the evolution of the beam profile as a continuous curve. We refer to these figures as profile evolutions. Data processing for the Electron Scanner is discussed further in Chapter 4.

5.4.1 Configuration

In order to study a well-defined beam, we increased the beam accumulation to 100 turns and, taking advantage of the Electron Scanner's rapid data collection, we extended the storage to 300 turns. A complete longitudinal scan, consisting of 40 separate transverse profiles along a single bunch length, is collected every 10 turns during accumulation and storage. The details of how the Electron Scanner works and how the data is processed and presented are discussed in Chapter 4. An overview of the beam configurations for experiment three are located in Table 5.5. The results of experiment three are presented in Section 5.4.2.

Table 5.5: Beam Configurations for Experiment Three

Primary Diagnostic Device	Electron Scanner (Located between QTH_D13 and QTV_A01 in the Ring)				
Accumulation & Storage	Accumulation Followed By Storage				
Shift Date	June 27th, 2015				
Beam Tune	Split Tune	Middle Split Tune	Equal Tune		
Q_x	6.20907	6.20044	6.19944		
Q_y	6.16866	6.19188	6.19781		
ΔQ	0.04041	0.00856	0.00163		
Injection Kickers	Flat-topped Waveform				
X Injection Size	17.3 mm	18.1 mm	17.9 mm		
Y Injection Size	6.5 mm	7.2 mm	8.5 mm		
Beam Geometry	Asymmetric				
Turns of Accumulation	100				
Turns of Storage	300				
Scan Steps	40 longitudinal slices collected every 10 turns starting at turn 5				
		Nominal		Medium	Low
Maximum Intensity	7.42e12 ppp 1.19 μC	7.51e12 ppp 1.20 μC	7.60e12 ppp 1.22 μC	4.36e12 ppp 0.70 μC	2.29e12 ppp 0.37 μC
Beam Energy	939.5 MeV				
Ring RF	Shorted				
Ring Pattern Width	39%				
Ring Chromaticity	Zeroed				
Linear Coupling	Checked and, if necessary, removed with skew quadrupoles				

Tune The equal tune was chosen to be the same as in experiment two. In order to investigate the dependence on the tune split, we collected data for two split tune cases by lowering the vertical tune. The most split tune case has a tune split almost five times larger than the intermediate tune split case.

Geometry During experiment three, we required a smaller beam size than the previous experiments in order to fit the entire beam into the apertures of the Electron Scanner. The vertical aperture has tighter size limitations than the horizontal beam due to misalignment of the vacuum beam pipe and a larger betatron function, therefore we configured a much smaller vertical beam size. The measured Twiss parameters at the Electron Scanner are ($\alpha_x = 0.78, \beta_x = 3.23, \alpha_y = -0.72, \beta_y = 10.21$), as discussed in Section 4.3.

Energy and Intensity The beam energy remained the same as in experiment two. For the equal tune configuration, we collected data for two lower intensities in addition to the nominal intensity. In order to preserve the other configuration settings, we lowered the intensity by limiting the output current from the H^- source. Figure 5.21 compares the configurations of experiment three in comparison with those of experiments one and two.

5.4.2 Results

In this section we review the results of the third experiment focused on using the new Electron Scanner. First, we will examine the effect of tune on the beam dynamics. Then, we will examine the effect of beam intensity on the coupled beam.

Effect of Tune

Figure 5.22 shows the horizontal and vertical profile evolution for the split tune (top row), middle split tune (middle row) and equal tune (bottom row) configurations. These correspond to the first three cases of experiment three as documented in

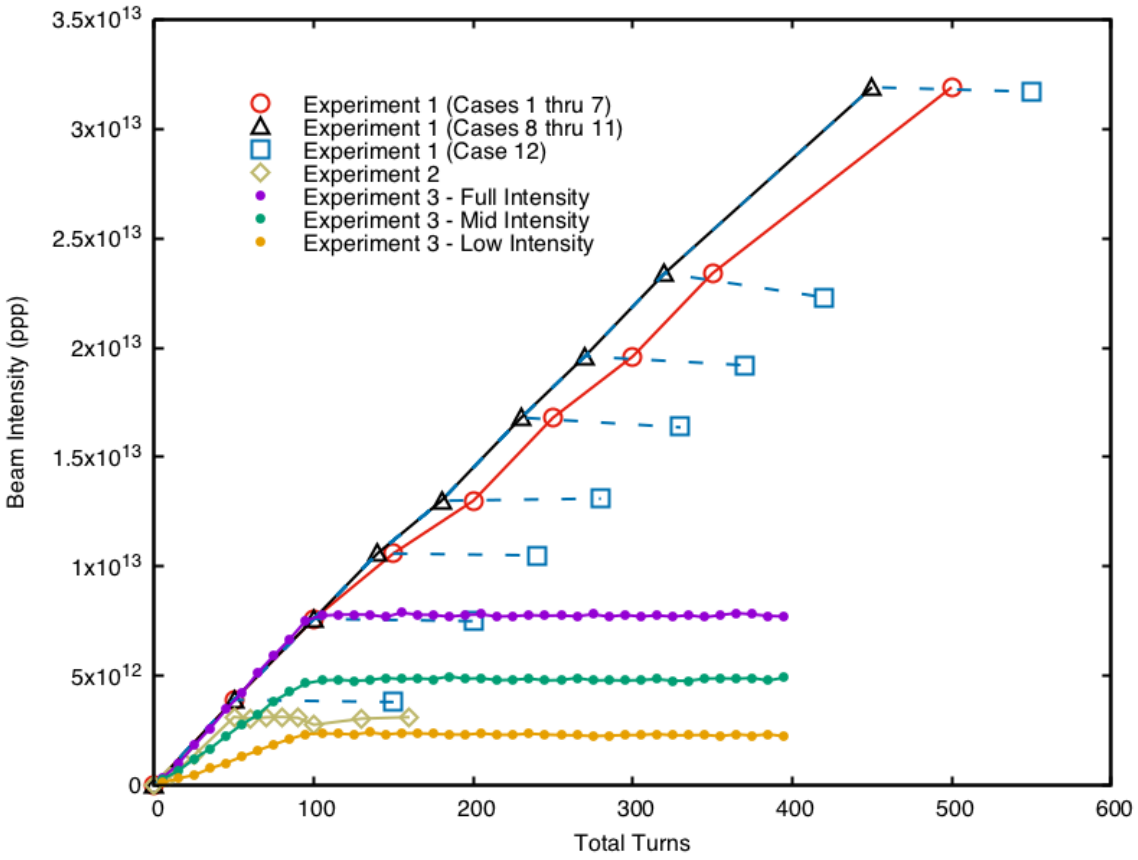

Figure 5.21: Comparison of configurations for experiments one, two, and three. The beam intensity is shown on the vertical axis and the total number of turns are shown on the horizontal axis. The split-tune accumulation-only configuration for cases 1 through 7 of experiment one are shown with a solid red line with '◯' points. The equal-tune accumulation-only configuration for cases 8 through 11 of experiment one are shown with a solid black line with '△' points. The accumulation extended with storage configuration for case 12 of experiment one is shown with dashed blue lines with '□' points. The stored beam configuration of experiment two is shown with a brown line with '◇' points. The three intensities of experiment three are shown with solid lines with '●' points. The intensities are nominal (purple), mid (green), and low (gold). Lines indicate the evolutionary path followed for each data point, and markers indicate the relative location of data collection. Sloped lines indicate periods of accumulation and flat lines indicate periods of storage.

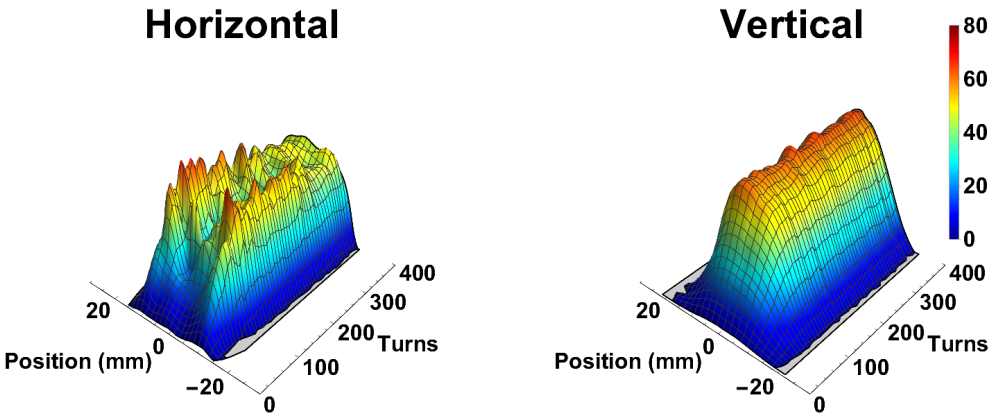

Split Tune Beam (7.42e12ppp)

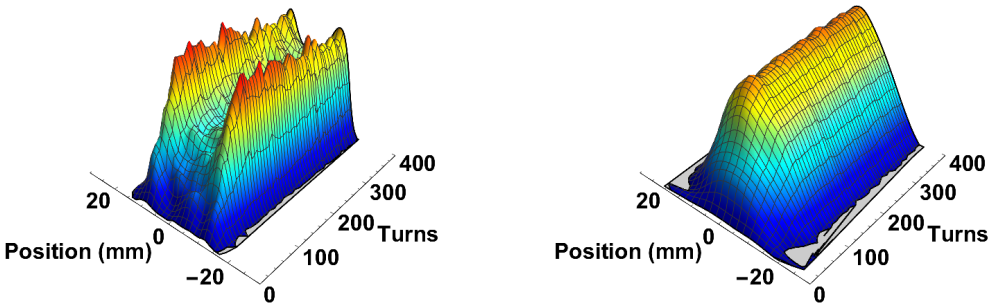

Middle Split Tune Beam (7.51e12ppp)

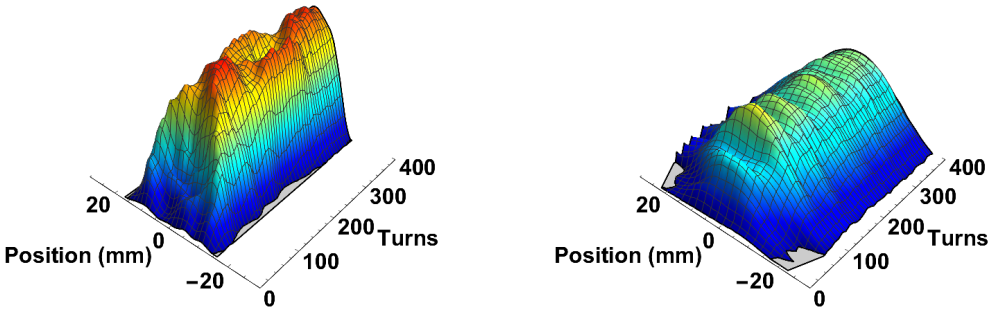

Equal Tune Beam (7.60e12ppp)

Figure 5.22: Summed profile evolutions for the split tune (top), middle split tune (middle), and equal tune (bottom) configurations for experiment three. The horizontal evolutions are shown on the left and the vertical evolutions are shown on the right.

Table 5.5. The overall behavior of both split tune cases follow our understanding of the nominal beam evolution. During accumulation, the horizontal profiles are hollow due to the injection pattern defined by the flat-topped injection kickers and the choice of betatron tunes. While the beam is stored, space charge forces cause the horizontal profiles to dilute and the profiles become flat-topped after a few hundred turns. Due to the small vertical injection offsets, the vertical profiles are seen as single peaks with no discernible features. This implies that the coupling effect requires the tune split to be less than $\sim$0.009. This is generally considered a small tune split beam and is far from the nominal working point of the SNS. These cases provide uncoupled beams as references for our experiment. By contrast, the equal tune case shows full oscillations of the beam shape. The horizontal profile starts hollow but quickly becomes peaked midway through accumulation. It then proceeds to oscillate between peaked and hollow during storage. The vertical profile, to a lesser extent due in part to its limited size, also oscillates. The evolution indicates coupled beam dynamics that are significantly different from the split tune configurations. This represents a unique measurement of the profile evolution during the coupling. Prior to this research, no published works ever considered profile shape change during coupling. The primary focus of other works has always been on oscillations of the RMS size. There has usually been an implicit assumption that either the profile shape was preserved or that there was only a slow change in the shape. However, with this measurement, we have documented a major shape change over the span of approximately 75 turns.

Figure 5.23 shows the evolution of the horizontal and vertical RMS beam sizes for the split tune (top), middle split tune (middle) and equal tune (bottom) configurations, as documented in Table 5.5. When comparing the RMS sizes, it is important to remember that the betatron values at the location of the horizontal and vertical ES apertures are not equal, as noted in Section 4.3. Additionally, the horizontal emittance of the beam is designed to be larger than the vertical emittance. Excluding the initial period of accumulation, the split tune and middle split tune RMS sizes remain constant during beam storage from turn 100 to 400. This continues to

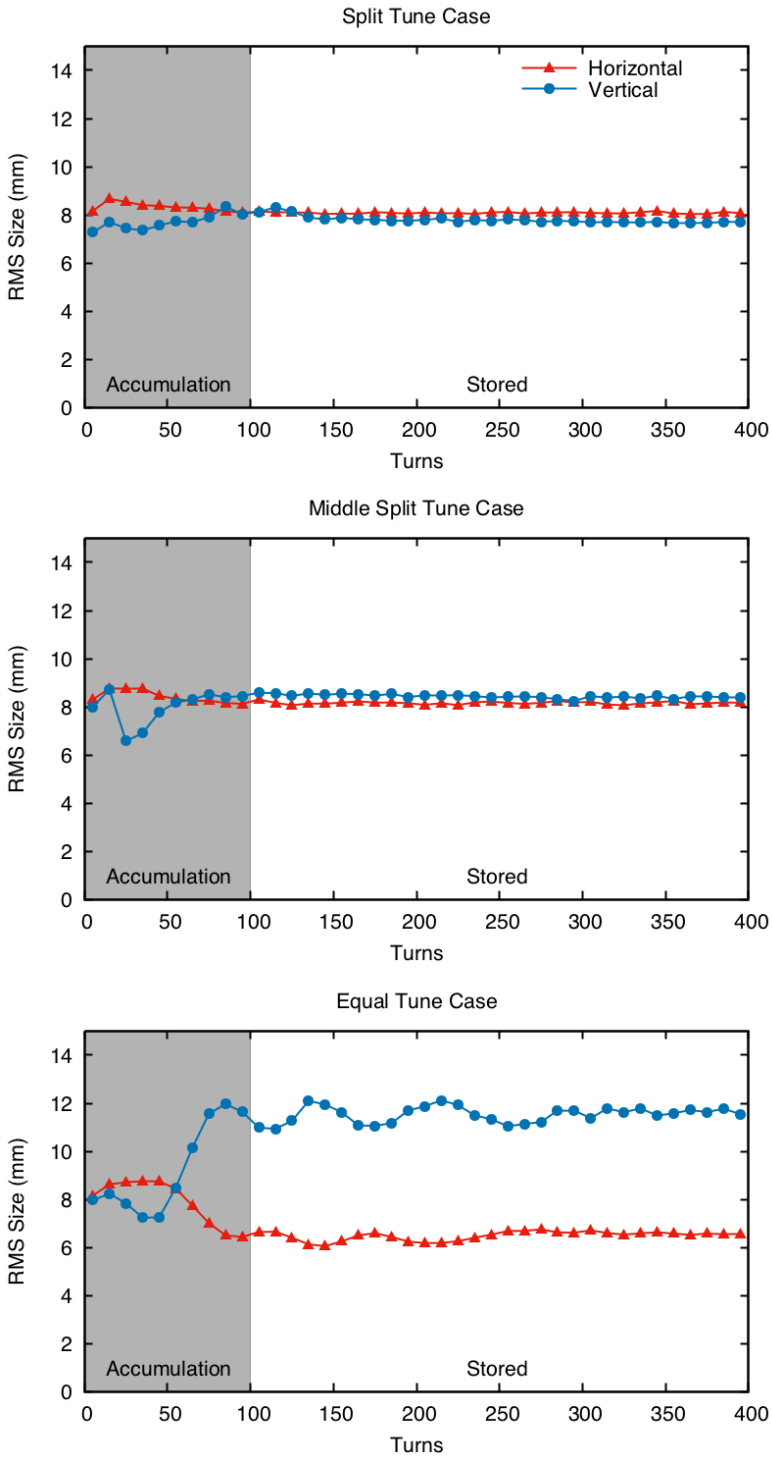

Figure 5.23: RMS size evolutions for the split tune (top), middle split tune (middle), and equal tune (bottom) configurations for experiment three. The horizontal RMS sizes are shown in red and indicated with '▲', and the vertical RMS sizes are shown in blue are indicated with '●'.

fit our description for the evolution of uncoupled beams. For the equal tune case, we see an exchange between the RMS sizes of the two planes within the first 50 turns. By the time accumulation has stopped at turn 100, an oscillation has been created between the transverse planes. This oscillation matches the oscillation seen in the profile evolutions. From the RMS sizes, we can see that the oscillation dampens as the storage continues.

Effect of Beam Intensity

Figure 5.24 shows the profile evolutions for the three equal tune configurations of experiment three, as documented in Table 5.5. The full intensity figure (bottom) represents the same equal-tune case presented in the previous section. The oscillations of the profiles decrease with increasing beam intensity. Figure 5.25 shows the RMS size evolutions for the three equal tune configurations in experiment three. Each of the RMS size evolutions has been fit with an exponentially-damped sinusoid of the following form:

$$f = A \exp^{(-K\,x)} \sin(B\,x + C) + D. \tag{5.1}$$

In this fit, A is the amplitude of the oscillation, B is the oscillation frequency, C is the frequency offset, D is the amplitude offset and K is the damping coefficient. The fits are started at the first data point in the storage period, turn 105. The results of the fits are shown in Table 5.6.

Figure 5.26 shows that the oscillation period for these fits decreases with increasing beam intensity. This result indicates that space charge forces dampen the oscillation in the beam, contrary to our original theory that the coupling was due to a Montague resonance.

As mentioned previously, the tune of the SNS beam is often changed during production setup to minimize losses in the ring while optimizing the beam size and shape on the target. The dynamics demonstrated in experiment three have two important consequences. First, the beam no longer responds as expected to

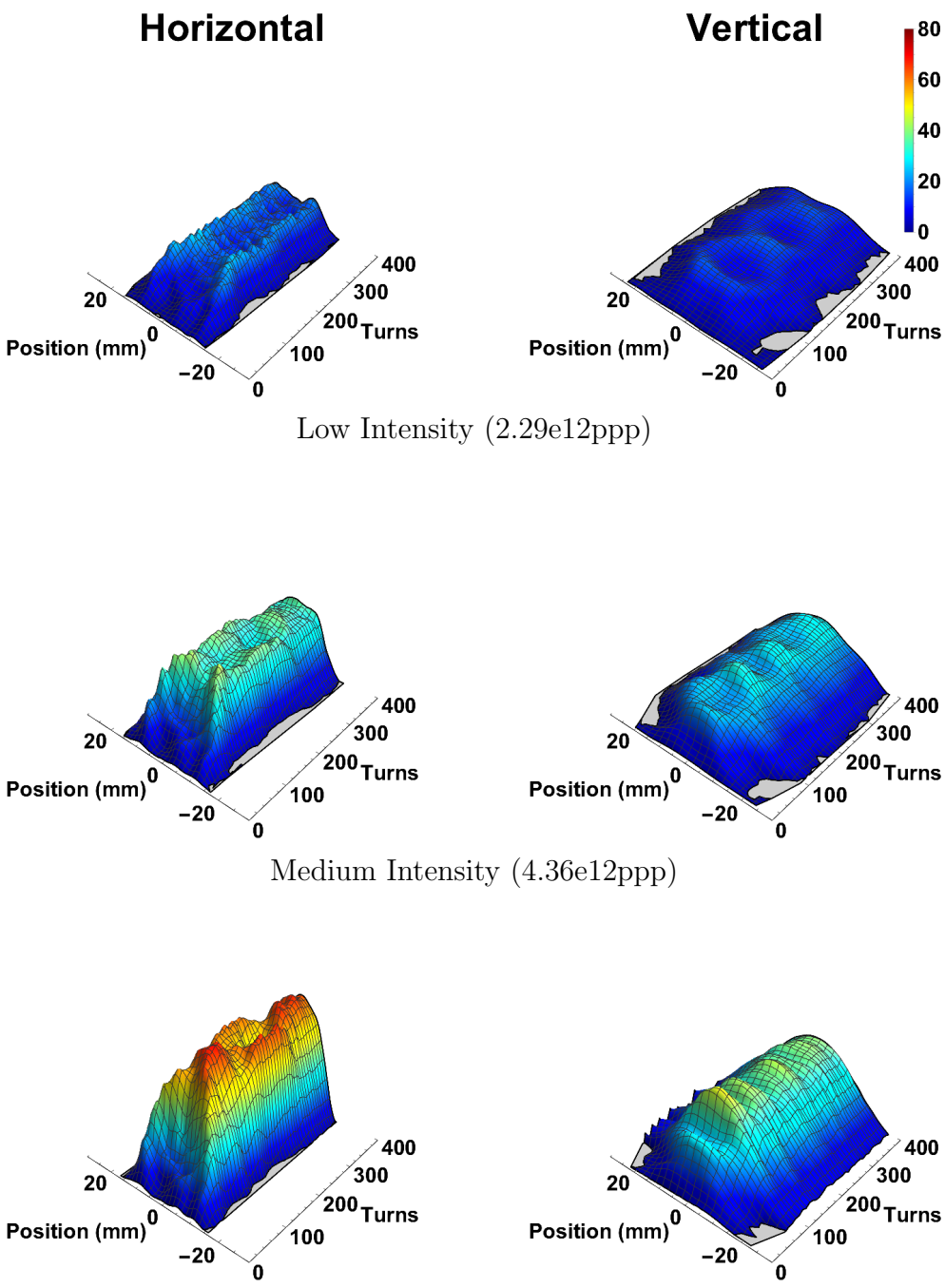

Figure 5.24: Comparison of the summed profile evolutions for the equal-tune low intensity (top), middle intensity (middle), and nominal intensity (bottom) configurations for experiment three. Horizontal evolutions are shown on the left and vertical evolutions are shown on the right.

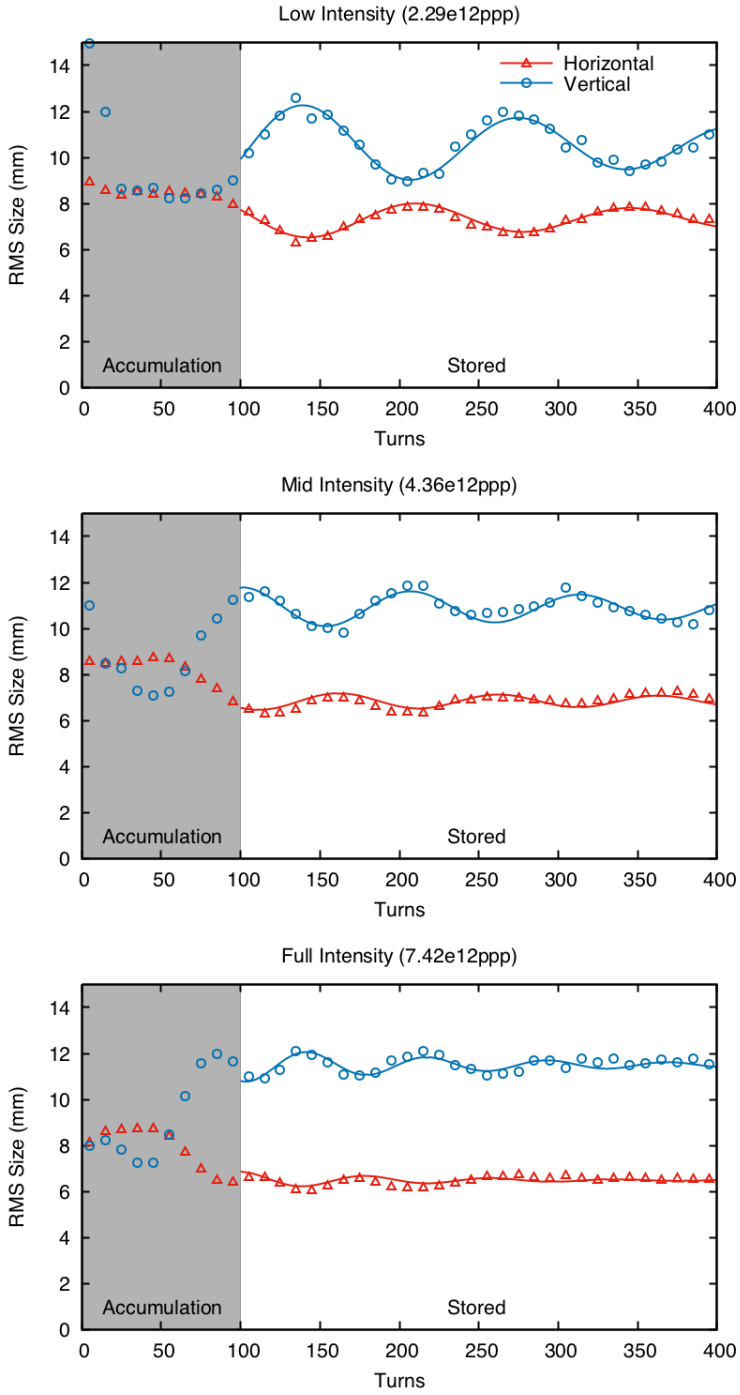

Figure 5.25: RMS size evolutions for the equal-tune low intensity (top), middle intensity (middle), and full intensity (bottom) configurations for experiment three. The horizontal RMS size measurements are shown as red '△'s and the vertical RMS size measurements are shown as blue '◯'s. The fits are shown as solid lines of the same colors.

Table 5.6: Fit Parameters for the Three Equal Tune Cases

		Horizontal			Vertical		
Beam Intensity	[e12ppp]	Low	Mid	Full	Low	Mid	Full
		2.29	4.36	7.60	2.29	4.36	7.60
	[μC]	0.37	0.7	1.22	0.37	0.7	1.22
Fit Parameters	a	1.16	0.461	0.871	2.58	1.1	1.44
	b	0.0465	0.0624	0.0796	0.0463	0.059	0.0829
	c	7.33	6.84	6.49	10.5	10.9	11.5
	d	10.6	10.3	6.15	7.64	8.18	2.35
	k	0.0026	0.0018	0.00859	0.00271	0.00209	0.00666
Period	[Turns]	135.12	100.69	78.93	135.71	106.49	75.79

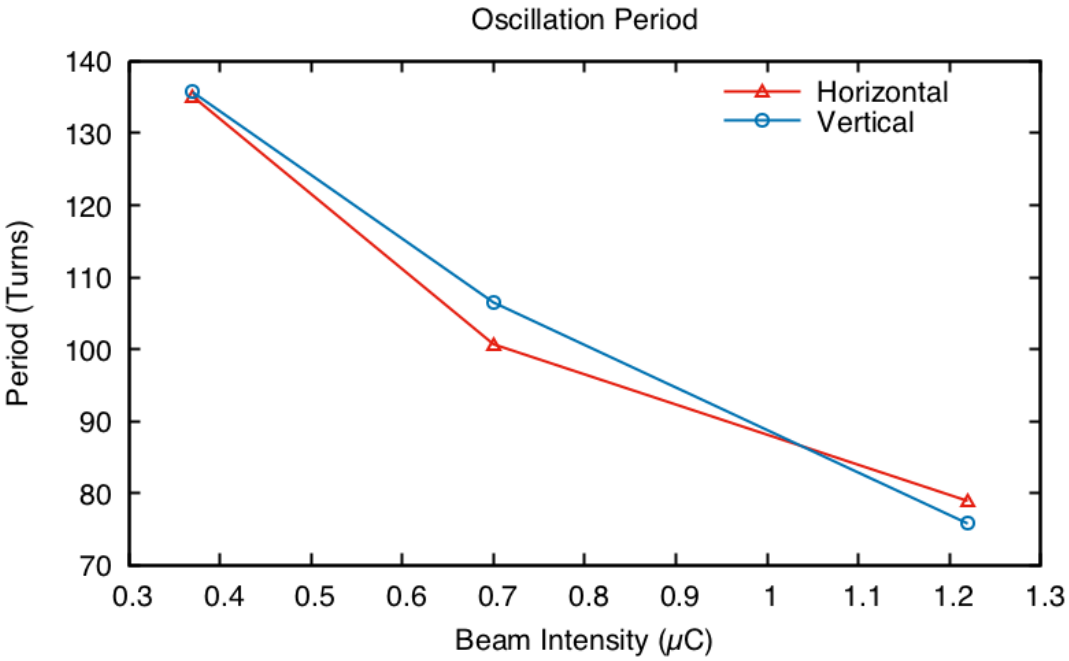

Figure 5.26: Oscillation period versus beam intensity for the equal tune cases in experiment three. The horizontal parameters are shown in red with '△' and the vertical parameters are shown in blue with '◯'.

systematic changes in the injection kickers. Second, the beam size and shape can change significantly if the extraction location during the beam evolution is altered. This could present an issue for satisfying beam-on-target requirements during production runs.

5.5 Conclusions

In experiment one, we used wire scanners to collect data for twelve different simplified accumulation beam configurations. We studied symmetric and asymmetric beams across six general tune points. We compared the results as profiles and emittances. We established nominal profile and emittance evolutions for split tune beams. We demonstrated that one transverse beam size could be altered without impacting the opposite transverse phase space in split tune beams. We established that equal tune beams have significantly different evolutions than beams with split tunes. The final equal tune profiles were peaked in the horizontal plane and had sloping edges in the vertical plane. Additionally, we demonstrated that the transverse beam profiles of equal tune beams were coupled. Any change to one plane would be carried over to the opposite plane. Finally, the equal tune beams demonstrated damped coupled oscillations between the two transverse emittances.

In experiment two, we used wire scanners to collect data for two different accumulation-followed-by-storage beam configurations. We established the existence of coupling at low intensities and documented coupling during storage. We showed that the coupling could create a complete exchange of both the profiles and the emittances during storage. By comparison with a similar beam configuration from experiment one, we demonstrated that continued accumulation dampens the amplitude and frequency of the oscillation.

In experiment three, we repeated experiment two using a new and more dynamic diagnostic device, the Electron Scanner. We confirmed the previously documented tune-dependent coupling effects. The new diagnostic device allowed us to collect more

data. This in turn allowed us to document multiple oscillations of both the profiles and the RMS beam sizes of an equal-tune beam at three different beam intensities. We demonstrated that the beam size and shape can change significantly if the extraction point is altered. Specifically, we presented the first experimental demonstration of a major profile shape change in a short time period due to coupling. Additionally, we were able to fit the stored beams with exponentially-damped sinusoids. The fit parameters showed that the oscillation period decreased with increasing beam intensity.

Our initial hypothesis was that the Montague resonance was the source of the coupling. However, experiment one demonstrated that the coupling starts much earlier than previously expected and dampens over time while the beam intensity is increasing. Experiment two confirmed and expanded upon these results, demonstrating that at low intensities the coupling could create a complete exchange in the transverse planes. Experiment three demonstrated that space charge forces damp the oscillations due to coupling in the beam. These results provided evidence contradictory to the original hypothesis and support the argument that the coupling is not due to a Montague resonance.

Chapter 6

SNS Production-Style Experiment

In Chapter 5, we began our investigation into the coupling by studying a simplified accumulation beam. Specifically, we simplified the injection process by removing injection painting, which might have concealed the source of the coupling. We also isolated the effects of space charge and tune split by using the sextupoles to reduce the chromatic effects. We were able to demonstrate several important results through three extensive experiments. First, the coupling was tied to an equal tune resonance. This was the only result which matched our original hypothesis. Second, the beam geometry did not have a significant impact on the coupling. Third, the effect of the coupling decreased with increasing beam intensity. Finally, the coupling could create full emittance exchange if the beam was stored at low intensities. Together these results suggest that the coupling is not due to a Montague resonance.

The next step in our investigation was to study the coupling of a beam with the full SNS production-style configuration. In Chapter 6 we follow a similar experimental procedure as described in Chapter 5, however, we use the most recent SNS production settings. In doing so we return to the initial motivation of this research, understanding, and mitigating the coupling effects seen during the regular production operations. In addition to studying the effects of tune on the coupling, we also study the effects of the skew quadrupoles.

In Section 6.1 we review the differences between the simplified accumulation experiment and the SNS production-style experiment. In Section 6.2 we review the experimental results. Finally, in Section 6.3, we summarize the results of the production-style experiment. This final experiment is essential to the recommendations we will present in Chapter 8 for mitigating the coupling.

6.1 Configuration

In this section we discuss the variation in beam configuration between the simplified accumulation experiments described in Chapter 5 and the final experiment described here. We specifically highlight the added complications present for an SNS production-style beam.

In this experiment, we use the SNS production run configuration. The beam is not stored. The injected beam intensity is ramped during the first 98 turns of accumulation. The nominal SNS dual-plane injection painting is used to produce a final beam with a flat-topped transverse profile with well-defined sides. The dual harmonic ring RF is used to limit the spread of the beam longitudinally and produce a final beam with a flat-topped longitudinal profile with well-defined sides. Finally, we allow for a natural beam chromaticity by not using the ring sextupoles. An overview of the precise beam settings for this experiment is documented in Table 6.1.

For this experiment, the beam size is larger and the final accumulated beam intensity is an order of magnitude higher than in the previous Electron Scanner experiment. Due to these changes, the vertical Electron Scanner had trouble viewing the entire beam. This limitation caused problems for most of the data acquisition. The horizontal aperture does not have the same restriction, as noted in Chapter 4. Therefore, the horizontal Electron Scanner was able to capture the entire beam up to turn 850. As a result of this, only the horizontal data will be presented. However, any coupling effects seen in the horizontal RMS size and profile evolutions would be mirrored in the vertical data.

Table 6.1: Beam Configurations for Experiment Four

Primary Diagnostic Device	Electron Scanner (Located between QTH_D13 and QTV_A01 in the Ring)			
Accumulation & Storage	Production-Style Accumulation			
Shift Date	November 16th, 2015			
Beam Tune	Production Tune		Equal Tune	
Q_x	6.20357	6.20432	6.16923	6.16398
Q_y	6.15914	6.16233	6.16907	6.16666
ΔQ	0.04443	0.04199	0.00016	-0.00268
Injection Kickers	Painted down from 100% to 48% in 1000 μseconds following one minus the square root of the number of turns			
Beam Geometry	Asymmetric			
X Injection Size	17.5 mm			
Y Injection Size	8.8 mm			
Turns of Accumulation	Ramped accumulation for 98 turns, followed by Full intensity accumulation of up to 878 turns			
Scan Steps	40 longitudinal slices collected every 10 turns starting at turn 5			
Maximum Intensity	Nominal 4.4e13 ppp 7.0 μC			
Beam Energy	939.5 MeV			
Ring RF	First Harmonic with an amplitude of 8.6kV and phase of 44.4° Second Harmonic with an amplitude of 5.0kV and phase of -155.0°			
Ring Pattern Width	47%			
Ring Chromaticity	Natural (Sextupoles Off)			
Skew Quadrupoles	On	Off	On	Off

Tune The production betatron tune was ($\nu_x = 6.20,\ \nu_y = 6.16$) with $\Delta\nu \approx 0.042$. We refer to this configuration as the production tune configuration. The second tune for this experiment was selected to be ($\nu_x \approx \nu_y \approx 6.17$). We refer to this configuration as the equal tune configuration.

Geometry The last production settings were for an injection size of (17.5 mm, 8.8 mm). The nominal production injection offset is cited as and expected to be approximately (30 mm, 30 mm) [31]. However, the operators have strayed from this expected beam during the production tune up. The smaller asymmetric production beam is much closer to the simplified beam previously used in the Electron Scanner.

Energy and Intensity The nominal beam energy during our experiment was 939.5 MeV. The production beam had 878 turns of full intensity injected beam with an additional 98 turns of ramping intensity beam. The final data presented goes to turn 850, which equates to a final accumulated beam intensity of approximately 4.4e13 ppp or 7.0 μC. Figure 6.1 compares the configurations of this experiment with the simplified accumulation configurations.

Skew Quadrupoles The nominal production configuration also consisted of several skew quadrupoles correctors. As mentioned in Chapter 5, skew quadrupoles are designed to allow the reduction of any lattice coupling that might be present. The following skew quadrupoles correctors were set to -5.3 A, producing a field of -0.025 T: QSC_A01, QSC_A03, QSC_A05, QSC_A07, QSC_A09, and QSC_D09. These skew quadrupoles were used during the initial SNS power up in 2006 - 2007 to correct for x-y coupling believed to be caused by strong higher order multipole modes in the injection region[74].

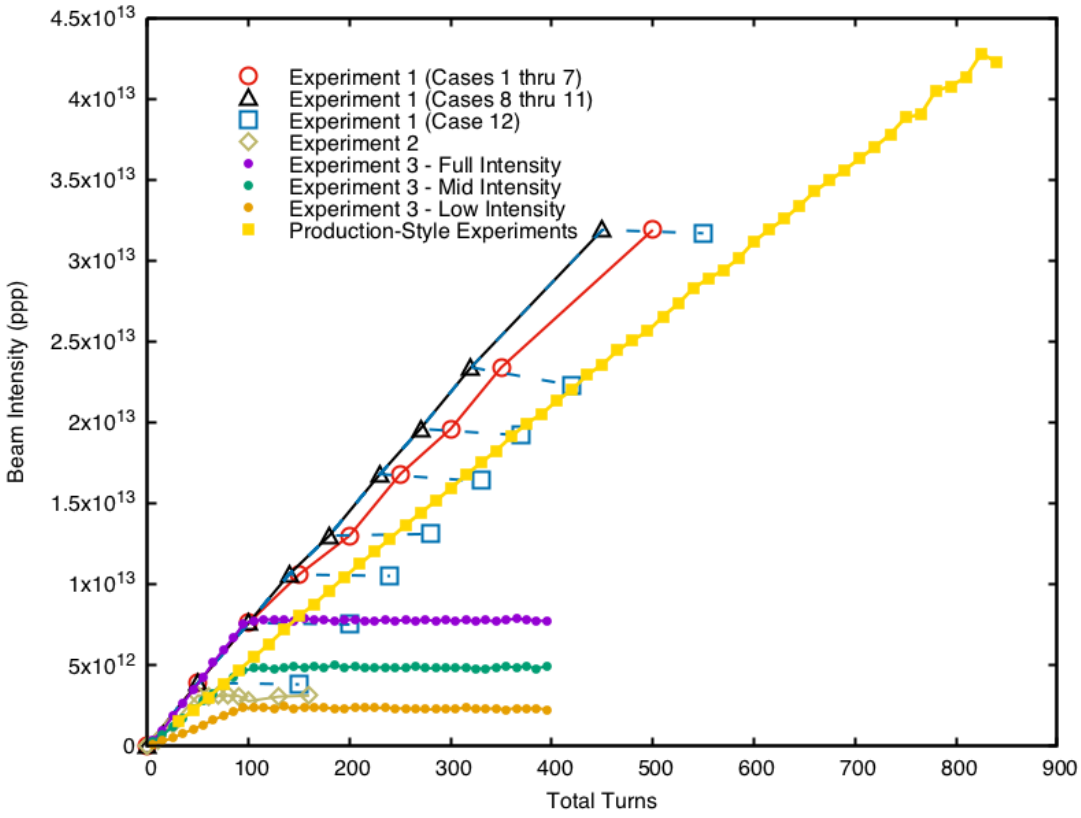

Figure 6.1: Comparison of configurations for both simplified accumulation and production-style experiments. The beam intensity is shown on the vertical axis and the total number of turns are shown on the horizontal axis. The split-tune accumulation-only configuration for cases 1 through 7 of experiment one are shown with a solid red line with '◯' points. The equal-tune accumulation-only configuration for cases 8 through 11 of experiment one are shown with a solid black line with '△' points. The accumulation extended with storage configuration for case 12 of experiment one is shown with dashed blue lines with '□' points. The stored beam configuration of experiment two is shown with a brown line with '◇' points. The three intensities of experiment three are shown with solid lines with '●' points. The intensities are nominal (purple), mid (green), and low (gold). The production-style experiment configurations are shown with a solid yellow line with '■' points. Lines indicate the evolutionary path followed for each data point, and markers indicate the relative location of data collection. Sloped lines indicate periods of accumulation and flat lines indicate periods of storage.

6.2 Results

In this section we review the experimental data for our production-style beam study. First, in Section 6.2.1, we will examine the effects of tune on production-style beams. We expect these results to parallel with those of experiment three in Section 5.4.2. Finally, in Section 6.2.2, we will examine the effects of the skew quadrupoles on production-style beams by comparing cases with and without skew quadrupoles for both tunes. Our primary use of skew quadrupoles has been to remove linear coupling in the single injected mini-pulse during configuration. The results of Chapter 5 indicate that the coupling is not caused by a Montague resonance. This raises the question of whether the skew quadrupoles would be able to relieve linear lattice coupling and, if not, what impact they were actually having on the coupling.

6.2.1 Effect of Tune

Figure 6.2 shows the horizontal RMS size evolution for both tune configurations without skew quadrupoles for the production-style experiment. As we saw in Section 5.4.2, the beam sizes are altered by the coupling. An equal tune configuration will have a decreased horizontal beam size and an increased vertical beam size in comparison to a split tune configuration with the same injection offsets. We see the same trend with the production-style configurations. Additionally, both production-style configurations display an expected slow increase in the RMS size during the continued accumulation. This increase is due to the production-style injection kicker waveform and increasing beam intensities during accumulation.

Figure 6.3 shows the horizontal profile evolutions for the same production-style configurations. While the horizontal RMS sizes follow a similar evolution for both tune configurations, the profile evolutions are not similar. The production tune profiles maintain a small hollowness even at the end of the evolution. However, the equal tune profiles become centrally peaked even at lower intensities. A similar effect was demonstrated in Section 5.4.2, where the split tune configurations were

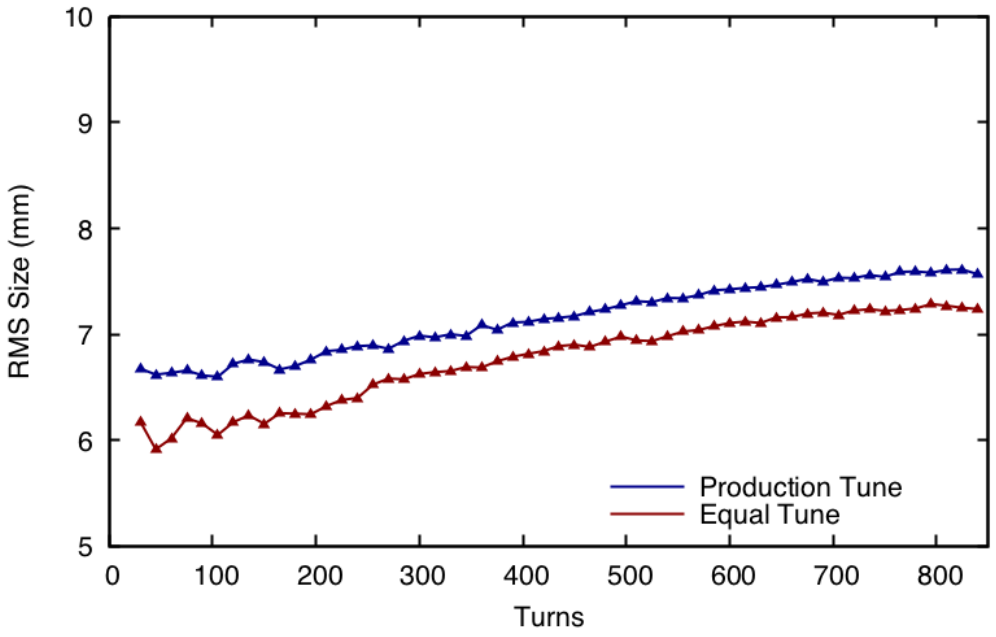

Figure 6.2: Comparison of the RMS beam sizes for the production tune (dark blue) and equal tune (dark red) configurations without skew quadrupoles for the production-style experiment.

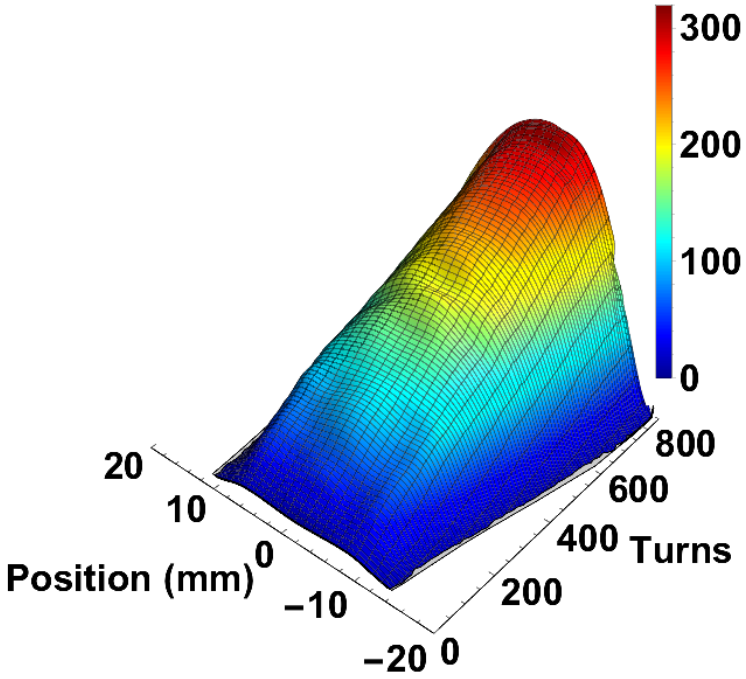

Equal Tune

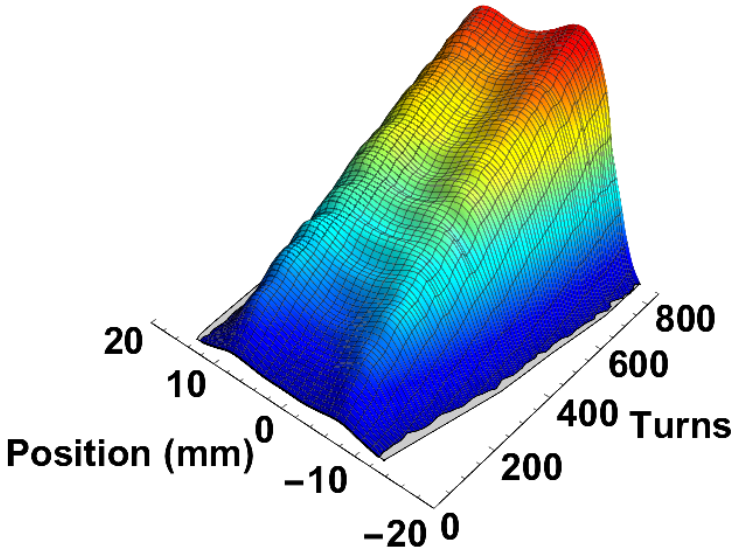

Production Tune

Figure 6.3: Horizontal profile evolutions are shown for the production-style experiment configurations without skew quadrupoles. The equal tune case is shown on the top and the production tune case is shown on the bottom.

shown to maintain the shape of their initial profile much longer than the equal tune configurations.

6.2.2 Effect of Skew Quadrupoles

The skew quadrupoles are used in order to reduce any coupling present in the beam. This correction is done by monitoring the turn-by-turn oscillations of a single injected mini-pulse and adjusting the skew quadrupole strengths. It was our expectation that using the skew quadrupoles would reduce the effects of linear lattice coupling seen in the final distribution of the beam. The question becomes what effect they had on the coupling in the production-style beams.

Figure 6.4 shows the RMS size evolution for the equal tune configurations with and without skew quadrupoles. While the general evolution of the RMS size is similar, the configuration with skew quadrupoles displays an additional level of coupling. This coupling appears as a small damped oscillation about the configuration without skew quadrupoles. Figure 6.5 compares the equal tune horizontal profile evolutions. We can see that this additional coupling appears as a rapid change in the shape and peak intensities of the profile evolution. In this experiment, the skew quadrupoles did not eliminate the primary effects of the coupling. We still see a centrally peaked profile at high intensities. This result is contrary to our expectations for the effects of the skew quadrupoles. In fact, they complicated the evolution of the coupling by adding a small damped oscillation. Additionally, the overall effect of the skew quadrupoles on the beam evolution was minor compared to the overall impact of the tune change.

Figure 6.6 shows the RMS size evolution for the production tune configurations with and without skew quadrupoles. The shifts in RMS sizes along the evolution of the production tune configuration with skew quadrupoles is a result of trying separate Electron Scanner configuration settings for different ranges of accumulating proton beam intensity. This was the first dataset collected during the production-style experiment. Prior to the shift, we made the decision that different settings would allow

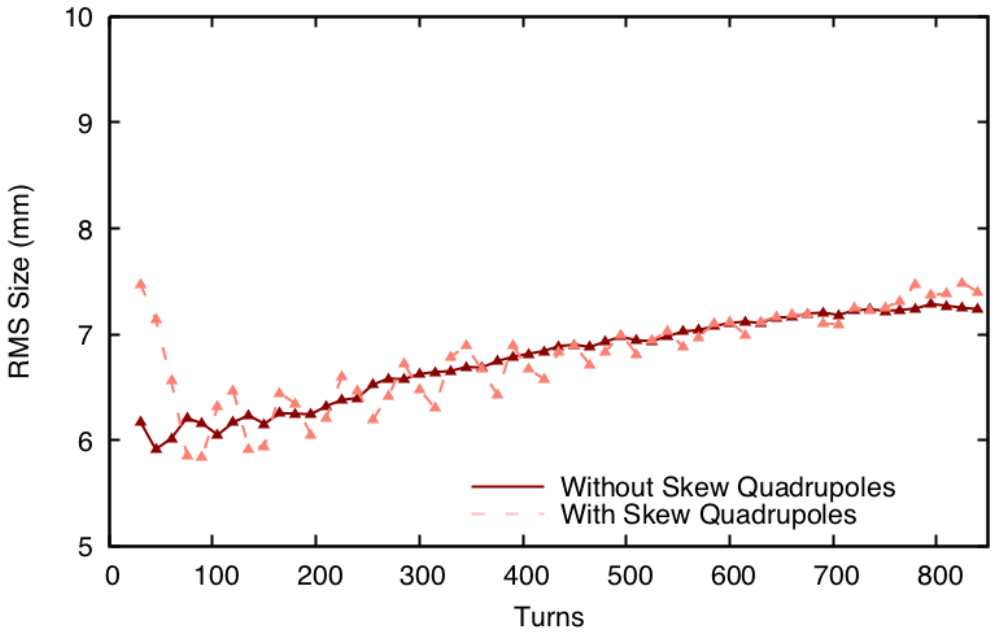

Figure 6.4: Comparison of the RMS beam sizes for both equal tune configurations of the production-style experiment. The configuration without skew quadrupoles is shown as a solid dark-red line and the configuration with skew quadrupoles is shown as a dashed light-red line.

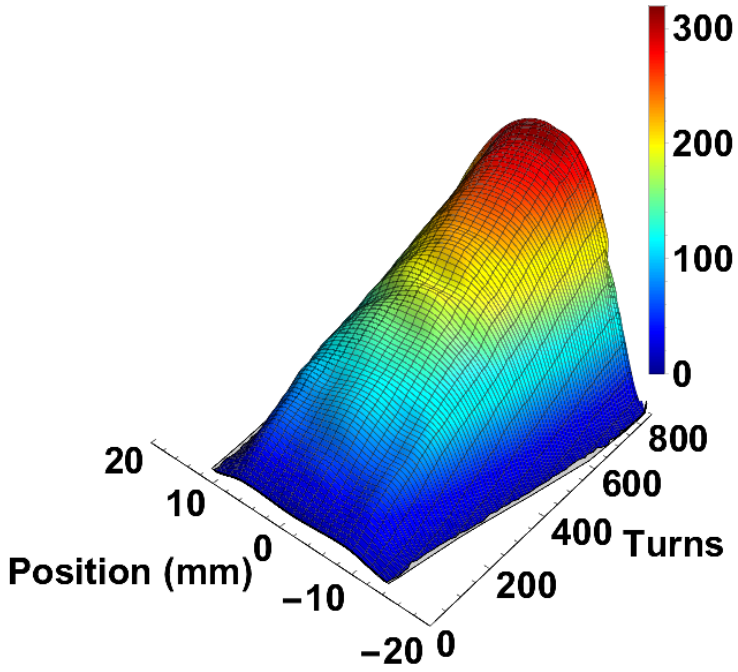

Without Skew Quadrupoles

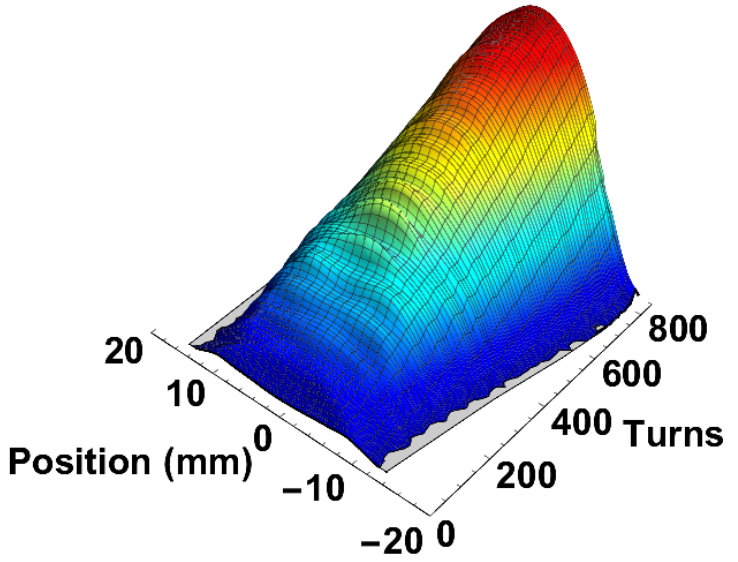

With Skew Quadrupoles

Figure 6.5: Horizontal profile evolutions are shown for both of the equal tune configurations of the production-style experiment. The configuration without skew quadrupoles is shown on the top and the configuration with skew quadrupoles is shown on the bottom.

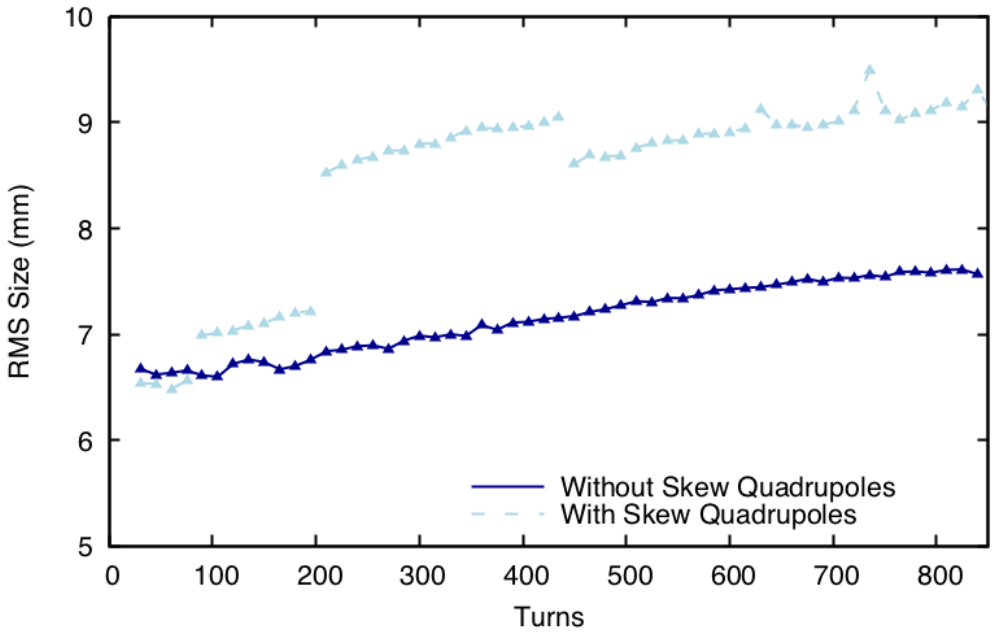

Figure 6.6: Comparison of the RMS beam sizes for both production tune configurations of the production-style experiment. The configuration without skew quadrupoles is shown as a solid dark-blue line and the configuration with skew quadrupoles is shown as a dashed light-blue line.

us to best capture the beam over the wide range of proton beam intensities. On-shift analysis showed us that this was not as helpful as we originally anticipated and that it could be difficult to directly compare the beam at different Electron Scanner settings. The other production-style experiment datasets were captured with a single Electron Scanner setting. Despite the effects of the different Electron Scanner settings for the configuration with skew quadrupoles, both cases follow similar trends of steady increasing RMS sizes. Figure 6.7 compares the production tune horizontal profile evolutions. Again, despite the effects of the different Electron Scanner settings, the general shape of the profile is consistent throughout the accumulation of the beam. We can see in comparisons of both the RMS size and profile evolutions that the skew quadrupoles had little to no effect on the uncoupled production tune configuration.

6.3 Conclusions

In our final experiment, we used the Electron Scanner to study the production-style beam. This experiment repeated the general procedure of the third experiment presented in Chapter 5. We studied the same asymmetric beam geometry for four total configurations, two different tunes both with and without skew quadrupoles. The first tune configuration had a large tune split and was used during the last production run. The second tune configuration was for an equal tune beam. We compared the results through the evolution of horizontal RMS sizes and profiles.

It is important to note that the effects of the coupling were weaker due to the combined impact of continued accumulation and the production-style injection painting. Based on the results presented in Chapter 5, we expected the coupling to decrease with continued accumulation. As shown in Figure 6.1, the production-style beam intensities are generally much higher than those previously explored using the Electron Scanner. Therefore, it is not surprising that the coupling effects continued to tapper off at higher beam intensities. The production-style injection painting schema was designed to create a flat-topped beam, as is seen in split-tune horizontal profiles

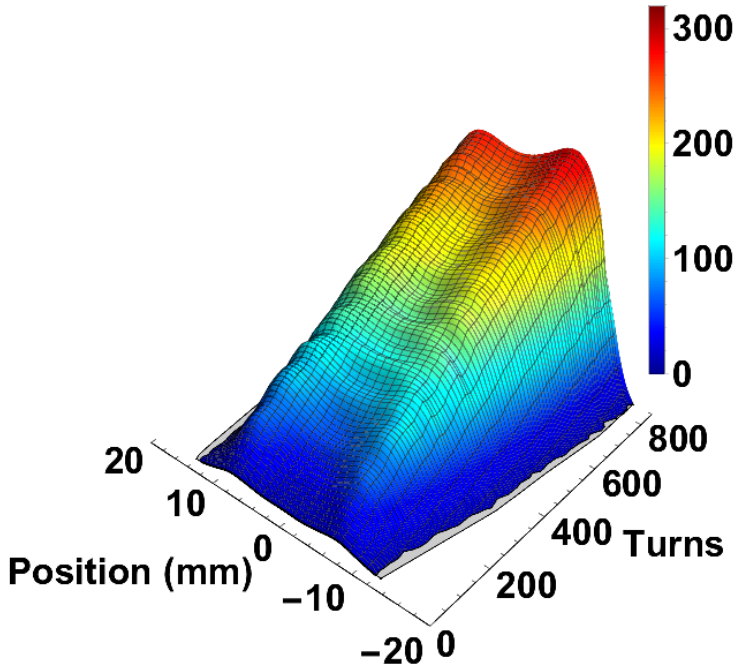

Without Skew Quadrupoles

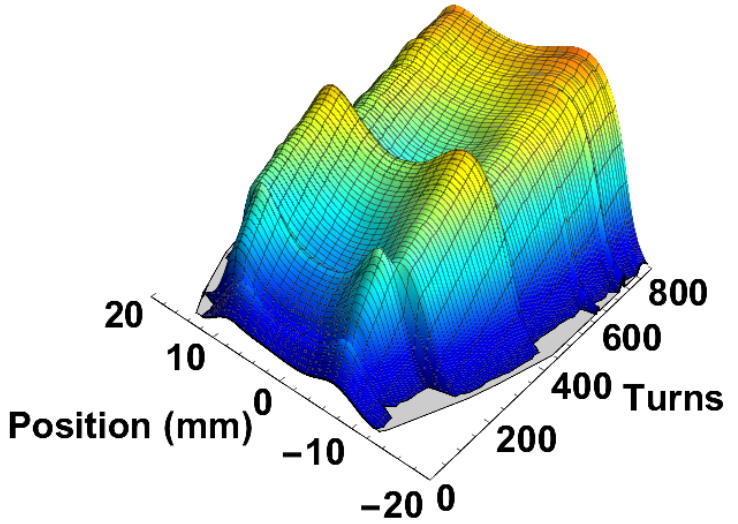

With Skew Quadrupoles

Figure 6.7: Horizontal profile evolutions are shown for both of the production tune configurations of the production-style experiment. The configuration without skew quadrupoles is shown on the top and the configuration with skew quadrupoles is shown on the bottom.

shown in Figure 6.7. Therefore, it would not be surprising if the production-style injection painting also masked some of the coupling later in accumulation, where it deviates from the previously used flat-topped injection kickers. As we did not explore the injection painting as an experimental parameter in Chapter 5, it is difficult to separate the effect of changing the injection painting scheme from the effect of continued accumulation.

In section 6.2.1, we showed that the equal-tune production-style beam quickly became centrally peaked due to the coupling effect. Over the same period of accumulation, the split-tune production-style beam remained slightly hollow. Both tune configurations displayed the same slow increase in RMS beam sizes. Therefore it is harder to determine whether the RMS beam sizes were coupled in the equal tune configuration. As we showed in experiment one in Section 5.2.2 and in experiment three in Section 5.4.2, continued accumulation at a high beam intensity dampens the oscillations due to coupling. This implies that the coupling of the RMS beam size for a high intensity accumulating beam may be difficult to detect under any circumstance. This reinforces our rationale for having first studied a beam under simplified accumulation configurations and using low intensity stored beams.

In section 6.2.2, we examined the effect of the skew quadrupoles. We expected the skew quadrupoles to have a large impact on the evolution of the beam by removing the coupling. We were able to show that the skew quadrupoles only produced small damped oscillations in the coupled evolution of the beam. The subtle nature of this coupling emphasizes the importance and unique diagnostic attributes of the Electron Scanner. It is important to note that it is possible that the skew quadrupoles may have simply been set incorrectly to remove the coupling. Without investigating an array of skew quadrupole setting, we can not establish whether the skew quadrupoles would have been capable of removing the coupling. Additionally, the decreased effect of the skew quadrupoles may have been due to the effects of continue accumulation and production-style injection offset. However, we did demonstrate that the skew quadrupoles were capable of introducing a new coupling on a smaller scale than

previously seen. This coupling created oscillations that were seen in the horizontal RMS size and profile evolutions.

In summary, experiment four corroborates the primary results presented in the first three experiments. The coupling is present at low intensities and has a strong and quick impact on the evolution of equal tune beams. Additionally, the strength of the coupling does not amplify with increasing beam intensity, but instead decreases. This result continues to indicate that the source of the coupling is not a Montague resonance. This experiment added insight by comparing the evolution of the coupling with and without skew quadrupoles. Skew quadrupoles are normally used to remove coupling of the single injected mini-pulse. We demonstrated that the use of skew quadrupoles actually complicates the coupling present during the evolution of the accumulating equal-tune beam. When skew quadrupoles are not used, the coupling still impacts the evolution of the equal tune beam but the profile oscillations are removed.

Chapter 7

PyORBIT Simulations

This chapter is devoted to simulations of the simplified accumulation followed by storage experiment conducted using the Electron Scanner in Section 5.4. This experiment was chosen because it has a simplified configuration that should allow it to be more easily and accurately simulated. Additionally, the Electron Scanner should provide a rich source of data for comparison with simulations. In Section 7.1, we will review several important aspects of particle accelerator simulations, such as modeling space charge and fringe field effects. In Section 7.2, we will present the specific configuration values used in these simulations. In Section 7.3, we will compare the results from simulation with those from experiment. We will also present two brief simulation studies into the dynamics of the coupling resonance. Finally, in Section 7.4, we will conclude the important points from our efforts to simulate this experiment.

7.1 Background

The Python-based Objective Ring Beam Injection and Tracking (PyORBIT) is a particle tracking code originally created and developed for use in designing, optimizing, and understanding the SNS accumulator ring[22]. PyORBIT is a particle-in-cell (PIC) tracking code that transports interacting macro-particle bunches through a series of nodes representing optical elements, dynamic effects, and diagnostics that

occur in the accelerator lattices[44, 69, 86]. PyORBIT is designed to provide realistic self-consistent beam dynamics calculations in high-intensity rings[43]. In accelerator physics, self-consistency refers to simulations where the distribution of particles is not fixed, but evolves during the simulation.

PyORBIT is written in C++ and utilizes Message Passing Interface (MPI)[21] protocols for parallel processing. PyORBIT is accessed through a python shell and user-configured python scripts[85]. In each script, the user defines beam parameters, such as particle species, beam energy, beam intensity, and the number of particle per injected pulse. The user imports a realistic accelerator lattice, typically designed using Methodical Accelerator Design (MAD)[25]. The user can then use PyORBIT to import an externally created beam distribution, initiate a specified beam distribution, or inject particles of a specified distribution on a turn-by-turn basis. The user then defines the injection configuration, space charge dynamics, RF cavities, diagnostic nodes, and other specialized nodes and distributes these appropriately in the lattice. When the simulation has been properly configured, particles are transported through the lattice and, if necessary, iterated according to the user's script. Transportation of the particles is carried out through second-order symplectic matrix multiplication of all linear elements, where nonlinear effects are interpreted as kicks interspersed between linear elements[45]. In computational physics, symplecticity refers to simulations, or integrators, that maintain the long-term validity of the Hamiltonian system. This requirement results in the determinant of the transportation matrix equaling one, i.e. the conservation of phase space area[7]. Therefore, symplecticity is essential for single particle tracking. However, space charge and impedance effects are non-symplectic, so symplecticity can be less important for short PIC simulations. Symplecticity can still play an important role in long PIC simulations where the objective is error mitigation and management.

While there are a number of modules to simulate various dynamic effects, special focus is given by the developers to the calculation of space charge forces. This is due to the role space charge forces play as a collective effect in defining the overall

beam dynamics. It is common to characterize accumulator rings and synchrotrons by separating the longitudinal and transverse dynamics. At the SNS, our longitudinal beam size is on the order of 100 m while our transverse beam size is on the order of 10 cm. Additionally, the longitudinal tune is on the order of 10^{-3} while our transverse tunes are roughly 6.2. Both the physical scale and the phase space oscillation frequency are orders of magnitude different. Therefore, splitting these dynamics is a reasonable approximation for the study of space charge effects.

PyORBIT has 2D, 2.5D and 3D space charge modules. Figure 7.1 illustrates how the beam distribution is binned for each module. All of the modules are implemented as a series of transverse kicks distributed between regular lattice elements. For the 2D module, the particles are binned in a 2D transverse rectangular grid using a bilinear distribution assignment to adjacent mesh points. To reduce the number of operations that are performed during each simulation, the method selected utilizes fast Fourier transforms (FFT) for their computational speed. The FFT of the space charge forces at the mesh points is obtained through the convolution of the FFT of the particle density with the force due to a unit charge. In order to avoid aliasing errors, a sufficient number of mesh points must be used to ensure the FFT accurately represents the charge distribution. Conducting beam pipe walls are imposed as a boundary condition. The inverse FFT provides the space charge forces on the mesh points. The forces on the mesh points are then weighted based on the local longitudinal density to account for bunching. Particle kicks are then obtained as a bilinear interpolation of the forces at the mesh points to the location of the macroparticles.[32, 45, 75]

The 2.5D space charge module follows the same procedure as the 2D space charge module, but replaces the single 2D grid with a series of 2D grids slicing the beam longitudinally. After the charge is binned into each slice using the local longitudinal charge density, the potential is solved on each slice using the same method as before. The conducting beam pipe is used to connect the 2D potential slices into a 3D potential grid. The final momentum kicks are then determined by interpolating in the 3D grid to the location of the macroparticle. We call this module '2.5D' because it is

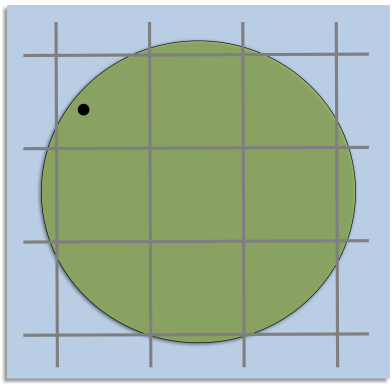

2D Space Charge

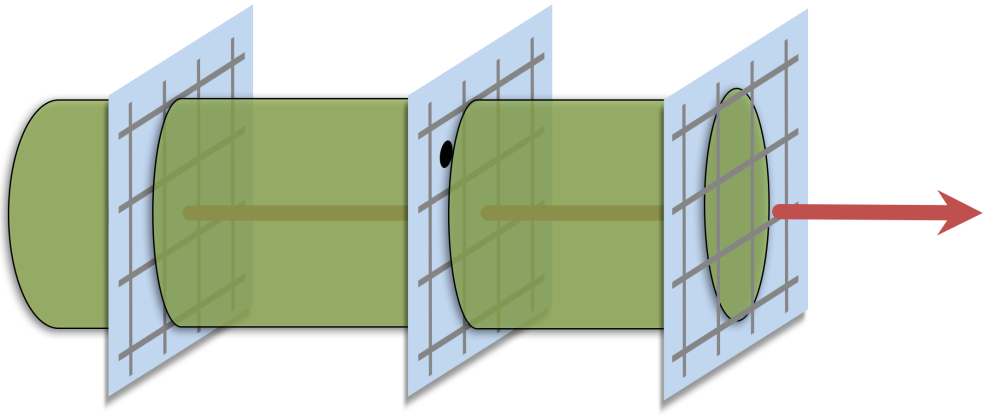

2.5D Space Charge

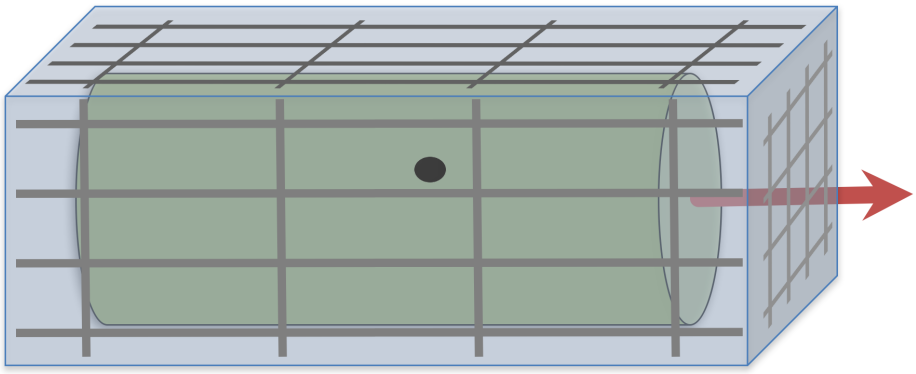

3D Space Charge

Figure 7.1: Diagrams of the 2D, 2.5D, and 3D particle-in-cell space charge modules. The beam is shown in green, with a sample particle shown in black. The space charge grid is shown in blue with grey lines.

a hybrid of the 2D and full 3D modules. The 3D module computes the particles in a full 3D grid using the same methodology used in the 2D module. The 2.5D and 3D space charge modules have been shown to be in agreement with each other and with analytic calculations[46]. Additionally, the 2.5D space charge module has been used to accurately simulate and further understand the beam profile at the Los Alamos Proton Storage Ring[23].

As previously mentioned, another important effect in the study of accelerators are fringe fields. In MAD, fringe fields are calculated using

$$\text{FINT} = \int_{-\infty}^{\infty} \frac{B_y(s)\big(B_0 - B_y(s)\big)}{2 \cdot \text{HGAP} \cdot B_0^2} ds \tag{7.1}$$

where FINT specifies the extent of the fringe fields to be modeled, HGAP refers to half the gap distance between adjacent magnets, s is the perpendicular distance measured from the entrance face of the magnet to the point in question, $B_y(s)$ is the magnitude of the fringing field on the magnetic mid-plane at a position s, and B_0 is the asymptotic value of $B_y(s)$ well inside the magnet entrance[6]. A value of zero for FINT indicates that the software should use a hard-edge approximation of the field. Other common values for FINT include 1/6 for a linear field drop off and 0.45 for a 'square-edged' non-saturating magnet.[19, 25] PyORBIT allows users to specify which magnet types have fringe fields and calculates those fringe fields using a linear field drop off.

Studies have been conducted demonstrating the modeling parameters necessary to obtain numerical convergence[45, 85]. Furthermore, confidence has been established that the PyORBIT code correctly simulates the beam transportation and evolution[14, 46, 82, 85, 87]. However, with each new experiment, it is important to confirm that the simulations agree with the data collected for a benchmark case. Agreement between the simulated beam and an ample amount of measured profile data is sufficient to provide confidence in the accuracy of the simulated results. This will be an important part of our results section.

7.2 Configuration

We are simulating the simplified accumulation followed by storage experiment conducted using the Electron Scanner, which was presented in Section 5.4. We followed the general configuration presented in that section with additional details as noted below. The simulations include turn-by-turn injection, injection foil scattering, symplectic nonlinear tracking through the ring lattice, RF bunching, and 3D space charge modeling. Fringe field effects were used. An overview of the configurations for the PyORBIT simulations are located in Table 7.1. The results of are presented in Section 7.3.

Tune The experimentally measured tunes were used as initial parameters in the MAD script to generate the accumulator ring lattice. The lattice and matching tunes are used as the basis of the PyORBIT simulation. In order to check that the MAD lattice produces the correct tunes, a simple PyORBIT simulation is run where a single turn of beam is injected into the accelerator and stored for 300 turns. During this storage, the Beam Position Monitor (BPM) diagnostic data is recorded. Analysis of the beam oscillations recorded in the BPM data allows an accurate calculation of the tunes modeled within PyORBIT. These tunes are then used to iteratively adjust the MAD script until the PyORBIT simulations produce the correct tunes. During this study, it was noted that the PyORBIT tunes around the equal tune resonance were especially sensitive to unusually small variations in the initial MAD tunes. A brief study of the sensitivity of the tune split is presented in Section 7.3.4.

Geometry The beam was simulated using the experimentally measured injection offsets. An important aspect of beam injection in the SNS is properly modeling the interaction of the beam with the injection foil. This was modeled using the full scattering capabilities of the collimation module. This module takes into account effects due to ionization energy loss, small angle coulomb scattering, Rutherford scattering, and nuclear elastic and inelastic scattering.

Table 7.1: Beam Configurations for PyORBIT Simulations

Accumulation & Storage	Accumulation Followed By Storage				
Beam Tune	Split Tune	Middle Split Tune	Equal Tune		
Q_xSim	6.209072	6.200439	6.199439		
Q_ySim	6.168656	6.191879	6.197816		
$\Delta QSim$	0.040416	0.008560	0.001623		
Injection Kickers	Flat-topped Waveform				
X Waveform Amplitude	0.648	0.631	0.635		
Y Waveform Amplitude	0.838	0.826	0.798		
X Injection Offset	48.60 mm				
Y Injection Offset	46.00 mm				
Beam Geometry	Asymmetric				
Turns of Accumulation	100				
Turns of Storage	300				
Number of Macro Particle Injected Per Turn	10,000				
		Nominal		Medium	Low
Maximum Intensity	7.42e12 ppp	7.51e12 ppp	7.60e12 ppp	4.36e12 ppp	2.29e12 ppp
	1.19 μC	1.20 μC	1.22 μC	0.70 μC	0.37 μC
Space Charge	3D Module with 256 x 256 transverse bins and 64 longitudinal bins				
Beam Energy	939.5 MeV				
Ring RF	Shorted				
Ring Pattern Width	39%				
Ring Chromaticity	Zeroed				

Energy and Intensity The beam was simulated with the experimentally measured energy and intensities. The beam was accumulated for 100 turns and stored for an additional 300 turns. This was simulated by injecting 10,000 macro particles per turn and storing the approximately 10,000,000 particles in the final distribution for an additional 300 turns. This number of macro particles is more than sufficient for numerical convergence and provides a high resolution simulation. The space charge interactions of the macro particles were modeled in 3D using 256 bins in each of the transverse directions and 64 bins longitudinally. The default beam pipe in the space charge module was set as circular with a radius of 110 mm. Collimation regions and sections of beam pipe were modeled to remove stray particles.

7.3 Results

In this section we review the results of our simulations. First, we will examine the effect of tune on the beam dynamics and attempt to establish a benchmark for the simulations. Then, we will examine the effect of beam intensity on the coupled beam. Finally, we will use the increased accessibility provided with simulations to study the sensitivity of key parameters. An investigation into the importance of fringe fields indicates the source of the resonance. Additionally, an investigation into the sensitivity of the tune split demonstrates the difficulty of accurately modeling resonances.

7.3.1 Effect of Tune

Prior to examining the results of new simulations around the resonance, it is important to make sure that we are correctly modeling the dynamics outside of the resonance. Outside of the resonance, we expect a strong agreement between simulation and experiment in both the profile and emittance evolutions. Our expectations for how

well we can model the resonance will be based on our ability to benchmark the split tune cases.

Figure 7.2 shows the horizontal and vertical profile evolution for the split tune (top row), middle split tune (middle row), and equal tune (bottom row) configurations. This figure shows the simulated results corresponding to the experimental results documented in Figure 5.22. For the split tune cases, the simulated horizontal profiles show similar hollowness to what was seen experimentally, with the addition of a few localized peaks. These localized peaks follow the placement of single minipulses during their oscillation in phase space. This was also seen in low intensity wire scanner profiles in Section A.1. Towards the end of the simulations, we do see the profiles fill in as they did experimentally. The vertical profiles are narrow peaks, as we expected based on the small vertical injection offsets. These dynamics fit the overall behavior that we expect during nominal beam evolution.

For the equal tune case, the coupling is not clearly visible in the horizontal profiles. While we would have expected to see strong oscillations in the horizontal profiles, this might be due to the large horizontal beam size. However, the vertical profile demonstrates the same strong profile oscillation that is seen in the experiment. This topic of matching the oscillations for the equal tune case will be discussed again when we view the emittance profiles.

Figure 7.3 shows the evolution of the horizontal and vertical emittances for the split tune (top), middle split tune (middle), and equal tune (bottom) configurations. This figure shows the simulated results corresponding to the experimental results documented in Figure 5.23. For the split tune cases, we see a strong agreement in the evolution of the beam. Any difference in the value of the split tune emittances is due to a discrepancy between the experimental and simulated injection offsets. In this study, we allowed for small adjustments of the injection parameters to more closely match the emittances in the split tune case. These injection parameters were then used for the other configurations.

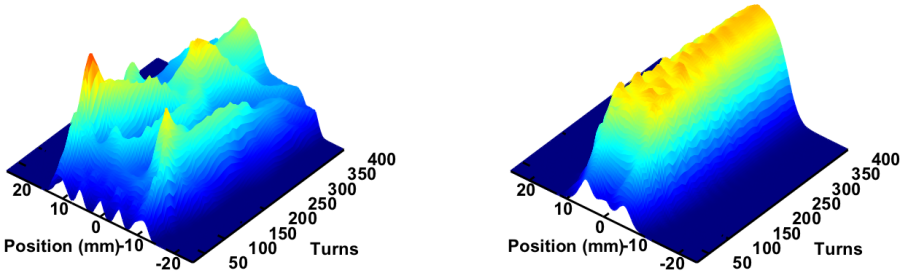

Split Tune Beam (7.42e12ppp)

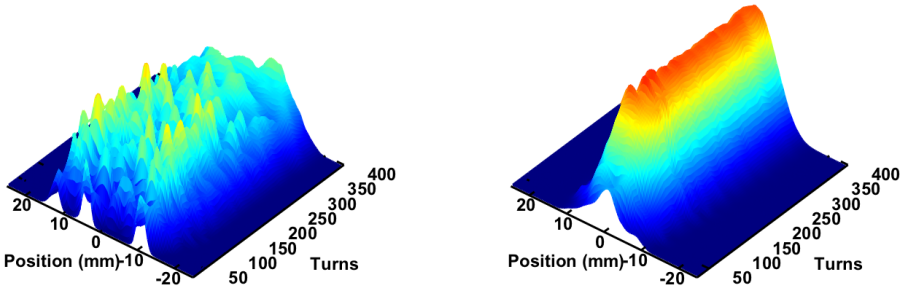

Middle Split Tune Beam (7.51e12ppp)

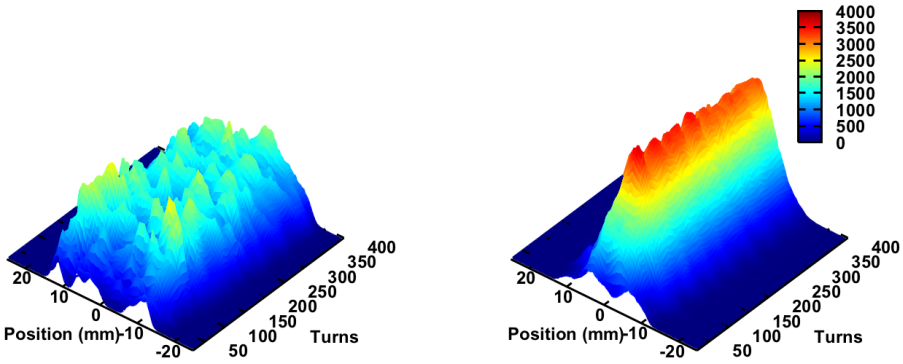

Equal Tune Beam (7.60e12ppp)

Figure 7.2: Simulated profile evolutions for the split tune (top row), middle split tune (middle row), and equal tune (bottom row) configurations. The horizontal evolutions are shown on the left and the vertical evolutions are shown on the right.

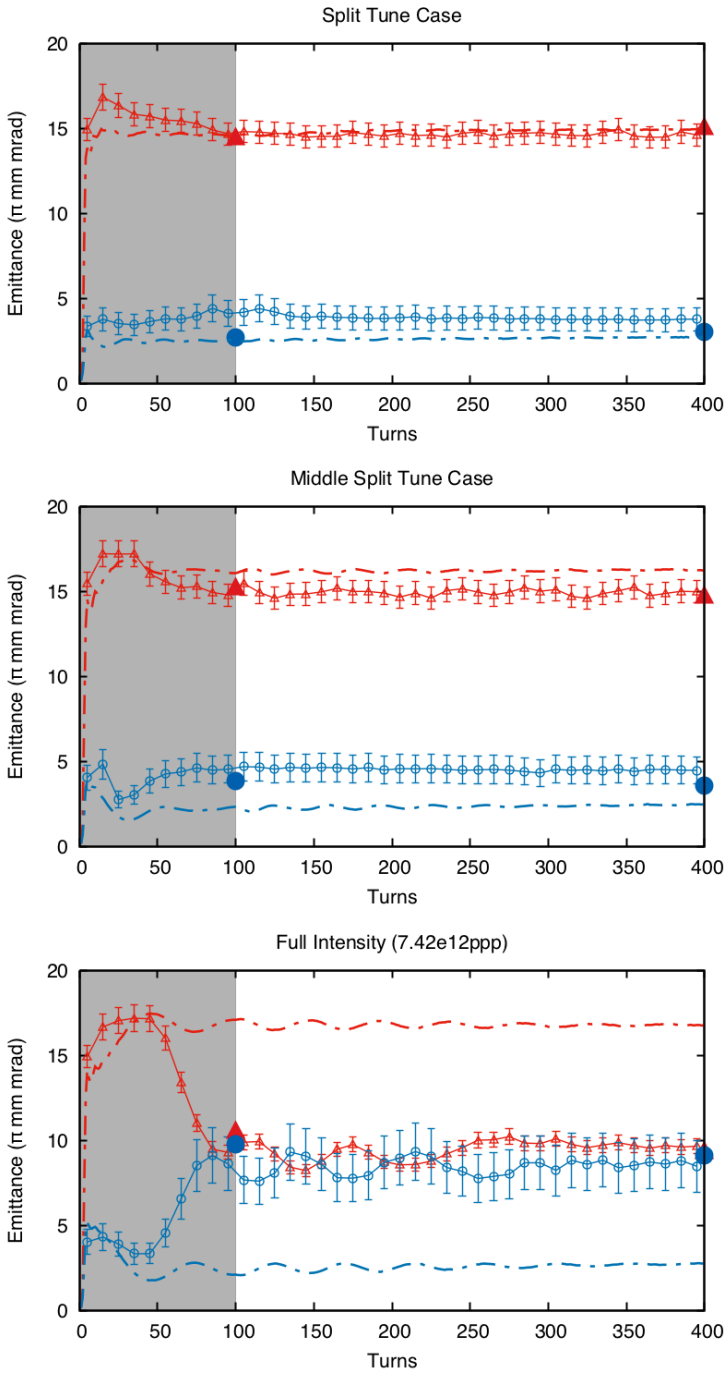

Figure 7.3: Emittance evolutions for the split tune (top), middle split tune (middle), and equal tune (bottom) configurations. The simulations are shown with dash dotted lines without points. The Electron Scanner data is shown with connecting lines and hollow data points. The wire scanner data is shown as solid data points without lines. The horizontal experimental data is shown with solid red lines with '▲', and the vertical experimental data is shown with solid blue lines with '●'.

For the equal tune case, the simulations are clearly coupled but greatly under predict the strength of the coupling. The experimental beam quickly reached and oscillated about the equal tune equilibrium. The simulated beam emittances oscillated close to the values of their split tune counterparts. The peaks of the oscillations seem to start out aligned following storage and then proceed to slip out of phase during storage. By general inspection, the amplitude of the simulated horizontal and vertical emittance oscillations are approximately the same. However, the percent oscillation of the vertical emittance is much larger than that of the horizontal emittance. Experimentally, we see strong coupling in both profiles and emittances. Additionally, the percent oscillations in horizontal and vertical emittances were very close in experiment. This equalization of the emittances might account for why the coupling was clearly visible in both experimental profiles, but only in the smaller simulated vertical profile.

7.3.2 Effect of Beam Intensity

Figure 7.4 shows the horizontal and vertical profile evolution for the equal-tune low intensity (top row), middle intensity (middle row), and nominal intensity (bottom row) configurations. This figure shows the simulated results corresponding to the experimental results documented in Figure 5.24. The full intensity figures (bottom row) represent the same equal-tune case presented in the previous section. For the two low intensity cases, the beam evolution is similar to what was seen experimentally. There is a general hollowness in the profiles which periodically dilutes and reappears. At low intensity the coupling was also difficult to detect in the experimental profiles. Qualitatively, the simulated results demonstrate some of the same features as the experimental results.

Figure 7.5 shows the horizontal and vertical profile evolution for the equal-tune low intensity (top), middle intensity (middle), and nominal intensity (bottom) configurations. This figure shows the simulated results corresponding to the

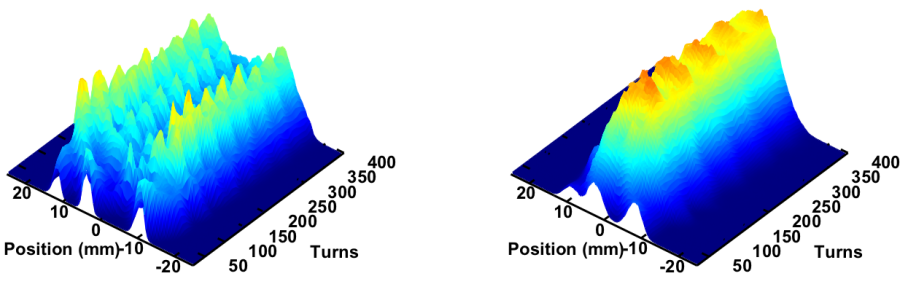

Low Intensity (2.29e12ppp)

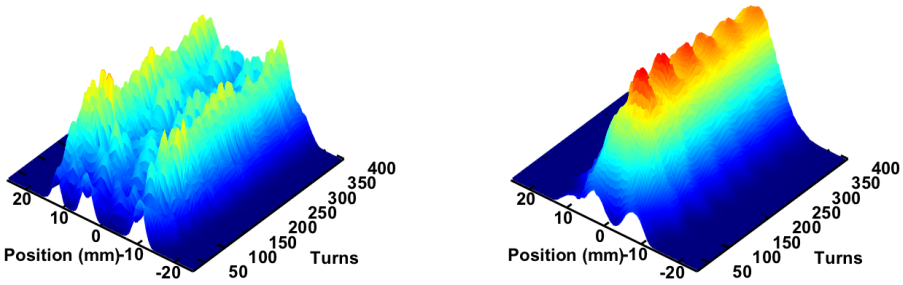

Medium Intensity (4.36e12ppp)

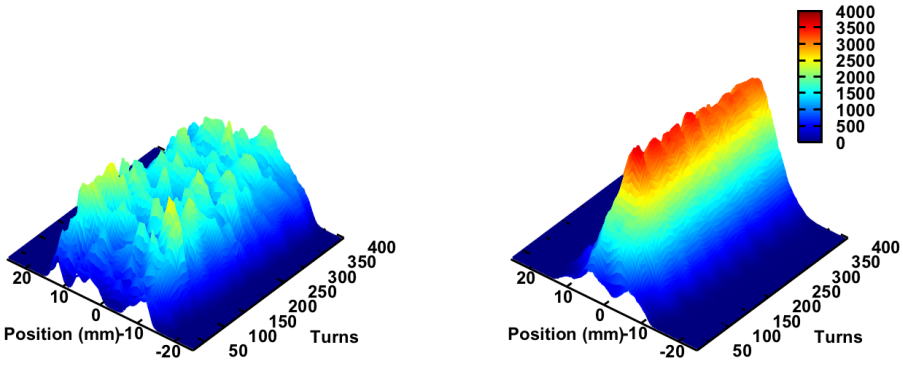

Nominal Intensity (7.60e12ppp)

Figure 7.4: Simulated profile evolutions for the equal-tune low intensity (top row), middle intensity (middle row), and nominal intensity (bottom row) configurations. Horizontal evolutions are shown on the left and vertical evolutions are shown on the right.

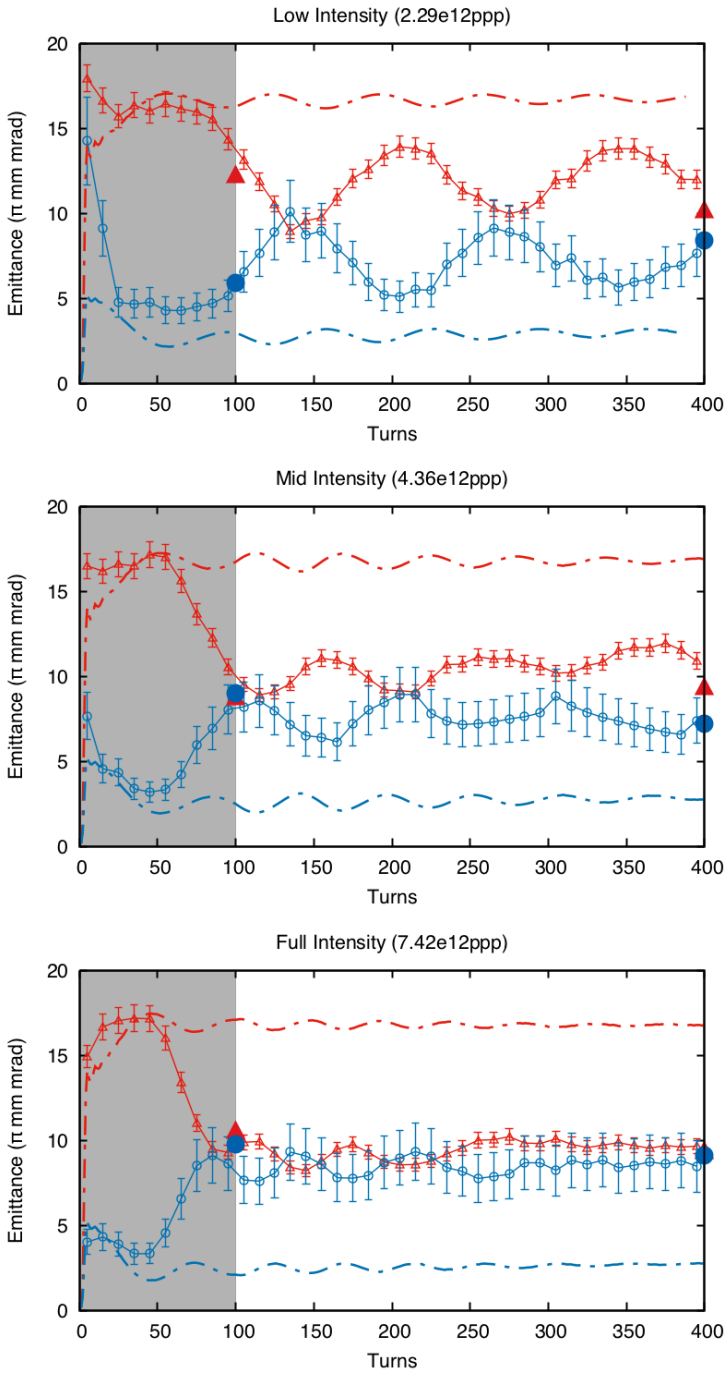

Figure 7.5: Emittance evolutions for the equal-tune low intensity (top), middle intensity (middle), and nominal intensity (bottom) configurations. The simulations are shown with dash dotted lines without points. The Electron Scanner data is shown with connecting lines and hollow data points. The wire scanner data is shown as solid data points without lines. The horizontal data is shown in red with '▲' and the vertical data is shown in blue with '●'.

experimental results documented in Figure 5.25. The nominal intensity figure (bottom) represents the same equal-tune case presented in the previous section. For the two low intensity cases, the simulations show strong coupling, but still greatly underestimate the strength of the resonance. In the context of all three beam intensities, it is easier to see how the simulations fail to follow the general evolution of the resonance in the nominal intensity case. It is likely that if we could better understand the short falls of the simulations at low intensity, then we would be better able to model the nominal intensity case. As we did in Section 5.4.2, we fit the emittances to a damped sinusoid. The fit results for the simulated three equal tune cases are shown in Table 7.2. Figure 7.6 shows the oscillation period for these fits decrease with increasing beam intensity. While the simulated and experimental frequencies are not the same, this shows that the simulated results follow the same trend as the experimental results. This supports the theory that this is not a Montague resonance. In Section 7.3.4, we will investigate the sensitivity of our simulations to the tune split. Those results imply that our simulations may not be as far off from modeling the resonances as they might seem.

7.3.3 Sensitivity Study: Fringe Fields

Figure 7.7 shows the three equal tune simulations with (top) and without (bottom) quadrupole fringe fields. By deactivating the effects of quadrupole fringe fields, the coupling is effectively removed at all intensity levels. The remaining variations in the emittances are small and, prior to turn 100, are likely due to the injection process. Similar effects were seen experimentally in the emittances of both split tune cases. This simple study indicates that the source of the resonance is the fringe fields. Specifically, we know that the fringe fields are strong in the quadrupoles around the injection region. This makes these magnets the most likely source of the resonance.

Table 7.2: Fit Parameters for the Simulated Three Equal Tune Cases

		Horizontal			Vertical		
Beam Intensity	[e12ppp]	Low	Mid	Full	Low	Mid	Full
		2.29	4.36	7.60	2.29	4.36	7.60
	[μC]	0.37	0.7	1.22	0.37	0.7	1.22
Fit Parameters	a	0.589	0.932	0.734	0.77	1.254	0.626
	b	0.093	0.112	0.139	0.091	0.113	0.140
	c	16.67	16.76	16.80	2.88	2.71	2.60
	d	2.64	7.79	6.18	-6.57	4.44	9.04
	k	0.00266	0.00426	0.00652	0.00343	0.00566	0.00577
Period	[Turns]	67.87	56.11	45.15	68.70	55.68	44.77

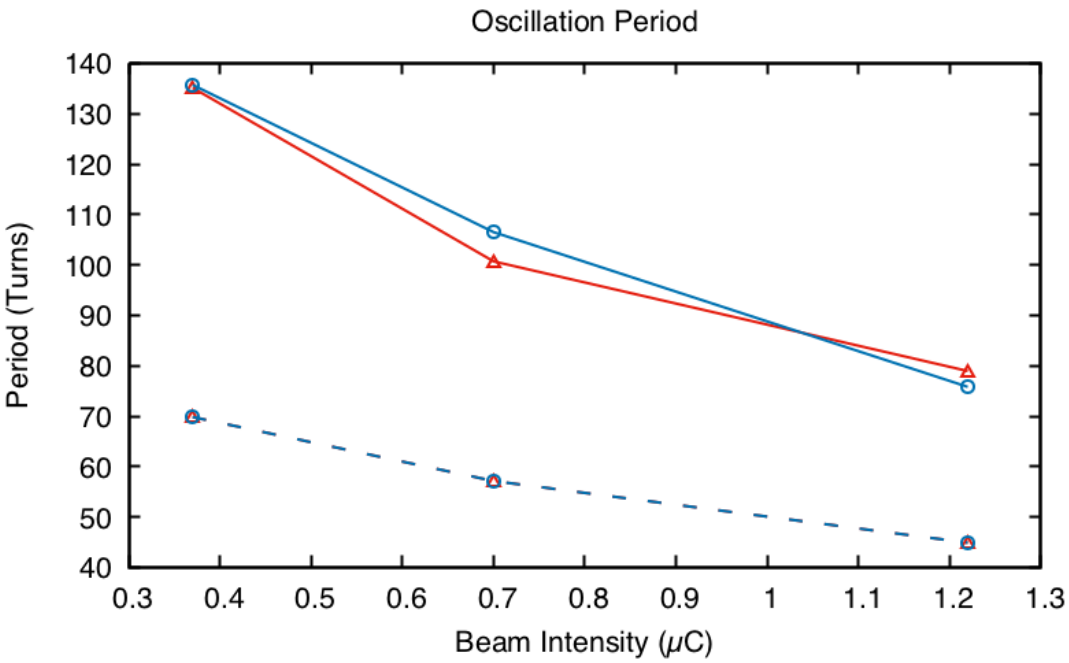

Figure 7.6: Simulated and experimental oscillation period versus beam intensity for the equal tune cases in the experiment three. The horizontal parameters are shown in red with '△', and the vertical parameters are shown in blue with '◯'. The simulations are shown with dashed lines. The experiments are shown with solid lines.

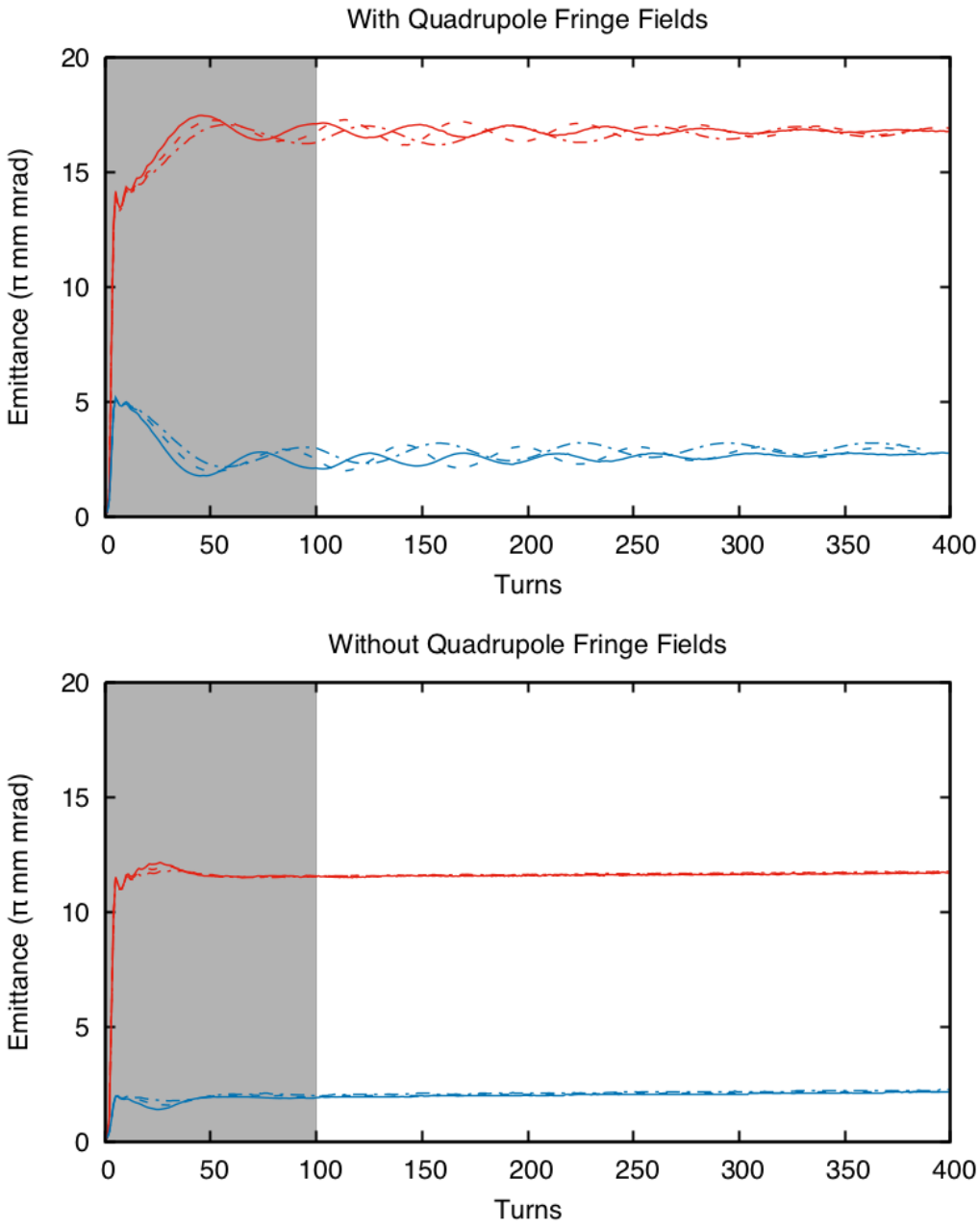

Figure 7.7: Simulated emittance evolutions for three equal-tune configurations with quadrupole fringe field (top) and without quadrupole fringe fields (bottom). In each figure, the nominal intensity case is shown with a solid line, the middle intensity case is shown with a dashed line, and the low intensity case is shown with a dash dotted line. The horizontal data is shown in red and the vertical data is shown in blue.

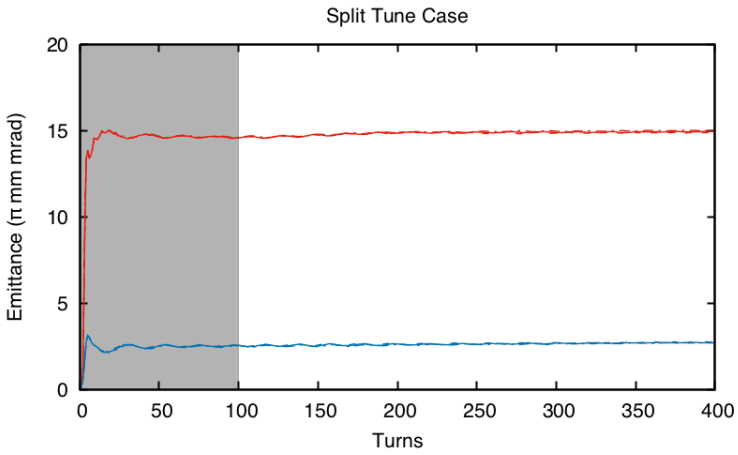

Figure 7.8: Variations in the emittance evolution for small variations in the tune split around the split tune configuration. The primary tune case is shown with a solid line, the case with the raised vertical tune is shown with a dashed line, and the case with the lowered vertical tune is shown with a dash dotted line. The horizontal data is shown in red and the vertical data is shown in blue.

7.3.4 Sensitivity Study: Tune Split

Figure 7.8 shows the variations in the emittance evolution for small variations in the tune split around the split tune configuration. Additional simulations were run with the vertical tunes raised or lowered by 0.001. As this figure demonstrates, this shift represents a change in the tune that is inconsequential in normal accelerator beam dynamics. Each simulation is so similar to the others that the differences in the emittance evolutions are imperceptible for the entire evolution of the beam.

Figure 7.9 shows the variations in the emittance evolution for small variations in the tune split around the equal tune configurations for the low intensity (top), middle intensity (middle), and nominal intensity (bottom) cases. For each intensity case, additional simulations were run with the vertical tunes raised or lowered by 0.001. Unlike the split tune cases, small variations in the tune had a large impact on the emittance evolution. This highlights the extreme sensitivity of the equal tune resonance. This demonstrates that the simulations are modeling the resonance. However, these simulations are very sensitive to the precise tune values around the equal tune resonance. Additionally, it indicates that reasonable variations of the tune split for each case could produce simulations that more accurately matched the experimental results.

7.4 Conclusions

In summary, we used PyORBIT simulations to realistically model our final simplified accumulation followed by storage experiment. The detailed profile and emittance evolutions of the Electron Scanner provided an excellent source for comparison. We began by benchmarking our simulations against experiment for the split tune cases. In these cases, there was a general qualitative agreement between the profile evolutions, and a strong quantitatively agreement between the emittance evolutions. Having established the accuracy of the simulations outside of the resonance, we then used

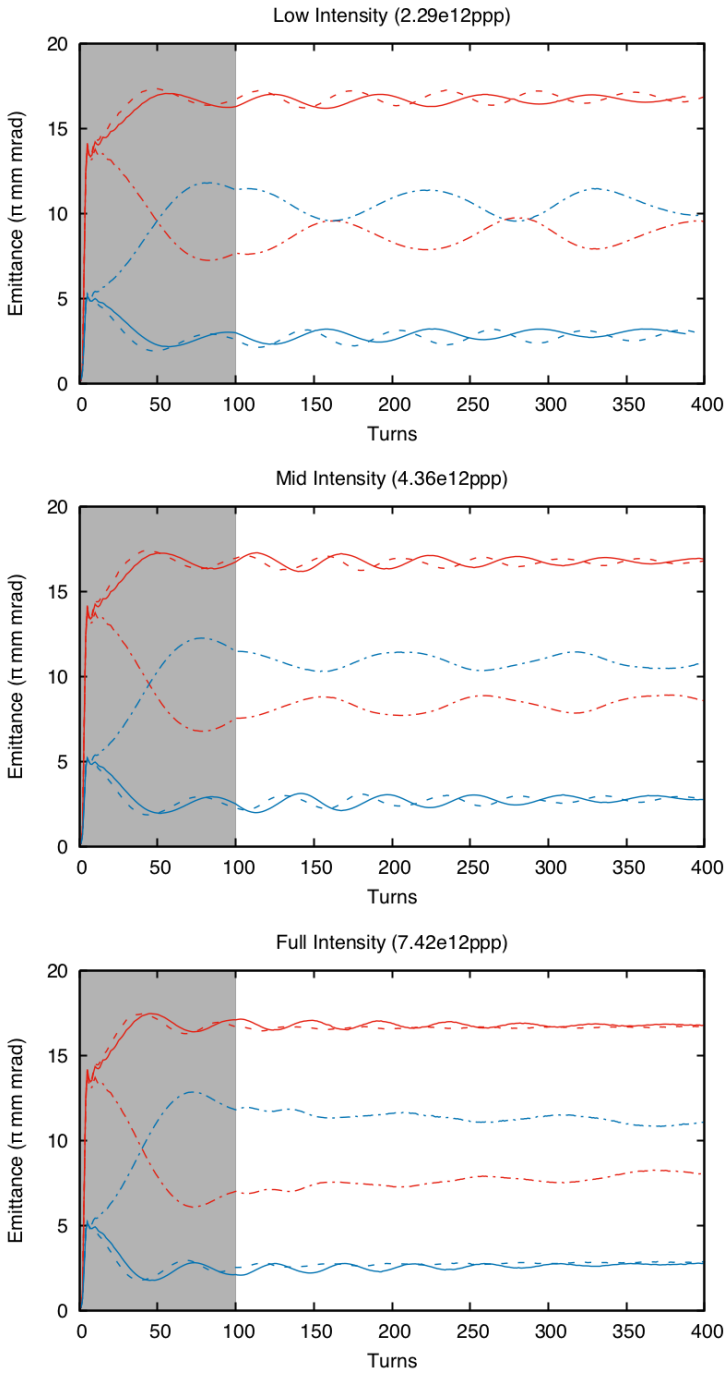

Figure 7.9: Variations in the emittance evolution for small variations in the tune split around the equal tune configurations for the low intensity (top), middle intensity (middle), and nominal intensity (bottom) cases. In each figure, the primary tune case is shown with a solid line, the case with the raised vertical tune is shown with a dashed line, and the case with the lowered vertical tune is shown with a dash dotted line. The horizontal data is shown in red and the vertical data is shown in blue.

PyORBIT to study the resonance. Our simulations supported our experimental results by showing that the resonance is highly dependent on the tune split. The degree of sensitivity was later shown to be larger than previously expected, with small variations in tune producing significant changes in beam evolution. Additionally, our simulations supported our experimental results by showing that the strength of the coupling decreases with increasing beam intensity. Our simulations were able to go beyond the experiments by indicating the source of the resonance. Through inspection of the effects of the fringe fields, we were able to conclude that the most likely source of the resonance is fringe fields from quadrupoles in the injection region. Further investigation into this area might provide a better understanding of whether the simulations actually deviate from the experiments. Specifically, based on the high level of sensitivity to the tune split, we found that it is feasible to match the simulations to the experimental results by using acceptable variations of the tune split and injection offsets. Additionally, more insight might be gained by simulating the fringe fields with different models or mapping the real fields. However, despite the need for further study, this work determined that the source of the resonance within the SNS accumulator ring are fringe field effects.

Chapter 8

Conclusions

In this study, we have investigated the effect of coupling on high intensity particle accelerator beams. The main focus has been the study of beam dynamics in the SNS accumulator ring to understand a recently documented coupling resonance. Prior to the start of this work, little was known regarding the coupling except that it could compromise independent control of the on-target transverse beam profiles, which is an essential part of configuring production operations. An initial exploration had shown that the effect had a dependence on the beam intensity. Therefore, the initial hypothesis was that the source was the space-charge-induced Montague resonance. This would only be possible with equal whole tunes, like those near the current production tune point. A key characteristic of a Montague resonance is an increase in coupling with increasing space charge. Therefore, tune split and beam intensity became the primary beam parameters studied. Specifically, we have gone beyond the traditional RMS size parameterization and examined the change in beam profile. We have studied the coupling experimentally for various beam configurations using traditional wire scanners and a novel Electron Scanner. We have modeled the final simplified accumulation experiment using a realistic self-consistent PIC simulation in PyORBIT. Additionally, we have aided in the calibration of the Electron Scanner recently installed in the SNS accumulator ring. There were three goals in this study:

1. To expand the understanding of equal tune resonances beyond the currently used RMS-based parameterizations,

2. To establish the source of the resonance in the SNS accumulator ring, and

3. To investigate mitigation of the coupling effect during normal SNS operations.

In conclusion, in fulfillment of the first goal, four unique experiments led to a stronger understanding of the overall effects of equal tune resonances on accumulating and stored beams. The most important discovery was that an equal tune resonance produces coupling that effects not only the RMS size but also the beam profile. This has important ramifications for facilities with specific beam profile requirements that currently operate near the equal tune resonance. Two other key observations were: the coupling has an inverse relationship with increasing beam intensity, whether the increase is due to increased injected beam intensity or continued accumulation of beam; and, the coupling is capable of creating full emittance exchange during periods of storage with stronger coupling at lower intensities.

In fulfillment of the second goal, simulations were performed for several of these configurations, providing the ability to control settings beyond those available experimentally. The results of these simulations indicate that the most likely source of the resonance is the fringe fields around the injection quadrupoles. These conclusions are supported by the experimental results, which contradicted the hypothesis that a Montague Resonance was the source of the coupling.

In fulfillment of the third and final goal, we studied a production-style split-tune beam with and without skew quadrupoles. We confirmed that the most recent SNS production settings produced no coupling, regardless of whether the skew quadrupoles were used. Typically, the production tune varies during and between production runs because the operators regularly optimize the machine for beam losses. The results indicate that this configuration meets the requirements of the SNS operations group for independent control of the transverse beam sizes and profiles. Therefore, we

recommend using the production settings studied. Based on the research presented, further mitigation of the resonance should not be necessary.

Additionally, we calibrated the SNS Electron Scanner and presented the results of the first major physics study using this novel device.

In summary, we have accomplished the three objectives of this study. This study constitutes an important and significant advancement to the overall knowledge of equal tune resonances in circular particle accelerators, especially the effect on the beam profiles in the SNS accumulator ring.

This work relied on existing hardware, software and analysis techniques employed at the SNS. During the period of this study, I contributed to the continued development of these tools. As the sole author of this work, my specific contributions to this work were as follows.

I was responsible for designing and conducting each experiment. I was responsible for making sure that any necessary preparations were made prior to each experiment shift. During each shift, I controlled the beam configuration and collected data in the SNS control room under the general supervision of the control room operators and, usually during experiment setup, my advisers. For each experiment using the Electron Scanner, I was joined by the technical expert for the initial setup of the prototype device. Following each shift, I was responsible for completing data analysis and presenting my work.

I was responsible for configuring and running all simulations. I was responsible for developing representations of data for comparison with the experimental data. I generated figures and tables. I received support from my primary adviser and a committee member, and relied on existing MAD and PyORBIT models of the SNS accumulator ring.

I was responsible for drafting all publications, including this dissertation. I received regular feedback from my primary adviser regarding both the structure and content of my work. I also occasionally received feedback from my committee members, and external reviewers. Unless cited, I created all figures and tables.

Bibliography

[1] Aleksandrov, A., Assadi, S., Cousineau, S., Danilov, V., Plum, M., Logatchov, P., and Starostenko, A. (2005). Feasibility study of using an Electron Beam for Profile Measurements in the SNS Accumulator Ring. In *Proceedings of the 2005 Particle Accelerator Conference*, volume 2, pages 2586–2588, Knoxville, TN. IEEE. 50, 56

[2] Blokland, W. (2010). Non-invasive Beam Profile Measurements using an Electron-Beam Scanner. In *Proceedings of HB2010*, pages 438–442, Morschach, Switzerland. xviii, 53, 57

[3] Blokland, W. (2013). Electron-beam scanner experience at ORNL. In *9th DITANET Topical Workshop on Non-Invasive Beam Size Measurement for High Brightness Proton and Heavy Ion Accelerators*, CERN. xix, 66, 67

[4] Blokland, W., Aleksandrov, S., Cousineau, S., Malyutin, D., and Starostenko, S. (2009). Electron Scanner for SNS Ring Profile Measurements. In *Proceedings of DIPAC09*, pages 155–157, Basel, Switzerland. xviii, 53, 54

[5] Blokland, W. and Cousineau, S. (2011). A Non-Destructive Profile Monitor for High Intensity Beams. In *Proceedings of 2011 Particle Accelerator Conference*, pages 1438–1442, New York, NY, USA. IEEE. 53, 58

[6] Brown, K. (1982). A First and Second order Matrix Theory for the Design of Beam Transport Systems and Charged Particle Spectrometers. Technical report, Stanford Linear Accelerator Center, Stanford University, Stanford, California. 173

[7] Chao, A. (2002). Lecture Notes on Topics in Accelerator Physics. Technical Report November, Stanford Linear Accelerator Center, Stanford University, Stanford, CA. 170

[8] Chao, A. W. (1993). *Physics of collective beam instabilities in high energy accelerators*. John Wiley & Sons, Inc., New York, 1st edition. 24, 45

[9] Courant, E., Livingston, M., and Snyder, H. (1952). The strong-focusing synchrotonA new high energy accelerator. *Physical Review*, 88(5):1190–1196. 3

[10] Courant, E. and Snyder, H. (1958). Theory of the alternating-gradient synchrotron. *Annals of Physics*, 3:1–48. 3, 4

[11] Cousineau, S. (2003). *Understanding space charge and controlling beam loss in high intensity synchrotrons*. PhD thesis, Indiana University. 7

[12] Cousineau, S. (2011). Status of High Intensity Effects in the Spallation Neutron Source Accumulator Ring. In *Proceedings of 2011 Particle Accelerator Conference*, pages 17–21, New York, NY, USA. IEEE. ix, 9, 47, 103

[13] Cousineau, S., Lee, S. Y., Holmes, J. A., Danilov, V., and Fedotov, A. (2003). Space charge induced resonance excitation in high intensity rings. *Physical Review Special Topics - Accelerators and Beams*, 6(3):034205. 7

[14] Danilov, V., Galambos, J., and Holmes, J. (2001). Transverse impedance implementation in ORBIT. In *Proceedings of 2001 Particle Accelerator Conference*, pages 1752–1754, Chicago. IEEE. 173

[15] Edwards, D. A. and Syphers, M. J. (1993). *An Introduction to the Physics of High Energy Accelerators*. John Wiley & Sons, Inc., New York, 1st edition. 22, 30, 31, 34, 36

[16] Fedotov, A., Malitsky, N., Papaphilippou, Y., Wei, J., and Holmes, J. (2001a). Excitation of resonances due to the space charge and magnet errors in the SNS ring.

In *Proceedings of 2001 Particle Accelerator Conference*, pages 2848–2850, Chicago. IEEE. 11

[17] Fedotov, A. V. and Gluckstern, R. L. (1999). Mismatch Correction for the Envelope Modes. In *The 7th ICFA Mini-Workshop on High Intensity High Brightness Hadron Beams*, volume 1, pages 38–39, Lake Como, WI. 7

[18] Fedotov, A. V., Holmes, J. A., and Gluckstern, R. L. (2001b). Instabilities of high-order beam modes driven by space-charge coupling resonances. *Physical Review Special Topics - Accelerators and Beams*, 4(8):084202. 8

[19] Forest, E. (1998). *Beam dynamics : a new attitude and framework*. Harwood Academic Publishers. 173

[20] Franchetti, G., Holmes, J. A., and Métral, E. (2012). Summary of Working Group A: Beam Dynmaics in High-Intensity Circular Machines. In *Proceedings of HB2012*, pages 606–611, Beijing, China. 9

[21] Gabriel, E., Fagg, G. E., Bosilca, G., Angskun, T., Dongarra, J. J., Squyres, J. M., Sahay, V., Kambadur, P., Barrett, B., Lumsdaine, A., Castain, R. H., Daniel, D. J., Graham, R. L., and Woodall, T. S. (2004). Open MPI: Goals, Concept, and Design of a Next Generation MPI Implementation. In *11th European PVM/MPI Users' Group Meeting*, pages 97–104, Budapest, Hungary. 170

[22] Galambos, J., Danilov, S., Jeon, D., Holmes, J., Olsen, D., Beebe-Wang, J., and Luccio, A. (1999). ORBIT - A Ring Injection Code with Space Charge. In *Proceedings of the 1999 Particle Accelerator Conference*, pages 3141–3145, New York. 169

[23] Galambos, J. D., Danilov, S., Jeon, D., Holmes, J. A., Olsen, D. K., Neri, F., and Plum, M. (2000). Comparison of simulated and observed beam profile broadening in the Proton Storage Ring and the role of space charge. *Physical Review Special Topics - Accelerators and Beams*, 3(3):034201. 7, 173

[24] Gluckstern, R. L., Fedotov, A. V., Kurennoy, S., and Ryne, R. (1998). Halo formation in three-dimensional bunches. *Physical Review E*, 58(4):4977–4990. 7

[25] Grote, H. and Iselin, F. C. (2013). The MAD Program User ' s Reference Manual CERN/SL/90-13 (AP). Technical report, European Laboratory For Particle Physics, Geneva, Switzerland. 170, 173

[26] Guignard, G. (1978). A General Treatment of Resonances in Accelerators. Technical report, CERN European Organization for Nuclear Research, Geneva. 5, 36

[27] Guignard, G. C. (1976). The General Theory of All Sum and Difference Resonances in a Three Dimensional Magnetic Field in a Synchrotron. Technical report, CERN European Organization for Nuclear Research, Geneva. 5

[28] Hagedorn, R. (1955). Stability of Two-Dimensional Non-Linear Oscillations with periodical hamiltonian; applied to the Non-Linear Betatron Oscillations of an Alternating-Gradient Synchrotron. Technical report, CERN, Geneva. 5

[29] Hagedorn, R., Hine, M. G. N., and Schoch, a. (1956). Non-Linear Orbit Problems in Synchrotrons. *CERN Symp*, pages 237–253. 5

[30] Henderson, S. (2005). SNS Parameters List. Technical Report June, Spallation Neutron Source, Oak Ridge. 48

[31] Henderson, S. and Al., E. (2014). The Spallation Neutron Source accelerator system design. *Nuclear Instruments and Methods in Physics Research Section A: Accelerators, Spectrometers, Detectors and Associated Equipment*, 763:610–673. 48, 80, 102, 156

[32] Hockney, R. W. and Eastwood, J. W. (1988). *Computer Simulation Using Particles*. IOP Publishing Ltd, London. 171

[33] Hofmann, I. (1998). Stability of anisotropic beams with space charge. *Physical Review E*, 57(4):4713–4724. 7, 46, 47

[34] Hofmann, I. (2002). Space Charge Resonances and Instabilities in Rings. In Chou, W., Mori, Y., Neuffer, D., and Ostiguy, J.-F., editors, *High Intensity and High Brightness Hadron Beams*, pages 248–252. American Institute of Physics. 46, 47

[35] Hofmann, I. (2008). Space Charge Resonances in High-Intensity Beams. In *Proceedings of Hadron Beam 2008*, Nashville, Tennessee, USA. 46

[36] Hofmann, I. and Boine-Frankenheim, O. (2001). Resonant Emittance Transfer Driven by Space Charge. *Physical Review Letters*, 87(3):034802. 45

[37] Hofmann, I. and Franchetti, G. (2006). Self-consistent study of space-charge-driven coupling resonances. *Physical Review Special Topics - Accelerators and Beams*, 9(5):054202. 46

[38] Hofmann, I., Franchetti, G., and Al, E. (2005). Benchmarking of Simulation Codes Based on the Montague Resonance in the CERN Proton Synchrotron. In *Proceedings of 2005 Particle Accelerator Conference*, pages 330–332, Knoxville, Tennessee. IEEE. 46

[39] Hofmann, I., Franchetti, G., Boine-Frankenheim, O., Qiang, J., and Ryne, R. D. (2003a). Space charge resonances in two and three dimensional anisotropic beams. *Physical Review Special Topics - Accelerators and Beams*, 6(2):024202. 7

[40] Hofmann, I., Franchetti, G., Qiang, J., and Ryne, R. (2003b). Self-consistency and coherent effects in nonlinear resonances. In *Beam Halo Dynamics, Diagnostics, and Collimation*, pages 65–68. American Institute of Physics. 46

[41] Hofmann, I., Franchetti, G., Qiang, J., Ryne, R., Gerigk, F., Jeon, D., and Pichoff, N. (2002). Review of beam dynamics and space charge resonances in high intensity linacs. In *Proceedings of EPAC 2002*, pages 74–78, Paris, France.

[42] Hofmann, I., Qiang, J., and Ryne, R. D. (2001). Collective Resonance Model of Energy Exchange in 3D Nonequipartitioned Beams. *Physical Review Letters*, 86(11):2313–2316. 45, 46

[43] Holmes, J., Cousineau, S., Danilov, V., Henderson, S., Shishlo, A., and Fedotov, A. (2003). Computational studies of collective beam dynamics in high intensity rings. *Proceedings of 2003 Particle Accelerator Conference*, pages 117–119. 170

[44] Holmes, J. and Danilov, V. (2002). ORBIT: A Code for Collective Beam Dynamics in High-Intensity Rings. In *High Intensity and High Brightness Hadron Beams*, pages 241–244. American Institute of Physics. 170

[45] Holmes, J., Galambos, J., and Jeon, D. (1998). Dynamic Space Charge Calculations for High Intensity Beams in Rings. In *Proceedings of the 1998 International Computational Accelerator Physics Conference*, pages 174–178, Monterey, California. Stanford Linear Accelerator Center Stanford, California. 170, 171, 173

[46] Holmes, J. A., Danilov, V., Galambos, J., Shishlo, A., Cousineau, S., Chou, W., Michelotti, L., Ostiguy, F., and Wei, J. (2002). ORBIT: Beam Dynamics Calculations For High-Intensity Rings. In *Proceedings of EPAC 2002*, pages 1022–1024, Paris, France. 173

[47] Holmes, J. A., Danilov, V. V., Galambos, J. D., Jeon, D., and Olsen, D. K. (1999). Space charge dynamics in high intensity rings. *Physical Review Special Topics - Accelerators and Beams*, 2(11):1–18. 7

[48] Hotchi, H. (2015). Space-charge induced beam loss and its mitigation in the J-PARC 3-GeV RCS. In *Space-Charge 2015 Workshop*, Oxford. 8

[49] Hotchi, H., Kinsho, M., Hasegawa, K., Hayashi, N., Hikichi, Y., Hiroki, S., Kamiya, J., Kanazawa, K., Kawase, M., Noda, F., Nomura, M., Ogiwara, N., Saeki, R., Saha, P. K., Schnase, A., Shobuda, Y., Shimada, T., Suganuma, K.,

Suzuki, H., Takahashi, H., Takayanagi, T., Takeda, O., Tamura, F., Tani, N., Togashi, T., Ueno, T., Watanabe, M., Watanabe, Y., Yamamoto, K., Yamamoto, M., Yamazaki, Y., Yoshikawa, H., Yoshimoto, M., Ando, A., Harada, H., Irie, Y., Ohmori, C., Satou, K., Yamazaki, Y., and Yoshii, M. (2009). Beam commissioning of the 3-GeV rapid cycling synchrotron of the Japan Proton Accelerator Research Complex. *Physical Review Special Topics - Accelerators and Beams*, 12(4):040402. 8

[50] Iselin, F. (1994). The MAD Program: Physical Methods Manual. 85

[51] J. Holmes, Y. H. Chin, and S. Machida (2014). Summary of Working Group A: Beam Dynamics in High-Intensity Circular Machines. In *Workshop on High Intensity and High Brightness Hadron Beams*. 9

[52] Jones, E., Oliphant, T., Peterson, P., and Etc (2001). Orthogonal distance regression (scipy.odr) SciPy v0.18.1 Reference Guide. 82

[53] Kapchinskij, I. M. and Vladimirskij, V. V. (1959). Limitations of proton beam current in a strong focusing linear accelerator associated with strong space charge. *Proceedings of the International Conference on High Energy Accelerators and Instrumentation*, pages 274–288. 7

[54] Laslett, L. (1963). On intensity limitations imposed by transverse space-charge effects in circular particle accelerators. *Summer Study on Storage Rings, BNL Report*, pages 324–367. 31

[55] Lee, S. Y. (2012). *Accelerator Physics*. World Scientific Publishing Company, New Jersey, 3rd edition. 5, 17, 24, 27, 30, 31, 34, 36, 41

[56] Lee, S. Y. and Okamoto, H. (1998). Space-Charge Dominated Beams in Synchrotrons. *Physical Review Letters*, 80(23):5133–5136. 6

[57] Lee, S. Y. and Riabko, A. (1995). Envelope Hamiltonian of an intense charged-particle beam in periodic solenoidal fields. *Physical Review E*, 51(2):1609–1612. 6

[58] Lee-Whiting, G. E. (1972). Comparison of calculated third-order aberrations of a magnetic quadrupole lens. *Nuclear Instruments and Methods*, 99(3):609–610. 43

[59] Logachev, P., Malyutin, D., and Starostenko, A. (2009). Scanning with parallel transfer of an electron beam for a transverse profile monitor of an intense ion bunch. *Instruments and Experimental Techniques*, 52(4):569–573. 53

[60] Logachev, P., Malyutin, D., and Starostenko, A. (2011). Application of a low-energy electron beam as a tool of nondestructive diagnostics of intense charged-particle beams. *Instruments and Experimental Techniques*, 51(1):1–27. 53

[61] Matsuda, H. and Wollnik, H. (1972). Third Order Transfer Matrices for the Fringing Field of Magnetic and Electrostatic Quadrupole Lenses. *Nuclear Instruments and Methods*, 103:117–124. 43

[62] Métral, E. (2005). Overview of Impedance and Single-Beam Instability Mechanisms. In *Proceedings of 2005 Particle Accelerator Conference*, pages 14–18, Knoxville, Tennessee. IEEE. 45, 46

[63] Métral, E., Franchetti, G., and Hofmann, I. (2004). Intensity Dependent Emittance Transfer Studies at the CERN Proton Synchrotron. In *Proceedings of EPAC 2004*, volume 3, pages 1894–1896, Lucerne, Switzerland. 46

[64] Métral, E., Giovannozzi, M., Martini, M., Steerenberg, R., Franchetti, G., Hofmann, I., Qiang, J., and Ryne, R. D. (2005). Space-charge experiments at the CERN proton synchrotron. *AIP Conference Proceedings*, 773:122–126. 8

[65] Montague, B. W. (1968). Fourth-Order Coupling Resonance Excited By Space-Charge Forces in a Synchrotron. Technical report, CERN. 6, 36, 45, 46

[66] Morton, P. L. and Spencer, N. C. (1971). Effects of Transverse Coupling in the SLAC Storage Ring. (March):3–4. 5

[67] Moser, J. (1956). The Resonance Lines for the Synchrotron. 5

[68] Ohnuma, S. (1973). Quarter Integer Resonance By Sextupoles. 6, 8

[69] Ostiguy, J. and Holmes, J. (2003). PyORBIT: A Python Shell for ORBIT. In *Proceedings of 2003 Particle Accelerator Conference*, pages 3503–3505. IEEE. 170

[70] Panel, P. (2008). US Particle Physics: Scientific Opportunities A Strategic Plan for the Next Ten Years Report of the Particle. ix, 1

[71] Papaphilippou, Y. and Abell, D. T. (2000). Beam Dynamics Analysis and Correction of Magnet Field Imperfections in the SNS Acumulator Ring. In *Proceedings of EPAC 2000*, pages 1453–1456, Vienna, Austria. 43

[72] Pasour, J. and Ngo, M. (1992). Nonperturbing electron beam probe to diagnose charged-particle beams. *Review of Scientific Instruments*, 63(5):3027. 50

[73] Plum, M. (2004). Interceptive Beam Diagnostics—Signal Creation and Materials Interactions. *AIP Conference Proceedings*, 732:23–46. 208, 220

[74] Plum, M. A. (2007). Commissioning of the Spallation Neutron Source accelerator systems. In *Proceedings of PAC07*, pages 2603–2607, Albuquerque, New Mexico, USA. IEEE. 156

[75] Press, W. (2007). *Numerical Recipes: The art of scientific computing*. Cambridge University Press, 3rd edition. 171

[76] Riabko, A., Ellison, M., Kang, X., Lee, S. Y., Li, D., Liu, J. Y., Pei, X., and Wang, L. (1995). Hamiltonian formalism for space charge dominated beams in a uniform focusing channel. *Physical Review E*, 51(4):3529–3546. 6

[77] Sacherer, F. (1971). RMS Envelope Equations with Space Charge. *Nuclear Science, IEEE Transactions on*, (9):1105–1107. 46

[78] Sacherer, F. J. (1968). *Transverse Space-Charge Effects in Circular Accelerators*. PhD thesis, University of California, Berkeley. 6, 34, 46

[79] Safranek, J. A. (1992). *SPEAR lattice for high-brightness synchrotron radiation*. PhD thesis, Stanford University. 5

[80] Sakai, I., Adachi, T., Arakida, Y., Irie, Y., Kitakawa, K., Machinda, S., Mori, Y., Shimosaki, Y., Someya, H., and Yoshimoto, M. (2000). Observation of Space-Charge Effects in the KEK Booster. In *Proceedings of the 2000 European Particle Accelerator Conference*, pages 2261–2263, Vienna, Austria. 8, 46

[81] Sakai, I., Machida, S., Adachi, T., Arakida, Y., Irie, Y., Kitakawa, K., Mori, Y., Shimosaki, Y., Someya, H., and Yoshimoto, M. (2001). Intensity Dependent Emittance-Exchange in a High Intensity Proton Synchrotron. In *Proceedings of the 2001 Particle Accelerator Conference*, pages 3185–3187. 8, 46

[82] Sato, Y., Shishlo, A., Danilov, S., Holmes, J., and Henderson, S. (2004). Simulation of e-cloud using ORBIT: Benchmarks and First Application. In *Proceedings of ECLOUD'04: 31st Advanced ICFA Beam Dynamics Workshop on Electron-Cloud Effects*, pages 257–262, Napa, California. CERN Scientific Information Service. 173

[83] Schoch, A. (1958). Theory of Linear and Non-Linear Perturbations of Betatron Oscillations in Alternating Gradient Synchrotrons. 5, 36

[84] Shishlo, A. (2013). Novel Methods for Experimental Characterization of 3D Superconducting Linac Beam Dynamics. In *Proceedings of PAC2013*, pages 397–401, Pasadena, CA USA. 215

[85] Shishlo, A. and Cousineau, S. (2006). The ORBIT Simulation Code: Benchmarking and Applications. In *Proceedings of ICAP 2006*, pages 53–58, Chamonix, France. 170, 173

[86] Shishlo, A., Holmes, J., and Gorlov, T. (2009). The Python Shell for the ORBIT code. In *Proceedings of ICAP09*, pages 351–354, San Francisco, CA. 170

[87] Shishlo, A., Sato, Y., Cousineau, S., Danilov, V., Henderson, S., Holmes, J., Macek, R., and Lee, S. Y. (2005). Self-Consistent Electron-Cloud Simulation for Long Proton Bunches. In *Proceedings of 2005 Particle Accelerator Conference*, pages 722–724, Knoxville, Tennessee. IEEE. 173

[88] Stupakov, G. (2011). Lecture notes on Classical Mechanics and Electromagnetism in Accelerator Physics. Technical report, The US Particle Accelerator School, Melville, New York. 17, 34, 46

[89] Teng, L. (1960). Transverse Space Charge Effects. 31

[90] Tsyganov, E., Meinke, R., Nexsen, W., Kauffmann, S., Zinchenko, A., and Taratin, A. (1993). Electron Beam Emittance Monitor for the SSC. In *Proceedings of the 1993 Particle Accelerator Conference*, pages 2489–2491. IEEE. 50

[91] Wei, J., Papaphilippou, Y., and Talman, R. (2000). Scaling Law for the Impact of Magnet Fringe Fields. In *Proceedings of EPAC 2000*, pages 1092–1094, Vienna, Austria. 43

[92] Wiedemann, H. (2007). *Particle Accelerator Physics*. Springer, New York, 3rd edition. 22, 34, 36, 43

[93] Wille, K. (2001). *The Physics of Particle Accelerators: An Introduction*. Oxford Univ. Press, Oxford, 1st edition. 24, 27, 36

Appendix

Appendix A

Wire Scanners

The accelerator contains a variety of diagnostic devices that provide information regarding beam position, profile, and other parameters. This information is used to optimize beam transport through the lattice and, ultimately, to meet the on-target beam requirements. Due to stringent beam loss requirements, the diagnostic devices in the accumulator ring must be non-interceptive. Consequently, the only profile measurement device in the accumulator ring is the recently installed Electron Scanner, which is still a prototype. The primary beam profile measurement devices are located in the Ring-to-Target Beam Transfer (RTBT), which transports the accumulated beam to the target. The RTBT contains multiple wire scanners and a harp for measuring beam profiles. Figure 4.1 shows the relative position of the Electron Scanner in the accumulator ring and the wire scanners in the RTBT. In Appendix A, we review the wire scanners.

Wire scanners provide low noise transverse beam density profiles in the horizontal, vertical, and sometimes diagonal planes. There are four wire scanners located near the end of the RTBT beamline that are commonly used in our research. Figure A.1 shows one of the wire scanners in the RTBT. Together, these four wire scanners allow us to measure the RMS emittance of the beam. Each wire scanner is composed of three $100\mu m$ tungsten wires mounted under tension on a fork. The fork is mounted

on an actuator that allows precise control of the position of the wires. The actuator is mounted at 45° with respect to the beam to allow each wire to passes through the center of the beam at different times. The profile signal is generated by the emission of secondary electrons as the beam enters and exits the wire. Based on nonlinearities in the fork and the precision of the stepper motor, the position error of each measurement has been measured to be at most $\pm 0.15\,\mathrm{mm}$. The error in the signal is less than 2% of the peak signal level[73]. Figure A.2 shows a set of typical beam profiles acquired from each wire scanner.

The primary disadvantage of wire scanners is that they are not capable of collecting the profile of a single accumulated pulse. Each data point is collected from one pulse and therefore the final profile is an aggregate of multiple pulses. Additionally, the wire scanners are limited to averages over the longitudinal distribution of the beam.

A.1 Reproducibility of Wire Scanners at Low Beam Intensity

During the course of this study, it has been necessary to collect beam profile measurements at low beam intensities. In order to confirm that these beam profiles were consistent, multiple profiles were taken for both split tune and equal tune configurations at 10 turns of accumulated beam. Figure A.3 shows the split tune case, and Figure A.4 shows the equal tune case. In both cases, individual injected beam pulses can be seen overlapping in the same position. The specific placement of pulses is due to the injection settings, and the horizontal and vertical tunes, which govern the movement of the pulses in phase space.

Figure A.1: Image of an RTBT Wire Scanner. Device image courtesy of S. Murray, SNS.

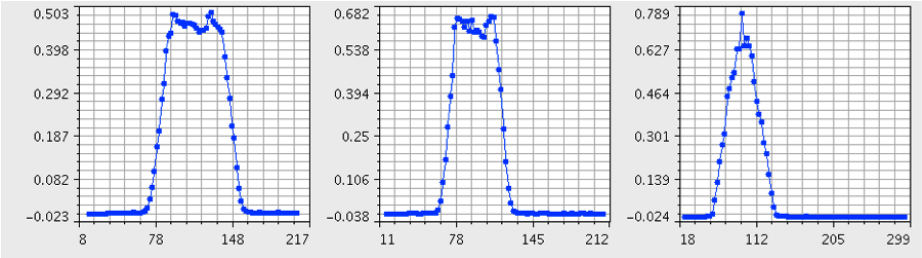

Figure A.2: Horizontal (left), vertical (center), and diagonal (right) profiles from one wire scanner, as displayed in the data collection application called WireAnalysis.

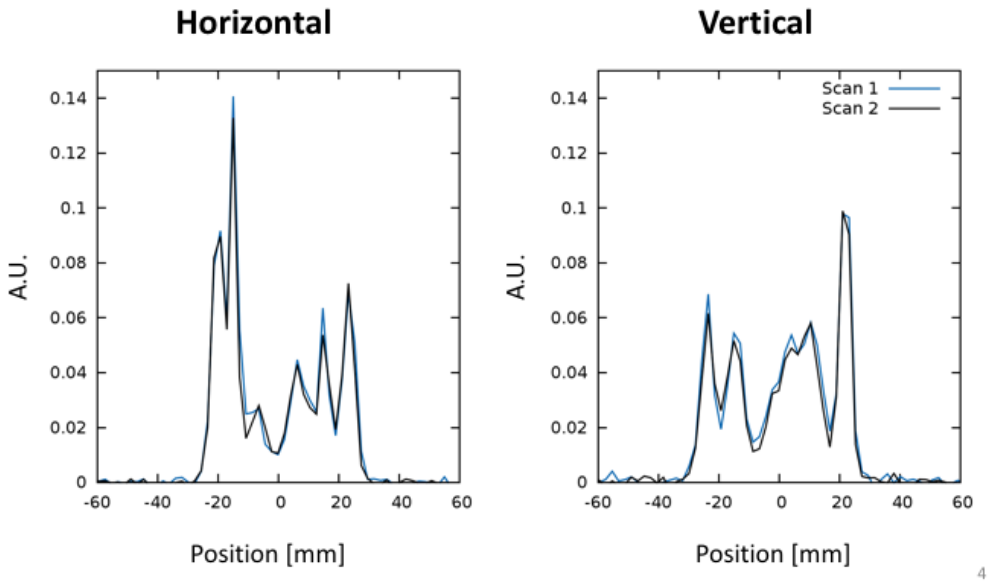

Figure A.3: Demonstration of the reproducibility of wire scanner beam profile measurements at 10 turns of accumulation for the split tune configuration.

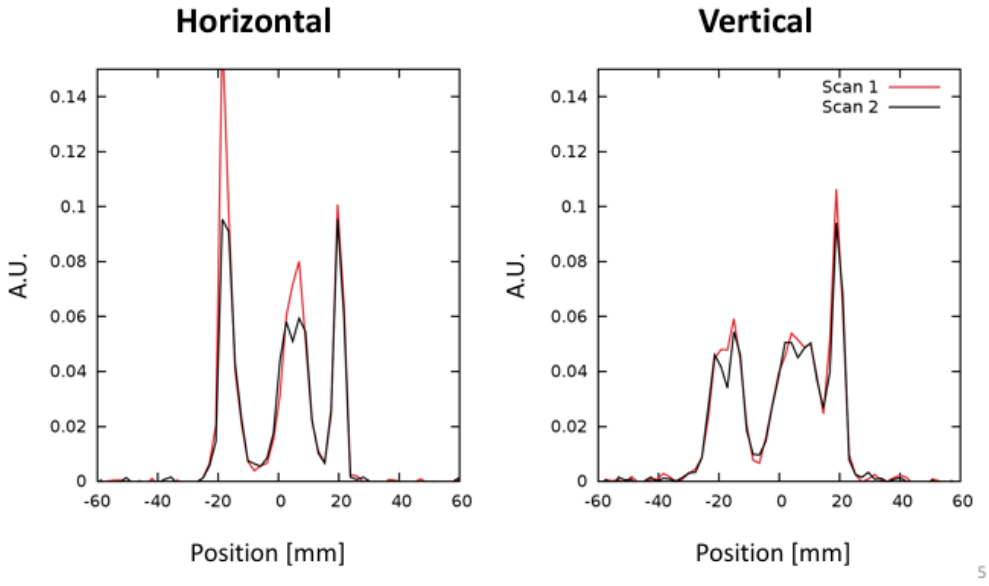

Figure A.4: Demonstration of the reproducibility of wire scanner beam profile measurements at 10 turns of accumulation for the equal tune configuration.

A.2 WireAnalysis: Using Wire Scanner Data to Calculate Twiss Parameters

An essential portion of this dissertation involves using the wire scanners to calculate the transverse emittances. This section aims to demonstrate the necessary steps using the WireAnalysis application. The example beam has a symmetric split-tune configuration with 500 turns of accumulated beam. Figure A.5 demonstrates how the application loads data that has been collected. The primary graphic shows the horizontal, vertical, and diagonal profiles for each of the four RTBT wire scanners that we used.

Figure A.6 shows the analysis screen where we will find a statistical RMS fit for each profile. For each individual horizontal and vertical profile, we load the data by clicking "Analyze". The raw data appears in red on the left. We then use "V Cute Below" to remove the floor, being careful to avoid removing the edges of the profile. Selecting "Statistical RMS" from the drop down, followed by "Fit Current Data Only" and "Store Results" calculates the statistical RMS fit and stores it in the data table. The data used for the statistical RMS fitting is shown on the right in blue.

Once the fit has been calculated for each of the horizontal and vertical profiles, we will be able to calculate the Twiss parameters. Figure A.7 shows the Twiss fitting screen. When loaded, they will appear as the user values in the top table. The machine state containing all magnet strengths are loaded from the logger ID contained in the data file. We then select the sequence of the dataset, in this case the end of the RTBT, and select the element to calculate the Twiss parameters at, in this case RTBT_Diag:WS20. We run the solver until it converges upon a set of Twiss parameters which fits the experimental data provided. These values can be stored and plotted. In the results data table, the values we are looking for are the alphas, betas, and emittances. As is demonstrated in this figure, we have analyzed two datasets with the same tune value. Therefore the magnet settings should be equivalent and

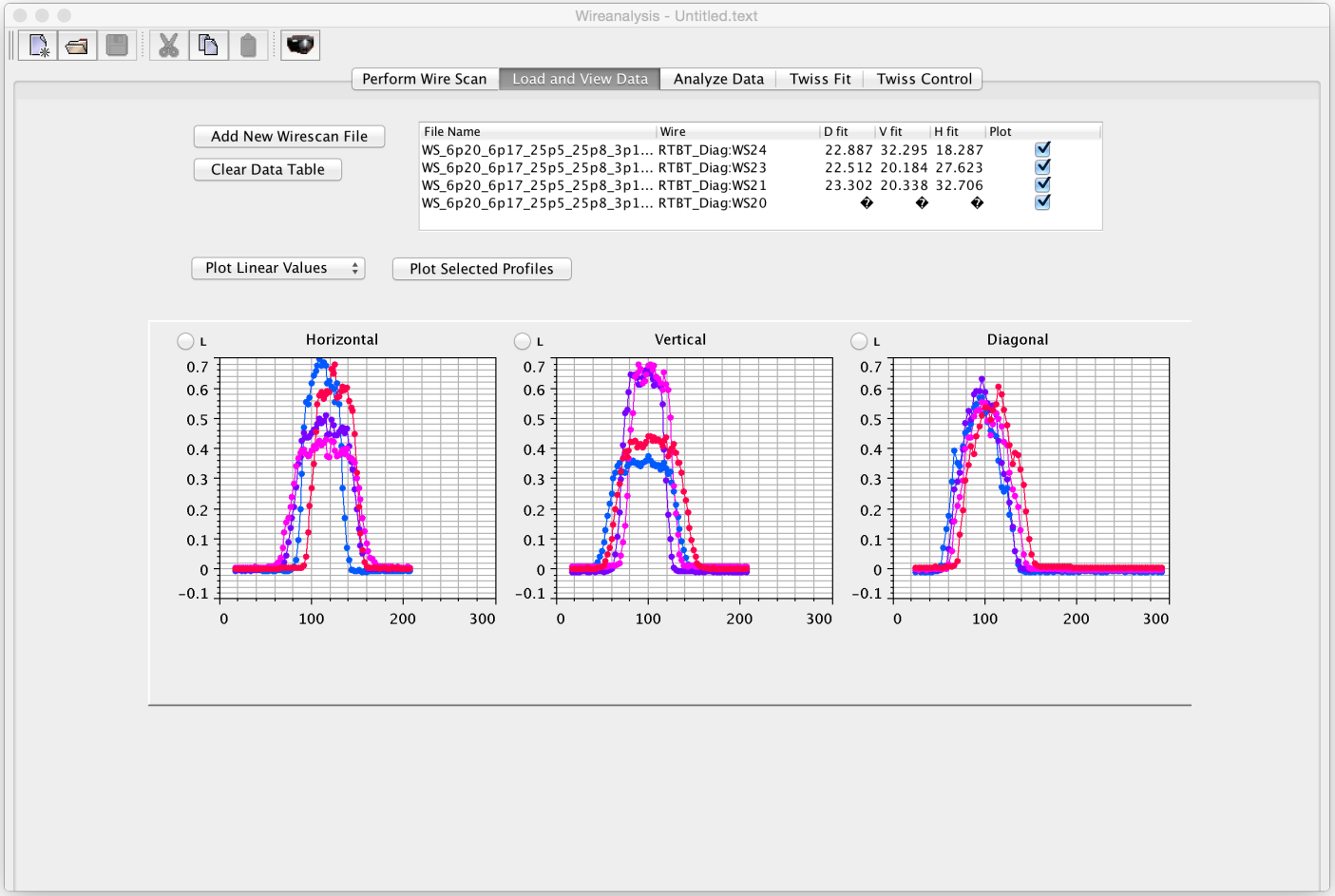

Figure A.5: WireAnalysis load data screen

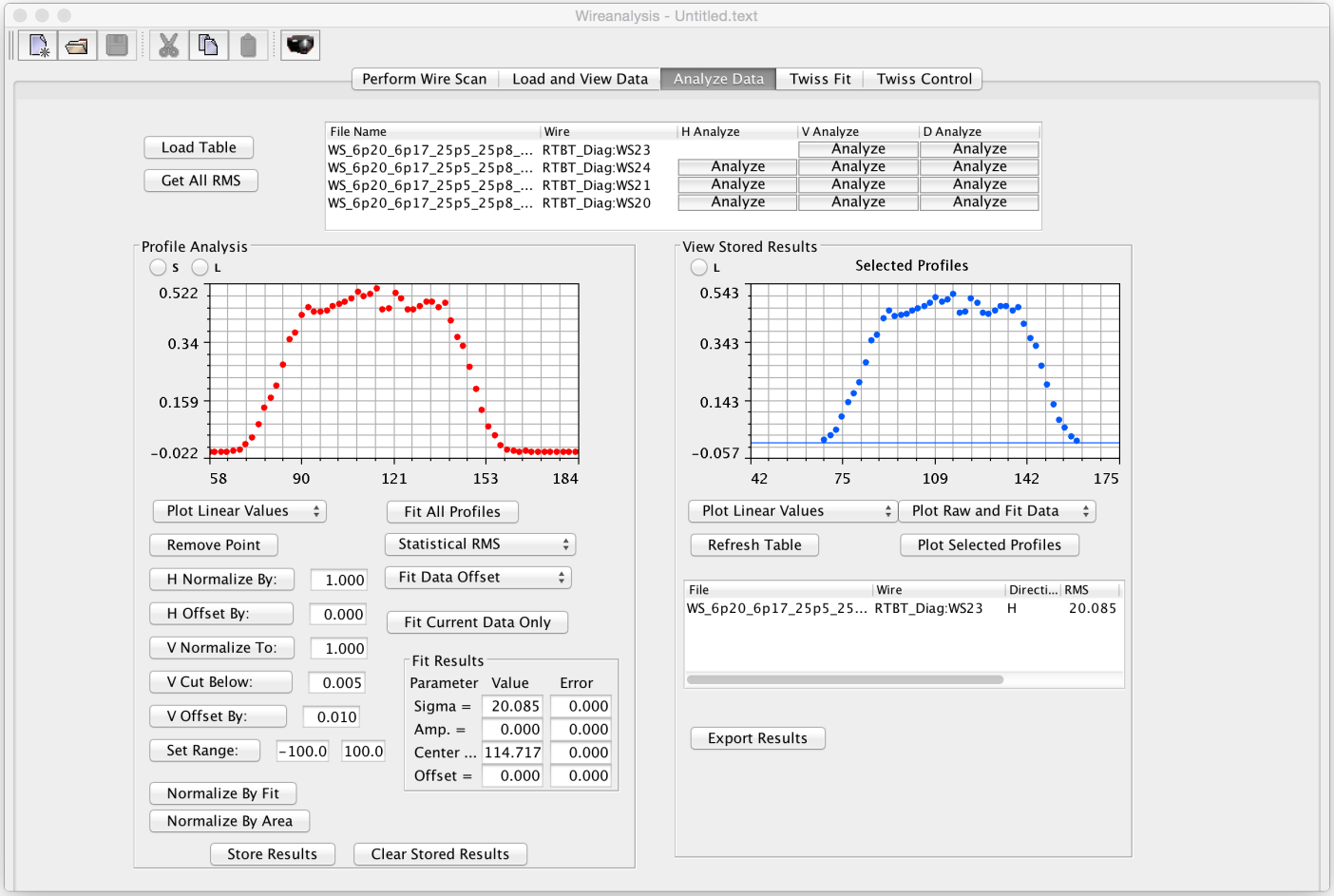

Figure A.6: WireAnalysis analyze data screen

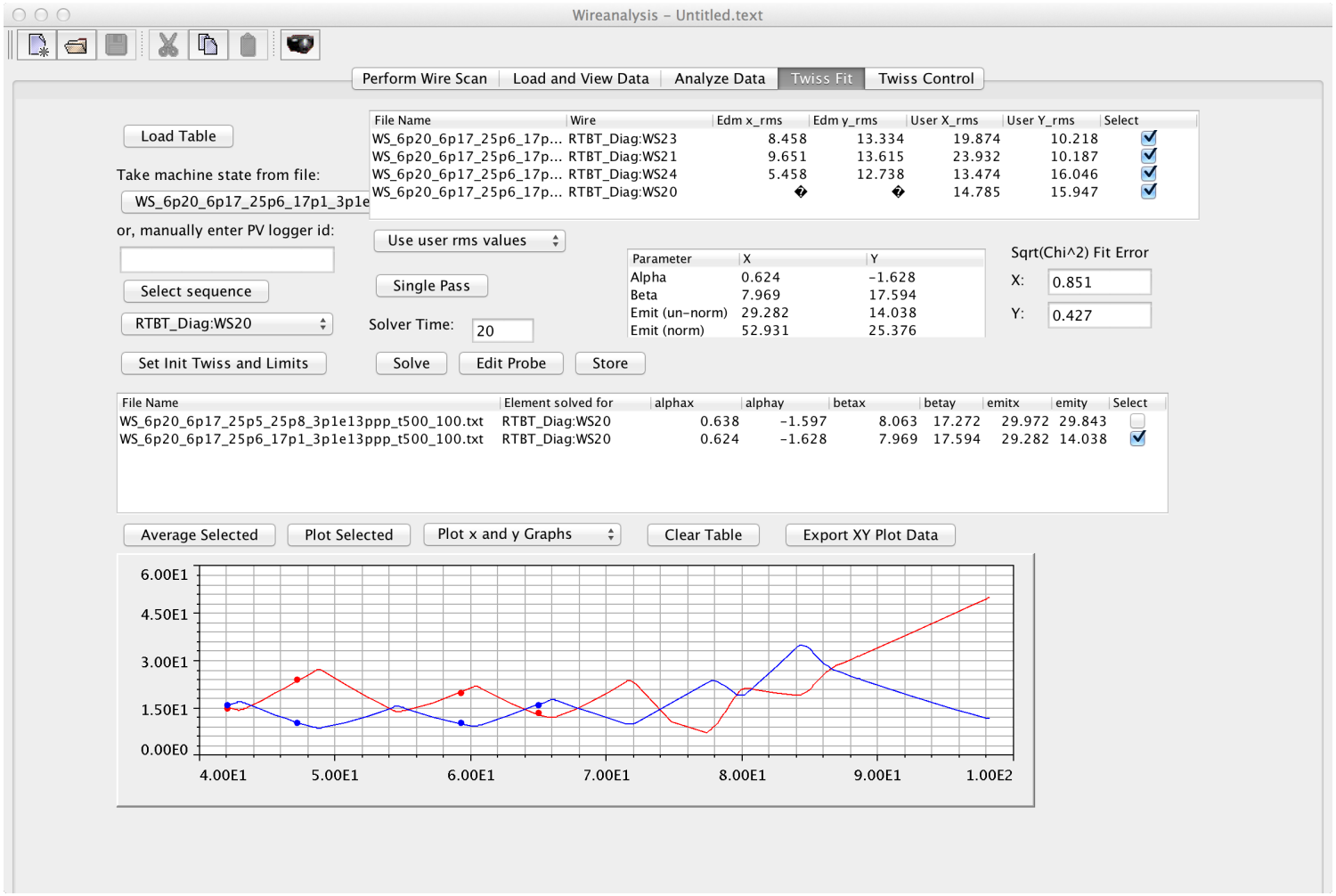

Figure A.7: WireAnalysis Twiss fitting screen

we can use the multiple data sets to find an average set of Twiss parameters. In the case shown, the solved Twiss parameter are relatively similar, excluding the vertical emittances. This makes sense as the two cases shown have different vertical injection offsets and, therefore, different vertical emittances.

We then repeat the previous analysis procedure of loading the data, analyzing the data, and loading the RMS sizes into the Twiss fit window. On the second pass, we enter the averaged alpha and beta values into the "Set Initial Twiss and Limits" window. This allows us to fix the alpha and beta parameters of the beam and instruct the WireAnalysis program to vary only the emittances in order to fit the data. Figure A.8 shows what the Twiss fitting window looks like for multiple beam profile measurements. The final results table at the bottom shows that each of the alphas and betas remained fixed and the emittances were varied. These fitted emittances will be used to show the evolution of the beam size during accumulation. In this case, the beam profiles were collected for the same beam configuration where the number of accumulated turns was increased from 50 turns to 250 turns in increments of 50 turns. The fact that the emittances are approximately similar indicates that the beam size remained constant during the accumulation, as we expected for a symmetric split-tune beam configuration.

A.3 Derivation of Initial Beam Distribution with Errors

Provided that we have measured the RMS beam size at multiple locations, we can calculate the initial beam distribution parameters and their errors. This requires using the Least Squared Method (LSM). The same application of the LSM was outlined in a 2013 paper[84]. When we have the initial beam distribution and the related errors, we can used them to calculate the Twiss parameters and their errors, as shown in Section A.4.

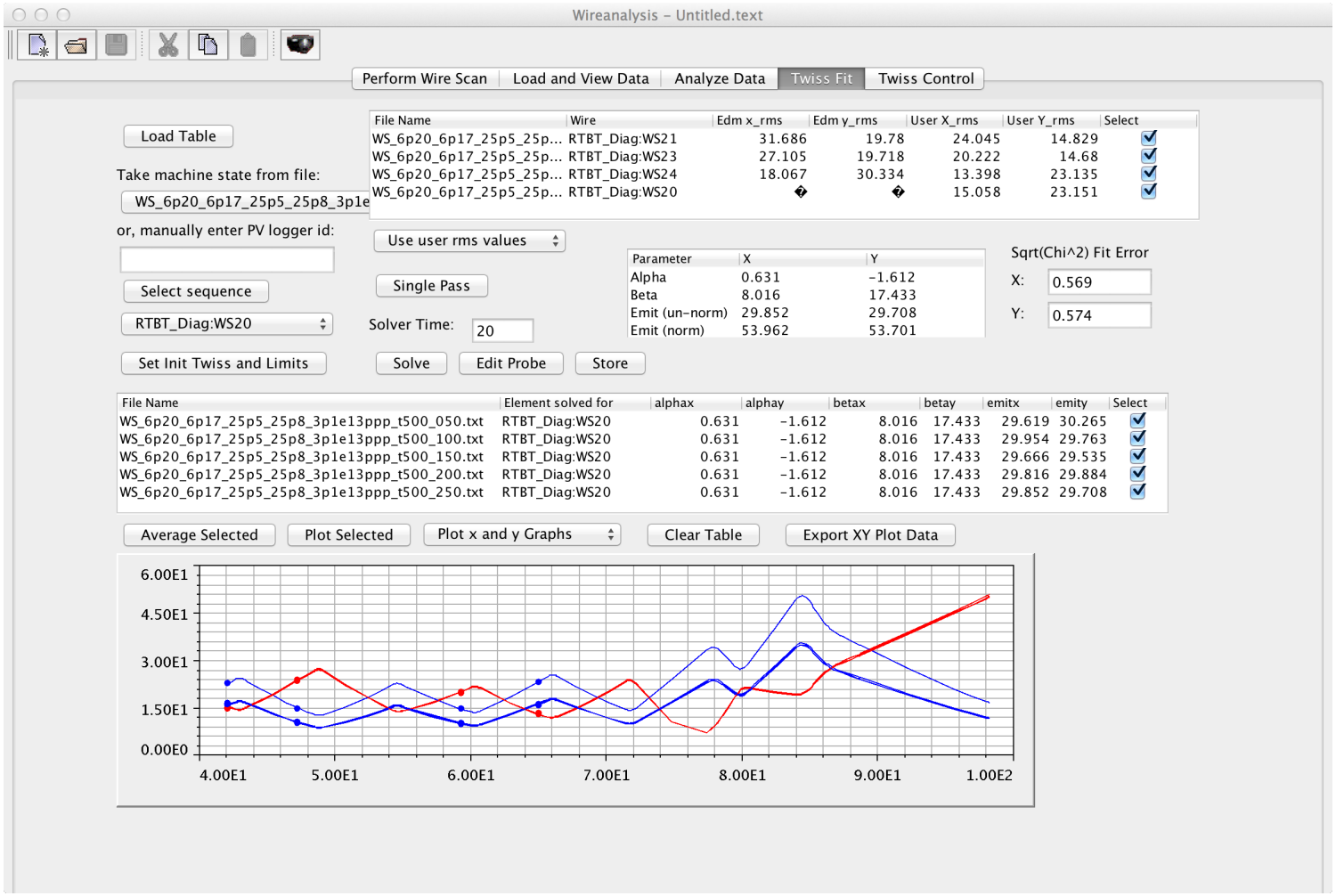

Figure A.8: WireAnalysis Twiss fitting screen after averaging

The single element advancement of the beam shown in Equation 2.1 can be written for an N element array of elements as

$$\begin{pmatrix} x_N \\ x'_N \end{pmatrix} = m^{(N)} \cdot \begin{pmatrix} x_0 \\ x'_0 \end{pmatrix} \tag{A.1}$$

where $m^{(N)}$ is the transport matrix for the N-th element. Therefore the position after element N would be

$$x_1 = m^{(N)}_{1,1} \cdot x_0 + m^{(N)}_{1,2} \cdot x'_0. \tag{A.2}$$

This represents the new position of a single particle advanced through the series of N elements. Next, square both sides and take the average

$$\langle x^2_N \rangle = (m^{(N)}_{1,1})^2 \cdot \langle x^2_0 \rangle + 2 \cdot m^{(N)}_{1,1} \cdot m^{(N)}_{1,2} \cdot \langle x_0 \cdot x'_0 \rangle + (m^{(N)}_{1,2})^2 \cdot \langle x'^2_0 \rangle \tag{A.3}$$

Therefore, the squared RMS beam size depends only on the initial beam distribution parameters $\left(\langle x^2_0 \rangle, \langle x_0 \cdot x'_0 \rangle, \langle x'^2_0 \rangle\right)$ and the transport matrices, $m^{(N)}$. We can build an array of squared RMS beam sizes at different points in the beam transport calculated from the same initial beam distribution parameters and each transport matrix.

$$\begin{pmatrix} \langle x^2_0 \rangle \\ \langle x^2_1 \rangle \\ \cdots \\ \langle x^2_n \rangle \end{pmatrix} = M \cdot \begin{pmatrix} \langle x^2_0 \rangle \\ \langle x_0 \cdot x'_0 \rangle \\ \langle x'^2_0 \rangle \end{pmatrix} \tag{A.4}$$

where

$$M = \begin{pmatrix} (m^{(0)}_{1,1})^2 & 2 \cdot m^{(0)}_{1,1} \cdot m^{(0)}_{1,2} & (m^{(0)}_{1,2})^2 \\ (m^{(1)}_{1,1})^2 & 2 \cdot m^{(1)}_{1,1} \cdot m^{(1)}_{1,2} & (m^{(1)}_{1,2})^2 \\ \cdots & \cdots & \cdots \\ (m^{(n)}_{1,1})^2 & 2 \cdot m^{(n)}_{1,1} \cdot m^{(n)}_{1,2} & (m^{(n)}_{1,2})^2 \end{pmatrix}. \tag{A.5}$$

Now we can rearrange the equation to place all of our known quantities on one side. This will allow us use our beam size measurements to determine our unknown quantities, the initial beam distribution parameters. Using the LSM, we find that

$$\begin{pmatrix} \langle x_0^2 \rangle \\ \langle x_0 \cdot x_0' \rangle \\ \langle x_0'^2 \rangle \end{pmatrix} = \left(M^T \cdot W \cdot M \right)^{-1} \cdot M^T \cdot W \cdot \begin{pmatrix} \langle x_0^2 \rangle \\ \langle x_1^2 \rangle \\ \cdots \\ \langle x_n^2 \rangle \end{pmatrix} \tag{A.6}$$

where

$$W_{i,i} = \frac{1}{\mathrm{cov}\left(\langle x_i^2 \rangle\right)} \tag{A.7}$$

and

$$C = \left(M^T \cdot W \cdot M \right)^{-1} \Big|_{i=j} = \begin{pmatrix} \mathrm{cov}\left(\langle x_0^2 \rangle\right) \\ \mathrm{cov}\left(\langle x_0 \cdot x_0' \rangle\right) \\ \mathrm{cov}\left(\langle x_0'^2 \rangle\right) \end{pmatrix}. \tag{A.8}$$

We have introduced a diagonal weighting matrix W that represents the error in the RMS size measurements. We have also introduced a covariance matrix C where the diagonal terms are the errors of the initial beam distribution parameters.

At this point, the covariance matrix C can be calculated using the known transportation matrix M and the weighted error matrix W. When we know C, we will also know the errors of the initial beam distribution parameters from the diagonal elements. After we have calculated C, we can calculate the initial beam distribution parameters at the position s_0. This beam distribution can then be transported to other points in the lattice or used to calculate the Twiss parameters.

A.4 Derivation of Twiss Parameters Errors

Now that we have the initial beam distribution and their errors, we can derive the Twiss parameters and their errors. We begin by stating the Twiss parameters in

terms of the initial beam distribution parameters

$$\varepsilon_{\mathrm{RMS}} = \sqrt{\langle x_0^2\rangle \cdot \langle x_0'^2\rangle - \langle x_0 \cdot x_0'\rangle^2},\ \alpha = -\frac{\langle x_0 \cdot x_0'\rangle}{\varepsilon_{\mathrm{RMS}}},\ \beta = \frac{\langle x_0^2\rangle}{\varepsilon_{\mathrm{RMS}}}. \tag{A.9}$$

We see that each of these three functions can be written as a general function of the initial beam distributions as such:

$$f = f(\langle x_0^2\rangle, \langle x_0'^2\rangle, \langle x_0 \cdot x_0'\rangle). \tag{A.10}$$

Therefore the error for each function can be defined as

$$\Delta f\left(\langle x_0^2\rangle, \langle x_0'^2\rangle, \langle x_0 \cdot x_0'\rangle\right) = \sqrt{\sum_{i=1}^{p} (\frac{\partial f}{\partial x_i})^2 \Delta x_i^2} \tag{A.11}$$

where x_i represents an array of the initial beam distribution parameters. The errors for the Twiss parameters are as follows:

$$\Delta\varepsilon = \frac{1}{2}\sqrt{\frac{\langle x'\rangle^2 \mathrm{cov}\langle x^2\rangle^2 + \langle x^2\rangle^2 \mathrm{cov}\langle x'^2\rangle^2 + 4\langle x \cdot x'\rangle^2 \mathrm{cov}\langle x \cdot x'\rangle^2}{\langle x^2\rangle\langle x'^2\rangle - \langle x \cdot x'\rangle^2}} \tag{A.12}$$

$$\Delta\alpha = \frac{1}{2}\sqrt{\frac{\langle x'\rangle^2\langle x \cdot x'\rangle^2 \mathrm{cov}\langle x^2\rangle^2 + 4\langle x^2\rangle^2\langle x'^2\rangle^2 \mathrm{cov}\langle x \cdot x'\rangle^2 + \langle x^2\rangle^2\langle x \cdot x'\rangle^2 \mathrm{cov}\langle x'^2\rangle^2}{\left(\langle x^2\rangle\langle x'^2\rangle - \langle x \cdot x'\rangle^2\right)^3}} \tag{A.13}$$

$$\Delta\beta = \frac{1}{2}\sqrt{\frac{(\langle x^2\rangle\langle x'^2\rangle - 2\langle x \cdot x'\rangle^2)^2 \mathrm{cov}\langle x^2\rangle^2 + 4\langle x^2\rangle^2\langle x \cdot x'\rangle^2 \mathrm{cov}\langle x \cdot x'\rangle^2 + \langle x^2\rangle^4 \mathrm{cov}\langle x'^2\rangle^2}{\left(\langle x^2\rangle\langle x'^2\rangle - \langle x \cdot x'\rangle^2\right)^3}}. \tag{A.14}$$

A.5 Harp

The harp, shown in figure A.9, uses the same concepts as the wire scanners to collect a beam profile. However, the harp is a fixed diagnostic that is comprised of 30 100-μm tungsten wires uniformly distributed in each transverse plane. In the horizontal plane, the wires are spaced 1.18 cm apart to measure the horizontal beam size of 17 cm FWHM. In the vertical plane, the wires are spaced 0.589 cm apart to measure the vertical beam size of 4.8 cm FWHM. A third set of wires is mounted along the diagonal. The wires in the harp collect data under SEM, the same physical principle discussed for the wire scanners. Unlike the wire scanners, the harp is capable of collecting full beam profiles from a single accumulated pulse. While the profiles have a fixed resolution lower than the typical wire scanner resolution, the ability to view a single accumulated pulse allows us to look for shot-to-shot variations in the beam distribution. Additionally, the harp is located at the end of the RTBT immediately before the target window and provides the closest beam profile to the on-target beam distribution[73]. Similar to the wire scanners, the harp is limited to averaging over the longitudinal distribution of the beam. Figure A.10 shows a set of typical beam profiles acquired from the harp.

Figure A.9: Image of the Harp located in the RTBT before the target window. Device image courtesy of W. Blokland, SNS.

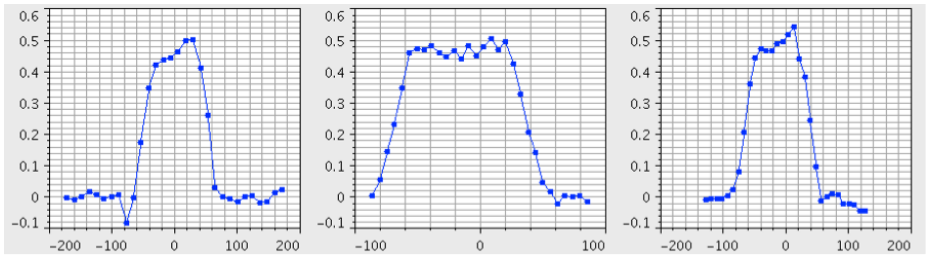

Figure A.10: Horizontal (left), vertical (center), and diagonal (right) profiles from the Harp, as displayed in the data collection application called WireAnalysis.

Vita

Robert Edward Potts III was born to Robert and Julia Potts in Fairfax, VA., on June 12, 1988. He is a proud member of the Class of 2006 from the McCallie High School in Chattanooga, TN. In 2010, he graduated from Embry-Riddle Aeronautical University in Prescott, AZ., with a Bachelors of Science in Space Physics and minors in Aerospace Engineering and Mathematics. Robert was first introduced to particle accelerators in January 2008 by the United States Particle Accelerator School. He has since attended numerous U.S. and international accelerator schools, and accelerator conferences. Robert started as a graduate student in the Department of Physics and Astronomy at the University of Tennessee in the fall of 2010. He joined the Beam Science and Technology (BeST) group, formerly the Accelerator Physics, Beam Instrumentation, and Ion Source (APBIIS) group, at the Spallation Neutron Source (SNS) located at Oak Ridge National Laboratory at the start of 2012. He defended his dissertation and graduated in the fall of 2017 with a Doctorate of Philosophy, with a major in Physics.